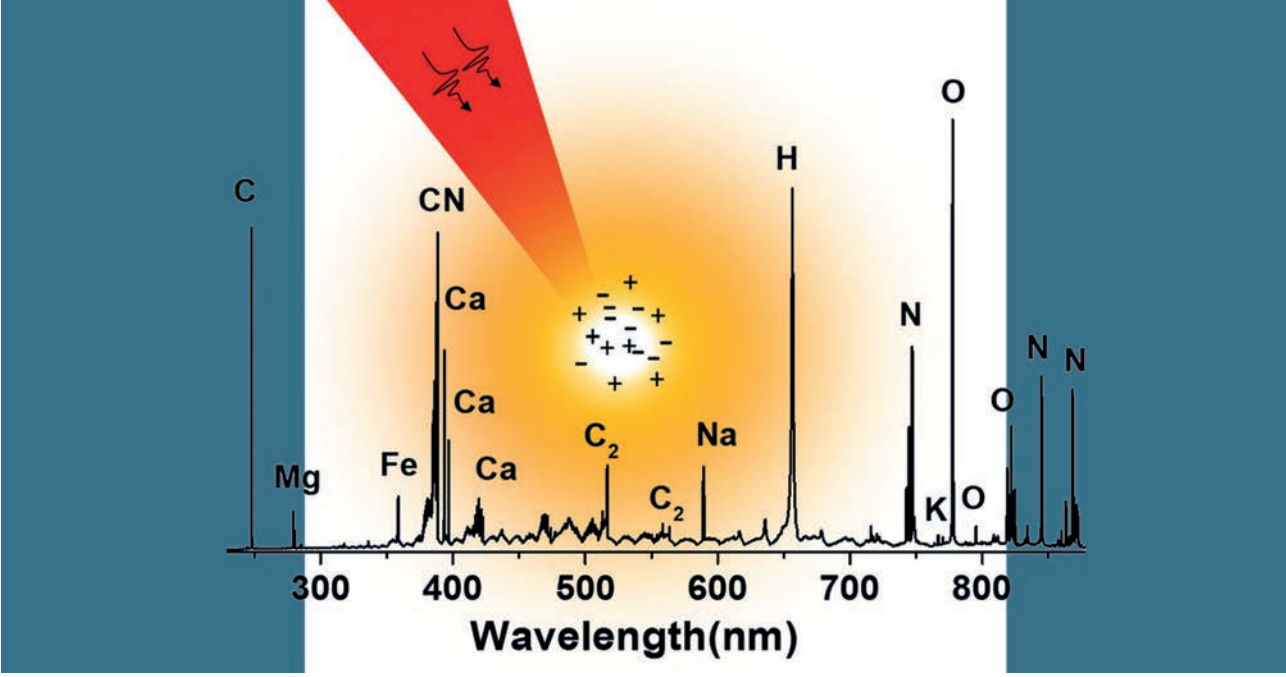

FAU Studien aus dem Maschinenbau 422

Fanuel Mehari

Laser-induced Breakdown Spectroscopy (LIBS) as a diagnostics tool for biological tissue analysis

FAU University Press

Fanuel Mehari

Laser-induced Breakdown Spectroscopy (LIBS) as a diagnostics tool for biological tissue analysis

FAU Studien aus dem Maschinenbau

Band 422

Fanuel Mehari

Laser-induced Breakdown Spectroscopy (LIBS) as a diagnostics tool for biological tissue analysis

Dissertation aus dem Lehrstuhl für Photonische Technologien (LPT) Prof. Dr.-Ing. Michael Schmidt

Erlangen
FAU University Press
2023

Bibliografische Information der Deutschen Nationalbibliothek:
Die Deutsche Nationalbibliothek verzeichnet diese Publikation in der Deutschen Nationalbibliografie; detaillierte bibliografische Daten sind im Internet über http://dnb.d-nb.de abrufbar.

Bitte zitieren als
Fanuel Mehari. 2023. *Laser-induced Breakdown Spectroscopy (LIBS) as a diagnostics tool for biological tissue analysis.* FAU Studien aus dem Maschinenbau Band 422. Erlangen: FAU University Press. DOI: 10.25593/978-3-96147-642-8.

Der vollständige Inhalt des Buchs ist als PDF über den OPUS-Server der Friedrich-Alexander-Universität Erlangen-Nürnberg abrufbar:
https://opus4.kobv.de/opus4-fau/home

Verlag und Auslieferung:
FAU University Press, Universitätsstraße 4, 91054 Erlangen

Druck: docupoint GmbH

ISBN: 978-3-96147-641-1 (Druckausgabe)
eISBN: 978-3-96147-642-8 (Online-Ausgabe)
ISSN: 2625-9974
DOI: 10.25593/978-3-96147-642-8

Laser-induced Breakdown Spectroscopy (LIBS) as a diagnostics tool for biological tissue analysis

Laser-induced Breakdown Spectroscopy (LIBS) als diagnostisches Werkzeug für die biologische Gewebeanalyse

Der Technischen Fakultät
der Friedrich-Alexander-Universität
Erlangen-Nürnberg

zur
Erlangung des Doktorgrades Dr.-Ing.

vorgelegt von

Fanuel Mehari, M.Sc.

aus Erlangen

Als Dissertation genehmigt
von der Technischen Fakultät
der Friedrich-Alexander-Universität Erlangen-Nürnberg

Tag der mündlichen Prüfung:	26.04.2022
Gutachter:	Prof. Dr.-Ing. habil. Andreas Siegfried Bräuer Universität Freiberg Prof. Dr.-Ing. Marc Stamminger Universität Erlangen

Preface

This thesis presents my work on the topic of using the optical analytical technique laser-induced breakdown spectroscopy (LIBS) as a diagnostic tool for biological tissues. My work on the thesis has been very educational both at personal and professional level. I am thankful for all the discussions and the help I have had from the colleagues and employees of the Lehrstuhl für Photonische Technologien (LPT) and Erlangen Graduate School in Advanced Optical Technologies (SAOT) over the years. It has been a privilege working with very talented people at LPT and the SAOT. My special thanks go to the members of my group, medizintechnik at LPT, for creating the wonderful working environment and all the fruitful discussions about my work and the other projects run by the group. The broad spectrum of activities in the group have been inspiring and educational.

I would like to thank especially my supervisor Prof. Dr.-Ing. Michael Schmidt for being supportive and for guiding me to stay focus on the main topic of my work. It is due to his openness to collaborate with different research groups that my thesis has had many successful results. I am also grateful for his support during the difficult times in my personal life. I want to thank Prof. Dr.med. Dr.med.dent. Florian Stelzle, Dr. med. dent. Dr. med. Maximilian Rohde and Prof. Dr. med. Maximilian Waldner for all the colaborations throughout my thesis. They have provided me with all the biological samples I worked with during this thesis and they were behind every medical advice and interpretation of my work.

I would also like to thank my entire family for being there for me. I am specially grateful for my wife Azieb for all the joy you bring in my life. I thank you for all the patience and for being on my side in every aspect of my life. I would like to end this topic by thanking my son Matthias for bringing endless joy in my life.

Table of Contents

List of Symbols and Abbreviations

List of Abbreviations

Abbreviation	Description
AES	Atomic Emission Spectroscopy
AOM	Azoxymethan
CF-LIBS	Calibration Free Laser-Induced Breakdown Spectroscopy
DSS	Dextran Sulfate Solution
ECM	Extra Cellular Matrix
FWHM	Full Width at Half Maximum
ICCD	Intensified Charge Coupled Device
LA-ICP-MS	Laser Ablation-Inductively Coupled Plasma-Mass Spectrometry
LDA	Linear Discriminant Analysis
LIBS	Laser-Induced Breakdown Spectroscopy
LTE	Local Thermodynamic Equilibrium
Micro-SRXRF	Micro-Synchrotron Radiation X-ray Fluorescence
NIR	Near Infra Red
NIST	National Institute of Standards and Technology
OCT	Optical Coherent Tomography
PC	Principal Component
PCA	Principal Component Analysis
ROC	Receiver Operating Characteristics
SGH	Second Harmonic Generation
S-OES	Spark Optical Emission Spectroscopy
UV	Ultraviolet
XRF	X-Ray Fluorescence

List of Symbols

Symbol	Unit	Description
A	s^{-1}	Transition probability
$\alpha_{\frac{1}{2}}$	m	Stark broadening coefficient
c_a	$m\,s^{-1}$	Longitudinal speed of sound
χ	J	Ionization energy
δ	m	Penetration depth
E	J	Energy of a transition
F		optical efficiency
g		Degeneracy of an energy level
K		Class size
λ	m	wavelength
M		Class mean
μ_a	m^{-1}	Absorption coefficient
μ_s	m^{-1}	Scattering coefficient
μ_s'	m^{-1}	Reduced scattering coefficient
n	m^{-3}	Number density
n_e	m^{-3}	Electron density
P		Partition function
S_w		Within class scatter
S_b		Between class scatter
T	K	Temperature
t_d	s	Thermal diffusion time
t_s	s	Stress propagation time
Z		Charge state

List of Figures

List of Tables

1 Introduction

After the invention of the laser, one of the areas of applications that actively sought and continues to use the laser technology is medicine. As early as 1961, the physiological implication of lasers was reported [68]. In 1963, the first application of lasers for dermatology was reported [31]. Ever since, lasers have been used and investigated for the applications of various medical specialties. Ophthalmology, dentistry, neurology, dermatology, otolaryngology, gynecology, cardiology, orthopaedics and general surgery are among the numerous fields that continue to use lasers. Their use ranges broadly from applications that require thermal biostimulation to those that aim to cause coagulation or ablation.

A laser has various characteristics that can be valuable to a physician. These include their monochromaticity and collimated nature. It can provide controllable high intensity of light that can be directed efficiently to desired areas without the need to come into contact with the target. In contrast with the ordinary light, laser light can be accurately quantified and reproduced enabling controllable treatment. Moreover, due to the fact that lasers can be guided through flexible optical fibers, it is possible to use them for minimally invasive treatments such as endoscopic applications. All these motivated the development of laser systems for clinical applications soon after the appearance of the first laser medical applications [15, 31].

The different interaction mechanisms of a laser with the interacting biological sample, owed to the properties of both the laser and the sample, make it suitable for its use in a specific medical application. One such interaction mechanism is damage/ablation of a biological sample through denaturation/vaporization. These effects can be achieved with high flexibility and spatial resolution down to the size of the laser focus. Moreover, these effects do not require the laser to come into contact with the tissue avoiding contamination. This ability to destroy biological samples with unprecedented precision and less complications of contamination has opened a new window for applications that would otherwise pose significant challenge for the traditional mechanical tissue cutting. For instance, with the traditional scalpel, it is extremely challenging to cut out a thin slice of safety margin during the resection of superficial skin cancer. As a result, unnecessary removal of healthy tissue can easily occur. Moreover, cell surgery and other microsurgical procedures would be unimaginable without the help of lasers and other technologies. All these advantages have been the driving factors for vast

research areas in medicine that attempt to exploit the potential of lasers in surgical applications.

To date, different types of lasers have been commercialized and are being used in a wide range of clinical applications. These systems include surgical lasers for both hard and soft tissue ablation. The use of lasers as surgical tools has a number of advantages over the traditional mechanical scalpel. However, the wide use of lasers as surgical tools is hindered by two main limitations: the lack of information about the tissue type being cut and the penetration depth of the laser. The present thesis work aims at addressing the challenge of tissue type determination during laser surgery by targeting elemental composition of tissues in real-time. The technique used here is the emerging optical analytical technique known as laser-induced breakdown spectroscopy (LIBS). Furthermore, the work also investigates the use of LIBS for cancer characterization/diagnostics by monitoring the elemental distribution in cancerous tissues.

2 State of the art

Background

In broad terms, laser surgery refers to the use of laser light to perform surgical procedures for the same effects a surgical mechanical scalpel intends to deliver. The underlying mechanism of tissue ablation using lasers is as a result of the interaction of the laser with the biological sample. To explain the mechanism of tissue ablation, it is first worth to have a brief discussion of the different mechanisms of laser tissue interaction.

The current chapter will first briefly discuss the different laser tissue interaction mechanisms and their medical applications. Following, a more detailed discussion of the interaction domain where tissue ablation occurs will be given. This highlights the interaction mechanism of pulsed-laser energy on biological tissues and the various ablation processes that result. The interaction of pulsed-lasers will be treated separately depending on pulse duration of lasers. Towards the end of the chapter, one section will summarize the reported applications of laser surgery in different medical specialties. At the end, the challenges of laser surgery and reports to address them will be summarized.

2.1 Laser tissue interaction

Like in all other materials, the effect of the irradiation of tissue with a laser light can be dictated by using different lasers and/or by manipulating the laser parameters. The unique monochromatic and collimated nature of laser light enables to easily manipulate its focus size and guidance through very thin fibers in order to adapt for different applications. This is particularly useful for medical applications where the target sample is biological tissue often with complex structure. Moreover, the highly flexible radiation geometry of lasers can also come with a wide range of power further increasing the window of applications. The effect of laser light on a biological sample is not only governed by the properties of a laser but also by the optical properties of the sample.

After reaching a biological sample, laser radiation can exhibit different physical interaction mechanisms. Part of it can be reflected at the boundary between

the tissue and the medium above, a mechanism commonly known as specular reflection. Another part can enter into the sample. After entering, it can be transmitted to subsequent layers, scattered multiple times diffusing back to the medium before or absorbed by the biomolecules in the tissue. The part of the radiation that enters the sample is the most important as it interacts with the sample and tells us about the sample or brings about desired changes in the sample. As a result, the penetration depth of the radiation becomes very important. The penetration depth of a laser light of certain wavelength and intensity depends solely on the absorption and scattering properties of the interacting sample. The absorption property of tissues is dictated by intrinsic electronic, vibrational and rotational structure of their biomolecules [37]. Beer-Lambert's law relates the initial intensity and the final intensity of radiation after passing a medium as follows [73]:

$$I = I_o \exp^{-(\mu_a + \mu_s)l} \tag{1}$$

where I and I_o are the intensities after and before the interacting sample, respectively. μ_a, μ_s and l are the absorption coefficient, the scattering coefficient and the thickness of the sample, respectively. The absorption coefficient can be defined as the probability that a photon can be absorbed per unit length of a medium. The scattering coefficient denoted by μ_s is the probability that a photon will be scattered per unit length of a medium. If evaluation of the penetration depth of radiation is desired, only the photons that are scattered in the direction of the travel of light need to be considered. This is accounted by taking the reduced scattering coefficient μ_s' rather than μ_s.

$$\mu_s' = \mu_s(1 - g) \tag{2}$$

where g is the anisotropy factor expressed as a probability function describing the degree of forward scattering. Its value ranges between 0 and 1. The diffusion theory relates the penetration depth (δ) of light in turbid media such as tissue to the parameters μ_a and μ_s' as follows:

$$\delta = \frac{1}{\sqrt{3\mu_a(\mu_a + \mu_s')}} \tag{3}$$

The aforementioned absorption and scattering properties of tissue molecules vary depending on the wavelength of light. Hence, one wavelength can penetrate deep into the tissue while another can reach only shallow parts of the

tissue. Table 1 shows pulsed lasers that are commonly used for medical applications. The table shows different lasers have different penetration depths in water, pigmented tissue and bloodless unpigmented tissue.

Table 1: Commonly used pulsed medical lasers and their penetration depth in water, pigmented and unpigmented tissue [28, 55].

Laser	Wavelength(nm)	Pulse duration	δ_{water}	$\delta_{unpigm.tissue}$	$\delta_{pigm.tissue}$
ArF	193	5-25 ns	25 cm	<1 μm	
KrCl	222	250 ns	90 cm	1 μm	
KrF	248	2-50 ns	1.5 m	1.2 μm	
XeCl	308	20-300 ns	2.5 m	5 μm	
XeF	351	1-30 ns	5 m	20 μm	
Nd:YAG	532	100 ns-250 μs	10 m	1.1 mm	0.2 mm
Nd:YAG	1064	30-100 ps	3 cm	4 mm	0.9 mm
Ruby	694	20 ns-1 ms	60 cm	5 mm	0.4 mm
Alexandrite	720-800	100 μs	0.2 m	6-8 mm	0.5 mm
GaAS	904	150 fs	5 cm	4 mm	
Ti:sapphire	700-1000	10-100 fs	60-1 cm	5-8 mm	
Ho:YAG	2100	100 ns-250 μs	0.1 mm	1 mm	0.4 mm
Er:YAG	2940	10 ns	0.3 μm	1 μm	
Free electron laser	800-6000	2-10 ps	20 cm-2μm	8 mm-30 μm	
CO_2	10 600	100 ns-1 ms	10 μm	20 μm	

Depending on the requirement of a desired therapeutic or diagnostic technique, a laser with wavelength in the UV, visible or infrared region can be chosen. Superficial ablation of tissues can be easily met by using UV lasers. If deeper probing of a target tissue is needed then infrared lasers are suitable. If the target is some specific body constituent such as water then a laser such as Er:YAG that is strongly absorbed by water can be used.

The absorption of unpigmented tissue (haemoglobin, water, melanin and proteins) as a function of wavelength is shown in Figure 1 [28]. The absorption spectrum of tissue accounts for a number of contributors. The absorption of proteins, DNA and other molecules increases in the UV region [12]. In the near infrared (NIR) absorption is minimal and hence the name diagnostic and therapeutic window is commonly referred to this region. Blood particularly hemoglobin strongly absorbs in the NIR region. This does not have a strong effect on the transport of light as its volume fraction in tissues is low. It should however be noted that in local sense, absorption of blood governs the interaction of light with tissue as it is the main absorber in the body [28].

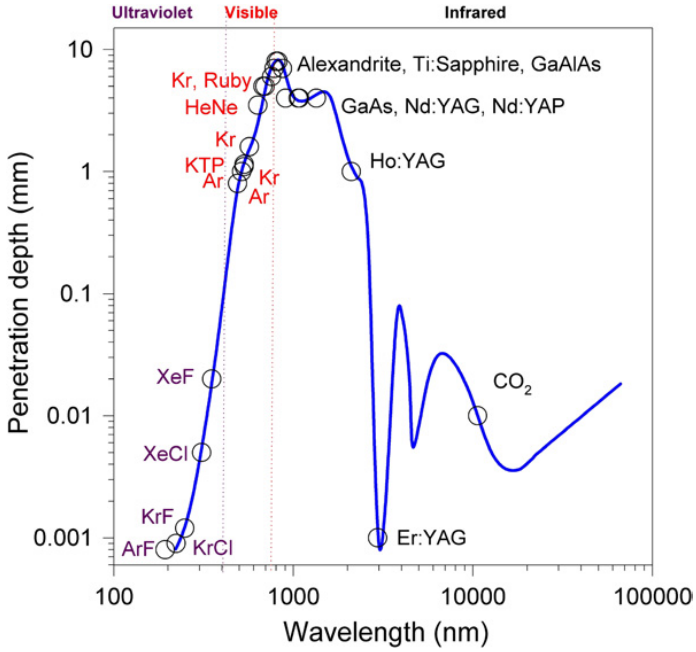

Figure 1: Dependence of absorption and scattering of unpigmented (hemoglobin, water, melanin and proteins) on wavelength.

So far, we have only been focusing on the response of some biomolecules to different wavelengths of light and also briefly on the penetration depth of some pulsed medical lasers in tissues. However, any medical treatment with lasers can not be successful without understanding the required dose or radiation energy supplied. This is commonly termed as the energy fluence and is measured in J/cm^2. When working with pulsed lasers, the duration of the laser pulse becomes the decisive factor since the effect of two lasers pulses with the same fluence and different pulse duration can have completely different effects. This necessitates the use of power density instead of fluence to measure the radiant energy supplied. Power density is interchangeably used with the term irradiance and has a unit of W/cm^2. The interaction of biological tissue with laser radiation depending on the irradiance value (also known as exposure rate) has been elegantly described by the medical laser interaction map [12]. The map depicts the tissue interaction modes depending on the irradiance and the interaction time, in other words duration of the laser pulse. Figure 2 shows the medical laser interaction map reproduced by Peng et al.[55].

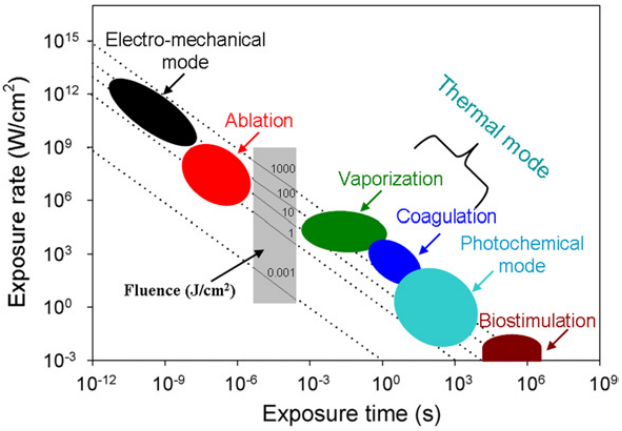

Figure 2: Medical laser interaction map [55].

Biostimulation: This refers to the use of low energy laser radiation at a non-thermal irradiance to stimulate a biological activity. This mechanism is some times named as low-level laser therapy (LLLT) and has medical applications that include reducing pain and inflammation, tissue repair and facilitation of tissue regeneration [7].

Photochemical: This mode mainly concerns with applications that use chromophore compounds capable of inducing specific reactions upon interaction with light. The chromophore has usaully a resonant excitation wavelength that is not absorbed by the tissue it is intended to treat. A good example of application under this category is photodynamic therapy (PDT). In PDT, a photo-sensitizing agent that predominantly accumulates in cancerous tissue is first administered locally or intravenously. The target tissue is then irradiated with a monochromatic light source to excite the photosensitizer which then interacts with other molecules to produce cytotoxic species that irreversibly damage the affected tissue [3].

Photothermal (coagulation and vaporization): Here, the interaction mechanism involves conversion of electromagnetic radiation into thermal energy to vaporize or coagulate a target tissue. A few medical applications of photothermal process and their corresponding temperature range include: protein denaturation (50 - 60°C), dehydration (80 - 100°C), enzyme inactivation (45 - 50°C) and tissue ablation/vaporization (100 - 300°C) [55]. Critical aspect of this mechanism is to perform selective heating that minimizes collateral damage. To do so, thermal diffusion time must be carefully studied often requiring the laser pulse duration to be less than the thermal diffusion time.

Ablation: Ablation involves the expulsion or removal of evaporated material with the help of pulsed lasers. All surgical applications of lasers for tissue cutting and LIBS rely on the ablation process. Since it is essential to this thesis work, a detailed discussion of the ablation process of tissue with pulsed lasers will be given in the next section.

Electro-mechanical: Also known as photomechanical or photodisruptive mode, requires extremely high irradiance in which non-linear processes that result in plasma formation can be observed. Some laser surgery applications and also the tissue differentiation technique used in this work (LIBS) involve the generation of plasma under this interaction mechanism. Hence, the detailed explanation of the photomechanical mode will be part of the various upcoming sections.

2.1.1 The process of tissue ablation with pulsed lasers

Tissue optical and mechanical properties play a major role during the interaction with a pulsed laser. These properties are affected by the composition and morphology of the tissue. We have briefly seen that the optical property is mainly governed by the biomolecular composition and is important in transforming the laser energy to thermal energy. The mechanical property is mainly affected by the structure and morphology. During the interaction with a pulsed laser, the laser induced thermal-mechanical response leads to the ablation of the tissue. Thus, the mechanical property of tissue is also of significant importance during laser ablation of tissues.

Water and extracellular matrix (ECM) dominate the percentage by mass[1] of the majority of soft tissues constituting 55 - 99% and 0 - 35%, respectively [76]. Some of the constituents of the ECM are: water, collagen and other proteins [53]. The portion of the ECM from the total mass changes from tissue to tissue. Some tissues such as corneal stroma, cartilage, skin-dermis and tendons are almost entirely composed of ECM [76]. The ECM has the main function of maintaining the structural integrity of tissues [53, 76]. Hence, it plays important role in forming the mechanical property of tissues. The evidence of the effect of the tissue mechanical strength on the ablation rate of a pulsed laser was reported decades ago. Under the same irradiation conditions, varying ablation rates of tissues with similar optical and thermal properties but different mechanical properties can be observed. This demands a careful

[1] Mass is easier to measure and almost all the elemental composition of tissues in the literature is in mass percentage. This is sufficient in this work since the interest is in the relative concentration rather than the absolute concentration of elements.

consideration of tissue mechanical properties during the development of surgical lasers. On the other hand, this may be beneficial for tissue discrimination techniques which involve tissue ablation like LIBS. This means when tissue is ablated for quantifying its constituents, a tissue with higher ablation rate means higher concentration of its constituents are measured.

The role of the intrinsic properties of tissue such as optical (mainly absorption) and mechanical properties during tissue ablation process has been briefly mentioned above. Governed by these properties, the time scale of thermal rise and thermal diffusion induced by the laser energy are among the driving forces of laser tissue ablation. Upon irradiating a tissue with a laser energy, the absorbed energy results in volume thermal rise and is subject to distribution to the surrounding by diffusion. Thermal diffusion time t_d after volumetric irradiation of tissue and its dependence on the absortption coefficient μ_a and thermal diffusivity k is given by [42]:

$$t_d = \frac{1}{k\mu_a^2} \tag{4}$$

If the laser pulse duration t_p is shorter than t_d (thermal diffusion time), then there will be thermal confinement. In this case, the ablated material can be restricted to the irradiated volume meaning no unintended damage to the surrounding tissue. If there is considerable thermal diffusion, then ablation rate decreases and collateral damage might rise. In the attempt to perform absolute quantification of elements by sampling using a pulsed laser ablation (in techniques such as LIBS), the ratio of t_p to t_d needs to be carefully considered. If the ratio is considerably greater than one, then diffused portion of the energy will not be useful for ablation instead it will contribute to the collateral damage.

Another effect that plays significant role during the process of ablation is the mechanical stress generated by pulsed lasers. The rapid heating of tissue with a pulsed laser, like in other materials, generates a stress confinement. Similar to thermal confinement, the stress confinement depends on the propagation time of stress t_s. The stress propagation time t_s depends on the absorption coefficient μ_a and the longitudinal speed of sound in the medium c_a as follows [76]:

$$t_s = \frac{1}{\mu_a c_a} \tag{5}$$

When the pulse duration t_p is less than or comparable to the stress propagation time t_s, stress confinement may lead to fracturing and spallation of the irradiated volume assisting the ablation process [22]. Therefore, in order to have precise ablation of tissue either for surgery or analysis, it is important to consider the volume of interaction that confines the laser energy. However, this works effectively only when there is a careful consideration of the relation of the pulse energy and the thermal diffusivity as well as the stress propagation time. Laser ablation is a complex process that involves thermodynamics and kinetics of different phase changes, and other properties that are time dependent. The brief treatment of the process of tissue ablation with pulsed lasers here attempts only to highlight the importance of the laser pulse duration with regard to the ablation process.

Over the years, there have been numerous studies of femtosecond and nanasecond pulsed lasers in surgery and medical applications of LIBS. Little has been reported about the use of picosecond lasers in these regards. In the case of femtosecond lasers, the heat transfer from the irradiated area is negligible and there is no interaction of the laser with the plasma. As a result, the laser energy is highly localized resulting in a controlled precise ablation[60, 76]. Whereas in nanosecond lasers, the plasma propagates into the remainder of the laser pulse resulting in a further heating of the plasma. In nanosecond lasers, there is a relatively increased heat affected zone. Consequently, the crater of a nanosecond laser is characterized with less controlled geometry. These characteristics of lasers have motivated the use of lasers for various surgical applications.

2.2 Lasers as scalpels in various surgical specialties

The main reasons for the choice of using a laser for a surgical procedure are the benefits it delivers both to the patient and the clinician. When an appropriate laser is used the patient may experience less pain due to the sealing of nerve endings. The patient may also benefit from reduced risk of infection as there is no contact involved and the laser may also kill bacteria along its path. The benefits to the clinician can be improved visibility due to less bleeding and less need for suturing which can reduce the procedure time. The surgeon also benefits from high precision and controllability. Below are some of the common surgical applications of lasers.

Dentistry: Among the different applications of lasers in dentistry include soft tissue surgery, hard tissue treatments and periodontology. Some of soft tissue surgery applications are tumor removal and gingivectomy where diseased gum

is removed or reshaped. Treatment of hard tissue include removal of caries and preparation of cavity during refilling. There have been reports that indicate using laser for hard tissue removal causes far less discomfort and reduced over excavation compared to mechanical drills. In periodontisis, which is among the infectious bacterial diseases, the removal of the bacteria by laser irradiation is being advocated as an alternative technique. A photosensitizer chemical is first applied and then a laser is used to induce photochemical reaction that kills the bacteria.

Dermatology: Laser ablation can be used to remove skin lesions or layers of skin that would otherwise be challenging for traditional scalpel to cut without having precise control on the thickness of the safety margin of the healthy tissue. Lasers are also used to remove spider and varicose veins. In general, they are used to vascular lesion removal, hair removal, skin resurfacing, tatoo removal and to treat capillary vascular malformations.

Urology: Owed to endoscopic access to urologic organs, different therapeutic procedures in urlogoy now use fiber based lasers. Laser lithotripsy and prostatectomy now widely use lasers in the photothermal, photochemical and photomechanical modes.

Opthalmology: Without the laser, perhaps it would not have been possible to perform minimally invasive eye micro-surgery. Here, the laser stands on top of other techniques mainly due to the natural access the eye provides for light to reach its different parts. Intraocular structures can be disrupted with the help of the shock wave when a laser is used in the photodisruption mode. Photoablation mode can be used for refractive eye surgery. Vascular eye diseases can be treated using lasers working in the photocoagulation mode.

Gynecology: Due to high precision of lasers, they are being used in gynecology for resection, ablation, coagulation and haemostasis of tissue including cancer. The advantage of lasers in the destruction of any cancerous tissue in gynecology (generally in oncology) with the help of different modes is that the risk of buildup of new colonies elsewhere by seeding tumor cells is low. This is due to less bleeding and the killing of cells along the path of the laser.

The above fields are among other therapeutic applications of lasers that include: orthopedics, cardiology, craniotomy, neurology and many others. All these fields are already using laser systems in clinical environments. A vast and growing research of using lasers for various clinical applications has been and continues to be reported.

2.3 Challenges of laser surgery

As was briefly discussed, the application of lasers as surgical tools is growing and is entering a wide spectrum of medical specialties. However, there are some limitations of the technique that hinder its wider expansion. One of the major limitations is the lack of information of the tissue type that is being ablated by the laser. Due to the remote nature of laser ablation process, the surgeon does not have tactile feeling which is available in the traditional mechanical surgery. With the help of the tactile feeling, a surgeon can be able to tell among different tissue types in order to differentiate them. The lack of such information means that unintended damage of tissues/organs such as nerve may occur. Even though unnecessary removal of any functional body part is not required, the damage may not be significant when the laser incision is in known anatomical structure with no potential implications. However, in procedures where deeper cuts are involved in sensitive regions and also during removal of diseased part of an important tissue/organ, any damage by the laser may have significant implications in the health of the patient or can even be life threatening. Therefore, laser surgery needs a means of remote tissue differentiation that can be used as a feedback to perform tissue specific ablation.

Another major challenge for laser surgery is the unknown penetration depth of the laser. This limitation is also connected to the fact that laser based surgery is contact less. As the laser cuts deeper into the tissue, especially for high ablation rates, damage could easily be inflicted to tissues found deeper at the point of ablation. In order to prevent such damages, a common practice is measuring the incision geometry and continuous visual inspection. These lead to increased time of treatment and complicates the surgical procedure. At times, visual monitoring and measurement of incision depth may not work. This is true in procedures requiring microns scale precision. An example is laser cochleoctomy where an opening in the ear cochlea is drilled to access the inner ear requiring beyond human visual accuracy. Therefore, another requirement for laser surgery process is remote monitoring of the laser incision depth.

An ideal laser scalpel should be able to provide information about the type of tissue that is being ablated and the penetration depth of the laser in real-time, remotely, with high accuracy and under the normal surgical environments. One means to achieve this goal is to integrate a feedback mechanism that guides the surgical laser while fulfilling the requirements. Therefore, the feedback mechanism should either provide both tissue type information and the penetration depth of the laser or two different techniques need to be

combined. In the effort towards addressing these problems, solutions based on optical techniques have been proposed and continue to be subjects of investigations. In the coming section, a brief summary of some of the reported optical based techniques for the application of laser surgery feedback system and their limitation for the application is discussed.

2.3.1 Optical techniques for tissue discrimination

Almost all the reported tissue discrimination techniques for laser surgery feedback mechanism are optical based. This is due to the ability to measure remotely. This section will summarize some of the reported optical techniques for tissue discrimination.

Diffused reflectance spectroscopy (DRS): DRS is a technique that measures and analyses scattered light. When a tissue is illuminated with white light, the part that enters the tissue is scattered multiple times and part of it returns to the surface carrying information about the interaction with the tissue. Since different tissues have different interaction properties, DRS could be used to differentiate tissues. It has already been used to differentiate mice soft tissues (fat, muscle, nerve and skin) under in-vivo conditions [70]. Due to the sensitivity of DRS to the surrounding light, the study used minimized environment light and obtained very high differentiation accuracy.

Fluorescencespectroscopy (FS): FS is the measurement and analysis of the fluorescence emission that originates from one or more fluorophores in tissue. Depending on the content of tissue, the intensity and profile of the fluorescence signal may vary. Discrimination of different ex-vivo tissues (different bones, soft tissues and salivary gland) with the help of fluorescence spectroscopy has been studied [71]. Here was also the surrounding light dimmed in order to minimize its effect on the FS signal. Fluorescence guided selective removal of caries in tooth in-vitro has also been reported [24]. The study concluded that based on a threshold level determined, the endpoint of the treatment of a caries could be accurately determined as opposed to the traditional subjective means.

Raman spectroscopy (RS): This is a molecular-vibrational spectroscopy technique used to detect molecular fingerprints. The technique involves excitation of a sample with a monochromatic light source and detecting the very weak inelastically scattered light. The weak nature of the signal often requires a darkened environment if not without direct illumination of the measurement point with other light sources. RS has been used to increase the accuracy of brain tumor surgery [38].

Optical Coherence Tomography (OCT): OCT is an imaging modality similar to ultrasound imaging where the correspondence to the reflected acoustic waves is the intensity of the back reflected light. Typical image resolution is in microns scale and imaging depth is a few millimeters. OCT can be used to guide a laser surgery process by monitoring the geometry/depth of the incision in real-time [17]. Due to shallow penetration depth and high resolution, it is suited mostly for micro-surgery applications such as cochleostomy [84]. Obtaining qualitative tissue information using OCT depends on the scattering contrast among tissues hence can be feasible if the tissues in the target region have good scattering contrast.

The aforementioned techniques are some examples of the reported studies of remote tissue type detection and determination of the depth of incision during laser surgery. Other techniques such as photoacoustic and magnetic resonance imaging to guide the laser surgery process have also been reported [1, 6, 10, 46, 65]. One emerging approach to determine the type of tissue being ablated in real-time is LIBS. The current work uses LIBS to establish a differentiation model for various tissues based on their elemental composition reflected in their corresponding LIBS spectra. Hence, before going to the principles of LIBS, it is worth discussing the elemental composition of tissues briefly.

2.3.2 Tissue elemental composition

The study of the chemical composition of the human body is extremely wide. The vast body of the literature deals with the composition of specific organs in terms of constituent molecules. Often the details are limited to major organs such as: skin, bone, brain white/gray matter, liver, heart, kidney, lung, pancreas and other major organs. The elemental composition of these organs is often detailed the lowest down to the common molecules such as: water, lipid, ash/mineral elements and proteins. For elemental analysis techniques, a complete validation of measurements on tissues is only possible if the exact elemental composition of the target tissue is available. As far as this work is concerned, only indicative elemental composition of the tissues could be found and was found to be sufficient for comparison. This means some tissues will be assumed to have similar composition to an organ for which they are the building blocks. For example, since the composition of peripheral nerves is not given, it can be assumed to resemble the composition of white brain matter [36]. The table below summarizes the elemental composition percentage by mass of some of the samples used [80]. It is worth noting that there is no claim of one to one similarity of the tissues presented in the table and those used for experiments here under any circumstance. This is because the preparation

process for both could be completely different. Therefore, it is expected to see some differences in the presence of mainly trace elements.

Table 2: Elemental composition (% by mass) of body tissues [80].

Tissue	H	C	N	O	Elements with Atomic Nr. >8
Fat tissue	11.2	51.7	1.3	35.5	Na(0.1), S(0.1), Cl(0.1)
Gray matter brain	10.7	9.5	1.8	76.7	Na(0.2),P(0.3),S(0.2),Cl(0.3),K(0.3)
White matter brain	10.6	19.4	2.5	66.1	Na(0.2),P(0.4),S(0.2),Cl(0.3),K(0.3)
Connective tissue	9.4	20.7	6.2	62.2	Na(0.6),S(0.6),Cl(0.3)
Skeletal muscle	10.1	17.1	3.6	68.1	Na(0.1),P(0.2),S(0.3),Cl(0.1),K(0.4)
Skeleton-Cartilage	9.6	9.9	2.2	74.4	Na(0.5),P(2.2),S(0.9),Cl(0.3)
Skeleton-Cortical	3.4	15.5	4.2	43.5	Na(0.1),Mg(0.2),P(10.3),S(0.3),Ca(22.5)
Skeleton-Spongiosa	8.5	40.4	2.8	36.7	Na(0.1),Mg(0.1),P(3.4),S(0.2),Cl(0.2), 2* K(0.1),Fe(0.1),Ca(7.4)
Skin	10	25	4.6	59.4	Na(0.2),P(0.1),S(0.3),Cl(0.3),K(0.1)

The values in table 2 are exemplary taken from the indicated reference. For some tissues such as fat and skeletal muscle, three different compositions with slight changes of concentration of some elements are given in the source. However, the deviations are not significant enough to create ambiguity with other tissues and hence only one was selected to give indicative elemental composition. In the LIBS measurements of the samples used in this work, the information in table 2 will at times be taken as a reference for the relationship among the concentration of the different elements. In the case of cancerous tissue, the focus will be only on the relative distribution of elements between the cancerous and healthy tissue.

Differentiation of a specific tissue from all other tissues may not be necessary as all tissues are not found close to each other. However, there are some anatomical regions where several tissues are found in proximity. Therefore, in the investigation of the differentiation of healthy tissues here, the selection of tissues will be explicitly mentioned in their respective sections highlighting the target surgical application.

2.3.3 Healthy and cancerous tissues

In the study of cancer, the term carcinoma classically describes malignancy resulting from dysfuntional epithelial cells. However, new studies suggest that in addition to the epithelial disfunction, tumor microenvironment can also be crucial for carcinogenesis [2]. As a result, the diagnosis, therapy and

control of cancer need to consider the disease to occur in the tissue, not in the individual cells [2]. This has lead to a growing interest in the study of the tumor microenvironment.

There are a number of aspects of the tumor microenvironment that are notably different from normal tissue (e.g. acidity, overexpressed proteases, hypoxia) [81]. These properties have been the targets of many therapeutic and diagnostic studies. Apart from the molecular aspects of the tumor environment, observing the relative concentration of elements at a micron scale between normal and tumor tissue to reveal the relation between the distribution and the progress of the disease is also emerging. For example, it has been reported that there is a correlation between the distribution of mineral elements and oestrogen receptor status in breast cancer [25]. The imbalance of mineral elements between colorectal liver metastases and the surrounding normal liver tissue has also been used for detecting cancer in a tissue biopsy [26].

2.4 Techniques for monitoring the elemental distributions in tissues

Imaging tumor whether in-vivo or ex-vivo is one of the most active areas of research across a wide field of diagnostic and therapeutic medicine. Optical imaging techniques are among the actively used modalities. With the interest to study of the tumor microenvironment, a number of techniques have been used for the monitoring of elemental distributions in the microenvironment.

Endogenous mineral elements have been reported to be important constituents of cells. Elements like Ca and trace metallic elements such as Fe, Cu and Zn are involved in a number of biological processes and hence their relation to the development and progress of cancer is drawing the attention of various studies. Increased levels of Zn, Cu and Ca whereas reduced Fe level in breast cancer tissue than the surrounding healthy region have been observed using Micro-SRXRF [26]. To investigate the toxicological effects of cancer treatment drugs, LA-ICP-MS has been used to spatially resolve their accumilation in target tissues [74]. Time resolved ICP-MS based measurement of the masses of Fe, Zn, Cu, Mn, P and S were also found to be significantly higher in two cancer cell lines compared to control cells [77]. A study of colorectal cancer on 50 human subjects with conformed diagnosis of the disease has reported elevated levels of Zn, Cr, Mn, Sn, Cu, Al, Pb and Fe in the subjects based on measurement of flame absorption spectroscopy (no spatial information).

The details of the working principles of the above techniques are abundant in the literature. Here, what is important to highlight is that these techniques have very high sensitivity and accuracy. However, the complexity and the operation conditions of these techniques limit their wide usage in routine laboratory research activities. Therefore, an alternative technique that is: low cost, easy to use, that requires no/simple calibration and can readily be employed in normal laboratory conditions would have significant contribution in the understanding of the microenvironment of different diseases and particularly in the study of cancer pathologies. One potential technique with such capabilities is LIBS. LIBS has been used in studying the distribution of nano-particle drug agents in mice kidney [30]. This suggests that LIBS has the potential to offer a cheap and easy way of characterizing the distribution of endogenous elements in tissues.

2.5 Laser-induced Breakdown Spectroscopy (LIBS)

LIBS is an atomic emission spectroscopy (AES) of a laser-generated plasma that uses a focused pulsed laser for sampling, atomization and excitation of the sample material. Unlike other conventional AES techniques, LIBS does not require adjacent devices such as electrodes and coils to atomize and excite the sample. This allows the ability to analyze samples remotely and without the need for any preparation. LIBS is characterized by easy, fast, relatively cheap and capable of in-situ elemental analysis on all types of matter (solid, liquid or gas). These features make LIBS a versatile technique for a wide range of applications including nuclear power stations, deep in the ocean and space exploration. LIBS is also recently drawing attention for medical applications and the number of related studies is growing [14]. The advance in lasers, spectrographs, detectors and light delivery system has been the driving factor for using LIBS for conditions which would not be feasible with the conventional techniques. Qualitative and quantitative elemental analysis is possible with LIBS by investigating the wavelength and intensity of the emission lines, respectively.

2.5.1 Fundamentals of LIBS

For a laser in the nanosecond or shorter regime which is focused to reach irradiance value higher than 10^9 W/cm^2, the material at the laser focus experiences explosive ablation due to absorption of the laser energy [16]. Compared to the pulse duration, energy dissipation via vaporization is relatively slow. In addition, the high recoil pressure of the vaporized material above the surface prevents further vaporiztion. When the temperature of the interaction region

reaches more than the critical temperature, explosion and formation of plume is observed [78]. Russo and Chan [16] showed that the process of ablation at power densities larger than 1GW/cm² can be considered to be stoichiometric ablation owed to the rapid heating and the explosive ejection of the surface material. Therefore, for laser ablation processes under the indicated conditions, the composition of the material in the plume can be considered to be representative of the sample. This explains the requirement for LIBS to work with nanosecond or shorter pulsed lasers delivering irradiance values in the the $\frac{GW}{cm^2}$ or above when focused on the surface of a sample.

The typical irradiance value of a focused LIBS laser on a sample surface exceeds the breakdown threshold of the sample resulting in a high temperature and high density plasma. Absorption of the laser energy through processes such as multiphoton ionization first generates the core of the plasma when collision effects are negligible. Then the core rapidly grows through further absorption of the laser energy by electrons and through impact ionization. The plasma continues to expand even after the termination of the laser due to the difference in temperature and pressure with the ambient atmosphere. As the energy source terminates, the plasma starts to cool down through various processes some of which involve radiation of electromagnetic waves. These radiative processes particularly those involving atomic species are the primary targets in LIBS.

As LIBS measures the emissions from a plasma, it is worth briefly looking at the different emissions observed. *Free-free* radiation, a continuum emission occurs due to transitions between two free energy levels for instance radiation from a moving charge as it decelerates (Bremsstrahlung). *Recombination* (free-bound) radiation occurs when a free electrons recombines with an ion (continuous radiation). *Line* radiation, a primary interest in LIBS, occurs due to transitions between bound levels of the atoms in the plasma (neutrals and ions). The time periods of these emissions in relation to the laser pulse is depicted in figure 3. In contrast to conventional spectroscopy where the interest is mainly on the atomic structure of an isolated atom, the radiation from the plasma depends on the properties of the plasma as well. Therefore, the properties of the elements in plasma and that of the plasma play an important role in quantifying the elements using LIBS.

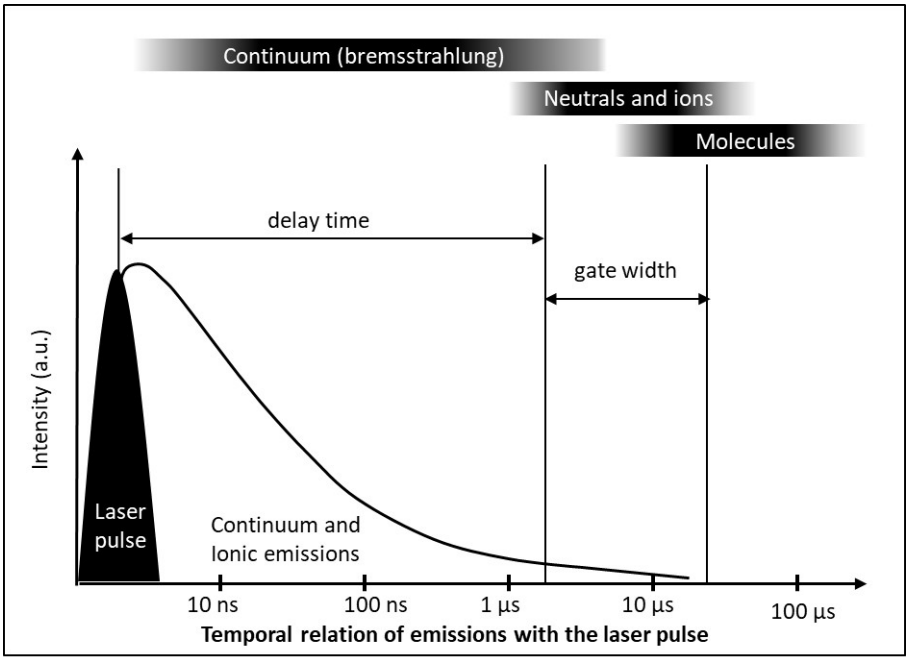

Figure 3: A rough temporal relation of different emissions from plasma with the laser.

The spatially integrated intensity of an emission line corresponding to k-i electronic transition of a species in charge state Z (for neutral atoms $Z = 0$, for singly ionized $Z = 1$, and so on) of element α in an optically thin plasma in local thermodynamic equilibrium (LTE) is given by [33]

$$I^{\alpha}_{ki,Z} = F n^{\alpha}_{Z} \frac{g^{\alpha}_{k,Z} A^{\alpha}_{ki,Z}}{\lambda^{\alpha}_{ki,Z} P^{\alpha}_{Z}} exp(-\frac{E^{\alpha}_{k,Z}}{k_B T}) \quad (6)$$

where F is a parameter that takes the optical efficiency of the collection optics as well as the plasma density and volume into consideration, n is the number density of the species in the ionization state Z, g is the degeneracy of the upper energy level k, A is the transition probability, λ is the transition wavelength, P is the partition function, E is the energy of the transition, k_B is the Boltzmann constant and T is the plasma temperature.

If the temperature of an optically thin plasma in LTE and the experimental factor are known, then it is theoretically possible to correlate the concentration of a given species with the intensity of its emissions provided that an intensity

and wavelength calibrated spectrometer is used. Determination of elemental concentration using the theoretical approach is called calibration-free LIBS (CF-LIBS)[18]. Another approach of quantifying elemental composition is calibration based LIBS. This is based on generating a calibration curve using samples of known concentrations. Before discussing the different approaches, a brief discussion of the most basic laboratory LIBS setup will be given. Figure 4 depicts a typical laboratory LIBS setup.

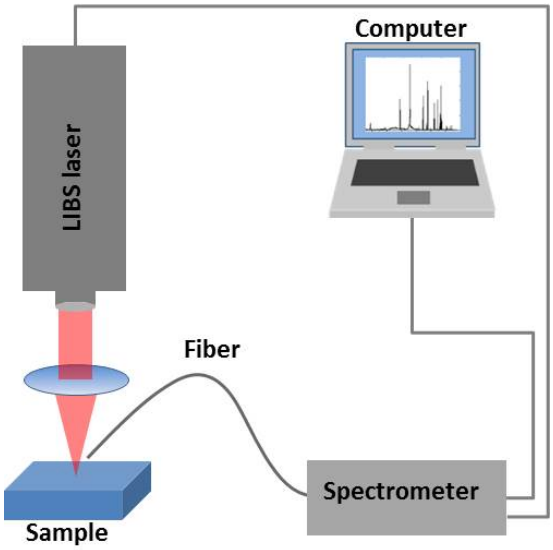

Figure 4: Typical laboratory LIBS setup.

The main components necessary for a LIBS setup are the LIBS laser, a spectrometer, a computer for data acquisition and control, and a lens to focus the laser light and a fiber to guid the plasma light to the spectrometer. Video microscope system can be included in the setup to visualize the sample and for ease of finding the focus of the LIBS laser.

Lasers for LIBS

In selecting a laser for LIBS, the basic parameters which need to be considered are: the pulse duration, the pulse energy, the wavelength and the number of pulses when a burst of lasers is used. The difference between measurements based on a single pulse and a burst of pulses is that in the later case the pulse energy is too low to generate analytically useful plasma. Therefore, multiple pulses are used per single measurement integration. The measurement is often synchronized with the last pulse in the case of double pulse LIBS and the

first pulse in case of more than two pulses (measurement time window sees all the lasers). The most common multi pulse approach is double pulse LIBS. In double pulse LIBS, two laser systems are used and synchronized in such a way that one is used for ablation and the other for analyzing. A collinear or orthogonal arrangement with temporal separation between them is used. The schemes of double pulse LIBS are complicated and the most commonly used approach is based on single pulse. Therefore, the focus will only be laid on a single pulse based system.

Pulse duration: The work horse lasers in LIBS typically have nanosecond pulse duration. On the other hand, there is also significant work in LIBS with femtosecond pulsed lasers. A considerable amount of heat transferred to the sample is observed when the period of lattice vibrations in a typical solid sample is much smaller than the laser pulse duration [62]. This is typically the case for nanosecond and picosecond pulsed lasers. In the case of femtosecond lasers however, the pulse duration is comparable to the period of lattice vibrations. Therefore, there is no significant heat transfer to the material [62]. This is evident when the ablation craters of a nanosecond and a femtosecond pulsed lasers are compared. The nanosecond laser crater is characterized by rough edges and condensed particles in its surrounding as a result of thermal effects. In contrary, the crater of a femtosecond laser is seen to have clean and smooth edges indicating minimal heat effects. The mechanisms of ablation and plasma generation is different for nanosecond and femtosecond lasers due to the pulse duration difference. In a nanosecond laser pulse, ablation and ionization occur during the laser pulse. Typically, the first few nanoseconds of the laser initiate the ablation and the remainder of the laser then ionizes the ablated material. Whereas in a femtosecond laser pulse, these processes do not occur until the end of the laser pulse [62]. Apart from the very high cost, femtosecond lasers are clearly beneficial for medical LIBS as they provide higher precision and minimal heat affected zone.

Pulse Energy: In general, the higher the pulse energy the more the ablated mass. However, the energy related parameter in LIBS is the irradiance at the focus of the laser. This is dependent on the pulse energy, pulse duration and the focus size which in turn depends on the wavelength. Hence, it becomes difficult to treat the pulse energy alone without considering these parameters. However, it is worth mentioning that in order to obtain reproducible results, the pulse to pulse energy stability, pulse duration stability and the uniformity of the intensity distribution of the laser need to be as high as possible.

Wavelength: Considering a nanosecond laser, the laser wavelength affects the LIBS process in two ways: the interaction with the material and the

plasma formation process [19]. For shorter wavelengths in the UV region, the penetration depth is shorter resulting in higher volumetric energy density compared to longer wavelengths. This is implicated with efficient ablation of the irradiated zone. The main influence of the wavelength falls on the plasma formation process. The electron generation and growth in the plasma can be a result of collision or multiphoton absorption. When longer wavelength lasers are used, collision induced ionization becomes the dominant mechanism. Whereas in the case of shorter wavelengths, ionization through multiphoton absorption becomes dominant.

Detection systems for LIBS

Since in LIBS emission lines from elements are measured, if a single emission line from an element is targeted, then a simple combination of a filter and a photomultiplier tube (PMT) can be used. However, LIBS applications predominantly target multiple emission lines in a given spectral range which is often in the spectral range from 190 nm to 1100 nm. Therefore, the most common detection systems used are those that cover a spectral range of interest with a desired spectral resolution. The most common devices in LIBS are the Echelle and the Czerny-Turner spectrometer designs [63]. In the Czerny-Turner design, light enters through an entrance slit and is measured by a detection optics after guiding and dispersing by a system of mirrors and a grating. Recently, the echelle spectrometer design has been commonly used [9]. In the echelle design, the grating is placed at high angle resulting in large dispersion. After the grating, a prism is used to separate the spatially mixed diffraction orders in the orthogonal direction to the dispersion. The two dimensionally distributed light is then detected by a 2-dimensional detector. The most common detectors used are charge coupled device (CCD) and the Intensified CCD (ICCD). The spectrometer software is then used to perform wavelength and intensity calibration. The ICCD based spectrometers are suitable for measurements that require high temporal resolution and are capable of providing with measurement delay time and gate width of a few picoseconds and a few nanoseconds, respectively.

The simplest application of LIBS with the help of the common devices used is to identify the type of elements in a sample by comparing the measured emission lines with emission databases in the literature such as the database of the National Institute of Standards and Technology (NIST)[57]. However, the most appealing application of LIBS is to perform quantitative analysis of elements. The following two sections will briefly describe the two approaches

used to perform quantitative analysis: LIBS based on calibration curves and calibration-free LIBS.

2.5.2 Quantitative LIBS based on calibration-curve

The conventional approach to perform quantitative analysis using LIBS is to construct a calibration curve using standard reference samples with different concentration of the elements of interest. The reference standards with different concentration of the target elements are first prepared and LIBS measurements are used to correlate the elemental concentration with the measured intensities of the elemental emissions. This is then used to determine the concentration of the target elements in a sample with the same matrix property but unknown concentration of the analyte element [18]. One calibration curve needs to be prepared for each type of substrate composition in which the element is embedded. This has the drawback that the sample and the references need to be matrix matched. If the sample and the standard do not have the same matrix, then the analysis becomes semi-quantitative that may not deliver accurate results. In order to overcome the requirement of reference samples, an approach that does not depend on calibration curve from reference standards was first developed and patented by Ciucci et al.[18]. Since then, different approaches for calibration free LIBS have been published. The main idea behind these techniques is understanding the physical properties of the LIBS plasma and this will be discussed in the next section.

2.5.3 Calibration-free LIBS (CF-LIBS) for quantitative analysis

The key aspect of the CF-LIBS approach is to understand the plasma process and its parameters. The CF-LIBS procedure is applied mainly under three assumptions of the plasma conditions [18]. These are: the ablation process is stoichiometric, during the measurement the plasma is optically thin and the plasma is under local thermodynamic equilibrium (LTE). Once these conditions are met, Saha equations can be used to estimate the density ratios of species in different ionization states allowing the absolute quantification of elements.

Stoichiometeric ablation: Stoichiometric ablation ensures that the plasma composition is the composition of the sample. Therefore, it is absolutely important for LIBS measurements to be undertaken with irradiance values that ensure stoichiometric ablation. It was already discussed that the typical irradiance value used in LIBS often exceeding 1 GW/cm^2 is sufficient for stoichiometric ablation of solids (mainly metals) according to Russo et al.[16].

Local thermodynamic equilibrium (LTE): For high density plasma, the collisional processes dominate and the radiative processes become negligible. In LTE, a detailed balance among the collisional processes exists. Under such conditions,"the population densities in the specific quantum states are those pertianing to a system in complete thermodynamic equilibrium, which has the same total (mass) density, temperature and chemical composition as the actual system" [34].

The temperature used under LTE is the electron temperature which is described as the distribution function (that follows Maxwell-Boltzmann distribution) of the electron velocities which dominate the reaction rates. Therefore, under this condition, the electron temperature can be used to describe the population of levels of a given species according to Boltzmann distribution and the relative populations of successive ionization states of a given element according to Saha distribution [34].

Optically thin plasma: One of the characteristics of the spectral lines measured during LIBS is that they are resonant to the transition states of the emitting species and hence get reabsorbed by the plasma itself. A process often referred as self-absorption [19]. As a result, the measured intensity of the lines can be lower than the actually emitted intensity by the species and often have broader line width [13]. Consequently, the concentration of the elements with self-absorbed lines can be underestimated. Therefore, it is recommended that the selected spectral lines for quantitative analysis are not those that suffer from self-absorption. One of the upcoming sections briefly describes the procedure to ensure LIBS measurements during the time window when the plasma can be assumed to be optically thin.

The challenges associated with CF-LIBS measurements are to fulfill the aforementioned conditions. For stoichiometric ablation, sufficient power density should be ensured and the laser should be focused slightly inside the sample to avoid ionization of the air above instead of the sample itself [16]. To ensure that the plasma is optically thin and under LTE, the common approaches taken will be briefly discussed in the coming sections.

Window for optically thin plasma

To check whether the plasma is optically thin, a criterion can be established using equation (6). To do so, two lines of a given element with transitions ki and yx in the same charge state Z can be taken [32]. If they are selected in such a way that they are closer in the spectrum, the efficiency factor of the

collection optics can be cancelled out and the ratio of the integrated intensity of the two lines I_{ki} and I_{yx} can be written as

$$\frac{I_{ki}}{I_{yx}} = \frac{\lambda_{yx,Z}}{\lambda_{ki,Z}} \frac{A_{ki,Z}}{A_{yx,Z}} \frac{g_{k,Z}}{g_{y,Z}} exp(-\frac{E_{k,Z} - E_{y,Z}}{k_B T}) \quad (7)$$

In order to go around the effect of temperature on the exponential factor, the two lines can be selected in such a way that they have similar upper energy levels [32]. Then the validity of optically thin plasma can be checked by comparing the ratio of the spectroscopic parameters on the right with the ratio of the experimentally measured intensities.

Determination of plasma temperature

It has already been mentioned that for the measurement of concentration of elements, the LIBS plasma needs to be under LTE during the measurement window. The temperature of the plasma determined under such condition can be derived from the measured emissions and used to describe the plasma properties including the density ratio of elements [33]. The common approach in determining the temperature of LIBS plasma is the Boltzmann plot method [33]. This approach requires the selection of spectral lines that are not affected by self-absorption. In other words, the lines measured when the plasma is optically thin. In addition, the lines should be those with known spectroscopic data. Equation (6) allows the evaluation of the spatially integrated intensity of a transition line of a species. To use the Boltzmann plot method, the equation can be rearranged and natural logarithm can be taken to yield

$$\ln(\frac{I^{\alpha}_{ki,Z}\lambda^{\alpha}_{ki,Z}}{g^{\alpha}_{k,Z}A^{\alpha}_{ki,Z}}) = \ln(\frac{Fn^{\alpha}_{Z}}{P^{\alpha}_{Z}}) + -\frac{E^{\alpha}_{k,Z}}{k_B T} \quad (8)$$

Equation (8) takes a form of an equation of a straight line. If the term in the left side of the equation is plotted as a function of E^{α}_{k} for two or more transition lines of a given species, then the resulting linear plot is called Boltzmann plot and the plane where the plot lies is called Boltzmann plane [33]. The measured spectral intensity of the species involved is represented by points on the Boltzmann plane. The plasma temperature is associated to the term multiplying the E^{α}_{k} and can be estimated from the slope of the Boltzmann plot.

Validity of the existence of local thermodynamic equilibrium (LTE)

For plasma to be in LTE, inelastic collisions with electrons, rather than radiative processes, should dictate the excitation and de-excitation among energy levels. The existence of LTE is an important requirement for the application of theoretical expressions to determine the concentration of elements. One of the relevant but not sufficient criterion for checking the existence of LTE is the McWhirter criterion [52]. It describes the minimum number of electron density n_e that warrants the existence of LTE and is given by

$$n_e \geq 1.6 \times 10^{12} T^{1/2} (\Delta E)^3 \tag{9}$$

Where T is the electron temperature and ΔE is the largest electron transition considered. The criterion was originally derived for homogeneous and stationary plasmas which certainly is not the case for transient plasmas involved in LIBS. Thus, checking only the above criterion to suggest the existence of LTE should be cautiously used and other arguments supporting LTE should accompany the criterion as was discussed in detail by Cristoforetti et al.[20] and Barthelemy et al.[8].

Determination of electron density

In order to relate the ratio density of analyte species in the plasma, in other words the ratio density of elements in the plasma, the electron density is required. To determine the electron density, the Saha-Boltzmann equation relating the intensity of species in two consecutive charge states Z and $Z+1$ can be used [49]. For the transition ki of the two states, it is given by

$$n_e = \left(\frac{I_Z^a}{I_{Z+1}^a}\right) 6.04 \times 10^{21}\, T^{3/2}\, exp\left[\frac{(-E_{k,Z+1} + E_{k,Z} - \chi_Z)}{k_B T}\right] \tag{10}$$

where

$$I_Z^a = \frac{I_Z \lambda_{ki,Z}}{g_{k,Z} A_{ki,Z}} \tag{11}$$

and χ is the ionization energy for the lowest atomic state. This energy can be neglected due to its lowering as a result of the interactions in the plasma [49]. The other approach used to determine the electron density in LIBS measurements is the stark broadening method. In typical LIBS experimental conditions, line broadening due to the interactions of the emitting atoms with

the electric field produced by the surrounding charged particles, known as stark broadening, is the main contributor to the spectral line widths. This method does not require the plasma to be in LTE and the electron density n_e in relation to the stark width of $\Delta\lambda_{H\alpha}$ can be estimated by [33]

$$n_e = 8.02 \times 10^{12} \left(\frac{\Delta\lambda_{H\alpha}}{\alpha_{1/2}}\right) \tag{12}$$

where $\alpha_{1/2}$ is the stark broadening coefficient of the atom for which the broadening is measured as the full width at half maximum (FWHM). This is a straight forward method. However, the challenge lies on the difficulty of finding the stark broadening coefficient which is scattered in the literature.

Density ratio of species of particular element

In order to determine the density ratio, in other words the concentration of the species of a particular element in the plasma, the Saha equation relating species of the same element in two consecutive charge states can be used [33]. For an element a of charge states Z and $Z+1$ it is given by

$$\frac{n^a_{Z+1}}{n^a_Z} = 6.04 \times 10^{21} \frac{T^{3/2}}{n_e} \frac{P^a_{Z+1}}{P^a_Z} exp\left(-\frac{\chi^a_Z}{T}\right) \tag{13}$$

where P is the partition function of the respective species. T and n_e are the experimentally determined plasma temperature (in eV) and electron density, respectively.

Density ratio of species of different elements

For an optically thin plasma in LTE, the number ratio of two elements a and b in different ionization states is given by the Saha-Boltzmann equation [33]. It can be determined by the intensity of their respective line emissions as

$$\frac{n^a_Z}{n^b_{Z+1}} = \frac{I^a_{ki}}{I^b_{ki}} \frac{g^b_{k,Z+1}}{g^a_{k,Z}} \frac{A^b_{ki,Z+1}}{A^a_{ki,Z}} \frac{P^a_Z}{P^b_{Z+1}} exp\left(-\frac{E^b_{k,Z+1} - E^a_{k,Z}}{k_B T}\right) \tag{14}$$

For the application of characterizing the distribution of elements in tissue reliably, the density ratio of species of different elements provides direct quantitative indication of an element of interest without the need to know its absolute concentration. This can play significant role in the characterization

of cancerous tissue from its surrounding healthy tissue with the help of any element of interest. To do so, one of the elements for the ratio density calculation can be an internal standard in which its concentration is not expected to change. The major elements in tissue such as oxygen, carbon, nitrogen and hydrogen are good examples of elements for internal standard. This approach has high significance since it elucidates potential ambiguities that may arise from signal fluctuations that are typical for LIBS measurements performed without considering the plasma physical parameters. However, it should be noted that for such CF-LIBS measurements, the three pre-requisites need to be fulfilled: stoichiometric ablation, the plasma has to be optically thin and in LTE. Therefore, within the context of tissue characterization this work focuses only whether or not these conditions for CF-LIBS are achievable for measurements of the distribution of elements in tissue.

2.5.4 Applications of LIBS

Most of the applications of LIBS reported are for the analysis of metals despite the existence of other well commercialized techniques such as X-Ray Fluorescence (XRF) and Spark Optical Emission Spectroscopy (S-OES). Even though S-OES has much better sensitivity than both XRF and LIBS, the later two have the advantage of performing in-line measurements. Considering this advantage, the main competitor of LIBS is XRF. XRF has already matured and is used in many industrial applications [82]. LIBS on the other hand is still more a topic of active research. Nevertheless, there are already hand-held LIBS systems used for in-situ determination of metals and alloys [82]. It is not the intention of this work to compare the advantages and disadvantages of LIBS in comparison with other techniques. However, in order to highlight the range of applications of the technique, a general overview on the different areas of applications of LIBS will be given with more emphasis on biological applications.

Industrial applications: Owed to the ease of use, the possibility of using it at large distances and/or with fibers, LIBS is in active use in the metallurgical industry and nuclear energy industry where access to the measurement cite can be hazardous due to high temperature or radiation [23, 50].

Archeology and environment: One area of application where LIBS has shown a big advantage is in the field of archeology or cultural heritage where preparation or moving samples is not desired [69]. LIBS can be used to determine the elemental composition of bones, ceramic samples, marbles and metals in order to help date and/or authenticate samples [29]. Another area

of application of LIBS is in chemical analysis under water where a fiber based system can be used to reach samples deep in the ocean.

Biomedical applications: The large number of applications of LIBS for qualitative and quantitative analysis of metals may indicate the suitability of the technique for successful analysis of metal samples. However, the number of published studies related to biological applications are very few. This might be due to the heterogeneous nature of the samples that results in poor reproducibility and also due to the fact that more interest lies on the molecular information of biological samples. Nevertheless, there is a growing interest in the use of LIBS for biological applications. Biological applications of LIBS can be classified as analysis of human clinical specimens and micro-organisms that affect human health.

LIBS based successful identification of carious from healthy tooth as well as the transition from carious to healthy tooth has been reported [64]. In order to understand the source of medical conditions such as kidney stones or gallstones, a study has analyzed the elemental composition of such samples [66, 67]. In clinical diagnosis applications, it has been shown that LIBS is able to differentiate between malignant and normal tumor cells in a histological section of a tissue.

The application of LIBS in analyzing micro-organisms is another area of research where LIBS can have significant contribution. Rehse et al. [58] have reported extensive studies of discrimination of different species of bacteria. Among their findings are:

- All species of bacteria they tested have unique elemental composition which allows LIBS to identify them
- There is a correlation between the bacteria membrane composition and the LIBS signal
- The LIBS finger print of a bacterial culture does not change with time which is crucial for the detection of surface contaminants
- Bacterial LIBS spectrum remains the same even after sterilization allowing safe handling of specimens

In their bacterial classification analysis, the group reported that although similar bacterial specimens cluster close together, the high sensitivity and specificity obtained provide evidence of the elemental diversity that exists among bacterial specimens. It was concluded the use of LIBS for rapid identification of pathogenic bacteria is feasible in clinical environments [58].

2.5.5 Other studies of LIBS as diagnosis tool for biological applications

There have been some studies of LIBS based tissue differentiation with a goal to use it for surgical application. One study has evaluated the ability of LIBS to classify brain, lung, spleen, liver, kidney and skeletal muscle tissues obtained from chicken [83]. The study demonstrated that for the known tissues their classification model worked reasonably well. However, for blind classification of unknown samples using known training data, poorer classification results were obtained. It was suggested that in order for the model to work well, more representative training data covering a wide range of spectral variations, due to experimental or environmental changes, need to be included in the model.

Another study has reported a LIBS guided smart surgical tool based on a femtosecond fiber laser [39]. Here, a femtosecond laser system with LIBS based real-time feedback and control of processing parameters (pulse energy, repetition rate and speed) to ablate different materials including tissues and metals is demonstrated. The control system includes machine vision, motion control, LIBS signal processing and process control. The machine vision system first brings the sample to the laser focus. Once the LIBS signal processing determines the type of sample by comparing the measured spectra with a reference material, the process parameters are adjusted accordingly. In the implementation of the system, laterally stacked flat samples of bovine bone and skin as well as two metals, to test the sensitivity of the system, were scanned and analyzed. It was highlighted that the LIBS signals were used to identify where the tissue boundary is and helps the system to decide when the process starts and ends. The study concluded that LIBS-guided femtosecond tissue cutting and drilling can be a powerful tool for robotic microsurgery procedures. For the application of macroscopic surgical applications however the system may not be suitable since a much higher ablation rate per pulse is required. Furthermore, the study did not show the accuracy of LIBS in discriminating among different tissues.

Jeong et al. [44] have proposed a LIBS and second harmonic generation (SHG) based feedback system for laser tissue ablation. The LIBS part is used to determine the tissue type and the SHG for range finding. Here, the feasibility of plasma-mediated tissue ablation using ultra-short laser pulses to both cut and generate optical feedback signals is suggested. The study aims to use feedback guided ultra-short pulsed lasers for craniotomies without inflicting damage to the surrounding soft tissues. It has been highlighted that the realization of craniotomy or thinned-skull preparation with the help of ultra-short lasers

can overcome the limitations of the traditional approach by hand-held dental drill. The outcome of the dental drills has been implicated in potential for inflammation, disturbed vasodynamics and cortical spreading depression. The proposed system utilizes LIBS for the identification of soft tissues from bone during the course of craniotomy [44]. To determine the thickness of the tissue at the surface, the focus of the laser is scanned starting from the surface of the sample into the sample and the SHG rises as the focus enters the sample. The intensity of the SHG can then be used to determine the thickness until a depth that the SHG signal can no longer be detected. The use of SHG was only proposed and its practical use needs to be investigated. The study shows a single LIBS spectra of bone and spinal cord ablated in air.

In the use of LIBS for the analysis element distribution in tissue particularily for the diagnosis of cancer, most of the available studies focus on characterizing an entire tissue by measuring at a number of points or not under ambient air [40, 48]. Almost none of the reported studies highlights the need for proper sample handling/preparation when using LIBS for the diagnosis of biological tissues under ex-vivo samples. There is a lack of information about the time of experiment after the dissection of the involved tissues. Even though, LIBS is inherently used without the need for sample preparation, ex-vivo tissue samples change their morphology after their extraction from the animal. LIBS as a technique is driven by the interaction of the laser with the sample. Therefore, the change in the matrix of the sample could lead into misinterpretation of the obtained signal. The study by Gimenez et.al.[30] has used LIBS to study the distribution of foreign nanaparticles in a mouse kidney embedded in epoxy. The study shows the potential of the technique for elemental mapping of biological samples but lacks other alternatives to epoxy based tissue preparation which takes upto a day.

2.6 Classification of LIBS spectra

In this section the methods used for the pre-processing and the classification of LIBS spectra in this work are briefly discussed. For the pre-processing of the measured LIBS spectra principal component analysis (PCA) is used. For the classification of the spectra, linear discriminant analysis (LDA) is used. The performance of the classification is evaluated using receiver operating characteristics (ROC).

2.6.1 Principal Component Analysis (PCA)

Principal Component Analysis (PCA) is a statistical analysis procedure that deals with revealing the covariance structure of the variables, often in multiple dimensions, representing a set of data. Covariance is the measure of how much two random variables vary together. This helps to identify the principal directions known as principal components (PCs) in which a given data is represented by new axes in such a way that the variation in the data is revealed. When differences in data groups is sought, the PCs which show negligible variance can be ignored so that the data is represented by fewer variables than the original ones. Hence, PCA can also be used as a powerful dimensionality reduction tool for example to pre-process high dimensional LIBS spectra. The details of how PCA works are abundant in the literature and will not be discussed here.

2.6.2 Linear Discriminant Analysis (LDA)

Discriminant analysis is a method for classifying samples or objects to one of several classes based on their observations. Discriminant analysis is useful when there is a set of observations that belongs to known classes. Based on these observations group membership of unknown observations that are members of the classes is determined (supervised learning). Linear Discriminant Analysis is one of the commonly used techniques of data classification. LDA finds linear combination of the variables of a data which maximizes the between-class variance and minimizes the within-class variance resulting in a maximum separability of a dataset of multiple classes.

The steps to perform LDA analysis will be summarized below. It should be noted that the algorithms used for classification in this thesis work are well established techniques and going into details is not within the scope of the work. The following steps are performed after the dimensionality reduction of the spectral data using PCA. The processing using LDA involves training data for generating linear discriminants and sample data for testing. This works for two or more classes.

1. Computing mean (M_i, *where i is the class number*) vector for each of the classes involved as well as the within-class scatter S_w and between-class scatter S_b.

S_w for m number of classes can be calculated by

$$S_w = \sum_{i=1}^{m} S_i \tag{15}$$

where S_i, the measure of the scatter which is the covariance matrix of each class.

S_b for m number of classes can be calculated by

$$S_b = \sum_{j=1}^{m} K_i(M_i - M)(Mi - M) \tag{16}$$

where M_i and K_i are the respective mean and size of each class and M is the global mean.

2. Solving the eigen vector and eigen value problem: To ensure the maximum separability of the classes, the ratio of the between-class scatter S_b to the within-class scatter S_w should be maximized. Therefore, we solve the eigen vector and eigen value problem for $S_b^{-1}S_w$ in order to obtain the linear discriminants.

3. Ranking the eigen vectors: Similar to PCA, LDA also allows projection of data into subspace of the input variables to improve separability based on the scattering of classes. Projection is not the only objective but is also dimensionality reduction process. Therefore, to drop unimportant eigen vectors, the corresponding eigen values are inspected and those with lowest values are ignored as they posses the least information. This is done by ranking the eigen values in descending order and ignore those with least values.

4. Until now the training data has been used to generate the linear discriminant model. The next step is to project the sample data on the linear classifier. This projection can be made in a way that the sample data will have only one dimension enabling the establishment of a binary classifier. The performance of this classifier can be evaluated using Receiver Operating Characteristic (ROC).

2.6.3 Binary classification model using Receiver Operating Characteristics (ROC)

A Receiver Operating Characteristic (ROC) allows pairwise evaluation of the performance of the LDA classifier for the envolved tissue classes. The ROC curve shows the relationship between the sensitivity and specificity of a diagnostic test (in this case LIBS based classification). In order to understand the terms sensitivity and specificity, we can consider a hypothetical group of individuals on which a disease screening will be performed. This is analogous to classification of LIBS spectra from two tissue classes. Let's assume the following notations:

True Positives(TP)
False Positives(FP)
True Negatives(TN)
False Negatives(FN)

$$Sensitivity = True\ Positive\ Fraction\ (TPF) = \frac{TP}{TP + FN}$$

$$Specificity = True\ Negative\ Fraction\ (TNF) = \frac{TN}{TN + FP}$$

$$1 - Specificity = False\ Positive\ Fraction\ (FPF) = \frac{FP}{TN + FP}$$

The ROC curve of a test plots has the TPF on the vertical axis and the FPF on the horizontal. TPF is the percentage of individuals with the disease and have positive outcome for the test, whereas FPF is the percentage of those without the disease but have positive outcome. TPF and FPF are calculated by assuming each score of the tests as a threshold for decision. These values are then plotted to form the ROC curve. Figure 5 depicts ROC curves of hypothetical tests A, B and C.

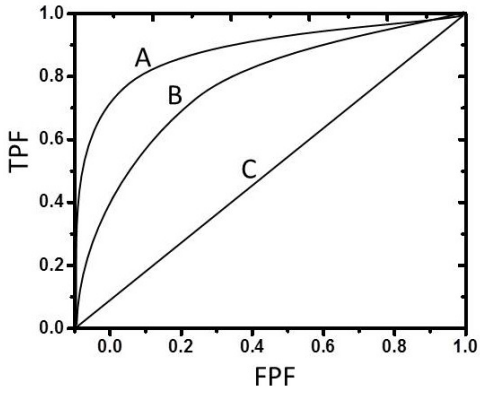

Figure 5: Schematic of a hypothetical ROC curve of three tests (A, B and C).

With increasing area under the ROC curve, the performance of the test increases. Test A shows better performance than B and C in figure 5. Test B outperforms test C. Test C can be considered as a random classifier equivalent to random guessing with 50% chance of TPF and FPF outcome. In fact, any test with a curve below the diagonal line can be considered better than a random classifier because by simply flipping it along the diagonal line outperforms a random test. Tests with curve area equal to 1 are perfect classifier with 100% sensitivity and specificity. Therefore, for all the groups of the tissues investigated, ROC analysis was performed to evaluate the performance of their respective classification model.

3 Objective

To date, the studies of LIBS for biological applications are limited despite the rapid growth of the technique for other applications. In this dissertation, the use of LIBS as a diagnostic tool for biological tissue analysis is investigated. Two main objectives are addressed. One is to proof that LIBS has the potential to discriminate different biological tissues for use as a feedback mechanism of a laser surgery process. The goal is to minimize the risk of damaging important tissues during ablation. The other main objective is to proof the viability of LIBS as an imaging tool to monitor the distribution of elements in cancerous tissue. Here, emphasis will be given on different tissue preparation methods. At the end, the results of the investigations of some physical properties of a LIBS plasma will be investigated with a goal to suggest ways to improve reproducibility of tissue LIBS spectra.

Hypothesis

- *Can LIBS be used to measure the qualitative elemental composition of tissues?*

  The elemental composition of a number of tissues that include soft and hard tissues will be investigated. The qualitative analysis of elements is essential in order to check the reliability of the results. The tissues will be grouped depending on their relevance for different surgical applications. The measured elemental composition of the tissues will be compared to those found in the literature. As LIBS is inherently probing the samples by ablation, if this damage is a concern for the proper functioning of especially nerve tissue will be addressed.

- *Can a statistical classification model for ex-vivo porcine tissue achieve high classification accuracy?*

  A LIBS based feedback mechanism should provide the surgeon with accurate and real-time information on the tissue type being ablated. One property of LIBS spectra is their relatively higher variability. In order to overcome this, the feasibility of using statistical classification analysis methods with the help of new pre-processing approach are investigated. Different classification models of a number of tissues will be presented. Each model is dedicated to a group of selected tissues based on a targeted surgical application. For each classification model established, evaluation of the accuracy of classification will be presented. As proof of principle, the system will be used to map tissue types in 2D and also if it works after tissue interacts with a surgical laser.

- *Can a classification model based on porcine tissue be directly used to classify mice tissue?*

  A successful establishment of an ex-vivo tissue classification model based on porcine animal models does not guarantee the same performance on human tissue. As in any new diagnosis modality, clinical studies on human tissue is critical. However, due to ethical reasons, LIBS experiments on human tissue both under ex-vivo and in-vivo conditions is beyond the scope of this work. In order to understand the robustness of LIBS for the application of different animals, a transferability study is presented. The classification performance of a model based on porcine tissue on corresponding mice tissue will be investigated.

- *Can LIBS be used to image tissue by spatially mapping of the constituent elements?*

  This can help in the diagnosis and/or understanding of the therapeutic outcomes of various pathologies. One such critical pathological application is cancer. There is a growing interest in understanding cancer from the view point of the microenvironment around it. One way to get such information is to look at the distribution of elements in order to trace back the causes for possible imbalance of elements. Using LIBS, the distribution of elements in healthy tissues will be first demonstrated. This is followed by similar investigation of elemental distribution in cancerous tissue. In the characterization of elemental distribution, the preparation of the sample plays a critical role. The results of different tissue preparation techniques will be presented.

- *Can understanding the physical properties of the LIBS plasma help improve the results?*

  In order to improve the reproducibility of LIBS measurements, understanding the physical properties of the LIBS plasma is important. This is especially crucial for measurements on samples such as tissues. Therefore, a few important physical properties of the LIBS plasma are investigated in order to validate the measured spectra.

The connections of the different hypotheses are summarized in the flowchart in figure 6. The focus of this thesis will be on the applicability of LIBS for laser surgery feed-back mechanism and the diagnosis of cancer. Limitations and further requirements will be discussed. The knowledge acquired from this work can be used to advance the use of LIBS for biological tissue analysis.

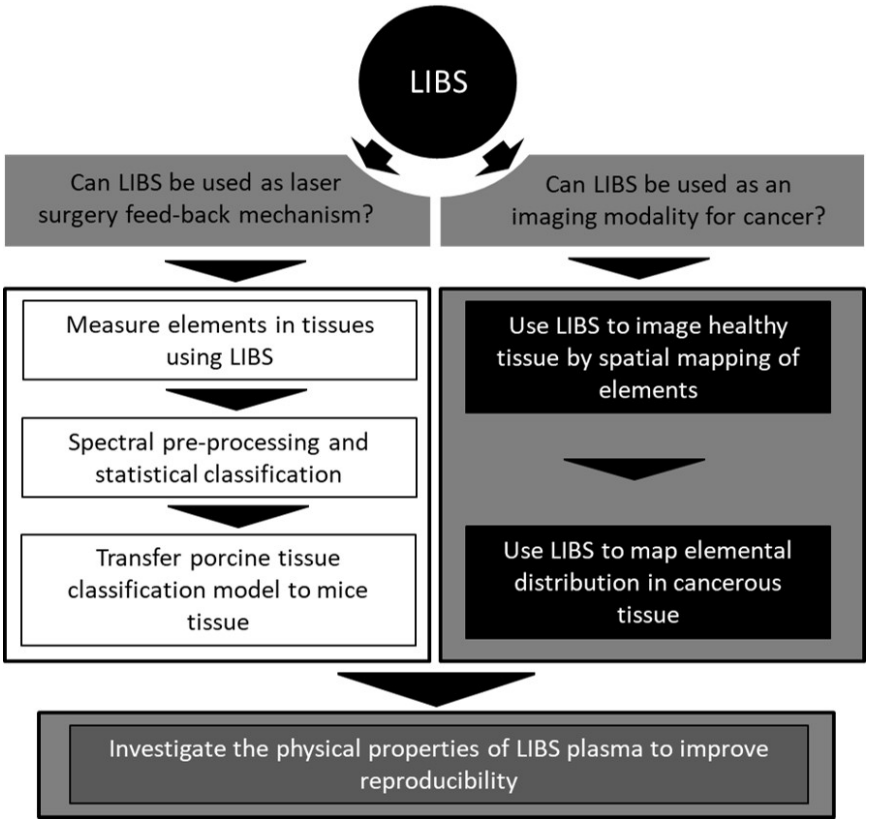

Figure 6: The flowchart shows the connection between the investigated topics.

4 Experimental setup and methods

4.1 Preparation of experimental tissue samples

For the different studies involved here, ex-vivo tissues obtained from porcine and mice animal models were used. The tissue classification models for the application of a laser surgery feedback mechanism were investigated mainly using porcine tissues. The transfer study was performed using tissues of porcine and mice animals. All the cancer studies were done on mice tissue samples. The porcine tissues were prepared from bisected ex-vivo domestic pig heads. The sagittally bisected pig heads were obtained from a local slaughterhouse and were free from any local or systemic diseases. Hence, approval of ethics committee was not necessary.

Nerve and gland: For the differentiation of nerve and gland, the infraorbital branch of the trigeminal nerve was chosen as it is easy to access. The *Nervus infraorbitalis* was cut and prepared as a nerve sample from each animal. The nerve samples were 4 - 6 cm long with an outer diameter of about 1 cm. The gland tissue samples (about $2\times2\,cm^2$) were obtained from the parotid gland located at the caudal and buccal of the ascending branch of the mandible after removing the surrounding soft tissue.

Nerve and fat: In the classification of this pair of tissues, again the nerve tissue samples were from the *Nervus infraorbitalis*. For fat tissue, the subcutaneous fat of the *Regio buccalis* covering the masseter muscle was prepared. The fat tissue samples had a size of about $2\times2\,cm^2$.

Cortical bone and cartilage: The cartilage samples were prepared from the hyaline cartilaginous support of the outer ear (regio helixauriculae). The cortical bone samples were cut from the ascending branch of the mandibular bone (ramus ascendens os mandilulare) using a water cooled band saw. Each of the cartilage and cortical bone samples had a size of about $3\times3\,cm^2$.

Soft and hard tissues in the oral cavity (prospect for feedback guided laser teeth preparation): Here, mixed tissue types containing both soft and hard tissues were prepared. These tissues are those that might be encountered during dental surgical procedures. Seven different ex-vivo tissues were prepared (nerve, mucosa, enamel, dentine, pulp, cortical and cancellous bone). The nerve sample was the *Nervus infraorbitalis*. The mocosa was prepared by vertically cutting along the periodontal sulcus of the incisors. The cortical and cancellous bone samples (about $3\times3\,cm^2$) were obtained from the ascending branch of the mandible and the mandibular angle. The dental samples

were prepared from the primary molars of the mandible by performing two horizontal cuts to get a cylinderical shape. The two bases of the cylinder allow for access of the three parts of the tooth (enamel, dentine and pulp).

The tissues were prepared from a targeted anatomical structure so as to address a specific surgical application. The details of the targeted applications will be provided in the results section. After preparation, each ex-vivo tissue was carefully washed with a sterile saline solution to remove all superficial contaminants without inflicting any mechanical irritation. The main tissue contaminant can be clotted blood which may contain all the tissue constituent elements. It should be noted that the same procedure was followed during the preparation of tissues from porcine and mice tissues for the transferability investigations. To reduce tissue alteration, the experiments were performed within 6 hours after the slaughter of the animals [59]. Figure 7 shows a picture of examples of each of the porcine tissue samples investigated for differentiation.

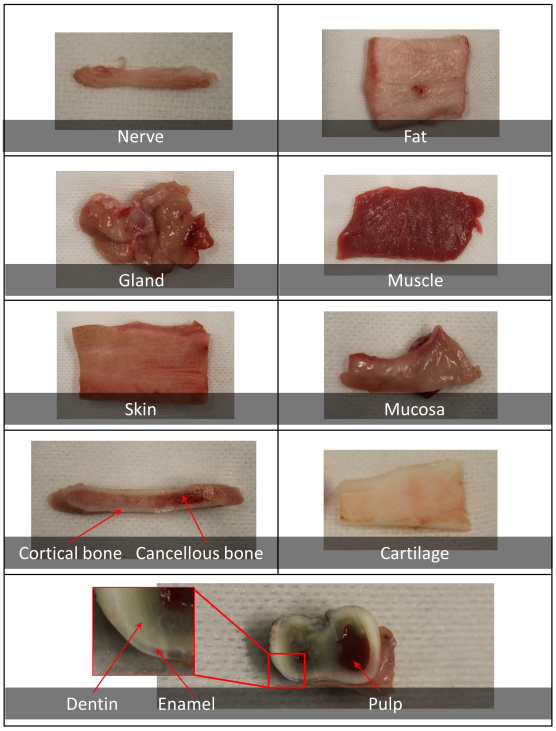

Figure 7: Exemplary tissues used as experimental samples.

In the transfer study from porcine to mice model, experiments on porcine fat and muscle tissue samples were used to classify mice fat and muscle tissues. The preparation of the porcine tissues is as described above. The mice fat and muscle samples were obtained from wildtype mice (B6/J mouse strain), after the mice were sacrificed by cervical dislocation.

In the investigations of the elemental distribution in a cancerous tissue, all the tissue samples were obtained from cancer mice models. To induce tumors in mice, the AOM/DSS model was used. Hif2-Vilincre mice were intraperitoneally injected with 10 mg/kg Azoxymethan (AOM). Afterwards, the mice received three cycles, for around one week, of 2% dextran sulfate sodium (DSS) in drinking water, followed by two weeks of drinking water. DSS induces chronic inflammation in the colon, and together with AOM, the mice develop tumors. Tumor growth was monitored via endoscopy. At the end of the experiment, the mice were sacrificed by cervical dislocation and colon samples were collected. The samples were provided by the Medical Department 1, Friedrich-Alexander-Universität Erlangen-Nürnberg, Hartmannstr. 14, 91052 Erlangen, Germany (Working group of Prof. Dr. med. Maximilian Waldner).

4.2 Experimental setup

The experimental setup used in the most part of the LIBS experiments in this thesis work generally follows the scheme shown in figure 8. It has a similar setting to a typical laboratory LIBS setup except that there is an extension for a video microscope setup. The focus of the LIBS laser and the microscope system are made to coincide in order to ensure that the same focal position is maintained for all the LIBS measurements. To bring the surface of the experimental samples at the focus of the system, a 3-dimensional stage was used. In the experiments of *nerve and gland differentiation* as well as *bone and cartilage differentiation*, the setup used was without a microscope system. However, effort was made to maintain the distance of the sample surface to the focusing optics.

The laser system used in this work is a flash lamp pumped Q-switched Nd:YAG laser system (Quantel-laser, Q-Smart) which can be set to work at the fundamental wavelength 1064 nm and its harmonics (532 nm and 355 nm). The laser can give a maximum pulse energy of 450 mJ, 220 mJ and 130 mJ at 1064 nm, 532 nm and 355 nm, respectively. The pulse duration of the laser is approximately 5 ns and has a maximum repetition rate of 10 Hz. It can be run either on single pulse mode or at a preferred repetition rate below 10 Hz. The pulse energy at any of the given wavelengths can be controlled by changing the delay

time between the flash-lamp and the Q-switch. To set the pulse energy to a required value, the corresponding laser power was measured using a power meter insuring a stable reading for a few minutes. In the investigations of cancer tissues, different laser energy settings were used in order to control the scanning resolution.

The spectrometer used in this work is an echelle spectrometer (Andor, Mechelle 5000) connected to a UV grade fiber to collect the light from the plasma. The spectrometer has a resolving power $\lambda/\delta\lambda$ = 6000. The requirement for very high resolution spectrometers in LIBS is due to the need to resolve the sub-nanometer, often a few tens of picometers, separation of many atomic emission lines of elements. The measurement range of the spectrometer is 200 - 975 nm with much less sensitivity in the range longer than 800 nm. It has an adjustable delay from 0 ns to 10 s in steps of 10 ps and minimum optical gate width of < 2 ns. Wavelength calibration of the spectrometer was done with a mercury-halogen calibration lamp. Intensity calibration was performed using deuterium tungsten-halogen calibration light source. Due to the spectrum of the intensity calibration light source, the calibrated measurement range of the spectrometer narrows to 230 - 850 nm. The intensity calibration is critical during absolute quantification of elements. This is because the grating of the spectrometer is used at the littrow/blazed angle in which the efficiency is maximum in the middle of each diffraction order. The efficiency drops at the extremities of each order. This can lead to underestimation of emission line intensities in different regions of the spectrum. Hence, the device was corrected with the help of standard/calibration light sources. One of the important steps during LIBS measurements is the optimization of the time window when the signal of interest (the atomic emissions) is high compared to the background signal. This is done by adjusting the gate width (integration time) and the delay of the spectrometer after the shooting of the laser on the sample surface. These parameters can be different for different sets of tissues and will be discussed in the results section.

The synchronization of the devices in the setup shown in Figure 8 is done in two main ways. One is when measuring LIBS spectra from individual tissues in order to build a classification model of different tissue groups. In this case, the surface of a sample under investigation is manually translated and brought to the focal position of the LIBS laser. The LIBS laser then triggers the spectrometer until the desired number of spectra is collected.

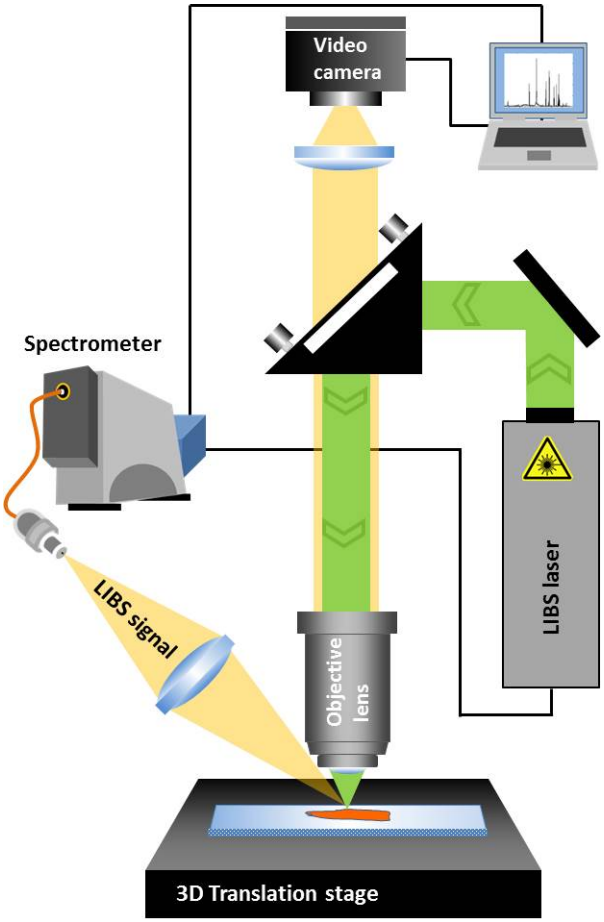

Figure 8: Schematic of the LIBS experimental setup used.

The other setting is when a 2-dimensional scanning is performed either for real-time tissue type classification or elemental mapping of cancerous tissues. In this setting, the sample surface is first brought manually to the focal position of the LIBS laser. After each number of desired measurements in one position is performed, the sample is automatically moved to the next position and LIBS measurement is performed. During each measurement in the entire grid, the spectrometer is triggered by the LIBS laser.

4.3 Classification of tissue LIBS spectra

In this section a brief discussion on the steps to establish a supervised machine learning algorithm for classification of tissues will be given. The learning

process involves determination of the class membership of unknown tissue spectra based on known inputs. The steps involved are first pre-processing of the spectra followed by classification of test data. This is then followed by evaluation of the performance of the classifier.

4.3.1 Pre-processing of LIBS spectral data

In the investigations of tissue differentiation, the approach used to measure the representative spectra of each sample is by first finding the time window for optimum signal strength in comparison to the background emission. This means, the plasma can not be assumed to be optically thin and in LTE. Given the heterogeneous nature of tissues and the sensitivity of LIBS to heterogeneity of samples, large fluctuations of the emission lines are expected even within the spectra of a given tissue. As a result pre-processing of the data becomes necessary in order to compare and analyze the measurements. The common approaches taken to minimize such variations in LIBS signals is to perform normalization. One way to normalize the spectra in LIBS is to use an internal standard. This is to normalize each spectrum by the intensity of the emission line of an element which is found in the same concentration in all the samples. This element is commonly termed as internal standard and the process as internal standardization. Such normalization process is impractical for the application of tissues as the heterogeneity also affects the element that would be taken as internal standard. The heterogeneous nature also rules out normalization by the maximum intensity which is commonly done in various spectroscopic techniques.

Another approach to standardize LIBS spectra, specially for heterogeneous samples, is using normalization by the total emission from the plasma as it is related to its total energy. In other words, each measured spectrum is divided by the integral intensity of the measurement range. This minimizes fluctuations as a result of the excitation conditions. This can be observed from the line intensity fluctuations which are higher than the corresponding integral intensity fluctuations of a set of measurements of a given sample. In table 3 the comparison of the fluctuations of the total emission of the plasma and the intensity of hydrogen line at 656.28 nm from investigations of fat, nerve and gland is shown. The numbers show by how much percent the intensity of the total plasma emission and that of the hydrogen line fluctuate within the measurements of a given sample. The investigations of the other tissues in this work also show similar behavior as shown in the table 3. Therefore, the total emission of the plasma was chosen as the normalizing factor.

Table 3: Comparison of intensity fluctuation between total intensity of plasma emission and intensity of hydrogen line.

Tissue	data size	std./total emission	std./hydrogen emission
Fat	324	.406	.406
Nerve	324	.416	.426
Gland	270	.469	.509
Nerve	270	.494	.525

4.3.2 Principal Component Analysis (PCA)

Due to the high resolution spectrometers often employed for LIBS measurements, data compression tools such as PCA are essential for the analysis of the LIBS spectra. In this work, PCA is used to reduce the high dimensional nature of the LIBS spectra (more than 27,000 measurement points/variables) in order to facilitate further classification analyses. Therefore, when ever necessary, the data for classification here is first standardized and then analyzed using PCA in order to represent it with fewer variables. The results of such compression process will be shown in each section of the classification results.

4.3.3 Linear Discriminant Analysis (LDA)

During LDA analysis, the normalized and dimensionally reduced spectra are used. The measured spectra are divided into two groups. The training data and test data. As a test data, the measurements from each animal are used one at a time while the data from the remaining animals is used as training data.

4.3.4 Binary classification model using Receiver Operating Characteristics (ROC)

For the evaluation of the performance of the classification using LDA and establishing a binary classifier, ROC analysis is performed during each classification.

5 Measurements of elements in ex-vivo porcine-tissues using LIBS

In this chapter, the question if LIBS can be used to monitor the constituent elements of biological tissues is addressed. The main goal here is to investigate if the monitored elements in tissue using LIBS correspond to their actual composition. The selection of tissues is relevant for laser surgery applications. Finding the exact elemental composition of some of the tissues for the validation of the obtained results posed significant challenge. This is because the literature often offers great deal of information about the type of molecules in tissues without full information on all the constituent elements. Even with complete molecular information, discerning the elements in each molecule proves difficult and is not the primary goal of this work. When ever available, reference to literature has been provided. Overview of the content of this chapter is shown in figure 9.

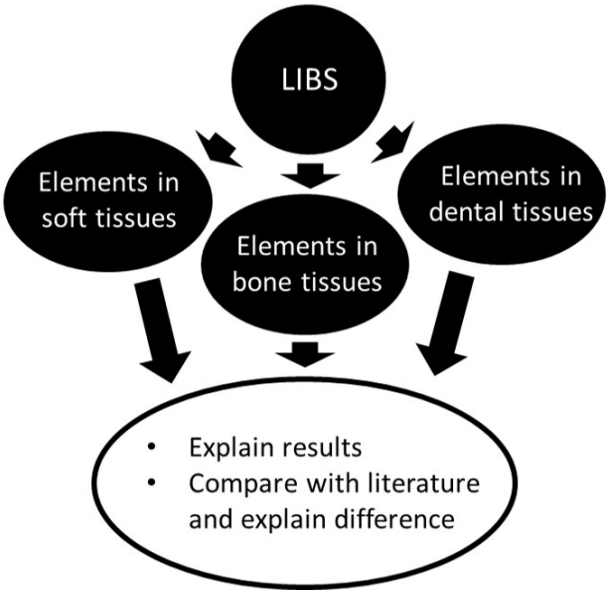

Figure 9: Chapter overview.

In LIBS measurements in general, particularly in the setup used in this work, the most important parameters are the delay of the spectral measurement from the laser, the integration time of the spectrometer, the laser pulse energy and the focus spot size. A typical delay values for LIBS measurements with nano second lasers are in the range of 1 to 2 microseconds. The choice is

often based on optimization of the signal to background (continuum)ratio. The integration time is not as critical as the delay time. This is because the typical plasma life-time for a nano second laser is few tens of microseconds. In the measurements of this work, a few measurements were performed to investigate these parameters and it was found that slight change in the delay and gate did not have any noticeable effect on most of the spectra. Therefore, These parameters were kept the same for all the measurements and are listed below. In most of the measurements, where multiple shots on a single spot is possible, the system fired two cleaning laser shots in all tissue types in order to remove any superficial contaminants.

- Delay and integration times were set to 2 µs and 200 µs, respectively
- pulse energy 80 mJ
- laser focus spot size 300 µm

5.1 Soft tissues

In this section, the elemental composition of five tissues (nerve, gland, fat, muscle and skin) monitored using LIBS will be discussed. Comparison with the information obtained from the literature will be done.

5.1.1 Nerve

One of the most important tissues involved during surgical interventions of various applications is nerve tissue. The type of nerve tissue studied in all of the experiments in this thesis work is peripheral nerve, particularly the *Nervus infraorbitalis*. One of the important aspect of this type of nerve relevant for LIBS study is its structure. It is a bundle of tiny nerve fibers which are aligned along the length of the nerve. A myelin sheath consisting of up to 70% lipids (fatty acids) covers each axon making out between 30% - 50% of its total cross-section [79]. The myelin elemental composition is highly similar to that of fat tissue. This poses a challenge in the differentiation of nerve from fatty tissues. The elemental composition of white brain matter has been shown in table 2. Even though the elemental composition of white brain matter may not be directly transferred to that of peripheral nerve, it may be taken as indicative reference for the general composition of nerve tissues [36]. It can be recalled that the composition of white brain matter is: H(10.6%), C(19.4%), N(2.5%), O(66.1%) and the trace elements (Na, P, S, Cl and K) making the remaining percentage. It is also expected that iron (Fe) is found as a trace element due to blood flow inside nerve tissue. The fibrous

nature of peripheral nerves makes them highly heterogeneous resulting in relatively higher variation in the total emission of the plasma. These can be seen as bright circular shapes (marked by the dotted lines) inside a nerve tissue in the OCT image in figure 10 of a nerve sample,

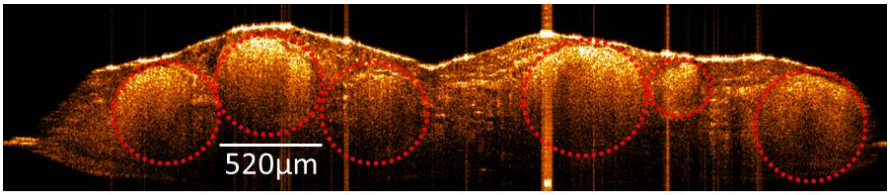

Figure 10: OCT image of a peripheral nerve showing its fibrous nature. The bright circular structures below the surface.

Figure 11 shows a typical LIBS spectrum of Nerve tissue. It is a spectrum averaged from 320 measurements and the fluctuations in the measurements are shown as a variance with the light gray color. The measurements were obtained from 6 samples of 6 porcine animals. It can be seen that most of the constituent elements of nerve tissue can be detected using LIBS. There are also weak intensity emissions that are observed in the spectra. These weak emissions were not labeled in all the experiments as they were not stable enough to appear in all the measurements. The weak emissions can be speculated as being contaminants that are not consistently expected to show up in the respective spectra.

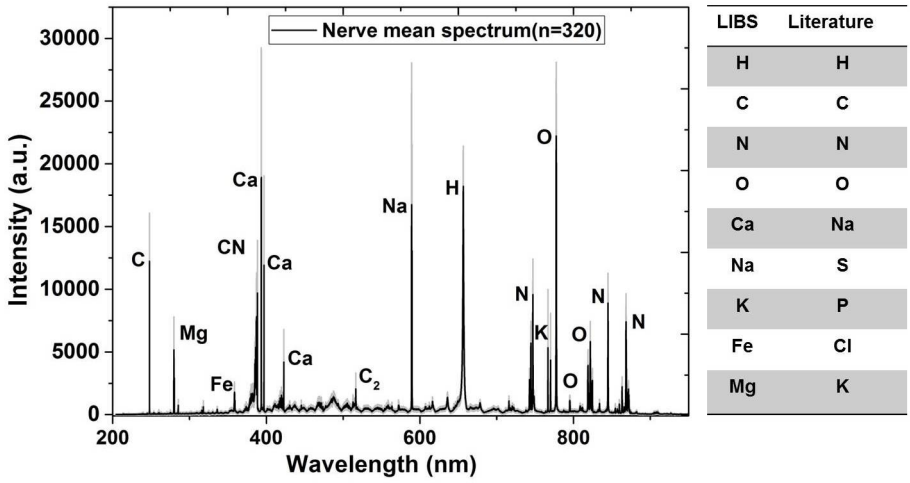

Figure 11: Representative LIBS spectrum of nerve tissue. The elements monitored during LIBS and those found in the literature are listed on the right.

Figure 11 lists the elements in nerve that were observed using LIBS and those that were found in the literature. There are some elements (such as S, Cl and P) that could not be easily measured in the experiments. These elements are mostly detected in the vacuum UV (VUV) and NIR region. They present very week emission lines in the spectral range investigated and are easily masked by strong emissions of other elements. These elements are also trace elements in tissues. As a result, usable emissions from these elements was not observed under the experimental conditions used for classification. However, separate experiments, under Argon(Ar) gas atmosphere, on samples containing phosphorus showed emission intensity of P is higher in Ar than in air which can explain why they were not observed in most of the experiments performed in air. The cooling rate of the plasma is inversely proportional to the mass of the ambient gas [61]. Therefore, the plasma in heavier gases such as Ar has less cooling rate resulting in high temperature and high electron density. High temperature and electron density plasma means enhanced signal intensity. On the other hand, the experiments also showed emissions of other elements such as iron (Fe) and magnesium (Mg) which are expected in nerve tissues. Mg plays a role in the excitability of nerves and Fe is expected due to the blood flow in nerve tissue. CN and C_2 are molecules related to carbon which form later on in the plasma. As C and N are also present in air which affects all tissue in the same way, the change in these molecules can reflect the difference of C and N in the samples.

5.1.2 Parotid Gland

In the experiments on parotid gland (normally called salivary gland) constituent elements of the tissue were monitored. Even after rigorous research, it was not possible to find a reference for the elemental composition of salivary gland as far as this work is concerned. Therefore, the composition of the tissue will be explained solely based on the observation of the LIBS experiments. Figure 12 shows the mean spectrum of measurements obtained from samples of 6 animals. The spectrum shows that the qualitative composition of gland is similar to that of nerve. However, the intensity of Ca, C and Fe reduces significantly while intensities of Mg and K show the opposite trend. This indicates that the concentration of these elements might be different when looked in nerve and gland samples.

The elements monitored during the LIBS experiments are listed in figure 12. The elemental information on gland tissue is important within the context of tissue differentiation in this work. As was mentioned earlier, it was not possible to find any reference in the literature for the comparison of the

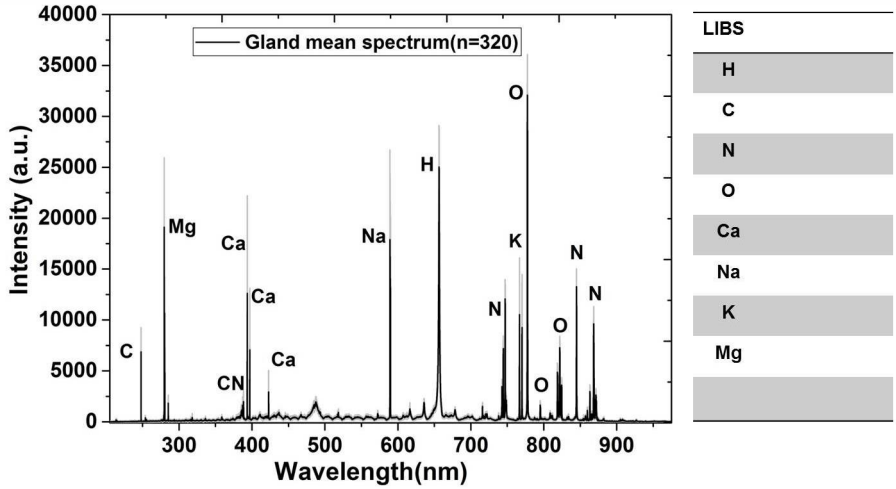

Figure 12: Representative LIBS spectrum of gland tissue. Reference of the elemental composition of glad could not be found.

monitored elements. The primary interest in various studies of tissue composition is molecular information as molecules provide information on the structural and functional foundation of tissues. For medical applications such as radiation therapy, molecular composition is not easily applicable for dosimetric calculations as molecular binding effects are very weak to affect therapy energies [47]. LIBS as analytical technique might give valuable information on elements related to tissues or specific molecules. Therefore, the information obtained using LIBS, in tissues such as gland could be important for medical applications such as radiation therapy. It might also be relevant for indirect measurement of molecules if direct measurements of molecules poses difficulty.

5.1.3 Fat

The elemental composition of fat tissue has already been discussed in one of the previous sections. The major constituent of adipose (fatty) tissue is carbon. It makes up more than 50% by mass. Therefore, the LIBS experiments are expected to reflect this by showing relatively high intensity of carbon emissions and emissions from carbon related species. Figure 13 shows an average spectrum of fat tissue.

Compared to the tissues above, particularly, nerve tissue, fat shows higher emission peaks of C, CN and C_2. This clearly indicates that fat tissue contains relatively higher concentration of carbon. In addition, relatively much weaker

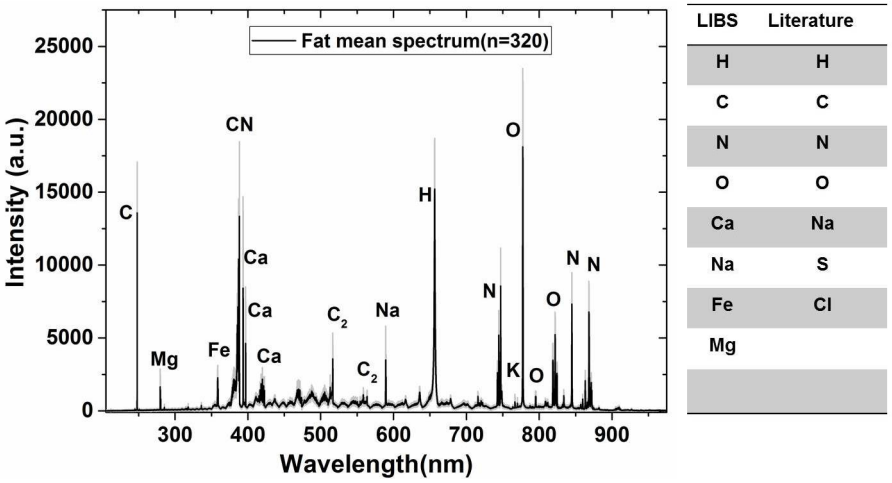

Figure 13: Representative LIBS spectrum of fat tissue. The list indicates the elements monitored during LIBS and those found in the literature.

emissions were observed from Mg, K and Na indicating their presence in reduced concentration. The comparison of constituent elements reported in the literature, shows that all the elements were observed with the exception of S and Cl. This is similar to the case of nerve which can be explained by the fact that these elements have appreciable emissions only in the VUV and NIR which is not within the working range of the spectrometer used here.

5.1.4 Muscle

The mean spectrum of muscle tissue in figure 14 shows higher intensities of Mg, Na and K. It is know that Na and K play important role in muscle contraction. Nerves communicate with muscle cells by sending electrical signals in order to perform contraction or relaxation. These electrical signals are transmitted via Na and K ions. This can explain the presence of these elements in relatively higher concentration in muscle and nerve than in fat for instance. On the other hand, Ca and Mg are essential to control muscle contraction and relaxation. The proteins responsible for muscle contraction rely on Ca to shrink. The same proteins rely on Mg to relax. The exact concentration of these elements in muscle is difficult to discern from the literature. However, the LIBS measurements indicate that Mg might be found in higher concentration in muscle than in the other tissues.

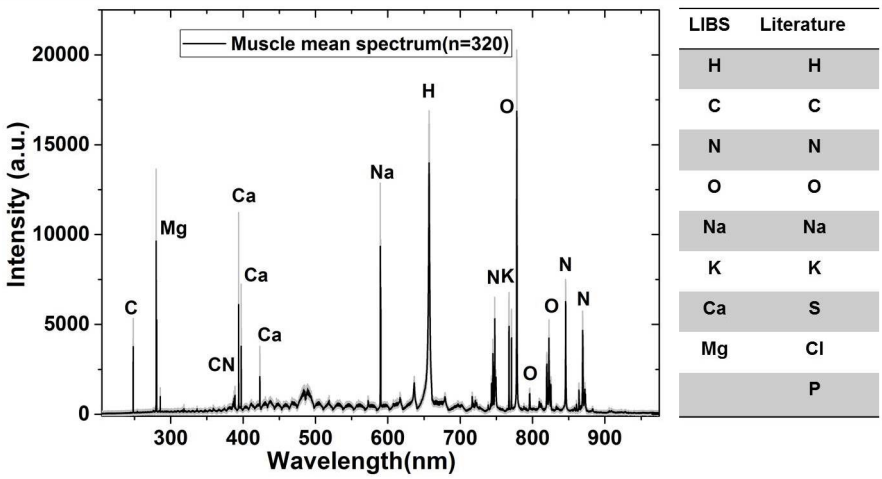

Figure 14: Representative LIBS spectrum of muscle tissue with the elements monitored during the LIBS experiments. The elements are compared with those reported in the literature.

5.1.5 Skin

Except for skin surgery applications or removal of skin cancer, the relevance of skin for surgical applications might be considered simply as a protection for the underlying tissues and needs to be removed or a flap has to be made to access the deeper tissues. The structure of the skin is very complex and several elements that compose the parts of skin might be considered for the representation of skin in terms of elements. Within the ablation crater of 10 pulses, it was assumed that the tissue is still the two upper parts (epidermins and dermins) of the skin without reaching the subcutaneous fat layer. The porcine skin tissue is very similar to that of human [72]. The human epidermis has a thickness in the range 60 µm to 100 µm in most parts of the body. The human dermis is in the range 0.6 mm to 3 mm. Therefore, for thin skin, care needs to be taken not to measure from deep in the tissue which can be the fat layer of skin.

The elemental composition of skin tissue as measured from the prominent atomic emission lines is shown in the mean LIBS spectrum in figure 15. The spectrum of skin posses much more atomic lines than the soft tissues already discussed. Especially, there is significant increase in intensity and number of Ca lines. The composition obtained from the literature for example does not report the existence of Ca in skin. This is contradictory to the LIBS measurements indicating the difficulty of finding information to validate the measurements from tissues. There are also emission lines, mainly in the

visible range, that were not labeled due to ambiguity caused by the limited resolution of the spectrometer. The information about atomic emission lines from the NIST data base contains huge number of emission data from various elements separated by a few pico-meters.

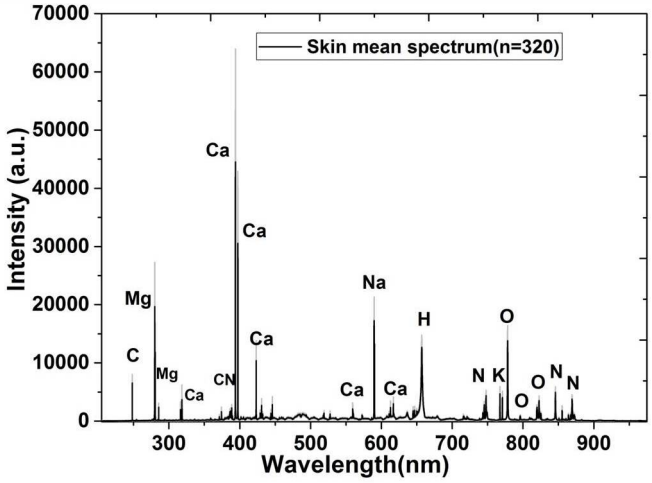

LIBS	Literature
H	H
C	C
N	N
O	O
Na	Na
K	K
Ca	S
Mg	Cl
	P

Figure 15: Representative LIBS spectrum of skin tissue with the list of monitored elements and those found in the literature.

5.2 Soft and hard bone tissues

The types of bones investigated under this group are: cancellous bone, cortical bone and cartilage. The two major types of bones found in the body are cortical and cancellous bones. Cortical is very dense and hard tissue whereas cancellous is porous and has spongy structure making it less harder than cortical. Cartilage is a type of bone which is soft and flexible often covering and protecting the ends of cortical bone. In light of laser surgery, these types of bones can be encountered during bone cutting. Therefore, to differentiate them can be essential for surgical applications.

5.2.1 Cortical Bone

Cortical bone forms the outer part of most bones and is dense and hard. In humans, it constitutes 80% of the skeletal system. It has the highest content of Ca from the other bone types. The LIBS spectrum of cortical bone shown in figure 16 is dominated by strong emissions of Ca supporting the presence of the element in higher concentration. In the visible region of the spectrum, the spectrometer was not able to resolve all the emissions lines. This is mainly

due to the numerous emissions of Ca in this region that are separated by spectral distances smaller than the resolution of the spectrometer. The entire spectrum of cortical bone has a vast number of emissions many of which are prominent. Others are much weaker than the high intensity peaks but still strong enough to be detected in most of the measurements. A typical example is phosphorus, shown in a small box in figure 16. Phosphorus has no appreciable emissions in the measured range. However, its presence in higher concentration in bone is clearly an indication for the appearance of its emissions. The spectral finger print of most of the elements in the periodic table in the measured range is enormous. The main challenge in LIBS of multi-elemental samples is that limited resolution of available spectrometers resulting in ambiguity of assigning lines to elements. Cortical bone and all the other samples also suffer from this problem.

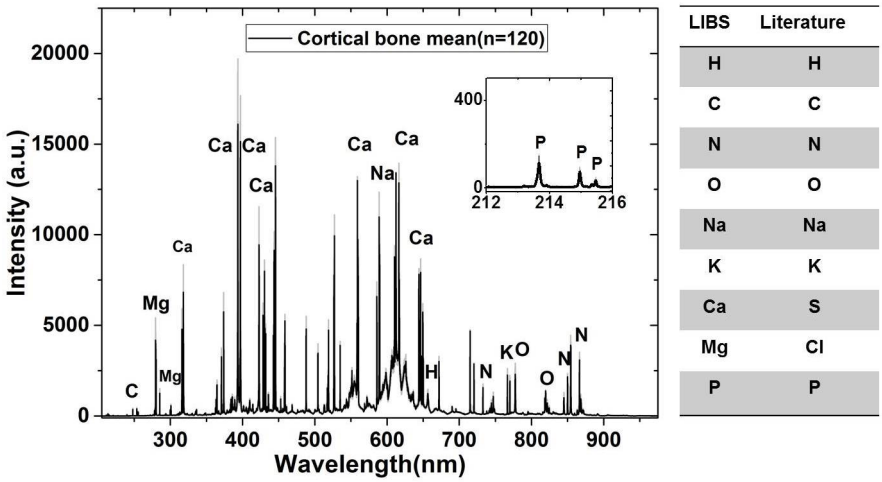

LIBS	Literature
H	H
C	C
N	N
O	O
Na	Na
K	K
Ca	S
Mg	Cl
P	P

Figure 16: Mean LIBS spectrum of cortical bone with the monitored elements. At the top-right corner is enlarged part of the spectrum to show phosphorus (P) emission lines.

5.2.2 Cancellous Bone

The composition of cancellous bone is qualitatively similar to that of cortical bone. Figure 17 shows the mean spectrum of the measurements on cancellous bone. The intensity of calcium ionic lines (at 393.36 nm and 396.84 nm) is seen to be higher in the case of cancellous bone for the same experimental conditions. This does not mean that higher Ca concentration is expected in cancellous bone which is in contrary to the composition of the two samples. This can be explained as follows. The neutral line for example at 430.25 nm is higher for cortical bone. For high temperature plasma, which is expected for

the parameters used in this experiments, the low value of ionization potential of neutral Ca leads to higher ion density. This in turn leads to higher self-absorption of ionic lines involving ground state levels with higher transition probability [35]. The effect of self-absorption also applies to neutral lines involving ground state levels with high transition probability.

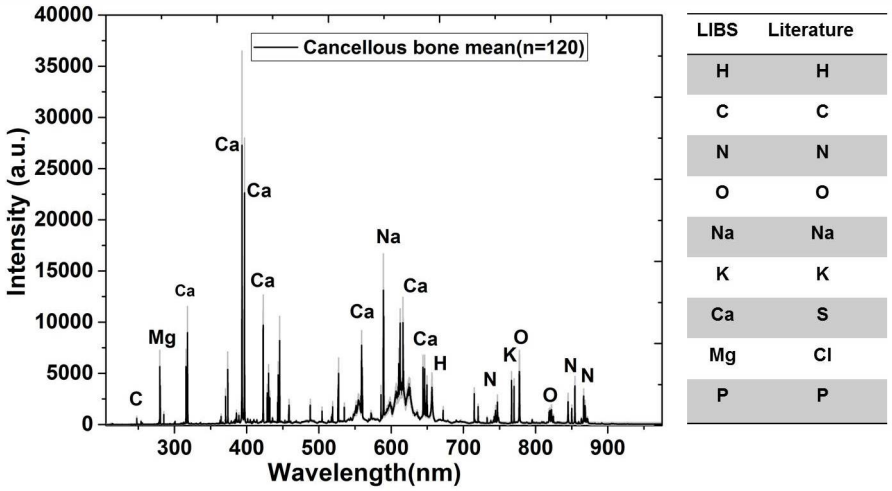

Figure 17: Mean LIBS spectrum of cancellous bone and its constituent elements monitored using LIBS. Reported composition of the tissue is also shown for comparison.

The two bone samples are very good examples for comparison of similar materials using LIBS as their nature is the same hence it is expected to find, from the measurements, the same elements with different concentrations. To compare the trace elements in the samples using the measurements would be unrealistic as the necessary conditions for absolute quantification of elements were not fulfilled in these investigations. However, for the major elements in the samples, the measurements should indicate conformity with the contents of the samples. For ease of reading, the composition of cortical and cancellous bone have been duplicated from table 2 and shown in figure 18. The spectra in the figure are a close up look of the corresponding spectral windows of those in figures 16 and 17. Multiple emission lines of P and Ca show higher intensities as shown in the figure 18 which is in agreement with the composition of the tissues. The intensity of C and H are also in agreement with the composition. Where as that of O and N are contradictory to the concentrations in the samples. As far as this work is concerned, explanation of the case of O and N could not be found or explained. In all other tissues samples investigated, these two elements show very good agreement to the reported portions of corresponding samples.

Sample	H	C	N	O	Ca	P
Cortical bone	3.4%	15.5%	4.2%	43.5%	22.5%	10.3%
Cancellous bone	8.5%	40.4%	2.8%	36.7%	7.4%	3.4%

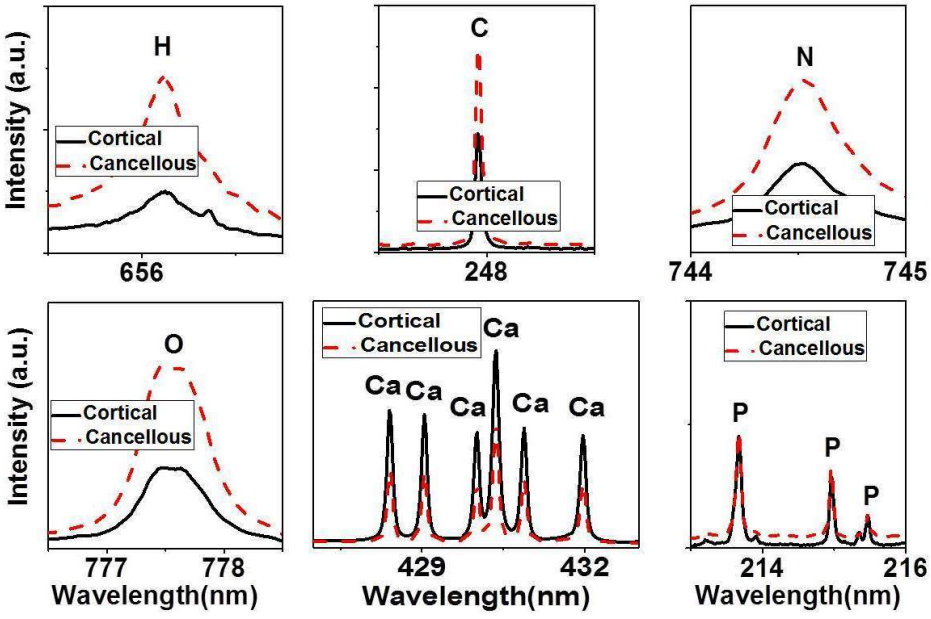

Figure 18: Comparison of emissions of major elements in cortical and cancellous bone.

5.2.3 Cartilage

Cartilage is a type of bone commonly know as soft bone. Cartilage has, relative to other tissues investigated here, higher content of Na but still less 1% by mass. This was evidenced from the high intensity of the Na line in the spectra of cartilage. Several Ca lines were also observed. In figure 19, C has been listed as one of the observed elements in the LIBS spectra of cartilage but not directly from its emission at 247.85 nm rather indirectly from the CN band around 390 nm. It might be argued that C might also come from air. However, measurement of air show no CN band. Therefore, it can be concluded that the C comes from the sample.

5.3 Dental tissues

In this group, the main tissues that are found in the oral cavity involved in dentistry applications were investigated. These include: cortical bone, cancellous bone, peripheral nerve, mucosa, enamel, dentine and pulp. The

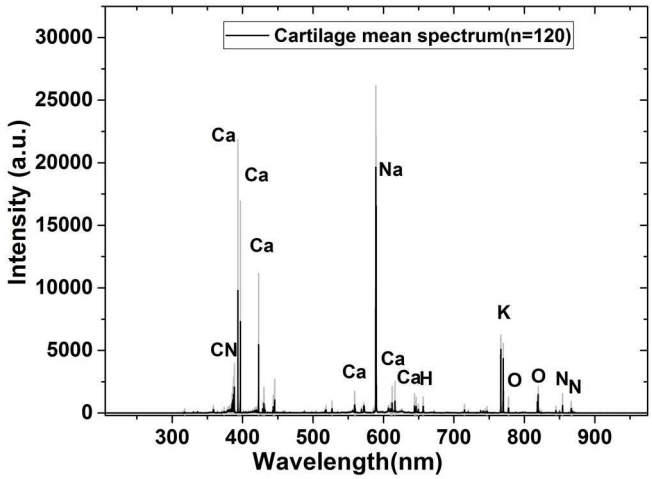

Figure 19: Mean LIBS spectrum of cartilage showing the elements observed using LIBS and those found in the literature.

details of the spectra of the first three tissues (peripheral nerve, cortical and cancellous bone) have already been discussed in the previous sections. In this part, the spectra of mucosa, pulp, dentine and enamel will be discussed. These tissue can be further grouped as soft (mucosa and pulp) and hard tissue (dentine and enamel). The spectra of enamel and dentine are quite similar and resemble the spectrum of cortical bone. This is mainly due to intense Ca emissions. The prominent lines are more intense in enamel than in dentin. Therefore, instead of showing the entire spectrum of these samples, two spectral regions where qualitative difference between them is observed has been chosen for display in figure 20.

Figure 20 shows that certain emission lines appear in the spectrum of enamel that are not visible from dentin. The assignment of elements to peaks in LIBS is still one of the most challenging aspect of the technique. This presents even more difficulty in the UV region of the spectrum as there are numerous lines of the elements expected from the samples with lines that the spectrometer cannot resolve. As the determination of elements qualitatively was not the primary goal of the work, no further effort was put in determining the elements responsible for the lines.

Spectra from pulp and mucosa showed similar peaks to that of soft tissues already discussed. A clear difference in carbon (C) and potassium (K) content was observed between the two tissues. This can be seen from C emission line (247.85 nm) and K (766.48 nm and 769.89 nm) in figure 21. The C and K

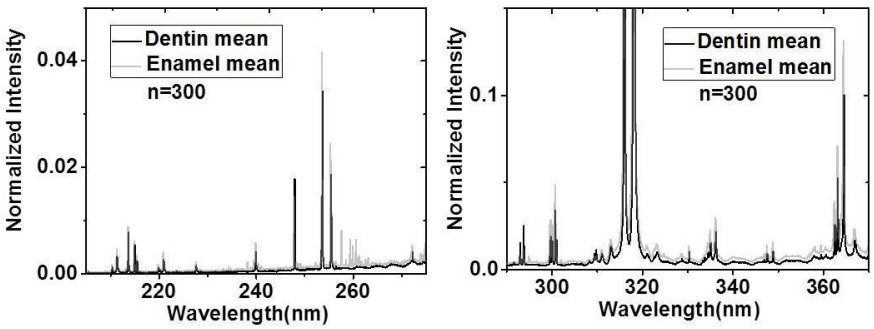

Figure 20: Normalized mean LIBS spectrum of enamel and dentin. The spectral region where clear difference between the two tissues is observed has been chosen.

content of mucosa appears to be higher than that of pulp. Higher C is further supported by increased intensity of the CN band around 390 nm. The mean spectra shown in the figure are obtained from normalized spectra. Further more, the difference of these elements in the samples can be directly observed by the relation to other peaks.

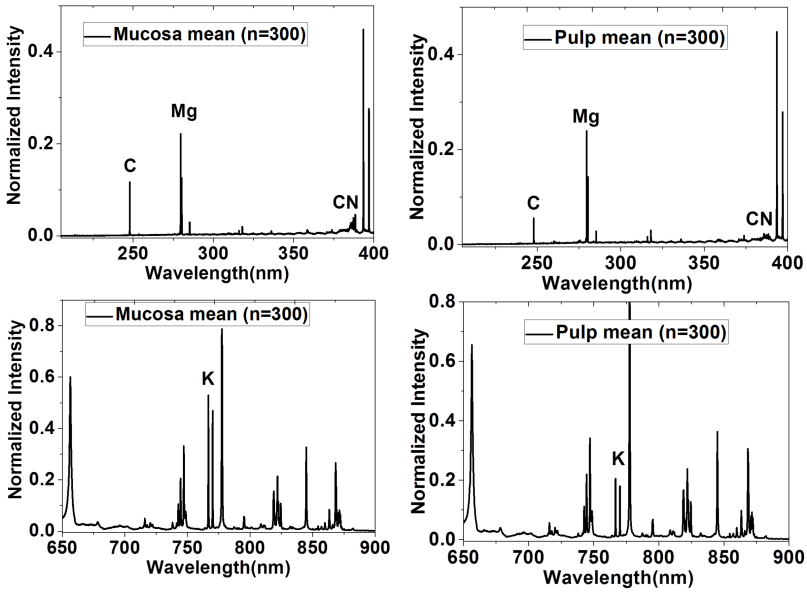

Figure 21: Normalized mean LIBS spectra of mucosa and pulp.

5.4 Summary measurement of elements in tissue using LIBS

In this chapter, the measured LIBS spectra from soft and hard tissues have been presented. From the results, the following conclusions are drawn:

- LIBS is able to measure all of the expected elements in the investigated tissue with the exception of P, Cl and S. These elements have very weak emission lines in the measured spectral range and were not measured under the ambient condition used. It was concluded that to measure these elements, a heavy gas atmosphere such as Ar has to be used. The results have proven the viability of LIBS for the direct and indirect measurement of elements and molecules in biological tissues, respectively.
- When a direct comparison of the intensity of emission lines of a major element is done, care needs to be taken not to use atomic transitions that involve ground state levels with high transition probability (for example Ca lines at 393.36 nm and 396.84 nm). Such lines are easily self-absorbed by the plasma and can lead to underestimation of the respective element.
- LIBS, as a sensitive analytical technique, is able to measure in ambient air the trace elements in tissues such as Na, K, Ca, Mg and Fe.
- A reproducible formation of CN and C_2 molecules during the cooling of the LIBS plasma of tissue was observed. The spectral feature of these molecules was observed to be proportional to the C and N present in the tissues. This proves that LIBS has a potential for indirect measurement of native molecules in tissues and those molecules formed during the process.
- The information obtained using LIBS, from tissues such as gland where there is a lack of compositional information in the literature both molecular and elemental, could be important for medical applications such as radiation therapy.
- The measurements done on both soft and hard tissues show that there is high similarity among the spectra of the tissues in each group. They also show that LIBS spectra of tissue are characterized by high variation despite the highly controlled experimental parameters. This necessitates the use of statistical classification methods to discriminate among the tissues in order to use the information for laser surgery feed-back system.

6 Statistical classification models for soft and hard tissue differentiation

The previous chapter has shown that the spectra of tissues are similar and are characterized by relatively high variation. As a result, a direct comparison of intensity of spectral peaks is not a viable solution to discriminate among tissue for the application of laser surgery. In this section various soft and hard tissue differentiation results based on the supervised machine learning LDA will be presented. A number of models, each addressing a specific group of tissues, depending on their anatomical proximity have been established. This means that some tissues may not be found close to each other hence including all tissues in one classification model would only mean introducing unnecessarily complications in the models. The need for spectral pre-processing in order to develop a successful model will be highlighted. The practical application of a classification model to classify tissue and generate a 2D tissue map will be presented. At the end, the transferability of a model developed from porcine tissue to differentiate mouse tissue will be presented. The contents of this chapter are summarized in the flowchart in figure 22.

6.1 Nerve and Gland

The pathologies of salivary glands range from infectious diseases to malignant tumors [41]. The major salivary gland (parotid gland) is where tumors mostly occur making up a considerable number of all head and neck neoplasms [27]. The parotid gland is the largest of the salivary glands [41]. Within the gland, the facial nerve starts to divide after exiting the temporal bone. The two tissues show close anatomic similarity and the primary goal of any surgery performed on the parotid gland is to completely remove the affected tissue without interfering with the facial nerve function [75].

Within this context, the use of an Nd:YAG laser parotidectomy, a surgical removal of the parotid gland, has been reported to cause less complications to the facial nerve [5]. The study highlighted that no significant or permanent facial nerve complications were related to the use of lasers except for the temporary postoperative mandibular nerve paresis. A muscular weakness due to nerve malfunctioning which was observed in 43% of the operated subjects which is less than the 50% expected after lateral lobe parotidectomy. The laser system used in this study has a sapphire tip enabling the surgeon to feel the operation providing tactile feedback similar to a scalpel. However,

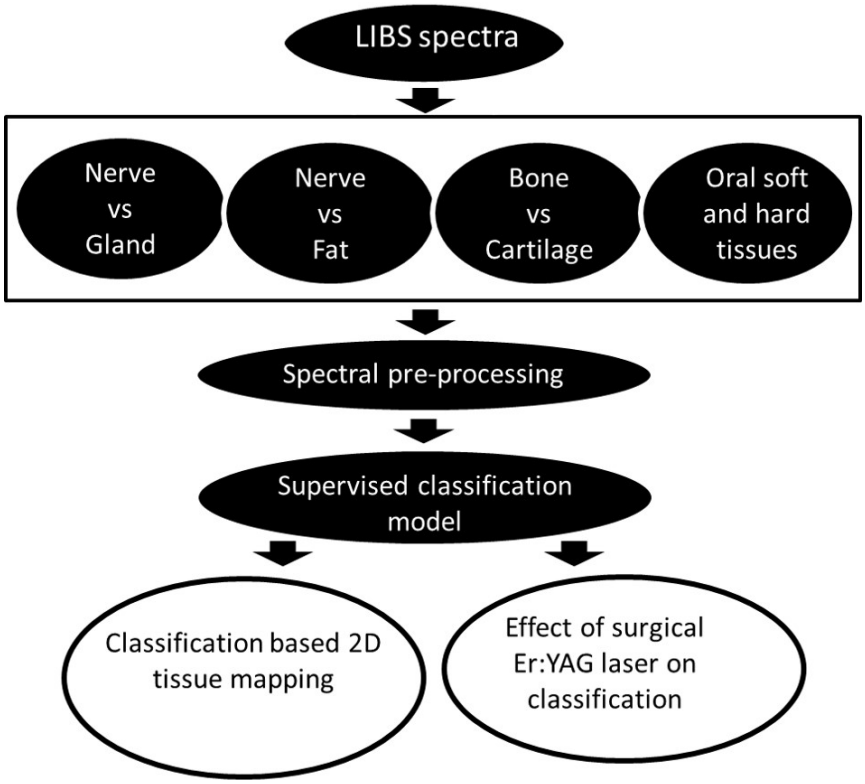

Figure 22: Chapter overview.

with other common free hand laser systems, the tactile feedback is lost and there is a high risk of damage of the facial nerve. The advantage of free hand lasers would be to avoid any bruising of the tissue while allowing operation with significantly smaller spot size compared to the sapphire tip that provides photothermal energy. This is due the the contact nature of the treatment. In addition, for tissue cutting applications, laser based tissue thermal cutting is likely to cause more collateral damage compared to short pulsed laser tissue ablation. Therefore, a feedback guided free hand laser would be expected to provide improved outcomes especially for micro-surgery applications. In this context, LIBS based differentiation of nerve and parotid gland would be a potential feedback system. The ability of LIBS to discriminate between the two tissues is demonstrated here.

To perform the discrimination between nerve and gland, each single spectrum from both tissues obtained from 6 animals was normalized by its total intensity.

Then the classification algorithm was optimized using 6 fold cross-validation of the 6 animals. Meaning, 5 animals were used for training and the remaining one for testing. In this manner all the animals are considered as a test sample one by one. To do so, the number of variables was first reduced from over 27,000 to 19 using PCA. The 19 new variables are the principal components (PCs) and were obtained by performing 5 fold cross-validation within the training data in order to make sure that the choice of the PCs is not influenced by the test data. Table 4 shows the percentage of variance contained in the 19 PCs.

Table 4: Percentage of variance in the first 19 principal components of the training data

Training set	PC1	PC2	sum(PC3-PC4)
Animals 1,2,3,4,5	34.52%	19.73%	28.04%
Animals 1,2,3,4,6	37.55%	20.51%	25.37%
Animals 1,2,3,5,6	36.66%	19.63%	27.27%
Animals 1,2,4,5,6	34.28%	22.67%	26.67%
Animals 1,3,4,5,6	34.21%	22.19%	27.27%
Animals 2,3,4,5,6	35.14%	21.70%	26.27%

Very well separation of the two classes can be seen in their scatter plot along PC1 and PC2 in figure 23.

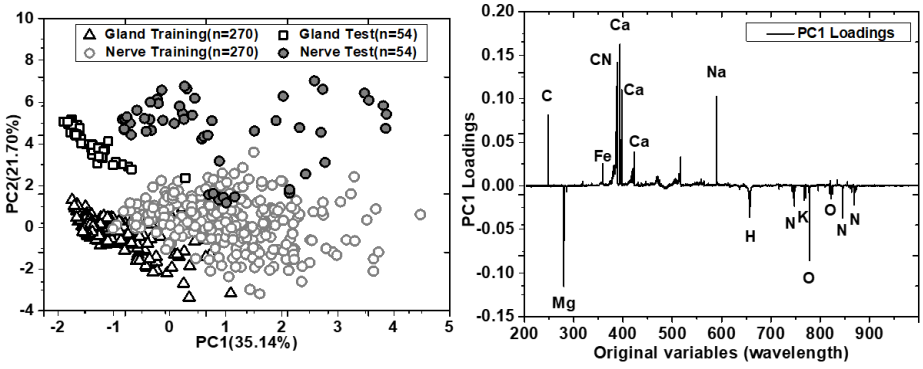

Figure 23: PCA analysis scores and loadings

The pattern of the test set is seen to be similar to that of the training set on the scatter plot shown in Figure 23(left) which indicates high classification performance of the classifier. The graph on the right shows the loading of PC1. These is the weights of the original variables that establish PC1. The

higher the absolute value of a given wavelength in the loadings graph, the more contribution it has in separating the dataset along PC1. The positive and negative values on the ordinate indicate the direction that a given wavelength takes up relative to the mid-point (zero-value) of the given one dimensional vector (PC). Following, supervised discriminant analysis was performed with LDA taking results of PCA as input. The confusion matrix of the six animals is shown in Table 5. The rows show the true class and the columns the prediction of the classifier. Therefore, classification errors can easly be seen.

Table 5: Confusion matrix of LDA classification of 6 animals

Animal 1	Gland	Nerve	Animal 2	Gland	Nerve
Gland	54	0	Gland	54	0
Nerve	0	54	Nerve	0	54
Animal 3	Gland	Nerve	Animal 4	Gland	Nerve
Gland	54	0	Gland	54	0
Nerve	0	54	Nerve	0	54
Animal 5	Gland	Nerve	Animal 6	Gland	Nerve
Gland	54	0	Gland	54	0
Nerve	0	54	Nerve	0	54

The confusion matrix shows there are no classification errors based on the features in the 19 PCs. However, for practical purposes a binary classifier is often desired. This is done by projecting the data on the linear classifier and analyzing the performance of the classifier using ROC analysis. The evaluation is performed based on the cut-off point where there is the best trade off between sensitivity and specificity. This is shown in table 6 which also shows 100% accuracy.

Table 6: Sensitivity of nerve and gland classification

Animal	Animal 1	Animal 2	Animal 3	Animal 4	Animal 5	Animal 6
Sensitivity	100%	100%	100%	100%	100%	100%

Besides the supervised classification model, these particular tissue classes can also be differentiated using simple ratio between a pair of some of the observed atomic emission lines. However, it must be noted that this might not be optimum for measurements outside the setting in the lab where control of the measurement parameters might be handled loosely. Meaning, a spectrum from a slightly defocused laser might show high intensity of emission lines

related to a transition involving a ground state than other states. In other words, for practical applications in surgery, slight defocus of the laser might occur which would affect the spectra significantly. Therefore, the supervised classifier is more robust as it considers all the emission lines at the same time. For the ratios to work reliably in practical applications, multiple of them can be used at a time in order to guarantee robustness. This leads to the scenario of finding the relationship among the different ratios. Meaning, the ratios themselves can establish a variable space where they can be analyzed in the same manner as the raw spectra have been with the classification analysis. A successfully implementation of this approach will be dealt in detail in the next section of the differentiation of nerve and fat. Here, the sensitivity and specificity values of a number of such single ratios is shown in figure 24.

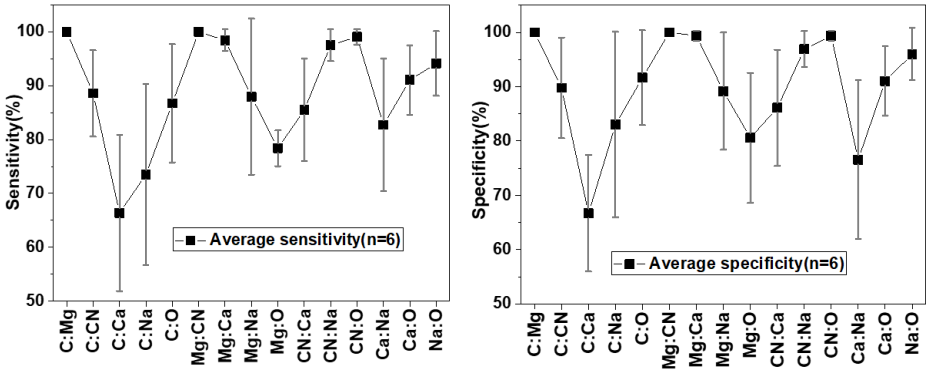

Figure 24: Sensitivity and specificity of emission intensity ratios for gland and nerve differentiation.

Visual inspection of the spectra from the two tissues shows significant difference in the intensity of the emissions of carbon (at 247.85 nm), magnesium (at 279.55 nm), calcium (at 393.52 nm and at 396.84 nm) and carbon related CN emission (band head near 388 nm). This is further supported by the contribution of these lines to the loading of PC1 as shown in figure 23. Overall, the results of differentiation between nerve and gland show very good prospect of LIBS for use as a feedback system for free hand laser parotidectomy.

6.2 Nerve and Fat

The relevance of fat tissue within the context of surgery is not to preserve it rather its resemblance with nerve when looked through the eyes without any aid. This means accidental nerve damage can occur when the intention is to remove fat in regions where they exist in close proximity. Mechanically, the

two tissues have differences which allows for detection of nerve from fat with acoustic based techniques or by tactile feeling. The established acoustic based techniques or tactile feeling by the surgeon need to come into contact with the tissue which is not aligned with the main reason to use lasers for surgery. The challenge of optical differentiation (visually, fluerescence spectroscopy or raman spectroscopy) is due to the fat content of nerves hampering the optical contrast from pure fat. LIBS as an optical technique provides unique opportunities targeting the elemental composition of the tissues.

It has been shown that nerve and fat have similar elemental composition but the concentration of these elements varies. In this section, the differentiation of the two tissues based on various features of their LIBS spectra will be discussed. Two main approaches will be considered for the classification. One is classification based on different spectral region where the variables for PCA are the measured wavelengths. The other approach is to use the ratio among emission lines as variables. For the investigations, tissues from 6 porcine animal models were measured.

Analysis on original variables (full spectrum)

After normalizing all the spectra, PCA was performed on the spectra in the same manner as in the previous section. This was done using training dataset from 5 animals and test dataset from the remaining animal. Selection of PCs was done based on 5 fold cross-validation of the training set. This is then followed by 6 fold cross-validation of final classification. In the analysis, only the first 5 PCs contained more than 75% of the variance of the data. Inclusion of any of the subsequent PCs showed no improvement to the classification of the two classes. Table 7 shows the portion of the variance shared among the first PCs.

Table 7: Percentage of variance in the first 5 principal components of the training data of the range 200 - 975 nm

Training set	PC1	PC2	sum(PC3-PC5)
Animals 1,2,3,4,5	43.11%	19.53%	16.66%
Animals 1,2,3,4,6	35.72%	27.09%	16.01%
Animals 1,2,3,5,6	42.39%	23.31%	13.97%
Animals 1,2,4,5,6	41.50%	23.05%	15.65%
Animals 1,3,4,5,6	41.55%	22.54%	15.17%
Animals 2,3,4,5,6	38.83%	24.34%	16.29%

The portions of the total variance contained in the first PCs suggests that the raw data can be represented sufficiently only by these PCs. Therefore, these PCs were used for further classification analysis. The scatter plot in figure 25 shows the separation of the two classes of the training and test dataset but with overlap of a significant portion of the data of both sets. The separation of the classes is better along PC2. It is a good example that a principal component (PC) containing a large portion of the total variance does not guarantee good separation of classes. This is because PCA only looks at the variance in the data regardless of its class belonging. Meaning, any variation even originating from the measurements will be regarded as information relevant for the difference in the data. A reason why discrimination analysis such as LDA is required.

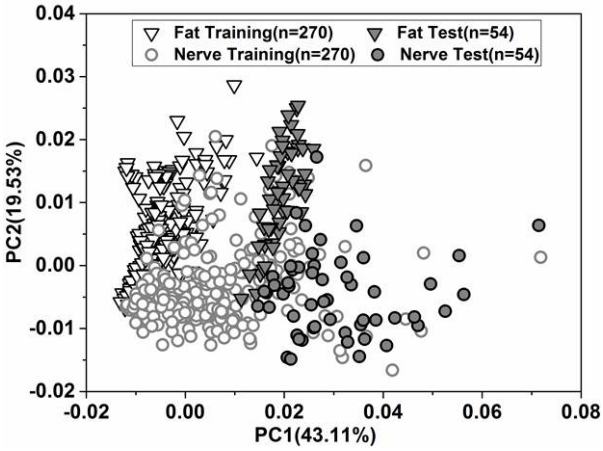

Figure 25: Nerve-fat pair scatter plot of training and test dataset on PC1 versus PC2 of 200 - 975 nm range.

The loadings of PC1 and PC2 in figure 26 show the contributions of the emission lines. Due to the relatively high shot to shot variation of the LIBS measurements, it is often the case that PC1 resembles the actual spectrum measured. Which is clearly evident in figure 26. This is can be the explanation for the overlap of the two classes along PC1. The dataset is well separated along PC2 hence the loadings of PC2 should show us which peaks are contributing to the separation. Oxygen and the molecular emission from CN, related to carbon content, have the most contribution. This is in a good agreement with the actual content of the two tissue. Carbon making less than 10% and more than 50% of the composition of nerve and fat, respectively. On the other hand, oxygen makes over 65% and less than 55% by mass of nerve and fat, respectively.

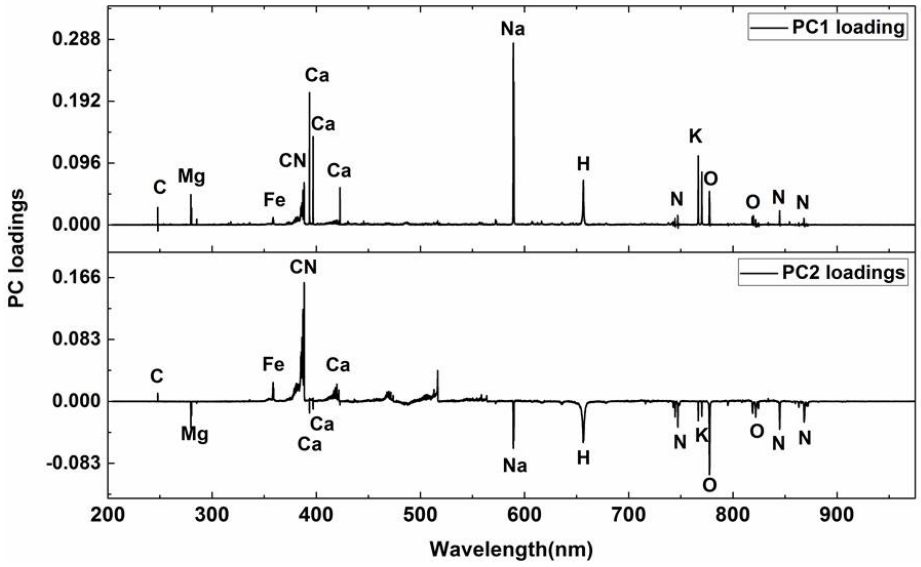

Figure 26: PC1 and PC2 loadings of PCA analysis of the range 200 - 975 nm for nerve and fat.

Analysis on original variables (specific spectral regions)

Besides analyzing the measurements based on the entire spectra, two spectral regions one targeting only the region where carbon emission is high and the other where the oxygen emission is high have also been investigated. This is an attempt to investigate if the classification out come can be improved by considering only the regions where the two classes have significant difference. As PCA is a rotation process to find new vectors using the original vectors, it is worth checking sub space of the original space. To do so, the regions from 200 nm to 450 nm (for carbon emission) and from 450 nm to 975 nm (for oxygen emission). These two regions were analyzed in the same manner as the entire range.

Table 8 shows the percentage of variance contained in the first 5 PCs of the training dataset. The scatter plot in figure 27 shows how the data of the two classes group along PC1 and PC2.

The plot of the data on the PCs obtained from the entire sub-spectrum above shows that the separation of the classes is not improved at least when visually inspected. The contribution of carbon related emissions are dominated by calcium emissions in the loadings. Meaning the resulting PCs are aligned in the direction that does not primarily favor the carbon emissions rather the calcium emissions. The mean spectra of the two tissues shows that the

Table 8: Percentage of variance in the first 5 principal components of the training data of the range 200 - 450 nm for nerve and fat classification

Training set	PC1	PC2	PC3-PC5
Animals 1,2,3,4,5	54.93%	23.33%	6.05%
Animals 1,2,3,4,6	51.60%	28.45%	5.76%
Animals 1,2,3,5,6	48.59%	31.65%	5.22%
Animals 1,2,4,5,6	49.91%	29.94%	5.37%
Animals 1,3,4,5,6	52.96%	26.40%	5.16%
Animals 2,3,4,5,6	49.73%	29.94%	5.13%

difference of the data in terms of calcium is not as pronounced as it is for carbon resulting in more overlap of the two classes.

Similarily, the investigation of the 450 - 975 nm range also provided results that have not shown improvement from the analysis of the entire spectrum. The amount of variance in the first 5 PCs was found to be similar to that of the two regions that have already been shown. A closer look at the loading of the PCs of this range shows that oxygen is one of the dominant emissions contributing to the loadings. However, there is also relative increase in the contribution of the other elements when compared to the loadings of the analysis on the entire spectrum. This changes in the PC loadings have not brought improvement on the separation of the classes. This will be shown in the evaluation of the classification performance of the LDA classifier based on the different regions. Before the evaluation is discussed, the next part will show how the classification of the classes can be significantly improved by considering the ratios among all the prominent peaks.

Analysis on ratios of emission lines

As was already discussed, the shot to shot variation of LIBS signals results in significant variation in the data. This is often observed by intensity drop of the emission lines without significant change in the profile of the spectrum. This is loosely termed and should not imply a stable spectral profile especially for tissue due to their heterogeneous nature. In order to exploit this property of LIBS spectra, ratios were generated among the prominent peaks measured from the two tissue types. In total 18 peaks (labeled in the average spectra of fat in figure 13) were selected. From these 18 peaks, 153 ratios were generated by performing permutation without repetition. The representation of nerve and fat spectra by these ratios is shown in figure 28. The ratios shown are the results of the measurements from all the investigated animals. The horizontal

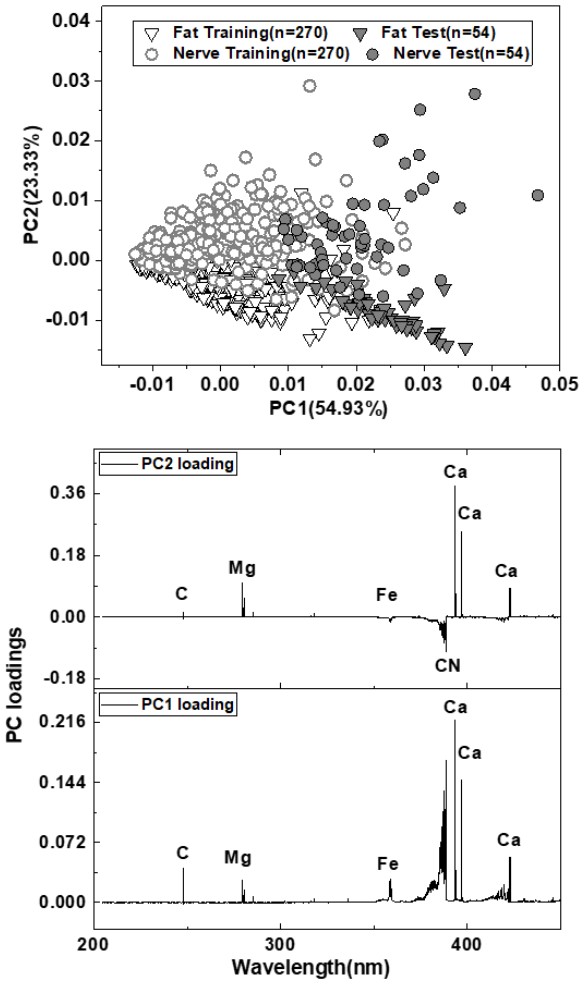

Figure 27: Nerve-fat pair scatter plot on PC1 vs PC2 and the loadings of PC1 and PC2 of the range 200 - 450 nm

axis is the index given to the ratio combinations. The first index belongs to the ratio between, going from left to right, the first element and the second. The next index is the ratio between the first and the third elements. In this manner all possible combinations are considered.

The above ratios are then used to perform PCA in order to exploit all the information in the ratios and are further reduced in the same way dimensional reduction was done with the raw variables. The result of the PCA by considering training and test dataset is shown in table 9. Up on 5 fold

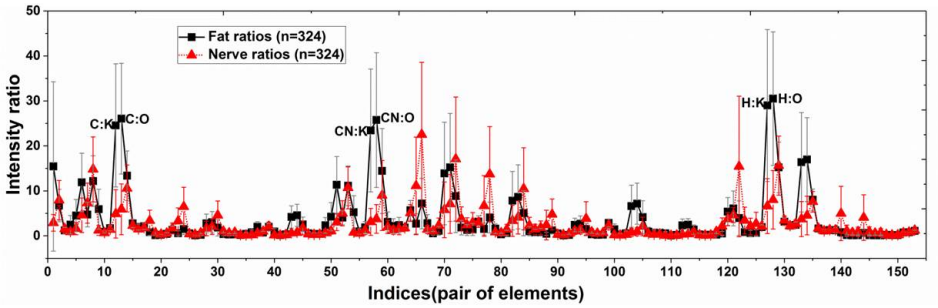

Figure 28: spectrum of nerve and fat represented by ratio of emission lines

cross-validation within the training dataset, only the first 5 PCs could be used to classify the dataset in which inclusion of the remaining PCs resulted in negligible improvement in accuracy. The variance contained in the 5 PCs is shown in table 9.

Table 9: Percentage of variance in the first 5 principal components of the training data of ratios taken as variables

Training set	PC1	PC2	PC3-PC5
Animals 1,2,3,4,5	49.95%	12.19%	20.94%
Animals 1,2,3,4,6	44.02%	15.32%	22.78%
Animals 1,2,3,5,6	49.06%	11.30%	21.78%
Animals 1,2,4,5,6	48.59%	12.63%	21.71%
Animals 1,3,4,5,6	50.51%	13.41%	20.17%
Animals 2,3,4,5,6	49.25%	12.90%	22.03%

The scatter plot of the data of a training and a test set is shown in figure 29. The two tissue classes are well separated along PC1. The loading of PC1 shows that the ratios that show clear difference between the two classes in figure 28 are among the most contributors to PC1. These ratios are related to the elements C, O and K. These elements allow for the possibility to separate nerve from fat by simple ratio between such elements. This will be considered when comparing the sensitivity of the different approaches. These elements have been shown to be found in different concentration in the tissues as can be seen in their respective spectra and also in the literature.

Looking at the scatter plot along the PCs, the analysis on the ratios among the selected peaks seems to be the most promising for the classification of similar tissues such as nerve and fat. The conclusion for the classification

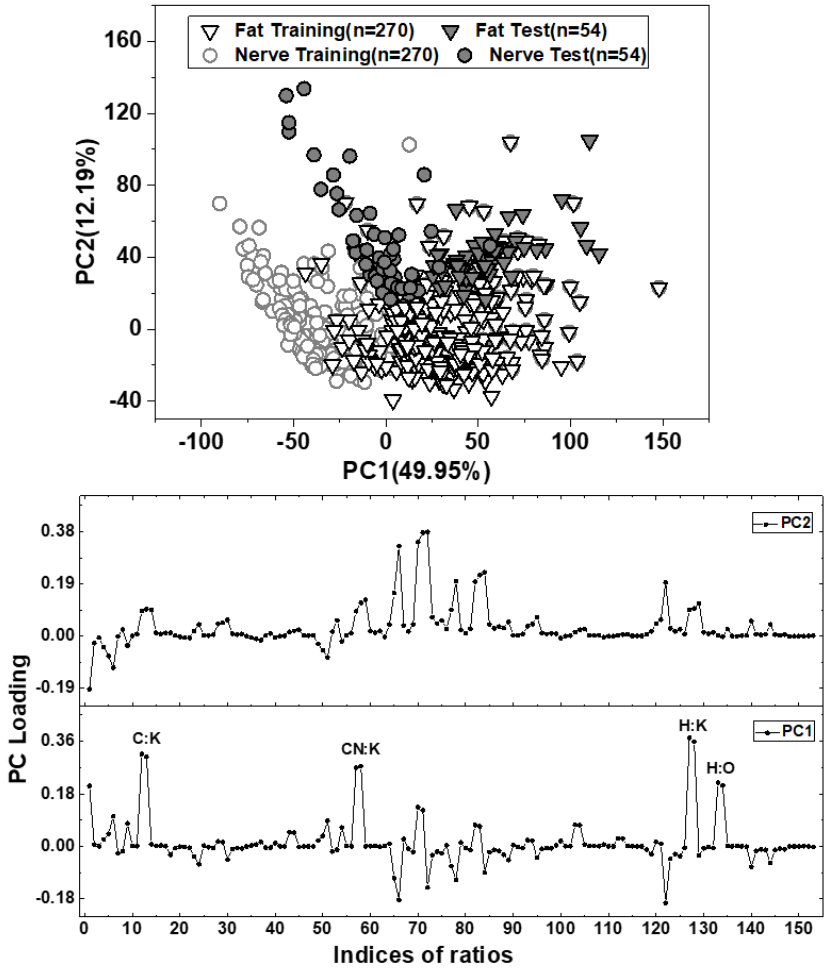

Figure 29: Scatter plot PC1 vs PC2 and loadings of PC1 and PC2 of ratios taken as variables.

result based on different pre-processing approaches is best reached after performing classification analysis and evaluation of the classifier. LDA analysis was performed on the PCA results of the 200 - 450 nm, 450 - 975 nm, 200 - 975 nm and on ratios. After analysis with LDA, ROC analysis was performed to evaluate the classification performance. In the case of simple ratio of two elements, the pair that provided the best results was the ratio between CN and O. For this ratio, only ROC analysis was performed to find the cut-off point for best sensitivity as the data is already one dimensional. Figure 30 shows the sensitivity values of individual animals and the average of 6 animals of each approach.

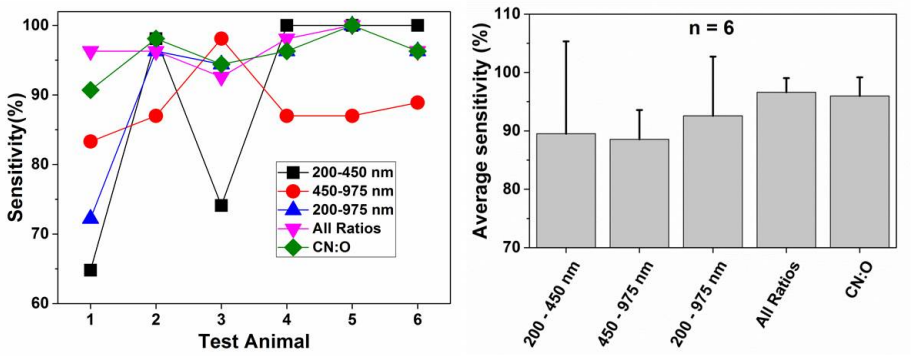

Figure 30: Individual sensitivity values of different nerve and fat classification approaches for each animal and the averaged values of all animals for each approach.

It is clearly visible that the reproducibility and performance of the approach using ratios is better than the others. The single ratio approach performs nearly as the one with all ratios. However, this may not work because the difference in the content of these pair of elements in this two tissue is significant and this may not work for all tissue types as the concentration of carbon and oxygen may be different. The conclusion from the study of nerve and fat is that the two tissues can be best differentiated when a new variable feature based on the ratios of the measured atomic emissions is generated from the raw spectra. In general, owed to the similarity among soft tissues, the classification of their spectra may be better performed when ratios are considered in order to minimize the shot to shot fluctuation.

6.3 Cortical Bone and Cartilage

The presence of cartilage in the body is often associated with bone joints. One such structure is the temporomandibular joint (TMJ). Inflammatory diseases and mechanical stress can affect the normal functioning of the TMJ [51]. While many treatments try to avoid surgery in the TMJ, there are some cases where surgery is the only treatment option [21]. The range of applications of surgery can be from removal of joint structures to replacement by prostheses. These require the procedure be selective to specific tissue for example the cartilage from the cortical bone. Within this context, a laser scalpel with a feedback mechanism may be an attractive option. Therefore, the investigation of the differentiation of cartilage from cortical bone can lay a ground for the application of a laser scalpel with a feedback system.

The spectra of cortical bone and cartilage have already been shown in figures 16 and 19. It is already clear that the spectrum of cortical bone is dominated by intense calcium peaks which are not observable in the spectra of cartilage. This means numerous ratios based on the detected peaks from cortical bone can be used to differentiate between the two tissues. Apparently, these ratios can be used as highly discriminatory variables as explained in the nerve and fat differentiation. A simple comparison among some of the ratios proofs their discriminatory power. The ratio between one of the persistent calcium lines (at 616.21 nm) and that of potassium (766.48 nm) can be used as an example. For visual comparison, the calcium line that is barely detectable from cartilage has been used. The values of the ratio of this pair for the 6 investigated animals is shown in figure 31. The sensitivity based on this pair of lines is 100% for all the animals. A number of intense calcium lines seen in the spectrum of cortical bone can be used in a similar manner further proving the effectiveness of taking ratios as discriminatory variables.

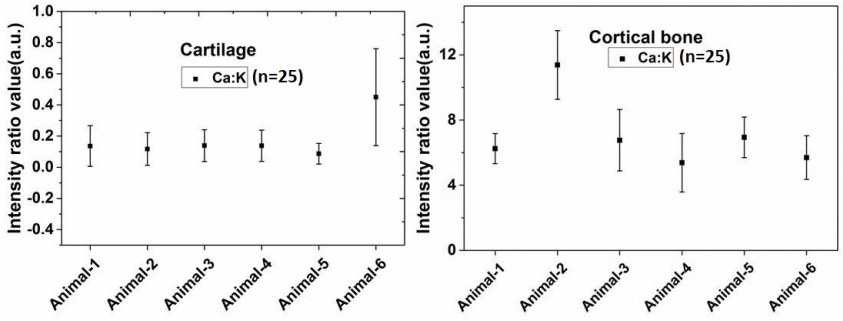

Figure 31: Sensitivity bone and cartilage differentiation based on ratio of Ca to K peaks.

Following the ratio analysis, the supervised classification of the two tissues also provided with very high accuracy values. The high classification accuracy can be attributed to the distinct difference of the spectra of the two tissues. The result of the PCA analysis and the scatter plot along PC1 and PC2 are shown in table 10 and 32, respectively. Owed to the significant difference between the spectra of the two tissues, classification analysis was done based on the raw spectra without any need for further feature extraction.

The scatter plot in figure 32 shows that the two classes are well separated along both PCs. This is different from what was observed in the classification of nerve and fat where their separation along PC1 was not good. It was explained that the reason is the relatively large shot to shot variation of the spectra. This is still existent here. However, the difference in the spectral profile of the two tissues is large enough to dominate the shot to shot spectral variation.

Table 10: Percentage of variance in the first 5 principal components of the training data

Training set	PC1	PC2	PC3-PC5
Animals 1,2,3,4,5	83.79%	11.53%	3.52%
Animals 1,2,3,4,6	86.55%	8.70%	3.48%
Animals 1,2,3,5,6	84.54%	10.63%	3.57%
Animals 1,2,4,5,6	84.43%	11.06%	3.27%
Animals 1,3,4,5,6	82.91%	11.86%	4.02%
Animals 2,3,4,5,6	85.32%	9.64%	3.65%

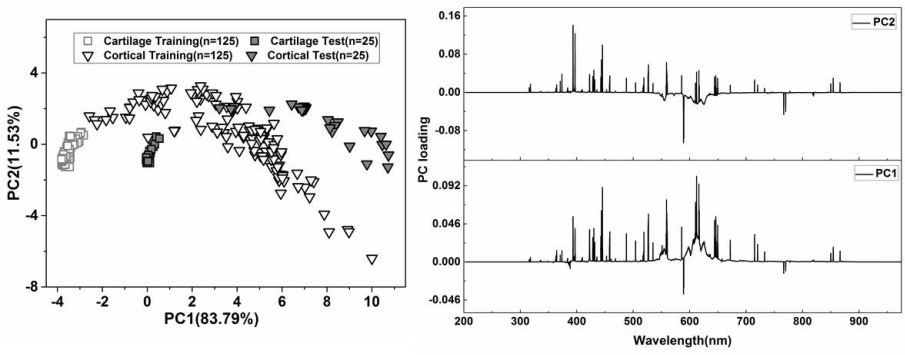

Figure 32: Scatter plot and PC loadings of a training and test dataset of bone and cartilage classification.

Apparent from the scatter plot, the classification accuracy of LDA on the results of PCA was 100% for all the investigated animals without a single misclassification of the measurements.

The investigation on cartilage and cortical bone has shown that they have significant difference in their calcium content and this can easily be measured with LIBS. In order to perform real-time discrimination between the two tissues, it has been shown that two approaches are possible to reach a 100% accuracy. These are an approach based on the ratio among emission lines (where Ca:K ratio was used as an example) and based on a the entire spectra using LDA. For practical applications, both classifications using ratios as variables and the entire spectra yield 100% classification accuracy.

6.4 Dental, Bone and soft tissues of the oral cavity

One of the attractive applications of lasers as surgical scalpels is in oral surgery including dentistry. It has been reported that bone healing is faster after laser ablation compared to mechanical drilling [56]. The presence of bacteria in blood was also observed to lower after ablation with CO_2 laser of oral mucosa when compared to that of electro-surgery or the traditional scalpel [45]. These are among the numerous reports of the advantage of using lasers for oral surgery interventions. Therefore, a sensitive feedback system that guides lasers in this area of surgery would have a great impact for the field. In this section, LIBS is investigated to discriminate among various oral tissues in order to address the challenges of using lasers in the area of oral surgery.

The tissues investigated here are porcine oral soft and hard tissues. These include: peripheral nerve, cortical bone, cancellous bone, oral mucosa, enamel, dentine and pulp. One of the most critical aspects of oral surgery interventions is the prevention of peripheral nerves located in proximity to the other tissues. For example, the tissues from which the *nervus lingualis*, responsible for the majority of the tactile sensation of the tongue, need to be identified are mucosa and bone [59]. This is because it is found within a thin layer of connective tissue and runs between oral mucosa and bone. Therefore, it is prone to damage when operating on the mucosa layer.

The clinical relevance of discrimination between cortical and cancellous bones is that the mandibular nerve responsible for the functioning of the lower teeth and the sensation around the chin, runs inside tube like cavities inside a bone structure. The cavities are found within a cancellous bone structure surrounded by an outer cortical bone structure. Therefore, identification of these tissues is important during laser osteotomy of the mandible. Here, the practical implementation of a feedback system would be to detect the transition from cortical to cancellous bone.

The differentiation of dental tissues may be essential in the application of lasers for dentistry. Many laser systems have now been cleared for use in clinical environment for the application of hard tissue such as ablation of caries, enamel and dentine. Such applications are reasoned based on clinical studies that report equivalent or better outcome than that of traditional drills without using anesthesia [54]. In this study, the identification of carries tissue with LIBS has not been performed but there are studies that showed the use of LIBS to identify carious from healthy tooth [64] without the use of the technique in differentiation of the various parts of tooth. Therefore, the differentiation

of the entire set of tissues, enamel-dentine-pulp-mucosa as well as peripheral nerve, cortical and cancellous bone is important.

The spectral feature of each of the tissues grouped under dental tissues has already been discussed in the previous sections. In this section the classification of these tissues will be discussed in detail. A work related to this project has already reported the grouping of the hard and soft tissues based on selected calcium and carbon peaks and further differentiation of the tissues in each group based on supervised classification by taking ratio of peaks as variables [59]. The steps used to classify the tissues will be briefly summarized first. Then improvement of the classification within the hard tissues (especially between dentin and enamel), which showed relatively poor accuracy, will then be presented and compared with our previously reported results using the same data. The first step of grouping a given tissue as soft or hard tissue still follows the same approach that looks at calcium to carbon ratio. The approach to differentiate the tissues within soft group is also still maintained. Meaning, the ratios among selected peaks are used as input variables for the supervised classification. To improve the classification accuracy of the hard tissues, a spectral region within the measurement range is considered. The entire procedure of the modified classification decision is shown in figure 33. The details of the approaches are already reported and the obtained results will be first briefly discussed followed by the details of the improved part.

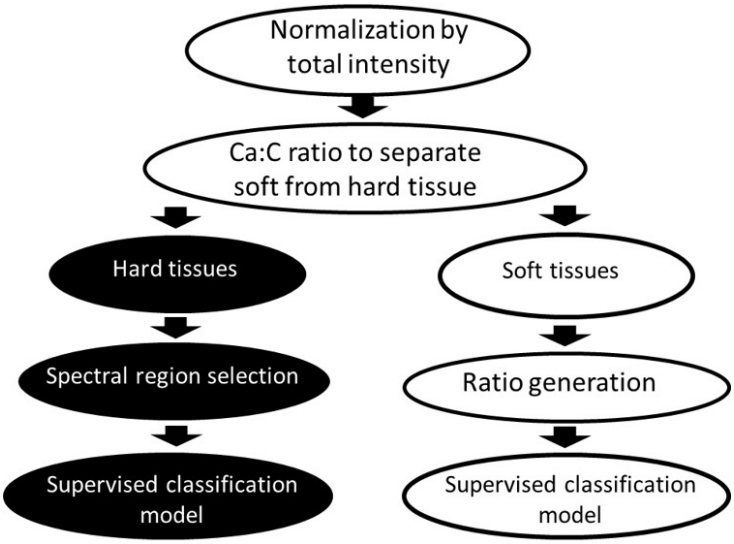

Figure 33: Classification procedure

Hard and soft tissue classification

With the help of the distinct difference between the spectrum of hard and soft tissues owed to their calcium content, the group membership of each measured spectrum (soft or hard tissue) can be determined by looking at ratios involving calcium peaks. This can be done by considering the ratio of calcium to another persistent line from another element. There are numerous emission lines of calcium in the visible range of the spectrum of hard tissues compared to that of soft tissues. Therefore, to make the separation of the two classes, four lines of calcium were chosen. These lines can be denoted by Ca-1 (430.25 nm), Ca-2 (445.47 nm), Ca-3 (612.22 nm) and Ca-4 (616.21 nm) [59]. The second element, to be combined with calcium for ratio generation, can be chosen to be one of the major elements. The emission line of carbon at 247.85 nm can be used for this purpose. The ratio with this line gives very high accuracy of classification between the two groups. The Ca and C lines chosen do not involve transition to a ground state level. This means the transsitions are not easily excited when the excitation conditions are far from optimal (example due to defocusing). This helps increase the robustness of the selection process. Figure 34 shows a re-plot of the values of the ratio of Ca-1 to C for the six animals investigated [59].

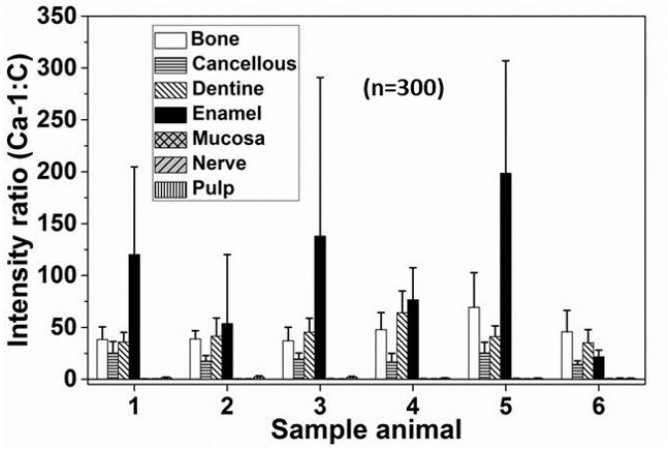

Figure 34: Ca-1 to C ratio for soft and hard tissue classification

The values of the ratios of the four calcium lines to that of the carbon line were checked for the classification of all the soft and hard tissue measurements of all animals. The way each of these ratio was evaluated was to perform ROC analysis based on a threshold value at the boundary of the two tissue groups. The sensitivity (detecting soft from hard tissue) was found to be 100% and the specificity (detecting hard from soft tissue) was found to be 99.91%.

From the results above, it can be concluded that the classification of a measurement as soft or hard tissue can be reliably done by considering simple ratio of calcium to carbon emission. Once the group of the measurement is decided, then class membership within the allocated group can be done by a model based on a supervised learning.

Classifications within hard and soft tissue groups using supervised learning

Soft tissue group: An average accuracy of more than 98% could be achieved for the tissues in this group. This is done by taking the ratio among 18 prominent peaks to yield 153 new features for use as input variables for classification [59]. Following the generation of ratios, classification based on supervised learning is done in the same manner as in the case of the nerve and fat study.

Hard tissue group: Some of the tissues in this group are among the difficult ones to differentiate using LIBS. As was already highlighted, the spectra of these tissues is dominated by numerous calcium peaks. The attempt to classify these tissues using the entire spectrum yielded very low accuracy. This is due to the high variance of the intensity of the prominent peaks diminishing the effect of weak intensity peaks. The classification of these samples, the ratio approach based on 38 prominent peaks (essentially 730 ratios), resulted in a high accuracy for many of the tissue pairs of the investigated animals except for the dentine-enamel pair and some of the other pairs in some animals. The details of the results will be discussed in detail at the end of this section. The relatively poor accuracy on some tissue pairs can be attributed to the fact that their spectra are quite similar showing difference only in a few weak emission lines in some spectral regions. This makes it difficult to differentiate between similar tissues such as enamel and dentine using ratios generated from prominent peaks. It has already been shown that a closer look at the spectra of this particular pair of tissues shows distinct difference in the spectral region 215 nm - 290 nm due to some weak lines possibly from calcium. To assign these peaks to a particular element is difficult as they can be attributed to more than one element that are present in bone (for instance Ca or Fe). Classification based on this region gives very high accuracy for the dentine-enamel pair while yielding a slightly reduced accuracy for the cortical-cancellous bone pair, compared to the ratio approach. In this section, improved overall classification results of the data from hard tissues, already reported, based on this region will be discussed. The reported results based on the ratio approach will be shortly compared to the new results. The representation of the spectra of dentine-enamel pair by the ratios is shown in figure 35 [59]. To demonstrate the

similarity of dentine-enamel pair, the ratio range with the most contribution to the loadings of PC1 and PC2 is shown in the figure. It can be seen that the resemblance between the two tissues is very high hence posing difficulty in their classification.

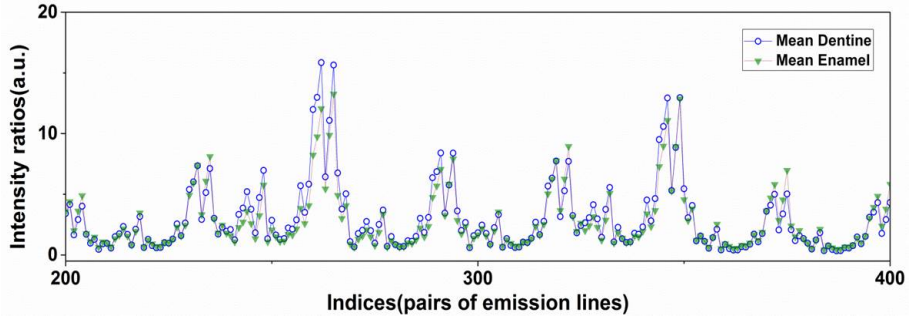

Figure 35: Representation of hard tissues using 730 ratios.

The classification analysis was done on the training and test data represented by 5 PCs (accounting on average 92.66%) in the ratio case and 10 PCs (accounting on average 99.5%) in the selected region. The classification sensitivity of all the tissue pairs of each animal using the ratios and the selected region are shown in figure 36. It can be seen that except for animal-6, the overall accuracy is higher for the selected region compared to the ratio. Most of the tissue pairs show improved accuracy in the results of the selected region.

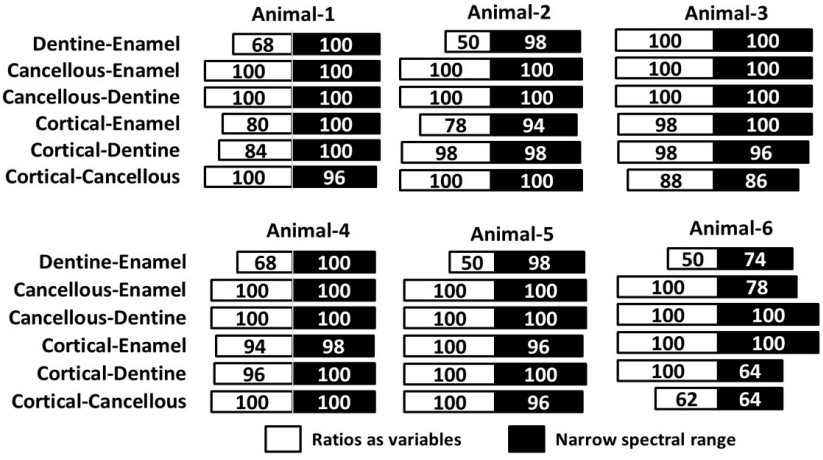

Figure 36: Classification sensitivity among hard tissues.

Similar to the sensitivity results, the specificity results also showed improvement in the classification using the selected region (Figure 37). Comparing the two approaches, the differentiation among cortical bone, enamel and dentine is improved in the classification based on the selected region. Especially, the dentine and enamel pair yielded sensitivity and specificity values in the range 50% - 60% in the ratio approach for the majority of the investigated animals. This range was considered to be random and hence set to 50%. In the selected region, this has been completely changed. Except for animal-6, the random classification could be improved to a 100% classification. Dentine and enamel consist of the same mineralized collagene matrix with slight difference in percentage and a small portion of organic material. Attempt to classify/separate samples with slight difference in their matrix without significant difference in elemental composition is a challenging task in LIBS owed to the shot to shot sensitivity of the signal. This is especially difficult in tissue due to their heterogeneous nature.

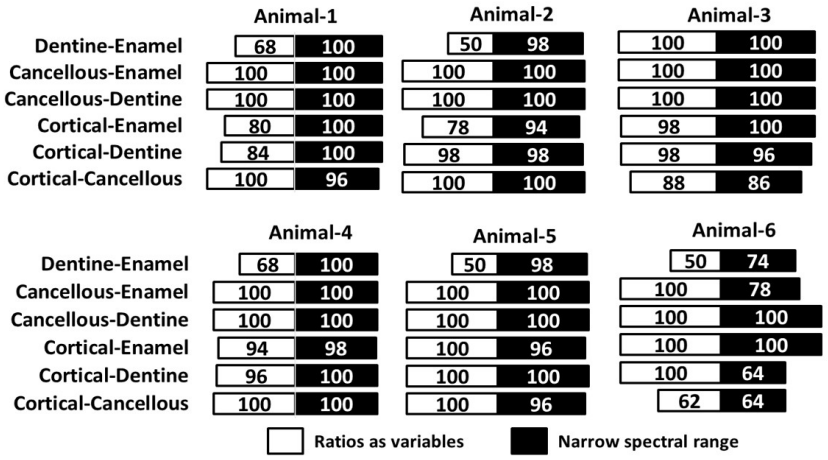

Figure 37: Classification specificity among hard tissues.

The results of classification show that most of the tissue groups can be differentiated using statistical classification approach with high accuracy. In all the results discussed so far, multiple LIBS measurements are taken from a few scattered points on the surface of each tissue in which each position is adjusted according to the laser focus position. In a real surgical application, this can be realized by an autofocus system if a point of measurement is at a defocused position of the LIBS laser. Since there was no autofocus system implemented, one way to look at the applicability of LIBS together with the classification algorithm is to put tissues together and perform measurements

by scanning an area whether all the tissues can be probed. This is presented in detail in the next section.

6.5 Tissue type mapping based on classification

This section demonstrates the transfer from single point measurement to two-dimensional scanning. So far, the samples were measured one after the other by making sure that the measurement positions were flat and level in order to minimize variations in laser spot size. Therefore, it is important to perform measurements where there could be a slight defocusing of the laser due to irregularities on the surface of samples. Such a setting is one way to check the robustness of the different supervised classification models against changes in the experimental parameters. Due to the irregular structure of tissues, different excitation conditions resulting in variations of laser spot size is one of the frequently expected occurrences in real applications.

In this experiment, soft tissues with similar thickness (fat, muscle, nerve and skin) and a bone tissue were prepared and stacked laterally. Due to the slight difference in the thickness of the tissues, measurement irregularities are expected. These irregularities are in turn expected to cause slight differences in laser spot size on the different tissue surfaces. The bone sample was slightly thicker than the soft tissues by about 1.5 mm because of the precision of the band-saw used to cut it. The entire LIBS system was synchronized in such a way that the LIBS laser triggers the spectrometer and a motorized stage via a pulse generator. There was no change made to the setup from the one used to measure the same tissue types individually. A classification model classifies the spectrum from each of the laser shots before moving to the next position. This is to check the performance of the classification technique in a real-time condition that is close to the actual surgical process. The supervised classification model was based on optimized measurements of separate four soft tissues (fat, muscle, nerve and skin) and a bone tissues measured individually. The scanned tissues and the classification result are shown in figure 38.

As was explained in the dental tissue group, the grouping of a given measurement as hard or soft tissue was done using the ratio of the four calcium lines (at 430.25 nm, 445.47 nm, 612.22 nm and 616.21 nm) and the carbon line (247.85 nm). The figure shows even with slight defocusing of the bone surface, the accuracy of detecting bone is high with two or three misclassification of bone as skin. Skin has much more calcium peaks compared to the other soft tissues. The calcium lines selected are also existent in skin and very weak

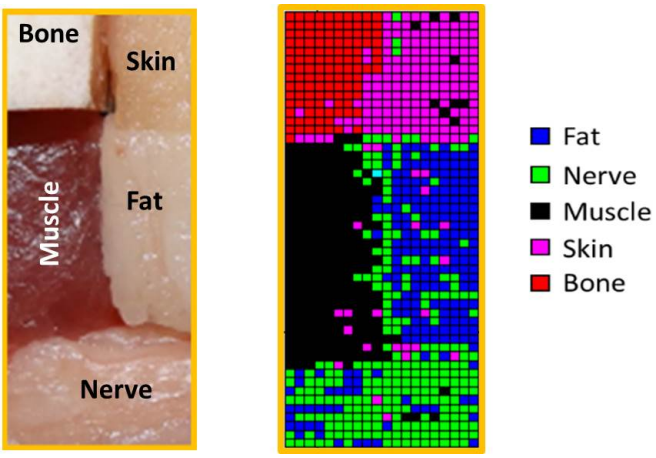

Figure 38: Image of laterally stack tissues and their scanned image based on prediction of the tissues.

ionization of bone results in the misclassification of bone as skin. This can be easily avoided by implementing a focus finding system which was not within the scope of this work.

The classification of the soft tissue spectra was done using the approach where ratios are used as input variables. Classification of skin and muscle showed higher accuracy than that of nerve and fat. The high accuracy of identifying muscle and skin can be implicated to a few elements. The potassium doublet with lines at 766.48 nm and 769.89 nm, one of which is used in the ratios, is high in skin and muscle. Besides, the sodium doublet with lines at 588.99 nm and 589.59 nm also shows higher intensity in these two tissues relative the carbon lines. On the other hand, the carbon line at 247.85 nm and its related molecular emissions CN and C_2 exhibit weaker emissions in muscle and skin spectra. Therefore, the ratios having been significantly influenced by the emissions of all these elements result in very good identification of muscle and skin from nerve and fat. It is clear that most of the boundaries at the tissues are classified as nerve. These are points where ionization of air is expected due to the gap between tissues. The classifier assumes the spectrum of air resembles that of nerve. Generally, the spectrum of air shows emissions of nitrogen, oxygen and hydrogen mostly in the infrared region. The misclassification of air as nerve was not given much attention here and can be resolved by including air as part of the training data if needed.

The nerve and fat region showed the most misclassification cases. This is expected because of the effect of the different focus size on the surfaces of the two tissues. As was already mentioned, the surface of the tissue was not prepared in such a way that there is a constant focal position allowing for reproducible excitation conditions. As a result, many of the measurements of nerve were classified as fat and vice versa. High classification accuracy of this tissue pair has already been demonstrated under controlled focus size spot. Therefore, a focusing system is important to have in a real-time application involving nerve and fat tissues. The performance of the scanning system if the distance of the surface of the tissue being scanned is kept constant is shown in figure 39. This experiment uses a tissue block containing both fat and muscle where a flat cut is achieved by freezing the tissue.

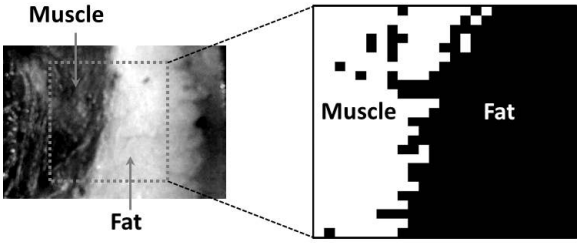

Figure 39: Lateral scan of fat and muscle tissue block.

The result of the scanning measurement on the fat and muscle block is a very good example of how well the system works if the focus of the LIBS laser is maintained for all of the measurement sites. The fat and muscle regions have been accurately detected. There are some dark spots in the muscle region which according to the classifier indicate the presence of fat. The misclassification is seen only on the muscle part and this might be due to the presence of connective tissues in some regions of the muscle area. Such connective tissues are common to in muscle tissue especially when looking to small structures comparable to the laser spot size(approximately to 250 μm). Another reason could also be the LIBS system (measurement or classification algorithm). It should be noted that the robustness of the system under the measured surface roughness/topology might be attributed to the relatively high pulse energy. At lower pulse energies the depth of focus along which useful plasma could be changed. Hence, changing settings should be handled with great care. tissue

The 2D-mapping has shown the performance of the trained model in a real-time application. In connection to this, it is imperative that a question is

raised as to how the entire process of classification can cope up with the speed of the surgical laser. The entire process starting from the shooting of the LIBS laser until analysis is done to reach a conclusion was made to run in 1.5 seconds. In principle, the limiting factor for the speed of the whole process is the spectrometer. The maximum readout rate of the 2-dimensional CCD detector for full resolution image is less than 4 Hz. Full resolution is needed because the echelle spectrograph disperses the light, in two stages using a combination of a grating and a prism, to two orthogonal directions for detection by the CCD array. This allows obtaining high spectral resolution within a wide spectral range. Therefore, a maximum speed of slightly below 4 Hz scanning speed could in principle be reached. However, the scanning speed was set to 1.5 seconds because the analysis was performed in Matlab software that reads the spectra saved by the OEM software of the spectrometer.

The investigation of the scanning system demonstrates that by using a LIBS system it is possible to obtain reliable real-time tissue type information to guide a laser surgery process. The study has shown that two aspects of the work, keeping the focus relatively constant and increasing the speed of decision, are important to consider when implementing the technique in a laser surgery system. The focus of the laser can be made to coincide with that of the surgical laser with the help of the focusing system of the surgical laser. The processing speed to reach decision can be increased by writing a custom Matlab software to operate the spectrometer which would allow processing the measured data without the need to save it first.

6.6 LIBS based tissue differentiation in combination with a surgical Er:YAG laser

If LIBS is to be incorporated to a surgical laser to provide a feedback information, then the influence of the treatment of the tissue with the surgical laser needs to be understood. This is important for example when a typical medical Er:YAG laser ablates a tissue, it targets the water content and hence a change in the matrix of the tissue around the ablation spot can be observed. This mainly results from the thermal effects of a laser. The change in the matrix of the tissue structure in this case means coagulated/denaturated tissue with less water content. This is expected to influence the LIBS spectrum of the affected tissue in terms of the emission lines and the ablation process when compared to the untreated part. Therefore, it is worth investigating if the LIBS spectrum of tissues changes after treatment with a surgical laser.

Another important factor for LIBS could also be the effect of body fluids that can not be completely removed from the incision region. Even though, one of the advantages of using lasers as surgical tools is to provide a clean operating field, the sensitivity of LIBS to even microns of volumes of any material makes it impossible to completely avoid the consideration of body fluids such as blood as spectral contaminants. Considering such contaminants is important because their elemental content is the same as that of tissues. Hence, investigation of the effect of thin layers of fluid both by interfering in the ablation process and in the spectral data becomes important.

To understand the influence of body fluids on the LIBS measurements, this work attempts to mimic the contamination of body fluids by applying a thin layer of saline solution (20 - 30 μm measured by OCT) on ex-vivo fat and muscle tissues. Even though, the actual contaminants such as blood have much more complex composition, a saline solution should provide an indication on the effect to the LIBS measurements. The measurements were performed based on two settings. In one, only LIBS measurements were done on both tissue types after putting a layer of saline solution and the same measurements on the same tissues without applying the solution. The second setting is done using the same sample preparation, by shooting first with a pulsed surgical Er:YAG laser (wavelength 2.94 µm, pulse duration 350 µm and pulse energy of 200 mJ). The Er:YAG laser was aligned at 45° degree to the sample surface and the LIBS laser was shooting perpendicular to the surface. Both lasers aiming at the same point (this is depicted in figure 40). The LIBS laser was triggered, with the help of a pulse generator connected to a photodiode that detects the arrival of a laser pulse from the Er:YAG laser. The delay between the two laser pulses was set to be 50 μs. All the measurements were performed at a repetition rate of 10Hz.

For comparison, we will designate the fat without any saline layer dry-fat and the one with the solution as wet-fat (the same designation will also be used for muscle). The spectra measured from dry and wet fat and muscle are shown in figures 43 and figures 44, respectively. The carbon line at 247.85 nm and its related molecular emissions are some of the most significantly affected peaks due to the presence of the solution on the surface of the tissues. These emissions are clearly weaker for the wet samples. The explanation for this could be that the LIBS laser is not able to ablate as much material as in the case without the solution. In this case the laser energy is absorbed by both the layer of the solution and the tissue leading to less amount of energy used to probe the tissue material. As a result, there are less carbon species ionized in the plasma plume. When the carbon emissions are affected so are the emission

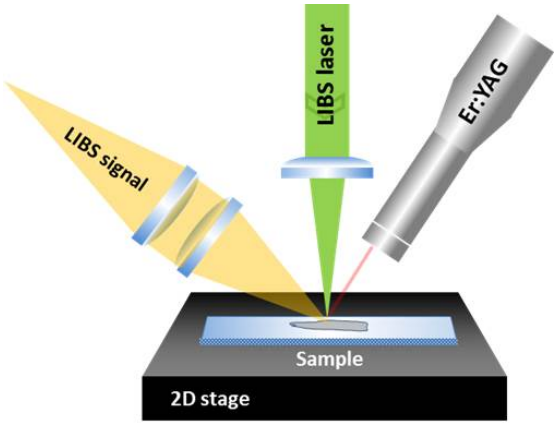

Figure 40: Schematic of the Er:YAG laser in combination with the LIBS system.

of carbon related molecules (CN with band head at approximately 388 nm). Similarly, the effect is also observed in the magnesium peaks (at 279.55 nm and 280.27 nm). On the other hand, the sodium doublet peaks (588.99 nm and 589.59 nm) have increased in the wet samples, which can be explained by the presence of the element in the saline solution (containing 0.9% of sodium chloride). The alteration of the intensity of the peaks of the different elements suggests that body contaminants will have significant impact on LIBS measurements.

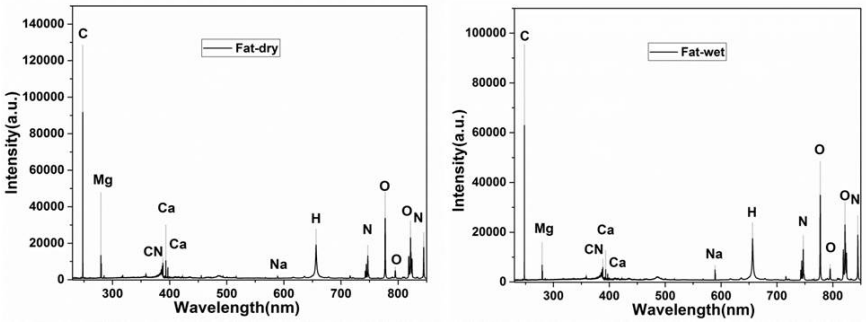

Figure 41: LIBS spectra of fat-dry and fat-wet.

The results of the second set of measurement where the two lasers were synchronized are shown in figures 43 and 44. For the wet-fat sample, the C and CN peaks decrease significantly compared to the dry sample. This could be due to the reduction of the carbonization effect of the tissue by the saline solution. The increase in carbonization of the tissues due to the Er:YAG laser can be justified by looking at the carbon content of the various experimental

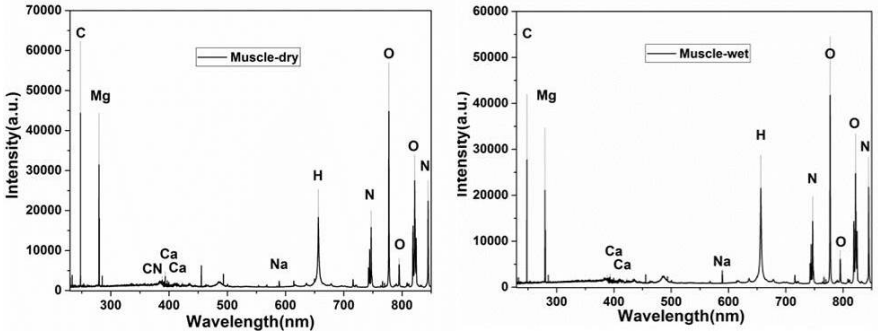

Figure 42: LIBS spectra of muscle-dry and muscle-wet.

settings. Figure 45 indicates the carbon content of the fat for all the settings. The CN band allows to look at C and N simultaneously. The experiment on dry-fat with Er:YAG laser followed by LIBS shows the highest content of carbon ablated. The Er:YAG laser is observed to cause carbonization even in the presence of the saline layer. In the experiments of LIBS laser only, the dry-fat shows more carbon content than the wet-fat. The sodium line intensity also increased in the fat sample with saline solution. Similar to the observations made during the fat measurements, carbon related emissions are higher for dry-muscle than wet. Sodium line also increased in the case of the dry-muscle.

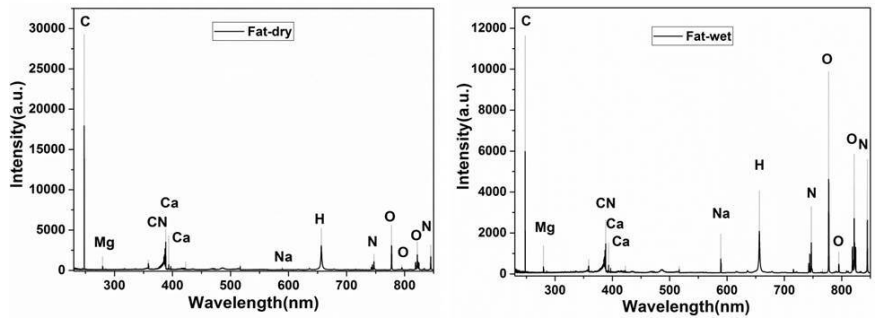

Figure 43: LIBS spectra of fat-dry and fat-wet obtained using LIBS laser synchronized with Er:YAG laser.

To understand the effects of the alteration of tissues on the statistical methods, classification analysis was performed. The analysis attempted to differential between dry and wet conditions of a given tissue when measured using LIBS only or LIBS in combination with Er:YAG laser. If classification using only LIBS proved to be difficult between a dry and wet tissue (fat or muscle), then the saline solution has no effect on the classification process. Difficulty in

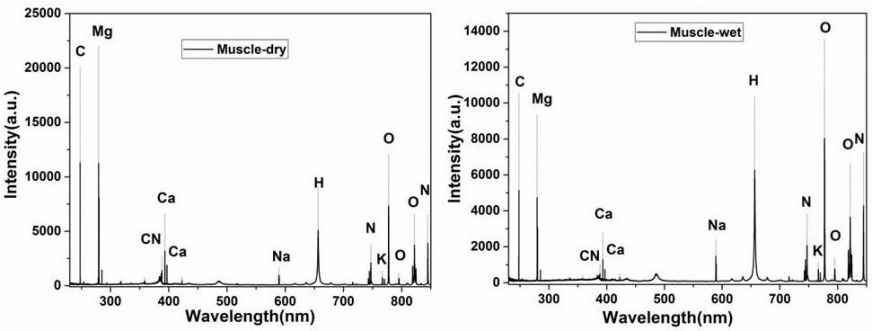

Figure 44: LIBS spectra of muscle-dry and muscle-wet obtained using LIBS laser synchronized with Er:YAG laser.

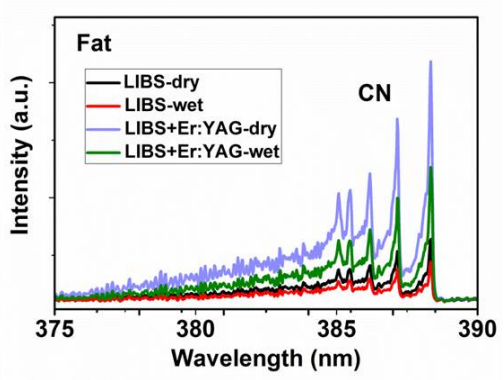

Figure 45: Intensity of the CN band for different fat tissue measurements.

differentiation means sensitivity and specificity values around 50% indicating the classification was random guessing. The same is true when a classification becomes difficult in the setting where the surgical Er:YAG laser is used before LIBS measurement. This was investigated using measurements under the following conditions:

- LIBS only (for the classification of fat-dry and fat-wet)
- LIBS only (for the classification of muscle-dry and muscle-wet)
- Er:YAG laser and LIBS (for the classification of fat-dry and fat-wet)
- Er:YAG laser and LIBS (for the classification of muscle-dry and muscle-wet)

Table 11 shows the sensitivity and specificity of the classification analysis. The classification approach was done on pre-processed entire spectra. For both

experimental setups, measurements were performed from 6 samples of each muscle and fat. From each sample, 100 LIBS spectra were measured in which half of the measurements were from a part where a layer of the solution was applied and the remaining from a dry part. The training and test set were grouped in such a way that the dataset of 5 samples are used to perform dimensionality reduction and generate the classification model. Similar measurement from a sixth tissue is then used to test its corresponding training set.

In the experiments involving LIBS only, very high accuracy of differentiation between dry and wet conditions of both tissues have been achieved. This means that the spectra measured from the same tissue under the two conditions are completely different. The visual inspection of the craters from one of the muscle tissues showed that those on the dry part are clearly larger than the wet counter parts. The explanation for this could be that much of the laser energy is shared by the layer of the saline solution. As a result less energy reaches the desired tissue resulting in a less tissue material in the plasma generated. Therefore, the effect of body contaminants especially existence of a liquid layer is critical when using LIBS as a feedback system of a surgical laser. This might be particularly significant when the same laser is intended to be used as both surgical and LIBS laser (for example in microsurgical applications).

The combination of LIBS with the Er:YAG laser provided quite interesting results. Even though the effect of the solution prevails in a similar manner as in the LIBS only measurements, the effect is much less. The sensitivity and specificity values drop significantly. This means that the Er:YAG laser has the effect of cleaning the surface by ablating the thin layer of solution leaving a more dried tissue surface to the LIBS laser. This is in agreement with one of the advantages of using lasers as surgical tools which is allowing to have a clean operation field. From the spectra measured under this setting, the matrix changes associated with the thermal effects of the Er:YAG laser also has contribution in difference of the spectra.

Two conclusions can be drawn from the investigations of these experiments. One is that the body fluids that are inevitable during in-vivo conditions affect the LIBS spectrum. Therefore, when using the same laser pulse to perform surgery and LIBS measurement, the effect of body fluids in the region of ablation is expected to pose difficulty in obtaining reliable results. However, this conclusion is based on the experiments performed under the described settings more specifically at a repetition rate of 10Hz. This might be different for

Table 11: Sensitivity and specificity values of fat and muscle tissues under different experimental conditions

Experimental setting	Sample-group	Sensitivity	Specificity
LIBS only	fat-dry vs fat-wet	99.67%	99.33%
	muscle-dry vs muscle-wet	91.33%	94%
Er:YAG laser and LIBS	fat-dry vs fat-wet	80%	86%
	muscle-dry vs muscle-wet	82.67%	75.67%

surgical applications with high repetition rate lasers where the time between pulses can be much shorter than the fall back of the body contaminants to the ablation point. In this case some of the laser pulses might be able to probe the tissue without a layer of the contaminants.

The second conclusion is that a surgical Er:YAG laser alters the tissue spectra through carbonization while at the same time providing cleaning effect of the body fluids which can interfere with the spectrum of tissues. The cleaning effect of the surgical laser is appealing for both the surgeon and the LIBS system. Therefore, to improve the performance of LIBS when used in combination with surgical lasers, it is important to include LIBS spectra of tissues measured in combination with a surgical laser in the training data. The values of the differentiation accuracy suggest that great care needs to be taken when dealing with highly similar tissues such as nerve and fat. In such cases, the classification model must include training data of tissues under in-vivo conditions where the actual body contaminants are present. On the other hand, for tissues with significant differences in chemical composition (such as cartilage and cortical bone), the cleaning effect of the surgical laser prior to the LIBS laser might be sufficient for successful differentiation. However, due to the process of supervised learning of the classification models, it is important to to train any of the models under similar conditions of the real application.

6.7 Summary of statistical classification models for soft and hard tissue differentiation

The results of the statistical tissue classification models lead to the following conclusions:

- Using supervised classification analysis, it is possible to overcome the high variance in the LIBS spectra of tissues in order to discriminate them for the application of laser surgery feed-back system.

- It is possible to discriminate among soft tissues with high accuracy. In most soft tissues cases, accuracy of higher than 95% can be achieved. In the classification of soft tissue spectra, a new feature extraction approach that uses ratio among the intensity of the measured atomic emissions as variables has been presented. The ratio approach proved to be superior over the analysis based on the entire spectrum or a narrow region of the spectrum.
- In the classification of hard tissues, the numerous intense calcium atomic emission lines play a significant role. Separation of hard from soft tissues can be done by using a threshold on the ratio of one of these emission lines with an emission of carbon or another common element. Among the hard tissues, classification results based on the ratio approach did not out perform the entire spectrum or a region of spectrum. A region of spectrum slightly out performed the ratio approach in the classification of hard tissues of the oral cavity (enamel, dentine, pulp, cortical bone and cancellous bone). In general, the classification among hard tissues was found more difficult than soft tissues.
- The investigations of using the LIBS based classification to map ex-vivo tissue types show that the system is able to handle typical tissue surface structures/topology. It was highlighted that the results might change if pulse energy lower than 80mJ is used. This is because the depth of focus over which useful spectra can be collected might change possibly requiring a new classification model. A model developed for a given setting requires a thorough validation before it is used for another experimental setting.
- Perhaps the most important investigation of the LIBS system and the development of the classification algorithms is the experiments involving LIBS together with a surgical Er:YAG laser. The results show that if a single laser is used to do surgery and LIBS, then a higher repetition rate laser is recommended. The time between pulses should be much faster than the fall back of any superficial liquid/contaminant. The most important observation was the laser induced tissue alteration. When the LIBS system is used in synchronization with a surgical Er:YAG laser, there was a clear evidence of tissue alteration. This leads to a conclusion that any LIBS based laser surgery feed-back mechanism must be trained by spectra measured under similar conditions to the intended application. This applies when the LIBS laser is used alone or in combination with another surgical laser.

7 Transfer study of ex-vivo tissue differentiation model from Porcine to Mice tissues

The previous section highlighted the importance of considering the effect of contaminants on LIBS spectra. The ideal condition to investigate the effect of the contaminants during laser surgery would be to perform measurements under in-vivo conditions of animal models. In order to evaluate the performance of a LIBS system, a number of measurements need to be performed. Without confirming that the physiological implications related to the ablation of the laser are harmless, performing numerous measurements under in-vivo conditions would be ethically unacceptable. Therefore, before going to in-vivo measurements, investigations that can minimize in-vivo experiments are beneficial. One way to achieve this goal is to investigate the performance of a model based on the ex-vivo tissues of one animal type on the tissues of another. This can reduce the need for ex-vivo human samples needed for training data. This has significant importance if data collected from ex-vivo tissue is useful as a training for in-vivo classifications. This paves the way to collecting large training data for future learning algorithms. Figure 46 shows a simple example of the decision flow of the use of the data in a transfer study. It shows if they transferability at each step works, the data from each previous steps can be used as a training for the next. For such extensive study, it is clear to see various combinations of steps can be taken to make use of the data from different animal models. Any in-vivo measurements were not within the scope of this work. Therefore, the results shown in this work are only transferability from ex-vivo porcine to ex-vivo mice.

Here, the use of the supervised classification model based on porcine tissue is investigated on the tissues obtained from mice animal models. This can be useful in understanding if there is difference in the elemental composition of a given tissue obtained from different animals. In this section, LIBS measurements from porcine tissue samples (nerve, muscle and fat) are used as training data and the measurements from the same tissue types obtained from mice animal models are used as test data. The choice to include particularly nerve and fat of both animals is because they are the most difficult to differentiate among soft tissues. All the other tissues from mice, soft and hard with the exception of muscle, were difficult to prepare and hence were not included in transferability study. Before discussing the classification results, comparison of the spectral feature of both tissues in both groups will be discussed.

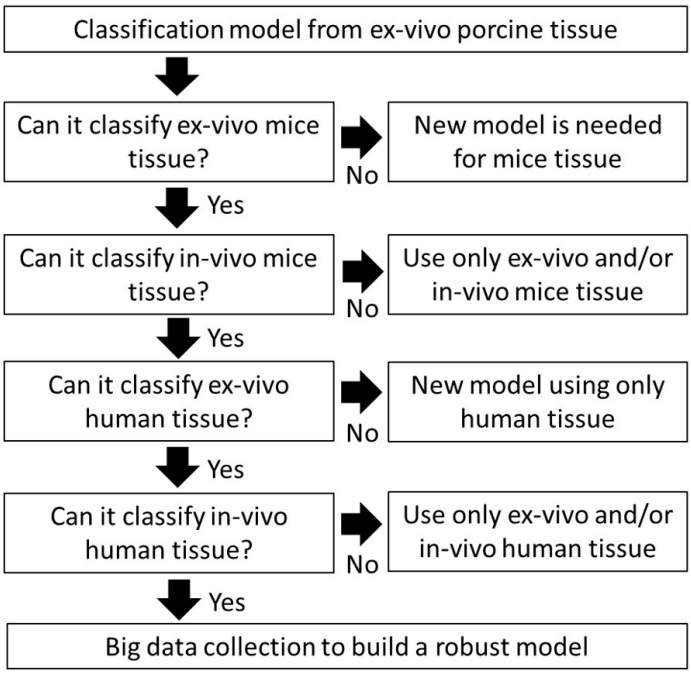

Figure 46: Simplified decision flow of transferability study.

7.1 Comparison of the LIBS spectra of mice and porcine tissues

The spectra from the mice tissues showed similarity to those of the porcine tissues. Even though all the elements monitored from porcine tissues were also present in their corresponding tissue obtained from mice, there were marked differences in the intensity of a number of emission lines. This may arise either from the difference in the concentration of the responsible elements in the two groups of tissues or the difference in the structure and morphology of the tissues. Rigorous literature research in the elemental composition of the three tissues of porcine and mice animals was fruitless. Most of the literature focuses only on the molecular aspects of the tissues separately without the aim to compare different tissues of either animal let alone between both.

There is a clear difference between the mechanical properties of the two tissues observed during the experiments. The mice tissues were extremely delicate and it was difficult to keep them stable and flat during the experiments. The tissues were fixed on glass slides which is then attached on the 3D-stage. After each ablation, the dynamics of the ablation process was strong enough to

move the tissue and slightly move the surface away from the original focal position of the laser. Moreover, the laser focus region was quickly changing to jelly like oily fluid right after each ablation. Which can be explained that the tissue, in the region of the laser focus, was getting molten by each of the laser pulse. To avoid splashing and ablation from the molten part the stage was always re-adjusted in order to measure from an unaffected tissue after each measurement. Therefore, the structure and morphology of the mice tissues might have played a significant role in the difference of the spectra between the tissue of the two animal models by influencing the ablation process. Figures 47 to 49 show the comparison between the spectra of corresponding tissues of the two animals.

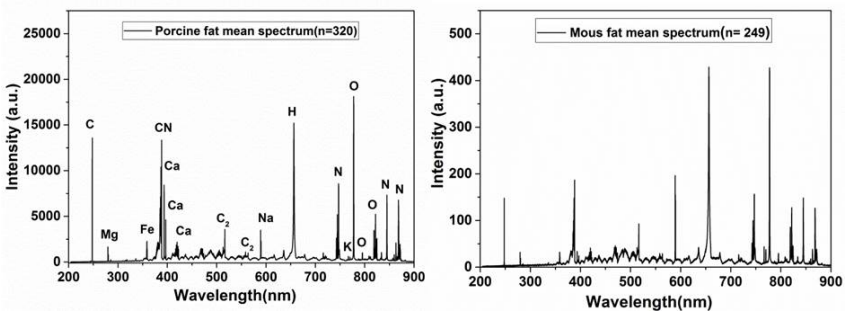

Figure 47: Mean spectra of porcine fat (left) and mouse fat (right).

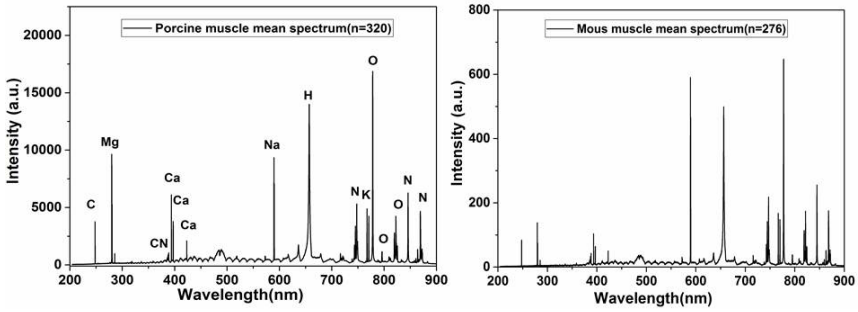

Figure 48: Mean spectra of porcine muscle (left) and mouse muscle (right).

Due to the strong thermal and mechanical response of the mice tissues to the laser energy at the settings of the measurements on porcine tissue, a different pulse energy was used for the mice tissue measurements. The pulse energy was 20 mJ with focal spot size 100 μm - 150 μm as opposed to 80 mJ with focal length approx. 300 μm for the porcine tissues. This keeps the irradiance of the LIBS laser comparable in both measurements. A few measurements with 80 mJ

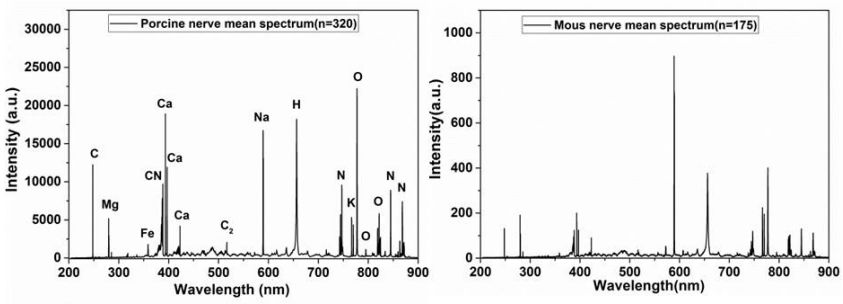

Figure 49: Mean spectra of porcine nerve (left) and mouse nerve (right).

pulse energy and 300 μm were attempted on the mice tissue samples. However, in this experiments the tissues were completely disintegrated, especially the nerve and fat samples, resulting in large spattering of tissue particles sticking on the surface of the focusing lens. These experiments were discontinued because one mice tissue sample was not enough to collect more than a dozen spectra due to the damage from the laser. Additionally, the spattered tissue particles reaching the focusing optics could cause damage when the tissue material absorbs the incident laser energy.

At the delay and integration times used for the porcine tissue experiments (2 μs and 200 μs), very weak emissions were detected from the mice tissues. By setting the delay time earlier to 0.2 μs, the strongest intensity of the atomic lines could be measured. This is evidenced by the evolution of the intensity of the carbon line at 247.85 nm with respect to its baseline at different delay times from the laser shown in figure 50. The evolution of the line suggests that the plasma has shorter life time compared to that of the porcine tissue which might be explained by the existence of lower electron density resulted from the lower excitation energy focused on a smaller area of the tissues. The smaller focus spot size in turn suggests less tissue material is interrogated. The intensity of the lines in the spectra when compared to the counterparts of the porcine tissue also agrees with the explanation that there is less material probed resulting in drop in the intensity of the emission lines.

Comparison of the spectra of fat of the two animals (figure 47) shows that the emissions from carbon and its related molecules follow similar trend. As the basis for classification of the tissues is the ratio approach it is also worth looking at the relation of the prominent peaks. The relation of carbon to magnesium seems to remain similar in both animals. There is a significant drop in the emissions of calcium and an increase in the emissions of sodium and potassium in relation to the elements emitting in the UV region (carbon,

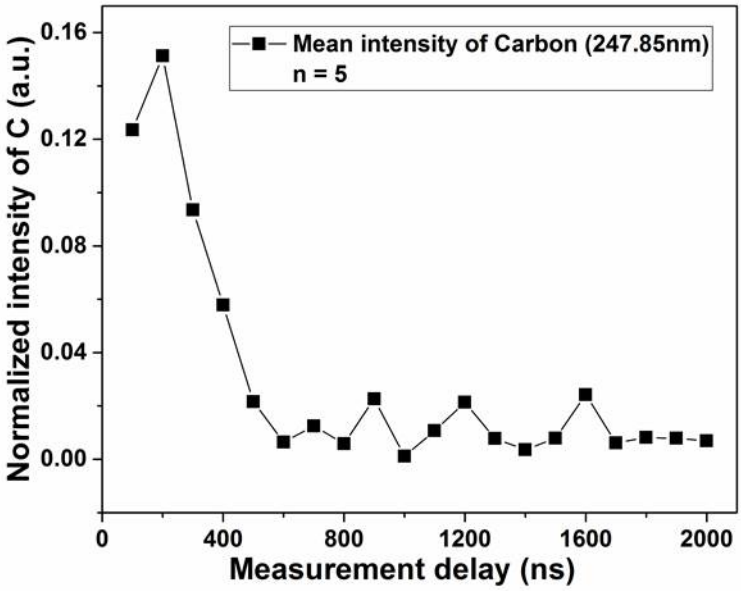

Figure 50: Evolution of carbon lines of mice tissues.

magnesium and calcium). Generally, the emissions from hydrogen, oxygen and nitrogen increased in relation to carbon for fat tissue of mice than porcine animals. Similarly, the comparison of muscle spectrum of mice also shows that the emissions in the UV region (from carbon, magnesium and calcium) are weaker compared to the rest of the spectrum. Relative increase of sodium emission is observed from the mice tissues. The spectra of mice nerve tissue showed a significant increase in sodium line which dominates the rest of the emissions. Moreover, magnesium line increased compared to carbon line in nerve of mice tissue. In contrast to the other tissues, the UV region of the nerve spectrum showed similar emission levels to that of porcine nerve when compared to the rest. The spectra of mice nerve and muscle tissue showed high similarity except in the content of sodium which the nerve samples showed comparatively higher level.

7.2 Classification performance of the Porcine model on Mice tissue spectra

In the classification of the mice tissue, the measurements from porcine tissue for training consisted of data from six animals. Six fold cross-validation was performed and the training data of five animals with the best performance

on the sixth animal was chosen as training data for the measurements from mice tissues. The classification performance was the highest when 10 PCs were used. The variance accounted by these PCs of the training data is shown in table 12.

Table 12: Percentage of variance in the first 5 principal components of soft tissue training data represented by 153 ratios of 18 peaks

Training set	PC1	PC2	PC3-PC10
Animals 1,2,3,5,6	22.19%	16.48%	22.48%

Based on the above PCs, LDA classification was performed on the measurements of each of the mice tissues. The results of sensitivity for the three tissues are shown in figure 51. High differentiation performance of muscle from fat was achieved (an average of 99.3%). The differentiation of nerve from fat is higher than 95% in four animals and above 80% for the other two animals (overall average of 93%). The performance of the model to identify nerve from muscle is relatively low (an average of 80.7%). The lower performance of the nerve-muscle pair can be explained by the similarity of the spectra of both tissues as discussed in the previous section.

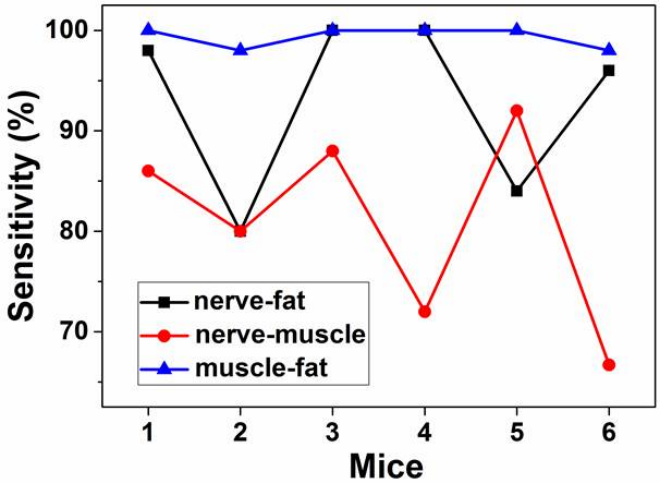

Figure 51: Sensitivity of classifying mice tissue spectra using porcine tissue training dataset.

7.3 Summary of transferability of classification model from Porcine to Mice tissues

In summarizing the study on the transferability of a LIBS based classification model from porcine to mouse tissue, the following conclusions are drawn:

- If there is matrix difference between the tissues of different animals, the experimental parameters need to be first adjusted to measure LIBS spectra. For the particular study on mouse tissues, this is needed to limit the damage of the LIBS laser to the delicate mouse tissue. Lower pulse energy was used and measurement delay time was adjusted in order to measure LIBS spectra from the short lived plasma.
- Detailed comparison of the spectral features from the two animals shows that there are some difference in the intensity of a few elements of similar tissues.
- Despite slight differences in the spectra, relatively high accuracies of predication of mouse tissues using the training data from porcine tissues was achieved. More than 95% overall accuracy for nerve-fat and muscle-fat pair and more than 80% for the nerve-muscle pair. In the later pair, very high similarity between their spectra was observed.
- The anatomical similarity between the training and the test animals is important. This is justified by the sensitivity of LIBS to the difference in the sample matrix.
- It can be concluded that transfer of tissue models from one animal to another is feasible. However, it is important first to investigate the performance of the model to be transferred.

8 Two-dimensional(2D) mapping of elements as an imaging modality

Recently, there has been a rapid increase in research towards chemoprevention of cancer. [2]. Chemoprevention is the control of carcinogenesis in its early stages by using active drugs [11]. The chemoprevention approach of treating cancer is drawing attention due to the increased understanding of the tumormicroenvironment. This complex microenvironment consists of various types of cells many of which having a role in the progression of the disease [2]. Considering the role of many cell types in the progress of the disease, there has been a suggestion that carcinogenesis is a phenomena that occurs in tissues rather than in individual cancer cells [2]. Moreover, the outcomes of treatments of the disease are also being studied through the microenvironment which includes vascular perfusion in the tumor tissue or tumor hypoxia [43].

All these approaches, to understand the progress of cancer or the outcomes of its therapy, have attracted imaging modalities that can reveal the tumormicroenvironment. Imaging modalities that target structural, molecular and elemental information at microns scale lie within the premise of the interests of the field. LIBS has the potential to show the distribution of elements in microns scale which can be interesting for cancer studies. As an emerging analytical technique, capable of providing elemental information down to the size of a laser focal spot size (a few micrometers), LIBS has not yet matured to the application of biological samples in general with the exception of a handful of research studies already mentioned at the beginning. Therefore, in this chapter the use of LIBS for revealing the distribution of both major and trace elements in different tissues focusing mainly on different cancerous tissues is discussed. The investigations performed in this work are aimed at investigating the potential of LIBS for such application and the importance of various aspects of the experiments. The results obtained should serve as foundation for further work of LIBS in the elemental characterization/imaging of cancer in particular and, physiological and pathological processes in tissues in general.

8.1 Elemental distribution as an imaging modality

The spatial distribution of a given element on the surface of a tissue sample can be used to generate an image of the tissue if the tissue structures are

characterized by different concentration of the element. Such information can be revealed with the help of techniques such as LIBS which detect elements by atomizing the sample. The tissue surface can be probed point by point until the entire surface is scanned. Each LIBS measurement from any given point allows to measure a full spectrum which covers the measurement range of the spectrometer. All the elements emitting within this range can then be measured to reflect their respective distribution in the tissue. By plotting the scanned area by the intensity of the desired element, an image based on elemental distribution can be generated. Traditionally, staining is used to obtain elemental contrast in tissues. Using staining, it is generally not possible to target multiple elements in a single tissue probe. Moreover, the staining process involves multiple steps and can be lengthy. In this regard, LIBS has the advantage of showing all elements in a single measurement within a short period of time. The resolution of a LIBS based image can be as small as the size of the laser at the focus. Its simplicity and the ability to perform rapid measurement in open air make LIBS an attractive technique for providing spatial distribution of elements. The main advantage of LIBS over elemental imaging techniques is that it is cheaper and the material sampling, atomization and the excitation of the sample is done with a single laser pulse.

The samples used can be fresh tissues or tissue slices cut after embedding them by different standard techniques. The tissue is first prepared in such a way that the surface to be scanned remains within the laser focal position. This is achieved with the help of the video microscope in which the objective lens (focusing the laser) is first optimized to get the desired spot size of the LIBS laser and then the tube lens of the camera is adjusted to obtain a sharp image. If the area to be investigated provides a sharp image on the microscope, it can be assumed that the laser spot size remains the same for all the scanning points. In the experiment of this chapter, the LIBS setup described for the classification of tissues in the previous chapters is used. The experimental parameters vary depending on the sample type and/or its preparation. For each type of sample and/or preparation, a desired resolution is achieved by adjusting the laser focus size and the laser energy to obtain a good LIBS-signal. Here, good LIBS-signal is ill-defined because it depends on which element is of interest and which emission intensity level of the element is sufficient for characterization. Therefore, the results in this work will simply show the possibility to qualify and show the relative intensity of emissions in arbitrary units. The mice tissue samples demonstrated here were provided to us by our collaborators from Medizin 1(Prof. Dr. med. Markus F. Neurath), University Hospital Erlangen (The group of Prof. Dr. med. Maximilian Waldner). The

mice were kept at their facility and the samples were prepared there and brought to our lab (CPL-SAOT, University of Erlangen-Nürnberg).

8.2 Fresh tissues

In this section, the result of a straight forward and speedy ex-vivo analysis of elements in a tissue surface using LIBS is demonstrated. The scanning results of two fresh ex-vivo tissues samples extracted from two mice cancer models will be shown. The first sample has tumor and healthy region where the tumor has grown out of the surface creating a bulged region and another one which is flat that is level with the surrounding tissue.

8.2.1 Tumor with bulged surface

Figure 52 shows the tissue and its structural features. The OCT image, just before starting the LIBS measurements, reveals that the surface of the tissue sample is not flat. This is expected to affect the laser spot size hence the irradiance of the LIBS laser. Whether very thin or thick slices are prepared, fresh tissues pose significant challenge in preparing a flat surface for scanning using the system. This is due to drying which causes structural alterations. Using a buffer solution to keep the tissues moist would interfere with the measurement and would also cause unwanted spattering of the liquid layer. The effect of wetting was already shown in chapter 6. Therefore, the samples are in any case dried with air blower or a tissue paper, and put on a glass plate for measurement.

Two other aspects of the measurement also contribute to the deformation of the tissue. Limited by the full spectrum readout speed (approximately 400 ms) of the spectrometer, scanning a 40 mm x 40 mm area with a spot size of 100 μm takes minimum 10 minutes. The tissue regions measured at the end of these 10 minutes, compared to those at the beginning, dry and deform significantly. Another experimental factor affecting the measurement is also the ablation process. If the tissue is not glued to the substrate attached to the stage, mechanical forces of the ablation process tend to disrupt the regions around the crater. This effect is severe for fresh slices of mice tissue. The fresh tissues investigated in this work were fixed on glass-plates using a double sided tape to minimize the detachment of the tissue from the substrate. Some of the results of the scanning experiment on the tissue above are shown in figure 53.

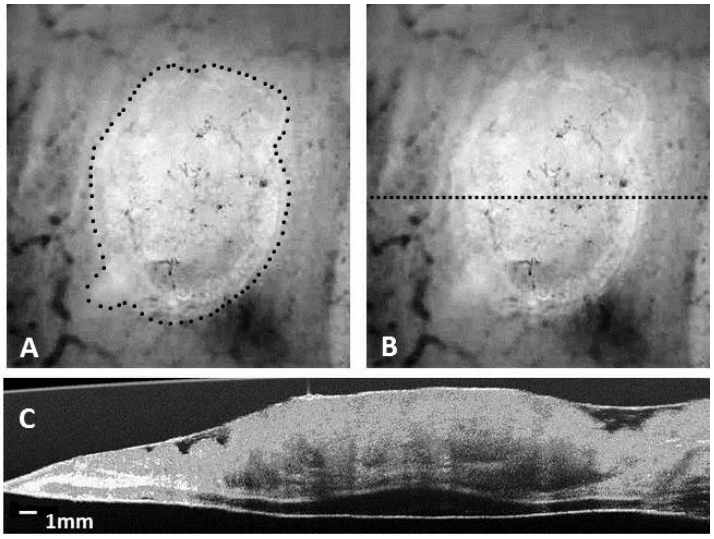

Figure 52: Cancerous colon tissue from mouse. (A) The dotted line marks the visible margins of tumor. (B) The dotted straight line marks the part on which the OCT B-scan shown in (C) was performed.

Figure 53 shows the characterization of the fresh tissue that includes a cancerous region (figure 52) in terms of Fe, Ca, C, O, H and N emissions. Most of the available reference in the literature focuses mainly in the mineral elements that are trace elements in tissues. Therefore, in order to have a comparison with the results other studies the principal interest here will be on the mineral elements Fe, Ca, Cu and Zn. The major elements will also be used as references. Meaning, to check whether or not the changes in intensity of emissions come from potential differences in the parameters that affect the LIBS process. With different laser spot size, the excitation conditions change significantly for major and trace elements. For higher irradiance values, the plasma density is expected to be higher and hence better excitation of trace elements. In the case of low density plasma, the competition for excitation from major elements would be high resulting in less excitation of the trace elements. Therefore, the effect of the excitation conditions is much more pronounced for the trace elements than the major elements. In a thorough literature search, it was not possible to find any study showing the difference of major elements in a cancerous and its adjacent healthy tissue, therefore the information of the major elements is used here as a basis for trace elements with caution. Assuming no significant concentration difference (emission intensity in a.u.) of the major elements, their distribution should indicate significant difference in excitation conditions.

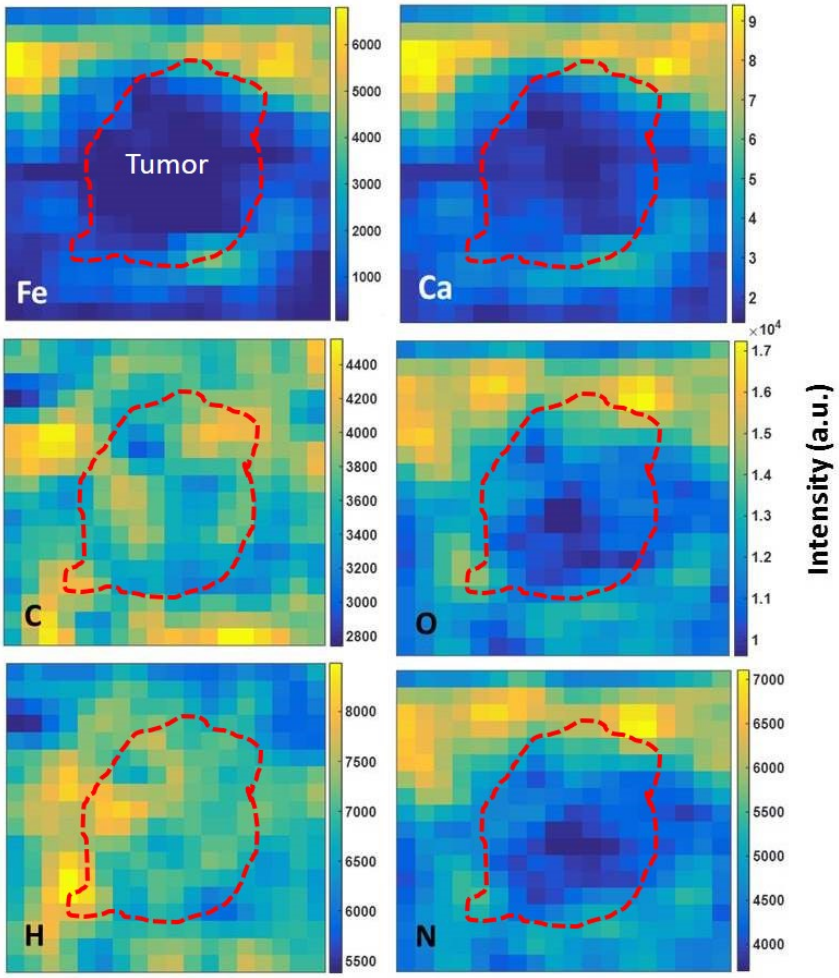

Figure 53: Image generated using Fe(top-left), Ca(top-right), C(middle-left), O(middle-right), H(bottom-left) and N(bottom-right) from measurement on a cancerous tissue with adjacent healthy part.

The representation of the tissue above by the major elements shows no marked difference in the distribution of C and H between the healthy and the cancerous part. Where as the images based on O and N show that the central region of the tumor is characterized by relatively lower level of these elements compared to the healthy region. With the limited number of available related studies, it is not possible to discern any conclusion from the distribution of the major elements. The results lead to two possible explanations based on the observation of the major elements. Either the irregular topography of the tissue has resulted in different plasma conditions (a plausible reason given

the sensitivity of LIBS) or the concentration of N and O is different for the two regions. The focus of the laser was on the healthy region of the tissue. The defocusing of the laser on the tumor part might have resulted in low density plasma from the region which leads to the reduced intensity of N and O. However, the different conditions would also affect the other major elements (carbon and hydrogen). For this sample, the observations based on the major elements tends to lean on to the conclusion that using fresh tissue samples is unreliable unless validated by another supporting technique.

The analysis of the sample based on the mineral element Fe shows that the observation is in agreement with those reported by Farquharson et al. [26]. The Fe results reported by the group is based on human breast cancer sample hence one to one comparison with a tissue of mice from a different region of the body is likely unjustifiable. The Ca result is contrary to the results obtained in the breast cancer report. The Ca level is higher in the tumor part than in healthy tissue which might be another supporting explanation for the effect of the difference in the excitation conditions. The observations based on the major and trace elements do not give a concrete indication on the elemental distribution. Given the sensitivity of LIBS and the irregular topography of cancerous tissues, the reliability of measuring the elemental distribution on fresh tissue is questionable. This is because different points that result in different laser focus spot size on the tissue surface will provide spectra from plasma generated under different conditions. Therefore, such measurements need to be considered with great care and is highly recommended that they are verified using another technique.

8.2.2 Tumor with flat surface

Scanning measurements on the other fresh sample (shown in figure 54) where the tissue surface was relatively flat, yields improved results that align with the measurement conditions to certain extent. The part of the sample scanned with the LIBS system included the tumor part and had dimension of 4 mm x 4 mm. The laser spot size was set to approximately 100 μm. The pulse energy of the laser was set to approximately 80 mJ. Even though much less than in the case of the previous sample, this sample also showed deformation effects after the experiments. The relative improvement of deformation might be due to its flat surface and its relatively thicker nature which was more stable when fixed using a double sided tape on a glass-plate.

The images generated using the emissions of the major elements are shown in figure 54. The distribution of O and C shows no marked feature of the

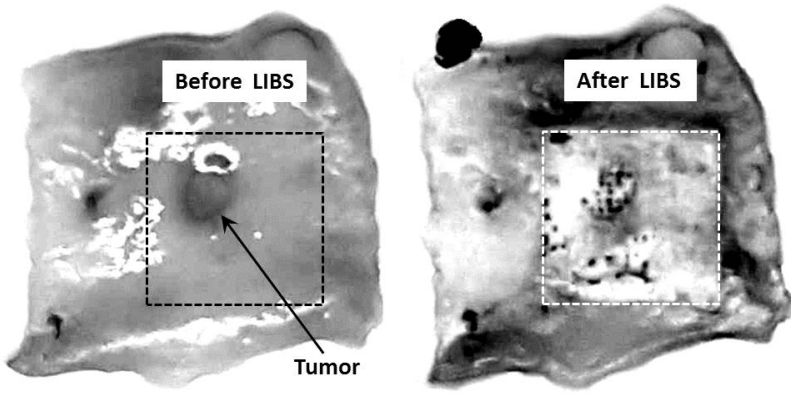

Figure 54: Image of fresh tissue with tumor generated from using the distribution of elements.

tumor part that can make it visible from the rest of the healthy tissue. Some point with higher intensity, at the bottom of the images of O and C are visible. This are regions where slightly denser tissue was observed (top-right image in figure 55). The O emissions appear to reflect to the tissue structure better than the other elements. The images based on H and N show regions with slightly less intensity which includes the tumor region. Higher intensities were also observed in some regions. However, given the fluctuations of LIBS signals, all the observed features based on the emissions of the major elements do not seem to draw particular attention. Here again, the purpose of investigating the major elements is to check whether or not similar trends are observed that may imply the topology of the tissue was the main reason for the observed features. In this sample, the effect of the topology of the surface appears to be less than the first sample.

In the measurements above, emissions from Ca, Cu and Fe could be observed (Figure 56). The images based on Ca and Fe lines show similar distribution to that of the major elements discussed above. The only remark about Ca and Fe is that the tumor part is among the regions where lower intensity of the elements was measured. This continues to be a similar behavior observed in the previous sample where much pronounced difference of the distribution of these two mineral elements from the major elements was observed. This is with the remark that the trace elements are much more sensitive to the ablation conditions than the major elements. This does not rule out that the changes in the distribution of elements might come from fluctuations due to experimental factors, especially the tissue surface topography.

Perhaps the most interesting observation from the current tissue is the emissions of Cu which could not be measured from the previous sample. Compared

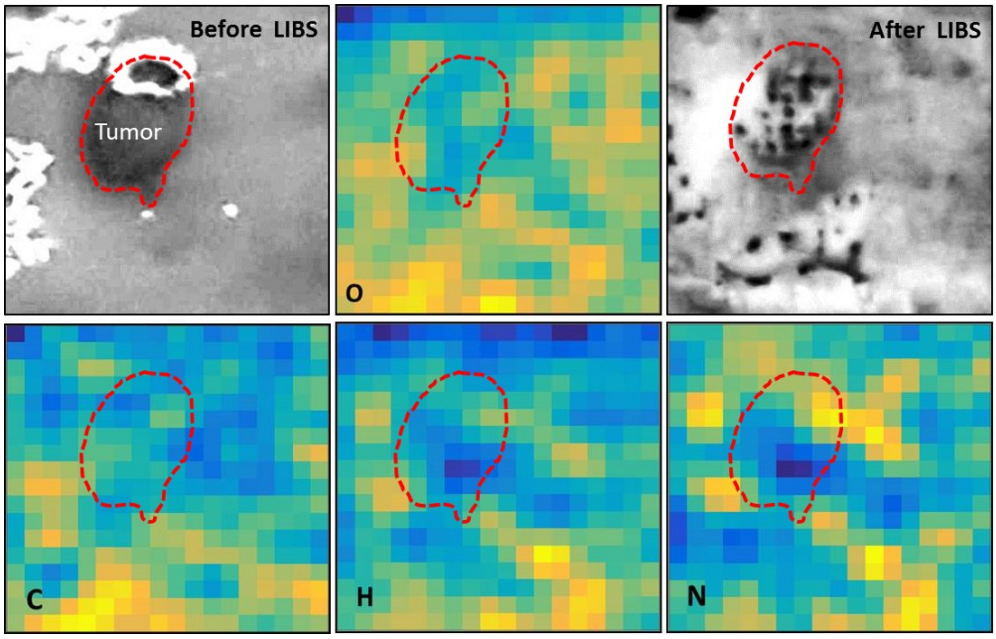

Figure 55: Image of fresh tissue with tumor generated from using the distribution of elements.

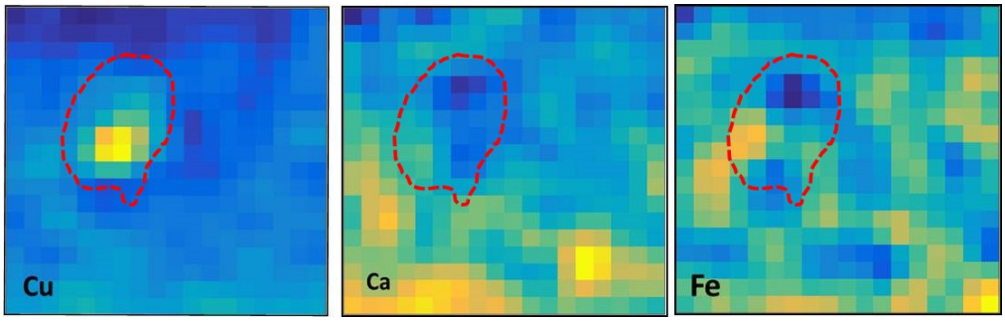

Figure 56: Image of fresh tissue with tumor generated from using the distribution of elements.

to the healthy region, the tumor region showed higher intensity of Cu emission. Unlike the emissions from the rest of the other elements, Cu showed relatively uniform distribution in the healthy part. As one of the important metallic elements in cancer characterization, the observation of Cu distribution in this tissue using LIBS suggests that improving the tissue surface to provide the same excitation condition across the scanned area could yield in more reliable results. The Cu line used to map the distribution of the element is shown in figure 57. The spectrum of the tumor region is an average of ten measurement points from the tumor area. It can be seen that the emission intensity is close

to the noise level of the measurement indicating how prone the line could be to small changes in the experimental conditions.

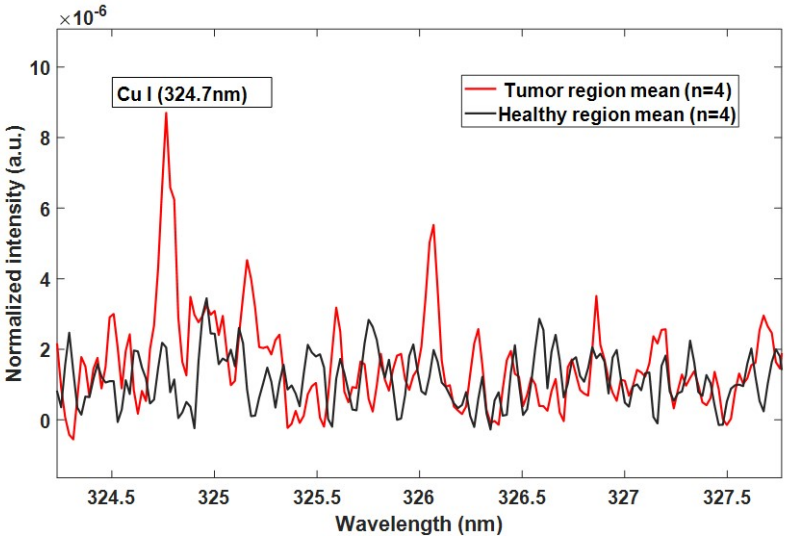

Figure 57: Average of Cu emission from the tumor and healthy regions.

The experiments on the fresh tissue samples have shown that LIBS has the potential to reveal the distribution of mineral and major elements. On the other hand, it was also indicated that the technique is sensitive to experimental parameters that affect the excitation conditions mainly the laser focus spot size. This was manifested by the improved results obtained from a fresh sample with relatively flat surface. It is also worth noting that the results obtained could not be disproved due to the lack of similar references. Another aspect that makes the results of the investigations here important is, no single study on the elemental distribution in colorectal cancer mouse tissue could be found as far as this work is concerned. Therefore, whether or not the results obtained reflect the actual distribution of elements in the tissue, LIBS opens a new window in looking at the microenvironment of tissues. The limited information about the distribution of mineral elements in human cancerous tissue obtained from the literature may not be appropriate for the mice samples used here but has provided with useful information on the analysis of the samples involved here.

Considering the potential of the technique for monitoring elements in tissue, a means of obtaining robust and reliable results becomes pertinent. As already explained, one major source of signal fluctuations can be the irregular topography of the fresh tissue. Such fluctuations can be reduced either using

an auto-focusing mechanism (e.g. using OCT) or by processing the samples to have a flat surface (that typically involves embedding) prior to measurements. In this work, to go around this problem and deformation/alteration due to drying, some of the common tissue processing approaches are used to embed the tissue. The next sections discuss about investigations on processed samples.

8.3 Processed tissues

Tissue processing has for many years been used to keep tissue in a form which can be made into sections mainly for microscopy. Tissue processing is done post fixation of tissue. The aim of the fixation process is to preserve the tissue as close to the life-like state as possible soon after biopsy/autopsy. Embedding in paraffin wax is the most common tissue processing technique routinely used for different studies. Another technique used is processing with epoxy-resin. Tissue samples processed using these two methods have been investigated here within the context of monitoring elemental distribution using LIBS.

8.3.1 Paraffin embedded mouse tissues

Paraffin embedded tissues can be cut to different thickness. Depending on the interest, either the slice or the bulk tissue left can be investigated. Only the sliced part is considered for investigation here. The use of the sliced part allows for using thinner sections. Measuring on the bulk layer after layer would mean to cut away slices to reach a surface where the effect of the laser ablation can no longer be observed. This could unnecessarily complicate the preparation process and possibly use much thicker layers. Once the measurement process is optimized for the slices, it gives an opportunity to map the elemental distribution in 3-dimensions by measuring slice after slice with much higher resolution (limited by the thickness of a given slice). One important aspect of the tissue preparation is the type of substrate used to fix the slices. The common way to prepare a slice is on a glass slide. However, many of the emissions of the impurities in glass overlap almost with all the emission lines observed from tissues(Figure 58). An alternative way to fix the slices is on aluminum substrate. Aluminum has a spectrum that has nearly no interfering lines with most of the elements in tissue.

Another advantage of using Al, generally metals, as substrates to fix the tissues is the enhancement of the emissions of the elements in tissue. The threshold for laser based ignition of plasma is much lower in metals than in tissue. Therefore, once the thin slice of the sample and the metallic substrate are

in the focal volume of the focusing optics, breakdown is generated. These results in a relatively higher density plasma than for the same condition where only tissue is in the focal volume. The higher density plasma allows for more possibilities of excitation of the tissue elements hence enhances the signal of the elements in a tissue. This is particularly advantageous for measuring the trace elements which are the primary interests of the investigations in this work. The enhancement of the signal from tissue can be observed by measuring the signal from fresh tissue, tissue embedded in a paraffin wax and a 5 μm slice from paraffin embedded tissue which is then fixed on Al plate((Figure 59).

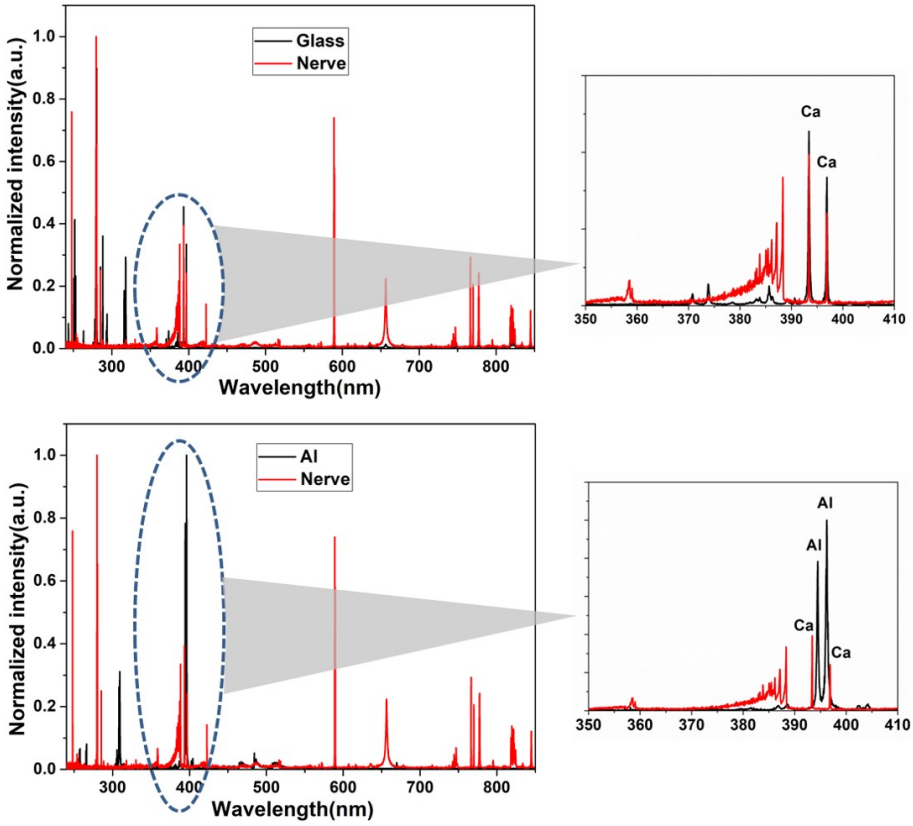

Figure 58: Comparison of glass and nerve spectra showing overlap of some elemental emissions (top). Comparison of Al and nerve tissue spectra (bottom).

The fixation of the tissue slices on the Al substrates comes with its own disadvantage. During measurement on every point, the ablation process removes larger tissue material than the tissue in the focal region of the laser. This reduces the resolution of the imaging process. The removal process of the

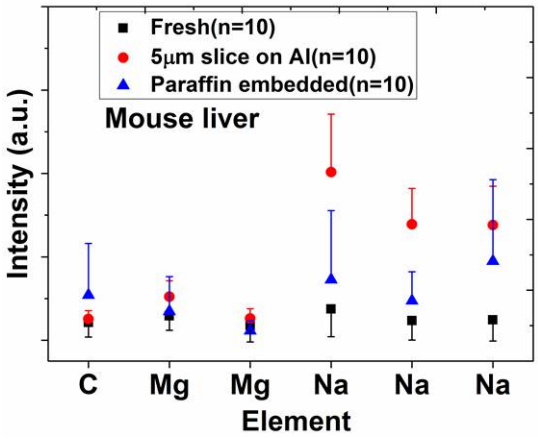

Figure 59: Comparison of the LIBS signal intensity of a tissue slice fixed on Al, paraffin embedded and fresh without embedding and fixing.

excessive region appears to be more due to mechanical process than thermal effects. This might also explain the increased removal of the tissue material in the case of the thicker samples than the thin samples as there is more intact material that tends to disrupt during the ablation process. Even though the area of the removed part is less as the slice gets thinner, it is still desired to be as small as the laser focal spot size. To reduce the removal of material outside the focal region, an Al-foil can be used instead of the Al plate. The explanation for this could be, the Al-foil is easily penetrated during the ablation process and this allows the escape of the high pressure created which drives the ablation process. Hence, the effect of mechanical removal of the tissue part outside the focal region becomes less. This is manifested in the measurement results shown in figure 60. As far as this thesis work is concerned, no other study or theory could be found to validate this effect.

In the figure 60, the removed part is much more wider in the case of the tissue slice on the Al plate than on the foil. Therefore, for better resolution, fixing the tissue slices on Al-foil is preferred. The amount of the removed material also depends on the thickness of the tissue slice even upon fixing on Al-foil. Thicknesses of 5 μm, 7 μm, 10 μm and 15 μm slices fixed on Al-foil were investigated. The size of the removed material outside the focal region is less in the 5 μm slice as shown in figure 61. The image (clear in the case of the 10 μm slice) indicates that there is less laser energy reaching the Al substrate resulting in a smaller hole. This means there is less escape of the pressure from the plume resulting in the removal of more tissue material outside the focal region of the laser. This suggests that the scanning measurements yield

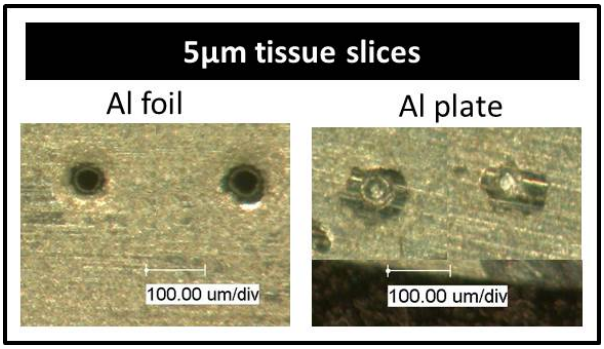

Figure 60: Comparison of the ablated tissue slices fixed on Al plate and Al-foil.

better result on thinner slices than thicker ones. Here, it must be noted that regardless of the choice of the substrate, impurities need to be investigated first for potential interference with the elements of interest. Al substrates used here showed nearly no interference with the elements of the tissues except for very weak iron lines. This might be due to impurities in the Al substrate.

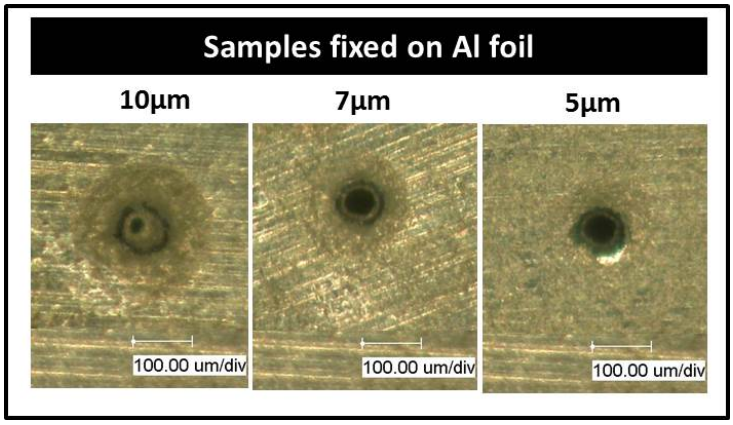

Figure 61: Comparison of ablated material for different slice thicknesses fixed on Al-foil.

The scanning image based on a 5 µm slice fixed on Al-foil and its corresponding Fe and Ca distribution is shown in figure 62. The measurement shows that the region with the highest intensity of these elements, indirectly, the highest concentration is associated with the tissue part. The image based on the Fe distribution shows the presence of low concentration of Fe outside the tissue part which can be due to the presence in the substrate as impurity. The distribution of Ca is pre-dominantly in the tissue region. One region of the tissues, shows the highest concentration of both these mineral elements. The image of this tissue based on C and O emissions is shown in figure 63.

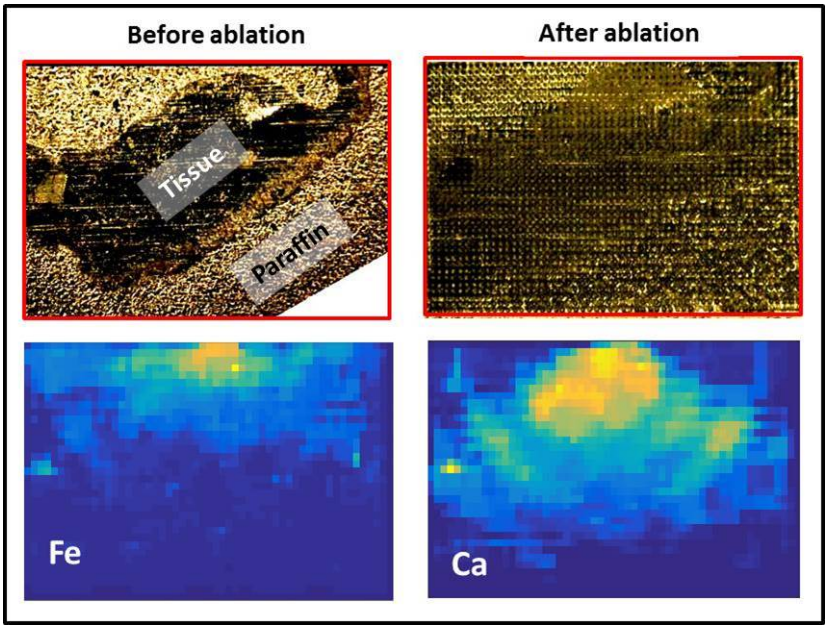

Figure 62: Actual image (top) and scanning image based on Ca and Fe (bottom) of a 5 µm tissue slice fixed on Al-foil.

The distribution of O is nearly homogeneous throughout the entire scanned region. This includes the region outside the tissue where there is only paraffin which is used to embed the tissue. The distribution of C shows higher concentration in the tissue part than in the majority of the paraffin region except in a small paraffin region where the highest intensity of C emission was observed. This is not agreement with the expected homogeneous presence of C in the paraffin region. No explanation could be found for this. However, it should be noted again that without any complementary information about the distribution the observed elements with the help of another technique, no conclusion can be drawn whether or not the results represent the actual distribution of the elements. In general, the results based on the four elements have shown no indication of the effect of experiment including sample topography or the preparation process.

8.3.2 Epoxy-resin embedded mouse tissues

Embedding tissue on epoxy-resin is another approach to perform measurements without having the issue of surface deformation. The process of embedding tissue requires several steps. A standard epoxy embedding kit used in this work for example (45359 Epoxy-Embedding Kit, Sigma-Aldrich) involves

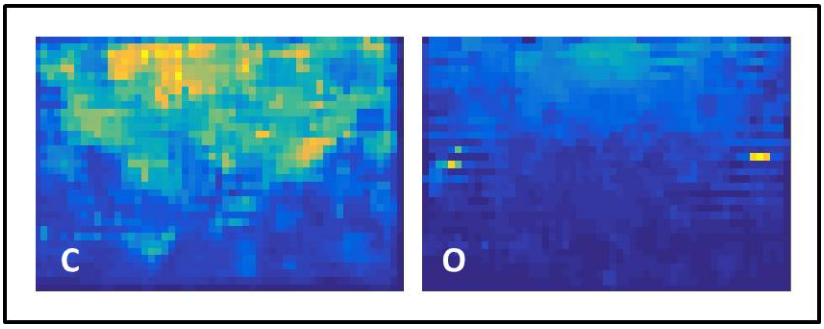

Figure 63: Ca and Fe based scanning image of a 5 µm tissue slice fixed on Al-foil.

50 minutes of washing the sample in 5 different solutions. This is followed by two steps of 30 minutes washing by two other mixtures. At the end, the tissue needs to be fixed by mixing the two chemicals of the embedding kit and then polymerize first at 45° C for 12 hours followed by 24 hours at 60° C. This is a lengthy process but allows for the preparation of the tissue in such a way that any section of the tissue can be accessed by preparing slices. The process of preparing the sample surface is done by cutting away thin slices, using a microtome, until the desired level is reached. The slices obtained from samples embedded in epoxy-resin are hard and show curling effect. Due to curling it requires strong gluing when the desire is to measure on the slices. This makes the preparation of slices for measurement difficult. However, the remaining block of the embedded tissue makes an excellent sample for LIBS scanning.

A measurement on a epoxy embedded block of a skin tissue obtained from a mouse is shown in figure 64. The image based on C, Ca and Fe emissions are shown. Relative to the trace elements Ca and Fe, C shows a homogeneous distribution on the surface both in the epoxy part and tissue part. Carbon is also present in epoxy-resin. Whereas the distribution of Ca and Fe resemble the tissue structure without any indication of the presence of these elements outside the tissue area.

In the actual image of the sample block, some parts of the tissue located inside the epoxy appear to be on the surface due to the transparency of the epoxy. This is reflected in the images based on Ca and Fe which are seen as parts with similar intensity as in the region outside the tissue part. The existence of such parts can be seen in the second OCT B-scan of the sample in figure 65.

The preparation of tissue samples for LIBS scanning in epoxy-resin involves a lengthy process. However, the resulting sample allows for having a flat and

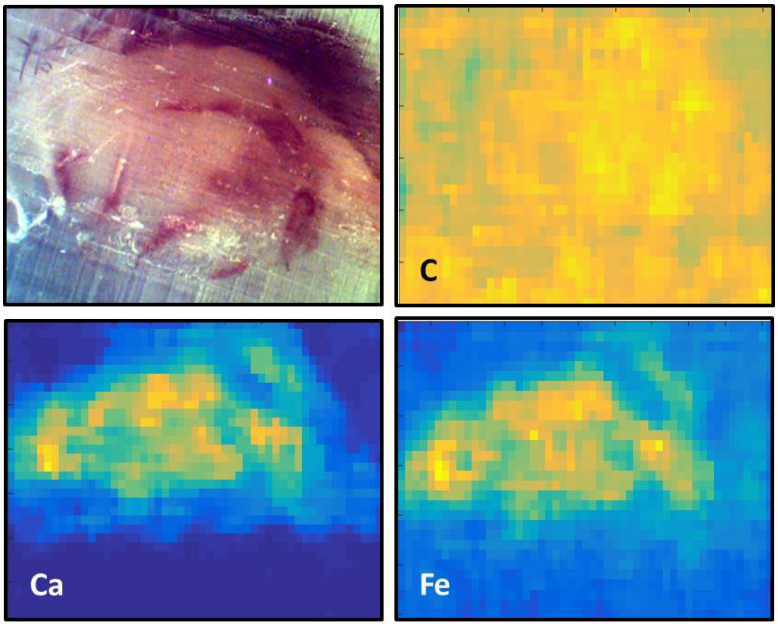

Figure 64: Actual (top-left corner) and scanning image (based on C, Ca and Fe) of a mouse muscle tissue embedded in epoxy-resin.

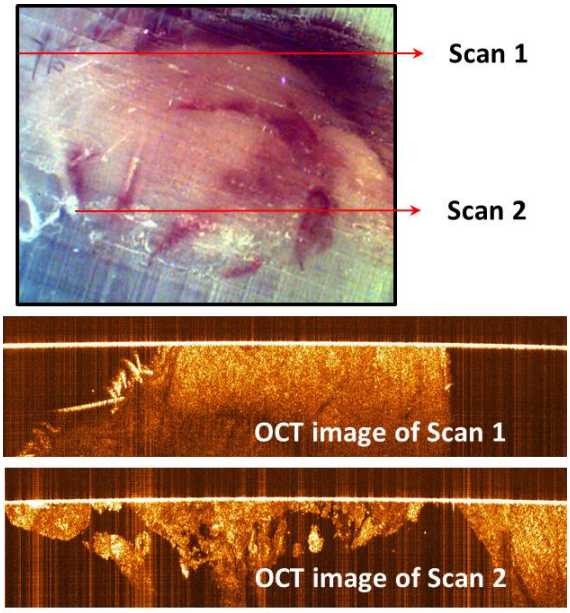

Figure 65: OCT image of sample showing the extent of the tissue embedded in epoxy resin.

hard surface which is optimum for sampling using LIBS. The mechanical rapture of the sample around the ablation crater is significantly reduced in epoxy-resin prepared samples compared to fresh tissue and paraffin embedded slices fixed on aluminum plate or glass plate.

In the investigation of the elemental distribution in tissues, it has been shown that LIBS has a great potential. At the same time, it has also been shown that LIBS is a sensitive technique that could lead to misinterpretation of results due to signal fluctuations during experiments as a result of the nature of the sample. The use of fresh ex-vivo samples poses the difficulty of having a flat surface that affects the excitation conditions of the LIBS laser due to changes in focus spot size. Therefore, it can be concluded that unless an auto-focusing system is used to keep the laser spot size on the surface of the sample constant, signal fluctuations will have a significant effect on the results. A simple solution without going to auto-focusing systems is to embed the samples in one of the standard techniques in order to prepare a flat surface for scanning. However, this should still be accompanied by extensive measurements that are validated with another established modality.

It should be noted that due to the scarcity of mice cancer models, repetitive investigations on cancerous tissues using the different preparation processes was not possible. However, the obtained results have allowed to reach a conclusion of which fixation process may provide the best results. Therefore, future investigation can use the findings of this work as a ground to perform extensive investigations on cancerous tissues in order to promote LIBS for biological tissue imaging. Another way to support the results of LIBS measurements is, to make sure that the physical conditions of plasma are understood. One of the important physical properties of the LIBS plasma is the focus of the next chapter.

8.4 Summary of two-dimensional(2D) mapping of elements as an imaging modality

- In the imaging of fresh-tissue using LIBS by spatial mapping of the major or trace elements, no concrete conclusions can be drawn. One major challenge of using fresh-tissue is matrix change due to drying. Therefore, the results should be verified by measurements on a large number of tissues or by another standard technique.

- Using LIBS on fresh-tissue to investigate elemental distribution is very interesting application. Therefore, further effort in exploring improved ways of tissue preparation are valuable and worth investigating.
- Slices of tissues fixed in paraffin can be used as alternative to fresh-tissue. It has been shown that using aluminium substrate enhances the LIBS signal from tissues. Moreover, paraffin fixed tissue slices put on aluminium foil have provided higher resolution results. The possible explanation for this is due to the reduction of mechanical effects of the ablation process when some of the pressure escapes through the holes generated by ablation. It was highlighted that the report of this effect could not be found in any other study. Therefore, this is worth further investigation.
- Whether the distribution of elements in paraffin embedded tissue reflect the true distribution still requires further validation. The results show that tissue embedded in paraffin and measured on aluminium foil offers better conditions of monitoring element distribution than fresh-tissue. The main advantage is the ability to cut uniform slices down to a few microns.
- Embedding tissue in epoxy-resin for LIBS measurements is another way to avoid the alteration due to drying. However, it involves a lengthy preparation process that consumes more than 36 hours. Epoxy-resin embedding offers better conditions for LIBS than fresh-tissue. Mean while, the required long preparation process takes away the rapid nature of LIBS which as a modality is still a cheap alternative.
- In conclusion, the different ways of tissue preparation for LIBS based elemental mapping have shown the importance of the matrix effect. Therefore, further extensive investigation based on the foundations of this work is important to promote LIBS as an imaging modality for biological tissues.

9 Validation of LIBS spectra by the physical properties of the plasma

A number of parameters related to the laser ablation and to the physical properties of the LIBS plasma play a role in obtaining reliable spectra. The ablation process is dictated by the interaction of the laser with the material [4]. For samples with the same homogeneous matrix, a direct comparison of element concentration using emission intensity is employed in what is commonly know as calibration based LIBS [19]. This is done under strictly controlled experimental conditions. Due to the heterogeneous nature of biological tissues, direct comparison of intensity of elements in tissues without validation by another technique or without large scale investigations could only help, at best, to lay a ground for further work. As already highlighted, this was one of the goals of the previous chapter. In this chapter, an approach to support the reliability of the LIBS spectra by investigating some of the physical properties of the LIBS plasma is briefly presented.

For simplicity, bronze that is primarily composed of copper has been used as a sample. Copper is an excellent sample because it has numerous emission lines across the measured spectral range which are helpful in the diagnosis of its plasma. The primary interest here is to establish a general procedure to perform measurements using the current setup that can be validated by the properties of the plasma. An extensive investigation of this conditions using tissue samples is not within the scope of this work. However, at the end of this chapter, how the procedure established with copper sample can be translated to tissue samples will suggested. The plasma conditions are crucial in determining the actual concentration of elements in any sample. If such precedure is followed for tissue experiments, the results can be reliably used to generate tissue images based on the element distribution. For example, one of the goals is ensuring negligeable self-absorption effect of emission lines. Self-absorption is particularly important for the application of tissues because tissues are primarily composed of four major elements (C,N,O and H). Elements in higher concentration especially major elements are prone to self-absorption[19]. To neglect self-absorption for any element, the measurements should be done in a time window when the plasma is optically thin. Another requirement is stoichiometric ablation. The validity of stoichiometric ablation of solids for typical LIBS irradiance values has already been discussed. Therefore, the investigations here will only focus on the existence of an optically thin time window when the plasma can be assumed in LTE.

9.1 Measurement procedure

In the investigations, LIBS measurements with pulse energy of 80 mJ were performed on a bronze sample. One spectrum is the average of 100 spectra obtained from 10 different spots. Each spectrum is a measurement obtained in a time window of 50 ns at a particular delay time from its corresponding laser pulse. The measurements were performed starting from a delay of 250 ns upto 2.55 µs with a time step of 50 ns. Before performing 10 measurements from each spot, one laser pulse was used as a cleaning pulse.

9.2 Existence of optically thin window

The purpose of investigating the existence of an optically thin window is to avoid self-absorption which is the absorption of photons by the laser-induced plasma. Self-absorption results in under estimation of the intensity of an emission line which when used for calculation of concentration can lead to underestimation of the responsible element. The criterion used to check the optically thin window was already discussed in chapter 2 in detail and is given by

$$\frac{I_{ki}}{I_{yx}} = \frac{\lambda_{yx,Z}}{\lambda_{ki,Z}} \frac{A_{ki,Z}}{A_{yx,Z}} \frac{g_{k,Z}}{g_{y,Z}} exp(-\frac{E_{k,Z} - E_{y,Z}}{k_B T}) \quad (17)$$

Equation 17 checks the ratio of the spatially and temporally integrated intensity of two emission lines corresponding to two transition states and compares the ratio with the theoretical value. The theoretical value can be calculated with the help of the spectroscopic data of the emission lines shown on the right side of the equality sign. To avoid the exponential dependence of the theoretical value on the temperature of the plasma, two lines with similar upper energy level can be taken. The two lines considered in this investigation are the neutral copper lines at 306.34 nm and 319.40 nm. These lines, from one of the measurements performed, are shown in figure 66. According to NIST atomic spectral database, these two lines at 306.34 nm and 319.40 nm have similar upper energy levels of 5.688 eV and 5.523 eV, respectively. They have the same values of transition probability (A) and degeneracy (g) of 1.55×10^6 s^{-1} and 4, respectively.

Since the two transitions have similar upper energy level, the exponential part of equation 17 can be approximated to 1. The remainder of the right hand side of the equation gives the theoretical value of the intensity ratio of the two lines. By considering the line at 306.34 nm the numerator of the

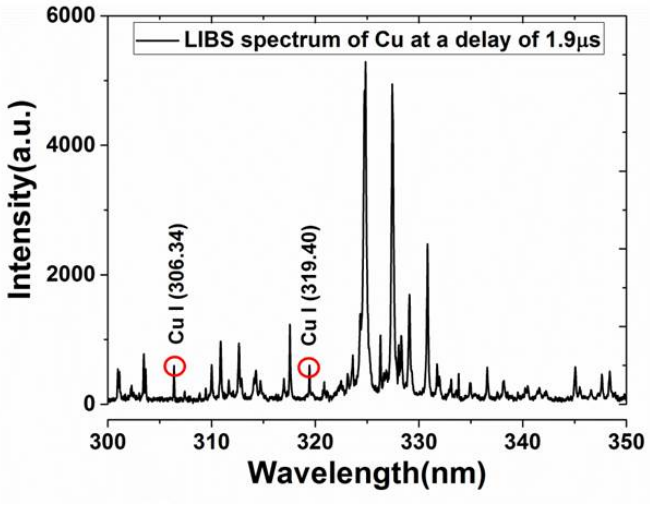

Figure 66: A mean of 100 LIBS spectra of copper obtained at a delay of 1.9 μs.

left side of the equation, the value of the right hand side becomes 1.04. By calculating this ratio from all the spectra obtained at different delay times, the optically thin window can be assumed the one with the value that is equal or closer to the theoretical value. Figure 67, shows the theoretical value and the corresponding experimental values at different delay times.

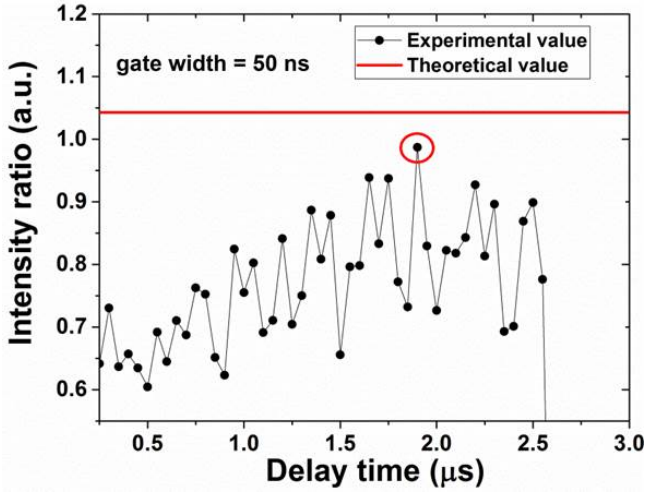

Figure 67: Theoretical (red) and measurement value (black) for optically thin window of copper plasma using emission lines at 306.34 nm and 319.40 nm.

The measurement at a delay of 1.9 µs with a value of 0.99 is the closest to the theoretical value. This can be considered as the best time window when there is less self-absorption. At this time window, a very good linear fit through the points related to the intensity of copper emission lines is expected in the Boltzmann plot method. This can further support the assumption of an optically thin plasma. The Boltzmann plot method is used to estimate the plasma temperature.

9.3 Determination of plasma temperature

It can be recalled that the linear equation used for Boltzmann plot is derived from the equation describing the intensity of a given emission line that is spatially and temporally integrated. The slope of the linear equation is used to estimate the plasma temperature. To use the Boltzmann plot, at least two lines of the same species (in this case from neutral or ionic Cu) with known spectroscopic data are required. A linear fit based on two points can lead to inaccurate temperature values compared to a fit on multiples points. Moreover, multiple points that are located as a cluster in the Boltzmann plane could also lead to inaccurate estimation of the plasma temperature. Therefore, seven Cu neutral lines with different upper energy level (located in different regions of the Boltzamann plane) have been used here to determine the plasma temperature. The selected neutral lines are 306.34 nm, 319.40 nm, 450.93 nm, 470.45 nm, 529.25 nm, 570.02 nm and 578.21 nm. Figure 68 shows the Boltzmann plot based on these seven lines. The slope of the linear fit is related to the temperature of the plasma through the Boltzmann constant as already discussed in chapter 2.

The Boltzmann plot in figure 68 shows that the fit through the points has R-sqaure value of 0.996 indicating the assumption of optically thin window at a delay of 1.9 µs is reasonable. The value of the plasma temperature in this time window is approximately 12.91×10^3 K. The existence of a time window when the plasma from the bronze sample can be assumed optically thin has been demonstrated by the complementing results of the ratio of two copper lines and the Boltzmann plot method. In conclusion, the experimental parameters used in this investigation, particularly, the delay time is crucial in ensuring the obtained results from a bronze sample.

The steps used to monitor the plasma properties from bronze can be adopted to tissue applications. For tissue applications, at least one element in the tissue needs to have multiple emission lines to check the validity of a time window when the plasma can be assumed optically thin. As far as the measurements

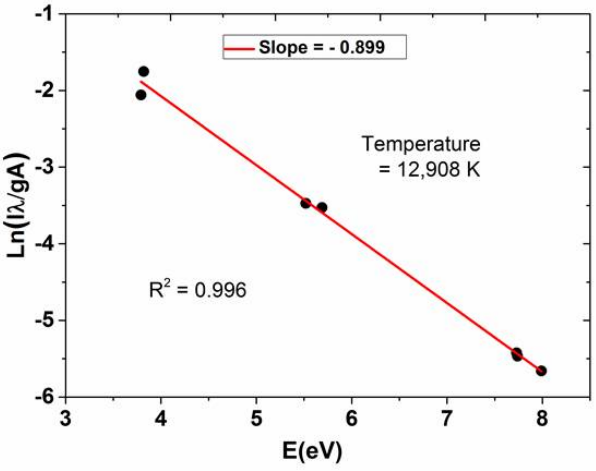

Figure 68: Boltzmann plot made by analysing the intensity of seven neutral Cu lines at a delay of 1.9 µs. I is intensity and λ is the wavelength of a given transition with upper level energy K, degeneracy g and transition probability A.

from tissue in this work are concerned, the only element with the same species (neutral or ionic) having more than two emission lines is neutral oxygen. However, these oxygen lines are not well resolved lines and have significant interference with each other. The oxygen triplet lines around 777 nm for example require a resolution of better than 0.1 nm at FWHM. The spectrometer used does not offer such resolution in this region. Therefore, the best way to use the procedure shown here for tissue applications is with the help a metallic substrate such as aluminium or copper based plates. In the previous chapter, paraffin embedded tissue slices were fixed on an aluminium plate or foil. This resulted in enhancement of the LIBS signal of the tissue and allowed to perform higher resolution scanning. The use of metallic substrates could also offer further benefit to investigate the plasma properties using the procedure demonstrated in this chapter. In order to advance the use of LIBS for biological applications, a synergy of efforts of that include large scale measurements, validation by other modalities and investigating the plasma properties are crucial. In conclusion, the brief procedure demonstrated to investigate the plasma properties can only be successful for tissue applications if the following suggestions are carefully considered:

- For low pulse energies, aluminium does not show many emission lines of neutral or ionic species. Therefore, the use of a copper substrate might be a better choice.

- In order to ensure the applicability of the procedure demonstrated here, the matrix of the chosen substrate should first be investigated without any tissue layer. For example, if a copper foil is opted, the effect of the hole that may be created by the ablation needs to be understood first.
- If a tissue on a metallic substrate/foil is used as a sample for measurements, the experimental parameters should provide similar plasma conditions in different regions of the tissue. A large deviation among the results from different regions of the tissue suggest that the tissue layer changes the plasma conditions. This could probably be attributed to the ablation process and complicates the measurement. In this case, a further analyse of each measurement point towards absolute quantification of all constituent elements can be done.
- Even after a seemingly successful implementation of the approach described here, it is highly advised to use it extensively for measurements on tissues already stained for the target elements. This helps in the validation of the results by the complementing the images of the stained tissue by LIBS images. Such an approach helps to easily identify potentially misleading results of LIBS that result from the large variables surrounding the complex nature of the laser generated plasma.

9.4 Summary of Validation of LIBS spectra by plasma properties

The following conclusions can be drawn from the establishment of a procedure to obtain reliable spectra:

- The importance of the validation tissue images based on elements measured by LIBS has been highlighted. Large scale measurements and using a standard suitable modality can support the LIBS results. In addition, fulfilment of some conditions by the LIBS plasma could be used to validate the LIBS spectra used for imaging.
- To pave a way for the application of tissues, the reliability of LIBS spectra measured from a copper sample by investigating the properties of the plasma has been demonstrated. A time window that the plasma could be assumed optically thin has been demonstrated. This is done by comparing the ratio of two emission lines measured experimentally with the theoretical value. The optically thin plasma assumption was further supported by the fit of a regression model on the Boltzmann plot to calculate the plasma temperature.

- The procedure explained in this chapter was established using a bronze sample. The copper in bronze allows to measure multiple emission lines in the measured spectral range. This is essential for minimizing the errors in the estimation of the plasma temperature.
- Under the condition of the measurements done in this work, to use the elements in tissue to investigate the plasma properties may not be feasible. This is because none of the charge states of the elements measured show multiple number of emission lines with varying values of upper energy levels.
- Using tissue slices on a copper plate/foil substrate to investigate the plasma properties according to the procedures used in this work has been suggested.

10 Summary and outlook

In this thesis, the application of LIBS as a diagnostic tool for biological tissue analysis has been presented. From the investigations the following conclusions can be drawn.

The viability of LIBS for the direct measurement of elements in biological tissue and indirect measurement of molecules has been presented. Both major and trace elements that constitute tissue could be measured. The lack of detailed information in the literature about the composition of tissues in terms of elements has been highlighted. This work has demonstrated the ability of LIBS to provide elemental information from some porcine and mice tissues for the first time. This can be used as a foundation for future works that aim to monitor the elements in any tissue.

In the experiments of tissue differentiation for laser surgery feedback mechanism, the inherent variability of the LIBS spectra together with the similarity of tissues make the differentiation by comparing the intensity of single emission lines impossible. To perform the discrimination task, supervised statistical classification method has been presented. The importance of data preprocessing methods has been highlighted and a new preprocessing approach based on generating intensity ratios has been presented. Very high classification accuracy among different tissues has been achieved. The applicability of one of the classification models has been demonstrated by mapping tissue types that were manually put close together. To approach the real surgical conditions, ex-vivo experiments involving LIBS together with a surgical Er:YAG laser have been presented. The surgical Er:YAG laser has a cleaning effect but changes the tissue properties that can be measured by LIBS. In future work related to surgical applications, the collection of LIBS data for classification should strictly include all the experimental devices of the target application.

In the experiments of the transferability of a classification models from one animal model to another, high classification accuracy of mice tissue based on the model from porcine tissues has been presented. This has been achieved despite some differences of spectral features between similar tissues. The results have shown that transfer of classification model trained by the tissues of one animal type to classify test tissues of another type of animal is feasible. The findings of the model transferability motivate an important future work. LIBS is able to generate large data from small samples due to its inherent requirement to probe only a few tens of microns of a sample. This can be

beneficial for models based on the emerging artificial neural network in which availability of human tissue can be difficult due to ethical concerns.

The experiments of using LIBS as element based imaging modality show that the robustness and reliability of the results is highly dependent on the way the sample is prepared. Using fresh tissues has a major drawback of surface irregularity and alteration due to drying. Promising results from tissues fixed using standard embedding techniques paraffin and epoxy-resin have been presented. A novel idea of using aluminium as a substrate to enhance the LIBS signal and improve the imaging resolution has been presented. The need for supporting information of the element based tissue images obtained using LIBS in future related studies has been addressed. A procedure to validate the reliability of LIBS spectra with the help of the physical properties of the LIBS plasma generated from a simple metallic sample (bronze) has been demonstrated.

The application of LIBS for diagnosis of biological tissues is very limited in the literature. This work has presented the potential of LIBS for the monitoring elements, differentiation and imaging for novel applications. The results have promising impact on the following applications:

- There is a clear lack of information on the elemental composition of many tissues in the literature. Trace elements have significant importance in cell life cycle and provide crucial information in histology applications [26]. Many of the techniques used to obtain tissue elemental information are expensive, time consuming or complicated to operate. LIBS offers a simple and versatile approach to get tissue elemental information. Further work needs to be done in having a standardized preparation method to homogenize tissue to make it easier for LIBS analysis. This will further require a standard LIBS device for the application.
- Laser surgery feedback system can greatly benefit from LIBS. The advance in deep machine learning can further improve the classification results. LIBS spectrum being one dimensional data, further work needs to be done in this area with deep learning using one-dimensional convolutional neural network.
- LIBS has the potential to highlight tissue features as well as to enhance the tissue contrast by targeting elements. It is a promising modality for the diagnosis of cancer. Future work needs to focus on optimizing the experimental parameters and sample preparation. Exploiting the

plasma physical properties is a promising approach to obtain reliable results and hence needs to be extensively investigated.

11 Zusammenfassung und Ausblick

11.1 Thema

Laser-induced Breakdown Spectroscopy (LIBS) als diagnostisches Werkzeug für die biologische Gewebeanalyse.

11.2 Zusammenfassung

In dieser Arbeit wurde die Anwendung von LIBS als diagnostisches Werkzeug für die biologische Gewebeanalyse vorgestellt. Aus den Untersuchungen können die folgenden Schlussfolgerungen gezogen werden.

Die Anwendbarkeit von LIBS für die direkte Messung von Elementen in biologischem Gewebe und die indirekte Messung von Molekülen wurde vorgestellt. Es konnten sowohl Haupt- als auch Spurenelemente,welche Gewebebestandteile sind, gemessen werden. Der Mangel an detaillierten Informationen in der Literatur über die elementare Zusammensetzung von Geweben wurde hervorgehoben. Diese Arbeit demonstriert erstmalig die Fähigkeit von LIBS, Elementinformationen von Gewebe von Schweinen und Mäusen zu liefern. Dies kann als Grundlage für zukünftige Arbeiten verwendet werden, die darauf abzielen, Elemente in weiterenGewebearten zu detektieren.

In den Experimenten zur Gewebedifferenzierung für den Feedback Mechanismus der Laserchirurgie macht die inhärente Variabilität der LIBS-Spektren zusammen mit der Ähnlichkeit der Gewebe die Differenzierung durch den Vergleich einzelner Emissionslinienintensitäten unmöglich. Um die Differenzierung zu erreichen, wurde eine überwachte statistische Klassifizierungsmethode vorgestellt. Die Wichtigkeit von Datenvorverarbeitungsmethoden wurde hervorgehoben und ein neuer Vorverarbeitungsansatz, der auf der Erzeugung von Intensitätsverhältnissen basiert, wurde vorgestellt. Es wurde eine sehr hohe Klassifikationsgenauigkeit zwischen verschiedenen Gewebetypen erreicht. Die Anwendbarkeit eines der Klassifikationsmodelle wurde durch die Zuordnung von Gewebetypen, die nahe nebeneinander positioniert wurden, demonstriert. Um sich den realen chirurgischen Bedingungen anzunähern, wurden ex-vivo Experimente mit LIBS zusammen mit einem chirurgischen Er:YAG-Laser vorgestellt. Der chirurgische Er:YAG-Laser hat eine reinigende Wirkung, verändert aber die Gewebeeigenschaften, die mit LIBS gemessen werden können. Bei zukünftigen Arbeiten mit Bezug aufchirurgische Anwendungen sollte die Sammlung von LIBS-Daten zur Klassifizierung unbedingt

alle Versuchsgeräte der Zielanwendung einschließen.

In den Experimenten zur Übertragbarkeit eines Klassifizierungsmodells auf ein weiteres Tiermodell wurde eine hohe Klassifizierungsgenauigkeit von Mäusegewebe basierend auf dem Modell von Schweinegewebe präsentiert. Dies wurde trotz vorhandenerspektraler Unterschiede zwischen ähnlichen Geweben erreicht. Die Ergebnisse haben gezeigt, dass die Übertragung eines Klassifikationsmodells, das mit den Geweben eines Tiertyps trainiert wurde, machbar ist, da Testgewebe eines weiterenTiertyps erfolgreich klassifiziert wurde.. Die Erkenntnisse der Modell- übertragbarkeit motivieren eine wichtige zukünftige Arbeit. LIBS ist in der Lage, große Daten aus kleinem Probenvolumenzu generieren, da es nur einige Mikrometer einer Probe untersuchen muss. Dies kann für Modelle, die künstlichen neuronalen Netzwerken basieren, von Vorteil sein, bei denen die Verfügbarkeit von Gewebe aufgrund ethischer Bedenken schwierig sein kann.

Die LIBS Experimente zur Verwendung als elementbasierte Bildgebungsmodalität zeigen, dass die Robustheit und Zuverlässigkeit der Ergebnisse stark von der Art der Probenvorbereitung abhängt. Die Verwendung von frischem Gewebe hat den großen Nachteil, dass die Oberfläche unregelmäßig ist und sich durch das Trocknen verändert. Vielversprechende Ergebnisse wurden von Geweben präsentiert, die mit den gängigenEinbettungschemikalienParaffin und Epoxidharz fixiert wurden. Zudem wurde eine neuartige Idee, Aluminium als Substrat zu verwenden, um das LIBS-Signal zu verstärken und die Bildauflösung zu verbessern, vorgestellt. Der Bedarf an unterstützenden Informationen zu den mit LIBS gewonnenen elementbasierten Gewebebildern in zukünftigen verwandten Studien wurde angesprochen. Ein Verfahren zur Validierung der Zuverlässigkeit von LIBS-Spektren basierend auf den physikalischen Eigenschaften eines LIBS-Plasmas, das aus einer einfachen metallischen Probe (Bronze) erzeugt wird, wurde demonstriert.

Die Literatur zur Anwendung von LIBS zur Diagnose von biologischen Geweben ist sehr begrenzt. Diese Arbeit hat das Potenzial von LIBS für die Überwachung von Elementen, Differenzierung und Bildgebung für neuartige Anwendungen demonstriert. Die Ergebnisse haben vielversprechende Auswirkungen auf die folgenden Anwendungen:

- In der Literatur gibt es einen deutlichen Mangel an Informationen über die elementare Zusammensetzung zahlreicher Gewebearten. Spurenelemente haben eine erhebliche Bedeutung für den Lebenszyklus von Zellen und liefern entscheidende Informationen bei histologischen Anwendungen [26]. Viele der Techniken, die zur Gewinnung von Gewe-

beelementinformationen verwendet werden, sind teuer, zeitaufwendig oder kompliziert in der Handhabung. LIBS bietet einen einfachen und vielseitigen Ansatz, um Gewebeelementinformationen zu erhalten. Es muss weiter an einer standardisierten Präparationsmethode zur Homogenisierung des Gewebes gearbeitet werden, um die LIBS-Analyse zu vereinfachen. Dies erfordert außerdem ein Standard-LIBS-Gerät für die Anwendung.

- EinFeedbacksystem für die Laserchirurgie kann von LIBS stark profitieren. Der Fortschritt im Bereich desmaschinellen Lernens kann die Klassifizierungsergebnisse weiter verbessern. Da das LIBS-Spektrum eindimensionale Daten zur Verfügung stellt, muss hier mit maschinellen Lernen anhand eines eindimensionalen neuronalen Netzwerks weiter gearbeitet werden.
- LIBS hat das Potenzial, Gewebemerkmale hervorzuheben sowie den Gewebekontrast durch das hervorheben vonElemente zu verbessern. Es ist eine vielversprechende Modalität für Krebs Diagnose. Zukünftige Arbeiten müssen sich auf die Optimierung der experimentellen Parameter und der Probenvorbereitung konzentrieren. Die Ausnutzung der physikalischen Eigenschaften des Plasmas ist ein vielversprechender Ansatz, um valideErgebnisse zu erhalten, und muss daher eingehend untersucht werden.

Bibliography

[1] Abbasi, H.; Guzman, R.; Cattin, P. C.; Zam, A.: All-fiber-optic LIBS system for tissue differentiation: A prospect for endoscopic smart laser osteotomy. In: *Optics and Lasers in Engineering* 148 (2022), 106765.

[2] Albini, A.; Sporn, M. B.: The tumour microenvironment as a target for chemoprevention. In: *Nature reviews. Cancer* 7.2 (2007), 139.

[3] Allison, R. R.; Downie, G. H.; Cuenca, R.; Hu, X.-H.; Childs, C. J.; Sibata, C. H.: Photosensitizers in clinical PDT. In: *Photodiagnosis and photodynamic therapy* 1.1 (2004), 27–42.

[4] Allmen, M. v.; Blatter, A.: *Laser-beam interactions with materials: physical principles and applications*. Vol. 2. Springer Science & Business Media, 2013.

[5] Astor, F. C.; Hanft, K. L.: Parotid surgery using Nd: YAG laser contact tips: clinical assessment of perioperative facial nerve function. In: *Journal of clinical laser medicine & surgery* 21.5 (2003), 297–299.

[6] Augello, M.; Deibel, W.; Nuss, K.; Cattin, P.; Jürgens, P.: Comparative microstructural analysis of bone osteotomies after cutting by computer-assisted robot-guided laser osteotome and piezoelectric osteotome: an in vivo animal study. In: *Lasers in medical science* 33.7 (2018), 1471–1478.

[7] Avci, P.; Gupta, A.; Sadasivam, M.; Vecchio, D.; Pam, Z.; Pam, N.; Hamblin, M. R.: *Low-level laser (light) therapy (LLLT) in skin: stimulating, healing, restoring*. In: *Seminars in cutaneous medicine and surgery*. Vol. 32. 1. Frontline Medical Communications. 2013, 41–52.

[8] Barthélemy, O.; Margot, J.; Laville, S.; Vidal, F.; Chaker, M.; Le Drogoff, B.; Johnston, T. W.; Sabsabi, M.: Investigation of the state of local thermodynamic equilibrium of a laser-produced aluminum plasma. In: *Applied spectroscopy* 59.4 (2005), 529–536.

[9] Bauer, H.; Leis, F.; Niemax, K.: Laser induced breakdown spectrometry with an echelle spectrometer and intensified charge coupled device detection. In: *Spectrochimica Acta Part B: Atomic Spectroscopy* 53.13 (1998), 1815–1825.

[10] Bay, E.; Deán-Ben, X. L.; Pang, G. A.; Douplik, A.; Razansky, D.: Real-time monitoring of incision profile during laser surgery using shock wave detection. In: *Journal of biophotonics* 8.1-2 (2015), 102–111.

[11] Benetou, V.; Lagiou, A.; Lagiou, P.: Chemoprevention of cancer: current evidence and future prospects. In: *F1000Research* 4.F1000 Faculty Rev (2015).

[12] Boulnois, J.-L.: Photophysical processes in recent medical laser developments: a review. In: *Lasers in Medical Science* 1.1 (1986), 47–66.

[13] Bulajic, D.; Corsi, M.; Cristoforetti, G.; Legnaioli, S.; Palleschi, V.; Salvetti, A.; Tognoni, E.: A procedure for correcting self-absorption in calibration free-laser induced breakdown spectroscopy. In: *Spectrochimica Acta Part B: Atomic Spectroscopy* 57.2 (2002), 339–353.

[14] Busser, B.; Moncayo, S.; Coll, J.-L.; Sancey, L.; Motto-Ros, V.: Elemental imaging using laser-induced breakdown spectroscopy: A new and promising approach for biological and medical applications. In: *Coordination Chemistry Reviews* 358 (2018), 70–79.

[15] Campbell, C. J.; Noyori, K. S.; Rittler, M. C.; Koester, C. J.: Intraocular temperature changes produced by laser coagulation. In: *Acta Ophthalmologica* 41.S76 (1963), 22–31.

[16] Chan, W. T.; Russo, R. E.: Study of laser-material interactions using inductively coupled plasma-atomic emission spectrometry. In: *Spectrochimica Acta Part B: Atomic Spectroscopy* 46.11 (1991), 1471–1486.

[17] Chang, F.-Y.; Tsai, M.-T.; Wang, Z.-Y.; Chi, C.-K.; Lee, C.-K.; Yang, C.-H.; Chan, M.-C.; Lee, Y.-J.: Optical coherence tomography-guided laser microsurgery for blood coagulation with continuous-wave laser diode. In: *Scientific reports* 5 (2015).

[18] Ciucci, A.; Corsi, M.; Palleschi, V.; Rastelli, S.; Salvetti, A.; Tognoni, E.: New procedure for quantitative elemental analysis by laser-induced plasma spectroscopy. In: *Applied spectroscopy* 53.8 (1999), 960–964.

[19] Cremers, D. A.; Multari, R. A.; Knight, A. K.: Laser-induced breakdown spectroscopy. In: *Encyclopedia of Analytical Chemistry: Applications, Theory and Instrumentation* (2006), 1–28.

[20] Cristoforetti, G.; De Giacomo, A.; Dell'Aglio, M.; Legnaioli, S.; Tognoni, E.; Palleschi, V.; Omenetto, N.: Local thermodynamic equilibrium in laser-induced breakdown spectroscopy: beyond the McWhirter criterion. In: *Spectrochimica Acta Part B: Atomic Spectroscopy* 65.1 (2010), 86–95.

[21] Dimitroulis, G.: Temporomandibular joint surgery: what does it mean to the dental practitioner? In: *Australian dental journal* 56.3 (2011), 257–264.

[22] Dingus, R.; Scammon, R.; Jacques, S.: *Laser-Tissue Interaction II*. In: *Proc. SPIE*. Vol. 1427. 1991, 45–54.

[23] Dong, F.-Z.; Chen, X.-L.; Wang, Q.; Sun, L.-X.; Yu, H.-B.; Liang, Y.-X.; Wang, J.-G.; Ni, Z.-B.; Du, Z.-H.; Ma, Y.-W., et al.: Recent progress on the application of LIBS for metallurgical online analysis in China. In: *Frontiers of Physics* 7.6 (2012), 679–689.

[24] Eberhard, J.; Eisenbeiss, A.; Braun, A.; Hedderich, J.; Jepsen, S.: Evaluation of selective caries removal by a fluorescence feedback-controlled Er: YAG laser in vitro. In: *Caries research* 39.6 (2005), 496–504.

[25] Farquharson, M.; Al-Ebraheem, A.: Micro-elemental mapping of trace elements in breast tissue. In: ().

[26] Farquharson, M.; Al-Ebraheem, A.; Theodorakou, C.; Ryan, E.; Bradley, D.; Gurusamy, K.; Davidson, B.: Measurement of K, Fe, Cu and Zn levels in secondary colorectal liver cancer and surrounding normal liver tissue, and their potential as a tissue classifier. In: *X-Ray Spectrometry* 38.2 (2009), 81–88.

[27] Foresta, E.; Torroni, A.; Di Nardo, F.; De Waure, C.; Poscia, A.; Gasparini, G.; Marianetti, T. M.; Pelo, S.: Pleomorphic adenoma and benign parotid tumors: extracapsular dissection vs superficial parotidectomy—review of literature and meta-analysis. In: *Oral surgery, oral medicine, oral pathology and oral radiology* 117.6 (2014), 663–676.

[28] Gemert, M. J. van; Welch, A.: Clinical use of laser-tissue interactions. In: *IEEE Engineering in Medicine and Biology magazine* 8.4 (1989), 10–13.

[29] Giakoumaki, A.; Melessanaki, K.; Anglos, D.: Laser-induced breakdown spectroscopy (LIBS) in archaeological science—applications and prospects. In: *Analytical and bioanalytical chemistry* 387.3 (2007), 749–760.

[30] Gimenez, Y.; Busser, B.; Trichard, F.; Kulesza, A.; Laurent, J.; Zaun, V.; Lux, F.; Benoit, J.; Panczer, G.; Dugourd, P., et al.: 3D imaging of nanoparticle distribution in biological tissue by laser-induced breakdown spectroscopy. In: *Scientific reports* 6 (2016), 29936.

[31] Goldman, L.; Blaney, D. J.; Kindel, D. J.; Richfield, D.; Franke, E. K.: Pathology of the effect of the laser beam on the skin. In: *Nature* 197.4870 (1963), 912–914.

[32] Gomba, J.; D'Angelo, C.; Bertuccelli, D.; Bertuccelli, G.: Spectroscopic characterization of laser induced breakdown in aluminium–lithium alloy samples for quantitative determination of traces. In: *Spectrochimica Acta Part B: Atomic Spectroscopy* 56.6 (2001), 695–705.

[33] Griem, H.: Principles of Plasma Spectroscopy, Cambridge Uni. In: *Press, Cambridge* (1997).

[34] Griem, H.; Baranger, M.; Kolb, A.; Oertel, G.: Stark broadening of neutral helium lines in a plasma. In: *Physical Review* 125.1 (1962), 177.

[35] Hannachi, R.; Cressault, Y.; Teulet, P.; Gleizes, A.; Lakhdar, Z. B.: Calculation of self-absorption coefficients of calcium resonance lines in the case of a CaCl2–water plasma. In: *Spectrochimica Acta Part B: Atomic Spectroscopy* 63.10 (2008), 1054–1059.

[36] Hildebrand, C.; Remahl, S.; Persson, H.; Bjartmar, C.: Myelinated nerve fibres in the CNS. In: *Progress in neurobiology* 40.3 (1993), 319–384.

[37] Hillenkamp, F.: *Lasers in biology and medicine*. Vol. 34. Springer Science & Business Media, 2013.

[38] Hollon, T.; Lewis, S.; Freudiger, C. W.; Sunney Xie, X.; Orringer, D. A.: Improving the accuracy of brain tumor surgery via Raman-based technology. In: *Neurosurgical focus* 40.3 (2016), E9.

[39] Huang, H.; Yang, L.-M.; Bai, S.; Liu, J.: Smart surgical tool. In: *Journal of biomedical optics* 20.2 (2015), 028001.

[40] El-Hussein, A.; Kassem, A.; Ismail, H.; Harith, M.: Exploiting LIBS as a spectrochemical analytical technique in diagnosis of some types of human malignancies. In: *Talanta* 82.2 (2010), 495–501.

[41] Iro, H.; Zenk, J.: Salivary gland diseases in childhood. In: *Laryngo-rhino-otologie* 93 (2014), S103–25.

[42] Jacques, S. L.: Laser-tissue interactions: photochemical, photothermal, and photomechanical. In: *Surgical Clinics of North America* 72.3 (1992), 531–558.

[43] Jansen, J. F.; Schöder, H.; Lee, N. Y.; Wang, Y.; Pfister, D. G.; Fury, M. G.; Stambuk, H. E.; Humm, J. L.; Koutcher, J. A.; Shukla-Dave, A.: Noninvasive assessment of tumor microenvironment using dynamic contrast-enhanced magnetic resonance imaging and 18F-fluoromisonidazole positron emission tomography imaging in neck nodal metastases. In: *International Journal of Radiation Oncology• Biology• Physics* 77.5 (2010), 1403–1410.

[44] Jeong, D. C.; Tsai, P. S.; Kleinfeld, D.: Prospect for feedback guided surgery with ultra-short pulsed laser light. In: *Current opinion in neurobiology* 22.1 (2012), 24–33.

[45] Kaminer, R.; Liebow, C.; Margarone, J. 3.; Zambon, J.: Bacteremia following laser and conventional surgery in hamsters. In: *Journal of oral and maxillofacial surgery* 48.1 (1990), 45–48.

[46] Kenhagho, H. N.; Rauter, G.; Guzman, R.; Cattin, P. C.; Zam, A.: Optoacoustic Tissue Differentiation Using a Mach–Zehnder Interferometer. In: *IEEE Transactions on Ultrasonics, Ferroelectrics, and Frequency Control* 66.9 (2019), 1435–1443.

[47] Kim, Y. S.: Human tissues: chemical composition and photon dosimetry data. In: *Radiation Research* 57.1 (1974), 38–45.

[48] Kumar, A.; Yueh, F.-Y.; Singh, J. P.; Burgess, S.: Characterization of malignant tissue cells by laser-induced breakdown spectroscopy. In: *Applied optics* 43.28 (2004), 5399–5403.

[49] Lochte-Holtegreven, W.: Plasma-diagnostics. In: *Amsterdam: North-Holland Publication Co., 1968, edited by Lochte-Holtegreven, W.* (1968).

[50] Martin, M. Z.; Allman, S.; Brice, D. J.; Martin, R. C.; Andre, N. O.: Exploring laser-induced breakdown spectroscopy for nuclear materials analysis and in-situ applications. In: *Spectrochimica Acta Part B: Atomic Spectroscopy* 74 (2012), 177–183.

[51] McNamara Jr, J. A.; Seligman, D. A.; Okeson, J. P.: Occlusion, orthodontic treatment, and temporomandibular disorders: a review. In: *Journal of orofacial pain* 9.1 (1995), 73–91.

[52] McWhirter, R.: Plasma diagnostic techniques. In: *Academic, New York* (1965).

[53] Motta, P.; Ruggeri, A.: *Ultrastructure of the connective tissue matrix*. Vol. 3. Springer Science & Business Media, 2012.

[54] Pelagalli, J.; Gimbel, C. B.; Hansen, R. T.; Swett, A.; Winn, D. W.: Investigational study of the use of Er: YAG laser versus dental drill for caries removal and cavity preparation—phase I. In: *Journal of clinical laser medicine & surgery* 15.3 (1997), 109–115.

[55] Peng, Q.; Juzeniene, A.; Chen, J.; Svaasand, L. O.; Warloe, T.; Giercksky, K.-E.; Moan, J.: Lasers in medicine. In: *Reports on Progress in Physics* 71.5 (2008), 056701.

[56] Pourzarandian, A.; Watanabe, H.; Aoki, A.; Ichinose, S.; Sasaki, K. M.; Nitta, H.; Ishikawa, I.: Histological and TEM examination of early stages of bone healing after Er: YAG laser irradiation. In: *Photomedicine and Laser Therapy* 22.4 (2004), 342–350.

[57] Ralchenko, Y.; Jou, F. C.; Kelleher, D. E.; Kramida, A.; Musgrove, A.; Reader, J.; Wiese, W. L.; Olsen, K. J.: NIST Atomic Spectra Database (version 3.0). In: *http://physics. nist. gov/asd3* (2005).

[58] Rehse, S. J.; Salimnia, H.; Miziolek, A.: Laser-induced breakdown spectroscopy (LIBS): an overview of recent progress and future potential for biomedical applications. In: *Journal of medical engineering & technology* 36.2 (2012), 77–89.

[59] Rohde, M.; Mehari, F.; Klämpfl, F.; Adler, W.; Neukam, F.-W.; Schmidt, M.; Stelzle, F.: The differentiation of oral soft-and hard tissues using laser induced breakdown spectroscopy–a prospect for tissue specific laser surgery. In: *Journal of biophotonics* 10.10 (2017), 1250–1261.

[60] Rohwetter, P.; Yu, J.; Méjean, G.; Stelmaszczyk, K.; Salmon, E.; Kasparian, J.; Wolf, J.-P.; Wöste, L.: Remote LIBS with ultrashort pulses: characteristics in picosecond and femtosecond regimes. In: *Journal of analytical atomic spectrometry* 19.4 (2004), 437–444.

[61] Rumsby, P.; Paul, J.: Temperature and density of an expanding laser produced plasma. In: *Plasma Physics* 16.3 (1974), 247.

[62] Russo, R. E.; Mao, X.; Gonzalez, J. J.; Mao, S. S.: Femtosecond laser ablation ICP-MS. In: *Journal of Analytical Atomic Spectrometry* 17.9 (2002), 1072–1075.

[63] Sabsabi, M.; Héon, R.; St-Onge, L.: Critical evaluation of gated CCD detectors for laser-induced breakdown spectroscopy analysis. In: *Spectrochimica Acta Part B: Atomic Spectroscopy* 60.7-8 (2005), 1211–1216.

[64] Samek, O.; Telle, H. H.; Beddows, D. C.: Laser-induced breakdown spectroscopy: a tool for real-time, in vitro and in vivo identification of carious teeth. In: *BMC Oral Health* 1.1 (2001), 1.

[65] Schwarzmaier, H.-J.; Yaroslavsky, I. V.; Yaroslavsky, A. N.; Fiedler, V.; Ulrich, F.; Kahn, T.: Treatment planning for MRI-guided laser-induced interstitial thermotherapy of brain tumors—The role of blood perfusion. In: *Journal of Magnetic Resonance Imaging* 8.1 (1998), 121–127.

[66] Singh, V. K.; Rai, A.; Rai, P.; Jindal, P.: Cross-sectional study of kidney stones by laser-induced breakdown spectroscopy. In: *Lasers in medical science* 24.5 (2009), 749–759.

[67] Singh, V. K.; Singh, V.; Rai, A. K.; Thakur, S. N.; Rai, P. K.; Singh, J. P.: Quantitative analysis of gallstones using laser-induced breakdown spectroscopy. In: *Applied Optics* 47.31 (2008), G38–G47.

[68] Solon, L. R.; Aronson, R.; Gould, G.: Physiological implications of laser beams. In: *Science (New York, NY)* 134.3489 (1961), 1506–1508.

[69] Spizzichino, V.; Fantoni, R.: Laser induced breakdown spectroscopy in archeometry: a review of its application and future perspectives. In: *Spectrochimica Acta Part B: Atomic Spectroscopy* 99 (2014), 201–209.

[70] Stelzle, F.; Adler, W.; Zam, A.; Tangermann-Gerk, K.; Knipfer, C.; Douplik, A.; Schmidt, M.; Nkenke, E.: In vivo optical tissue differentiation by diffuse reflectance spectroscopy: preliminary results for tissue-specific laser surgery. In: *Surgical innovation* 19.4 (2012), 385–393.

[71] Stelzle, F.; Knipfer, C.; Adler, W.; Rohde, M.; Oetter, N.; Nkenke, E.; Schmidt, M.; Tangermann-Gerk, K.: Tissue discrimination by uncorrected autofluorescence spectra: a proof-of-principle study for tissue-specific laser surgery. In: *Sensors* 13.10 (2013), 13717–13731.

[72] Summerfield, A.; Meurens, F.; Ricklin, M. E.: The immunology of the porcine skin and its value as a model for human skin. In: *Molecular immunology* 66.1 (2015), 14–21.

[73] Swinehart, D.: The beer-lambert law. In: *Journal of chemical education* 39.7 (1962), 333.

[74] Theiner, S.; Kornauth, C.; Varbanov, H. P.; Galanski, M.; Van Schoonhoven, S.; Heffeter, P.; Berger, W.; Egger, A. E.; Keppler, B. K.: Tumor microenvironment in focus: LA-ICP-MS bioimaging of a preclinical tumor model upon treatment with platinum (IV)-based anticancer agents. In: *Metallomics* 7.8 (2015), 1256–1264.

[75] Tweedie, D.; Jacob, A.: Surgery of the parotid gland: evolution of techniques, nomenclature and a revised classification system. In: *Clinical Otolaryngology* 34.4 (2009), 303–308.

[76] Vogel, A.; Venugopalan, V.: Mechanisms of pulsed laser ablation of biological tissues. In: *Chemical reviews* 103.2 (2003), 577–644.

[77] Wang, H.; Wang, B.; Wang, M.; Zheng, L.; Chen, H.; Chai, Z.; Zhao, Y.; Feng, W.: Time-resolved ICP-MS analysis of mineral element contents and distribution patterns in single cells. In: *Analyst* 140.2 (2015), 523–531.

[78] Wen, S.-B.; Mao, X.; Greif, R.; Russo, R. E.: Laser ablation induced vapor plume expansion into a background gas. II. Experimental analysis. In: *Journal of applied physics* 101.2 (2007), 023115.

[79] Williams, P.; Wendell-Smith, C.: Some additional parametric variations between peripheral nerve fibre populations. In: *Journal of anatomy* 109.Pt 3 (1971), 505.

[80] Woodard, H.; White, D.: The composition of body tissues. In: *The British journal of radiology* 59.708 (1986), 1209–1218.

[81] Wu, Y.; Zhang, W.; Li, J.; Zhang, Y.: Optical imaging of tumor microenvironment. In: *American journal of nuclear medicine and molecular imaging* 3.1 (2013), 1.

[82] Young, K. E.; Evans, C. A.; Hodges, K. V.; Bleacher, J. E.; Graff, T. G.: A review of the handheld X-ray fluorescence spectrometer as a tool for field geologic investigations on Earth and in planetary surface exploration. In: *Applied Geochemistry* 72 (2016), 77–87.

[83] Yueh, F.-Y.; Zheng, H.; Singh, J. P.; Burgess, S.: Preliminary evaluation of laser-induced breakdown spectroscopy for tissue classification. In: *Spectrochimica Acta Part B: Atomic Spectroscopy* 64.10 (2009), 1059–1067.

[84] Zhang, Y.; Pfeiffer, T.; Weller, M.; Wieser, W.; Huber, R.; Raczkowsky, J.; Schipper, J.; Wörn, H.; Klenzner, T.: Optical coherence tomography guided laser cochleostomy: Towards the accuracy on tens of micrometer scale. In: *BioMed research international* 2014 (2014).

Own publications referring to this work

[P1] Mehari, F.; Rohde, M.; Knipfer, C.; Kanawade, R.; Klämpfl, F.; Adler, W.; Oetter, N.; Stelzle, F.; Schmidt, M.: Investigation of laser induced breakdown spectroscopy (LIBS) for the differentiation of nerve and gland tissue—a possible application for a laser surgery feedback control mechanism. In: *Plasma Science and Technology* 18.6 (2016), 654.

[P2] Mehari, F.; Geißler, B.; Rohde, M.; Klämpfl, F.; Stelzle, F.; Schmidt, M.: Laser-induced Breakdown Spectroscopy (LIBS) based tissue type mapping of ex-vivo soft tissues-A prospect for tissue specific Laser surgery. In: *Optical Molecular Probes, Imaging and Drug Delivery* (2017), JS1A–2.

[P3] Mehari, F.; Lengenfelder, B.; Figura, R.; Klämpfl, F.; Schmidt, M.: LIBS based Tissue Differentiation for Er:YAG Surgical Laser. In: *Proceedings of the 6th International Conference on Photonics, Optics and Laser Technology - Volume 1: PHOTOPTICS* (2018), 247–251.

[P4] Mehari, F.; Rohde, M.; Knipfer, C.; Kanawade, R.; Klämpfl, F.; Adler, W.; Stelzle, F.; Schmidt, M.: Laser induced breakdown spectroscopy for bone and cartilage differentiation-ex vivo study as a prospect for a laser surgery feedback mechanism. In: *Biomedical optics express* 5.11 (2014), 4013–4023.

[P5] Mehari, F.; Rohde, M.; Kanawade, R.; Knipfer, C.; Adler, W.; Klämpfl, F.; Stelzle, F.; Schmidt, M.: Investigation of the differentiation of ex vivo nerve and fat tissues using laser-induced breakdown spectroscopy (LIBS): Prospects for tissue-specific laser surgery. In: *Journal of biophotonics* 9.10 (2016), 1021–1032.

Reihenübersicht

Koordination der Reihe (Stand 2023):
Geschäftsstelle Maschinenbau, Dr.-Ing. Oliver Kreis, www.mb.fau.de/diss/

Im Rahmen der Reihe sind bisher die nachfolgenden Bände erschienen.

Band 1 – 52
Fertigungstechnik – Erlangen
ISSN 1431-6226
Carl Hanser Verlag, München

Band 53 – 307
Fertigungstechnik – Erlangen
ISSN 1431-6226
Meisenbach Verlag, Bamberg

ab Band 308
FAU Studien aus dem Maschinenbau
ISSN 2625-9974
FAU University Press, Erlangen

Die Zugehörigkeit zu den jeweiligen Lehrstühlen ist wie folgt gekennzeichnet:

Lehrstühle:

FAPS	Lehrstuhl für Fertigungsautomatisierung und Produktionssystematik
FMT	Lehrstuhl für Fertigungsmesstechnik
KTmfk	Lehrstuhl für Konstruktionstechnik
LFT	Lehrstuhl für Fertigungstechnologie
LGT	Lehrstuhl für Gießereitechnik
LPT	Lehrstuhl für Photonische Technologien
REP	Lehrstuhl für Ressourcen- und Energieeffiziente Produktionsmaschinen

Band 1: Andreas Hemberger
Innovationspotentiale in der rechnerintegrierten Produktion durch wissensbasierte Systeme
FAPS, 208 Seiten, 107 Bilder. 1988.
ISBN 3-446-15234-2.

Band 2: Detlef Classe
Beitrag zur Steigerung der Flexibilität automatisierter Montagesysteme durch Sensorintegration und erweiterte Steuerungskonzepte
FAPS, 194 Seiten, 70 Bilder. 1988.
ISBN 3-446-15529-5.

Band 3: Friedrich-Wilhelm Nolting
Projektierung von Montagesystemen
FAPS, 201 Seiten, 107 Bilder, 1 Tab. 1989.ISBN 3-446-15541-4.

Band 4: Karsten Schlüter
Nutzungsgradsteigerung von Montagesystemen durch den Einsatz der Simulationstechnik
FAPS, 177 Seiten, 97 Bilder. 1989.
ISBN 3-446-15542-2.

Band 5: Shir-Kuan Lin
Aufbau von Modellen zur Lageregelung von Industrierobotern
FAPS, 168 Seiten, 46 Bilder. 1989.
ISBN 3-446-15546-5.

Band 6: Rudolf Nuss
Untersuchungen zur Bearbeitungsqualität im Fertigungssystem Laserstrahlschneiden
LFT, 206 Seiten, 115 Bilder, 6 Tab. 1989. ISBN 3-446-15783-2.

Band 7: Wolfgang Scholz
Modell zur datenbankgestützten Planung automatisierter Montageanlagen
FAPS, 194 Seiten, 89 Bilder. 1989.
ISBN 3-446-15825-1.

Band 8: Hans-Jürgen Wißmeier
Beitrag zur Beurteilung des Bruchverhaltens von Hartmetall-Fließpreßmatrizen
LFT, 179 Seiten, 99 Bilder, 9 Tab. 1989. ISBN 3-446-15921-5.

Band 9: Rainer Eisele
Konzeption und Wirtschaftlichkeit von Planungssystemen in der Produktion
FAPS, 183 Seiten, 86 Bilder. 1990.
ISBN 3-446-16107-4.

Band 10: Rolf Pfeiffer
Technologisch orientierte Montageplanung am Beispiel der Schraubtechnik
FAPS, 216 Seiten, 102 Bilder, 16 Tab. 1990. ISBN 3-446-16161-9.

Band 11: Herbert Fischer
Verteilte Planungssysteme zur Flexibilitätssteigerung der rechnerintegrierten Teilefertigung
FAPS, 201 Seiten, 82 Bilder. 1990.
ISBN 3-446-16105-8.

Band 12: Gerhard Kleineidam
CAD/CAP: Rechnergestützte Montagefeinplanung
FAPS, 203 Seiten, 107 Bilder. 1990.
ISBN 3-446-16112-0.

Band 13: Frank Vollertsen
Pulvermetallurgische Verarbeitung eines übereutektoiden verschleißfesten Stahls
LFT, XIII u. 217 Seiten, 67 Bilder, 34 Tab. 1990.
ISBN 3-446-16133-3.

Band 14: Stephan Biermann
Untersuchungen zur Anlagen- und Prozeßdiagnostik für das Schneiden mit CO_2-Hochleistungslasern
LFT, VIII u. 170 Seiten, 93 Bilder, 4 Tab. 1991. ISBN 3-446-16269-0.

Band 15: Uwe Geißler
Material- und Datenfluß in einer flexiblen Blechbearbeitungszelle
LFT, 124 Seiten, 41 Bilder, 7 Tab. 1991. ISBN 3-446-16358-1.

Band 16: Frank Oswald Hake
Entwicklung eines rechnergestützten Diagnosesystems für automatisierte Montagezellen
FAPS, XIV u. 166 Seiten, 77 Bilder. 1991. ISBN 3-446-16428-6.

Band 17: Herbert Reichel
Optimierung der Werkzeugbereitstellung durch rechnergestützte Arbeitsfolgenbestimmung
FAPS, 198 Seiten, 73 Bilder, 2 Tab. 1991. ISBN 3-446-16453-7.

Band 18: Josef Scheller
Modellierung und Einsatz von Softwaresystemen für rechnergeführte Montagezellen
FAPS, 198 Seiten, 65 Bilder. 1991.
ISBN 3-446-16454-5.

Band 19: Arnold vom Ende
Untersuchungen zum Biegeumformen mit elastischer Matrize
LFT, 166 Seiten, 55 Bilder, 13 Tab. 1991. ISBN 3-446-16493-6.

Band 20: Joachim Schmid
Beitrag zum automatisierten Bearbeiten von Keramikguß mit Industrierobotern
FAPS, XIV u. 176 Seiten, 111 Bilder, 6 Tab. 1991.
ISBN 3-446-16560-6.

Band 21: Egon Sommer
Multiprozessorsteuerung für kooperierende Industrieroboter in Montagezellen
FAPS, 188 Seiten, 102 Bilder. 1991.
ISBN 3-446-17062-6.

Band 22: Georg Geyer
Entwicklung problemspezifischer Verfahrensketten in der Montage
FAPS, 192 Seiten, 112 Bilder. 1991.
ISBN 3-446-16552-5.

Band 23: Rainer Flohr
Beitrag zur optimalen Verbindungstechnik in der Oberflächenmontage (SMT)
FAPS, 186 Seiten, 79 Bilder. 1991.
ISBN 3-446-16568-1.

Band 24: Alfons Rief
Untersuchungen zur Verfahrensfolge Laserstrahlschneiden und -schweißen in der Rohkarosseriefertigung
LFT, VI u. 145 Seiten, 58 Bilder, 5 Tab. 1991. ISBN 3-446-16593-2.

Band 25: Christoph Thim
Rechnerunterstützte Optimierung von Materialflußstrukturen in der Elektronikmontage durch Simulation
FAPS, 188 Seiten, 74 Bilder. 1992.
ISBN 3-446-17118-5.

Band 26: Roland Müller
CO_2 -Laserstrahlschneiden von kurzglasverstärkten Verbundwerkstoffen
LFT, 141 Seiten, 107 Bilder, 4 Tab. 1992. ISBN 3-446-17104-5.

Band 27: Günther Schäfer
Integrierte Informationsverarbeitung bei der Montageplanung
FAPS, 195 Seiten, 76 Bilder. 1992.
ISBN 3-446-17117-7.

Band 28: Martin Hoffmann
Entwicklung einerCAD/CAM-Prozeßkette für die Herstellung von Blechbiegeteilen
LFT, 149 Seiten, 89 Bilder. 1992.
ISBN 3-446-17154-1.

Band 29: Peter Hoffmann
Verfahrensfolge Laserstrahlschneiden und –schweißen: Prozeßführung und Systemtechnik in der 3D-Laserstrahlbearbeitung von Blechformteilen
LFT, 186 Seiten, 92 Bilder, 10 Tab. 1992. ISBN 3-446-17153-3.

Band 30: Olaf Schrödel
Flexible Werkstattsteuerung mit objektorientierten Softwarestrukturen
FAPS, 180 Seiten, 84 Bilder. 1992.
ISBN 3-446-17242-4.

Band 31: Hubert Reinisch
Planungs- und Steuerungswerkzeuge zur impliziten Geräteprogrammierung in Roboterzellen
FAPS, XI u. 212 Seiten, 112 Bilder. 1992. ISBN 3-446-17380-3.

Band 32: Brigitte Bärnreuther
Ein Beitrag zur Bewertung des Kommunikationsverhaltens von Automatisierungsgeräten in flexiblen Produktionszellen
FAPS, XI u. 179 Seiten, 71 Bilder. 1992. ISBN 3-446-17451-6.

Band 33: Joachim Hutfless
Laserstrahlregelung und Optikdiagnostik in der Strahlführung einer CO_2-Hochleistungslaseranlage
LFT, 175 Seiten, 70 Bilder, 17 Tab. 1993. ISBN 3-446-17532-6.

Band 34: Uwe Günzel
Entwicklung und Einsatz eines Simula-tionsverfahrens für operative undstrategische Probleme der Produktionsplanung und -steuerung
FAPS, XIV u. 170 Seiten, 66 Bilder, 5 Tab. 1993. ISBN 3-446-17604-7.

Band 35: Bertram Ehmann
Operatives Fertigungscontrolling durch Optimierung auftragsbezogener Bearbeitungsabläufe in der Elektronikfertigung
FAPS, XV u. 167 Seiten, 114 Bilder. 1993. ISBN 3-446-17658-6.

Band 36: Harald Kolléra
Entwicklung eines benutzerorientierten Werkstattprogrammiersystems für das Laserstrahlschneiden
LFT, 129 Seiten, 66 Bilder, 1 Tab. 1993. ISBN 3-446-17719-1.

Band 37: Stephanie Abels
Modellierung und Optimierung von Montageanlagen in einem integrierten Simulationssystem
FAPS, 188 Seiten, 88 Bilder. 1993.
ISBN 3-446-17731-0.

Band 38: Robert Schmidt-Hebbel
Laserstrahlbohren durchflußbestimmender Durchgangslöcher
LFT, 145 Seiten, 63 Bilder, 11 Tab. 1993. ISBN 3-446-17778-7.

Band 39: Norbert Lutz
Oberflächenfeinbearbeitung keramischer Werkstoffe mit XeCl-Excimerlaserstrahlung
LFT, 187 Seiten, 98 Bilder, 29 Tab. 1994. ISBN 3-446-17970-4.

Band 40: Konrad Grampp
Rechnerunterstützung bei Test und Schulung an Steuerungssoftware von SMD-Bestücklinien
FAPS, 178 Seiten, 88 Bilder. 1995.
ISBN 3-446-18173-3.

Band 41: Martin Koch
Wissensbasierte Unterstützung derAngebotsbearbeitung in der Investitionsgüterindustrie
FAPS, 169 Seiten, 68 Bilder. 1995.
ISBN 3-446-18174-1.

Band 42: Armin Gropp
Anlagen- und Prozeßdiagnostik beim Schneiden mit einem gepulsten Nd:YAG-Laser
LFT, 160 Seiten, 88 Bilder, 7 Tab. 1995. ISBN 3-446-18241-1.

Band 43: Werner Heckel
Optische 3D-Konturerfassung und on-line Biegewinkelmessung mit dem Lichtschnittverfahren
LFT, 149 Seiten, 43 Bilder, 11 Tab. 1995. ISBN 3-446-18243-8.

Band 44: Armin Rothhaupt
Modulares Planungssystem zur Optimierung der Elektronikfertigung
FAPS, 180 Seiten, 101 Bilder. 1995.
ISBN 3-446-18307-8.

Band 45: Bernd Zöllner
Adaptive Diagnose in der Elektronikproduktion
FAPS, 195 Seiten, 74 Bilder, 3 Tab. 1995. ISBN 3-446-18308-6.

Band 46: Bodo Vormann
Beitrag zur automatisierten Handhabungsplanung komplexer Blechbiegeteile
LFT, 126 Seiten, 89 Bilder, 3 Tab. 1995. ISBN 3-446-18345-0.

Band 47: Peter Schnepf
Zielkostenorientierte Montageplanung
FAPS, 144 Seiten, 75 Bilder. 1995.
ISBN 3-446-18397-3.

Band 48: Rainer Klotzbücher
Konzept zur rechnerintegrierten Materialversorgung in flexiblen Fertigungssystemen
FAPS, 156 Seiten, 62 Bilder. 1995.
ISBN 3-446-18412-0.

Band 49: Wolfgang Greska
Wissensbasierte Analyse undKlassifizierung von Blechteilen
LFT, 144 Seiten, 96 Bilder. 1995.
ISBN 3-446-18462-7.

Band 50: Jörg Franke
Integrierte Entwicklung neuer Produkt- und Produktionstechnologien für räumliche spritzgegossene Schaltungsträger (3-D MID)
FAPS, 196 Seiten, 86 Bilder, 4 Tab. 1995. ISBN 3-446-18448-1.

Band 51: Franz-Josef Zeller
Sensorplanung und schnelle Sensorregelung für Industrieroboter
FAPS, 190 Seiten, 102 Bilder, 9 Tab. 1995. ISBN 3-446-18601-8.

Band 52: Michael Solvie
Zeitbehandlung und Multimedia-Unterstützung in Feldkommunikationssystemen
FAPS, 200 Seiten, 87 Bilder, 35 Tab. 1996. ISBN 3-446-18607-7.

Band 53: Robert Hopperdietzel
Reengineering in der Elektro- und Elektronikindustrie
FAPS, 180 Seiten, 109 Bilder, 1 Tab. 1996. ISBN 3-87525-070-2.

Band 54: Thomas Rebhahn
Beitrag zur Mikromaterialbearbeitung mit Excimerlasern - Systemkomponenten und Verfahrensoptimierungen
LFT, 148 Seiten, 61 Bilder, 10 Tab. 1996. ISBN 3-87525-075-3.

Band 55: Henning Hanebuth
Laserstrahlhartlöten mit Zweistrahltechnik
LFT, 157 Seiten, 58 Bilder, 11 Tab. 1996. ISBN 3-87525-074-5.

Band 56: Uwe Schönherr
Steuerung und Sensordatenintegration für flexible Fertigungszellen mitkooperierenden Robotern
FAPS, 188 Seiten, 116 Bilder, 3 Tab. 1996. ISBN 3-87525-076-1.

Band 57: Stefan Holzer
Berührungslose Formgebung mit-Laserstrahlung
LFT, 162 Seiten, 69 Bilder, 11 Tab. 1996. ISBN 3-87525-079-6.

Band 58: Markus Schultz
Fertigungsqualität beim 3D-Laserstrahlschweißen vonBlechformteilen
LFT, 165 Seiten, 88 Bilder, 9 Tab. 1997. ISBN 3-87525-080-X.

Band 59: Thomas Krebs
Integration elektromechanischer CA-Anwendungen über einem STEP-Produktmodell
FAPS, 198 Seiten, 58 Bilder, 8 Tab. 1997. ISBN 3-87525-081-8.

Band 60: Jürgen Sturm
Prozeßintegrierte Qualitätssicherung in der Elektronikproduktion
FAPS, 167 Seiten, 112 Bilder, 5 Tab. 1997. ISBN 3-87525-082-6.

Band 61: Andreas Brand
Prozesse und Systeme zur Bestückung räumlicher elektronischer Baugruppen (3D-MID)
FAPS, 182 Seiten, 100 Bilder. 1997. ISBN 3-87525-087-7.

Band 62: Michael Kauf
Regelung der Laserstrahlleistung und der Fokusparameter einer CO_2-Hochleistungslaseranlage
LFT, 140 Seiten, 70 Bilder, 5 Tab. 1997. ISBN 3-87525-083-4.

Band 63: Peter Steinwasser
Modulares Informationsmanagement in der integrierten Produkt- und Prozeßplanung
FAPS, 190 Seiten, 87 Bilder. 1997. ISBN 3-87525-084-2.

Band 64: Georg Liedl
Integriertes Automatisierungskonzept für den flexiblen Materialfluß in der Elektronikproduktion
FAPS, 196 Seiten, 96 Bilder, 3 Tab. 1997. ISBN 3-87525-086-9.

Band 65: Andreas Otto
Transiente Prozesse beim Laserstrahlschweißen
LFT, 132 Seiten, 62 Bilder, 1 Tab. 1997. ISBN 3-87525-089-3.

Band 66: Wolfgang Blöchl
Erweiterte Informationsbereitstellung an offenen CNC-Steuerungen zur Prozeß- und Programmoptimierung
FAPS, 168 Seiten, 96 Bilder. 1997. ISBN 3-87525-091-5.

Band 67: Klaus-Uwe Wolf
Verbesserte Prozeßführung und Prozeßplanung zur Leistungs- und Qualitätssteigerung beim Spulenwickeln
FAPS, 186 Seiten, 125 Bilder. 1997. ISBN 3-87525-092-3.

Band 68: Frank Backes
Technologieorientierte Bahnplanung für die 3D-Laserstrahlbearbeitung
LFT, 138 Seiten, 71 Bilder, 2 Tab. 1997. ISBN 3-87525-093-1.

Band 69: Jürgen Kraus
Laserstrahlumformen von Profilen
LFT, 137 Seiten, 72 Bilder, 8 Tab. 1997. ISBN 3-87525-094-X.

Band 70: Norbert Neubauer
Adaptive Strahlführungen für CO_2-Laseranlagen
LFT, 120 Seiten, 50 Bilder, 3 Tab. 1997. ISBN 3-87525-095-8.

Band 71: Michael Steber
Prozeßoptimierter Betrieb flexibler Schraubstationen in der automatisierten Montage
FAPS, 168 Seiten, 78 Bilder, 3 Tab. 1997. ISBN 3-87525-096-6.

Band 72: Markus Pfestorf
Funktionale 3D-Oberflächenkenngrößen in der Umformtechnik
LFT, 162 Seiten, 84 Bilder, 15 Tab. 1997. ISBN 3-87525-097-4.

Band 73: Volker Franke
Integrierte Planung und Konstruktion von Werkzeugen für die Biegebearbeitung
LFT, 143 Seiten, 81 Bilder. 1998. ISBN 3-87525-098-2.

Band 74: Herbert Scheller
Automatisierte Demontagesysteme und recyclinggerechte Produktgestaltung elektronischer Baugruppen
FAPS, 184 Seiten, 104 Bilder, 17 Tab. 1998. ISBN 3-87525-099-0.

Band 75: Arthur Meßner
Kaltmassivumformung metallischer Kleinstteile – Werkstoffverhalten, Wirkflächenreibung, Prozeßauslegung
LFT, 164 Seiten, 92 Bilder, 14 Tab. 1998. ISBN 3-87525-100-8.

Band 76: Mathias Glasmacher
Prozeß- und Systemtechnik zum Laserstrahl-Mikroschweißen
LFT, 184 Seiten, 104 Bilder, 12 Tab. 1998. ISBN 3-87525-101-6.

Band 77: Michael Schwind
Zerstörungsfreie Ermittlung mechanischer Eigenschaften von Feinblechen mit dem Wirbelstromverfahren
LFT, 124 Seiten, 68 Bilder, 8 Tab. 1998. ISBN 3-87525-102-4.

Band 78: Manfred Gerhard
Qualitätssteigerung in der Elektronikproduktion durch Optimierung der Prozeßführung beim Löten komplexer Baugruppen
FAPS, 179 Seiten, 113 Bilder, 7 Tab. 1998. ISBN 3-87525-103-2.

Band 79: Elke Rauh
Methodische Einbindung der Simulation in die betrieblichen Planungs- und Entscheidungsabläufe
FAPS, 192 Seiten, 114 Bilder, 4 Tab. 1998. ISBN 3-87525-104-0.

Band 80: Sorin Niederkorn
Meßeinrichtung zur Untersuchung der Wirkflächenreibung bei umformtechnischen Prozessen
LFT, 99 Seiten, 46 Bilder, 6 Tab. 1998. ISBN 3-87525-105-9.

Band 81: Stefan Schuberth
Regelung der Fokuslage beim Schweißen mit CO_2-Hochleistungslasern unter Einsatz von adaptiven Optiken
LFT, 140 Seiten, 64 Bilder, 3 Tab. 1998. ISBN 3-87525-106-7.

Band 82: Armando Walter Colombo
Development and Implementation of Hierarchical Control Structures of Flexible Production Systems Using High Level Petri Nets
FAPS, 216 Seiten, 86 Bilder. 1998. ISBN 3-87525-109-1.

Band 83: Otto Meedt
Effizienzsteigerung bei Demontage und Recycling durch flexible Demontagetechnologien und optimierte Produktgestaltung
FAPS, 186 Seiten, 103 Bilder. 1998. ISBN 3-87525-108-3.

Band 84: Knuth Götz
Modelle und effiziente Modellbildung zur Qualitätssicherung in der Elektronikproduktion
FAPS, 212 Seiten, 129 Bilder, 24 Tab. 1998. ISBN 3-87525-112-1.

Band 85: Ralf Luchs
Einsatzmöglichkeiten leitender Klebstoffe zur zuverlässigen Kontaktierung elektronischer Bauelemente in der SMT
FAPS, 176 Seiten, 126 Bilder, 30 Tab. 1998. ISBN 3-87525-113-7.

Band 86: Frank Pöhlau
Entscheidungsgrundlagen zur Einführung räumlicher spritzgegossener Schaltungsträger (3-D MID)
FAPS, 144 Seiten, 99 Bilder. 1999. ISBN 3-87525-114-8.

Band 87: Roland T. A. Kals
Fundamentals on the miniaturization of sheet metal working processes
LFT, 128 Seiten, 58 Bilder, 11 Tab. 1999. ISBN 3-87525-115-6.

Band 88: Gerhard Luhn
Implizites Wissen und technisches Handeln am Beispiel der Elektronikproduktion
FAPS, 252 Seiten, 61 Bilder, 1 Tab. 1999. ISBN 3-87525-116-4.

Band 89: Axel Sprenger
Adaptives Streckbiegen von Aluminium-Strangpreßprofilen
LFT, 114 Seiten, 63 Bilder, 4 Tab. 1999. ISBN 3-87525-117-2.

Band 90: Hans-Jörg Pucher
Untersuchungen zur Prozeßfolge Umformen, Bestücken und Laserstrahllöten von Mikrokontakten
LFT, 158 Seiten, 69 Bilder, 9 Tab. 1999. ISBN 3-87525-119-9.

Band 91: Horst Arnet
Profilbiegen mit kinematischer Gestalterzeugung
LFT, 128 Seiten, 67 Bilder, 7 Tab. 1999. ISBN 3-87525-120-2.

Band 92: Doris Schubart
Prozeßmodellierung und Technologieentwicklung beim Abtragen mit CO_2-Laserstrahlung
LFT, 133 Seiten, 57 Bilder, 13 Tab. 1999. ISBN 3-87525-122-9.

Band 93: Adrianus L. P. Coremans
Laserstrahlsintern von Metallpulver - Prozeßmodellierung, Systemtechnik, Eigenschaften laserstrahlgesinterter Metallkörper
LFT, 184 Seiten, 108 Bilder, 12 Tab. 1999. ISBN 3-87525-124-5.

Band 94: Hans-Martin Biehler
Optimierungskonzepte für Qualitätsdatenverarbeitung und Informationsbereitstellung in der Elektronikfertigung
FAPS, 194 Seiten, 105 Bilder. 1999. ISBN 3-87525-126-1.

Band 95: Wolfgang Becker
Oberflächenausbildung und tribologische Eigenschaften excimerlaserstrahlbearbeiteter Hochleistungskeramiken
LFT, 175 Seiten, 71 Bilder, 3 Tab. 1999. ISBN 3-87525-127-X.

Band 96: Philipp Hein
Innenhochdruck-Umformen von Blechpaaren: Modellierung, Prozeßauslegung und Prozeßführung
LFT, 129 Seiten, 57 Bilder, 7 Tab. 1999. ISBN 3-87525-128-8.

Band 97: Gunter Beitinger
Herstellungs- und Prüfverfahren für thermoplastische Schaltungsträger
FAPS, 169 Seiten, 92 Bilder, 20 Tab. 1999. ISBN 3-87525-129-6.

Band 98: Jürgen Knoblach
Beitrag zur rechnerunterstützten verursachungsgerechten Angebotskalkulation von Blechteilen mit Hilfe wissensbasierter Methoden
LFT, 155 Seiten, 53 Bilder, 26 Tab. 1999. ISBN 3-87525-130-X.

Band 99: Frank Breitenbach
Bildverarbeitungssystem zur Erfassung der Anschlußgeometrie elektronischer SMT-Bauelemente
LFT, 147 Seiten, 92 Bilder, 12 Tab. 2000. ISBN 3-87525-131-8.

Band 100: Bernd Falk
Simulationsbasierte Lebensdauervorhersage für Werkzeuge der Kaltmassivumformung
LFT, 134 Seiten, 44 Bilder, 15 Tab. 2000. ISBN 3-87525-136-9.

Band 101: Wolfgang Schlögl
Integriertes Simulationsdaten-Management für Maschinenentwicklung und Anlagenplanung
FAPS, 169 Seiten, 101 Bilder, 20 Tab. 2000. ISBN 3-87525-137-7.

Band 102: Christian Hinsel
Ermüdungsbruchversagen hartstoffbeschichteter Werkzeugstähle in der Kaltmassivumformung
LFT, 130 Seiten, 80 Bilder, 14 Tab. 2000. ISBN 3-87525-138-5.

Band 103: Stefan Bobbert
Simulationsgestützte Prozessauslegung für das Innenhochdruck-Umformen von Blechpaaren
LFT, 123 Seiten, 77 Bilder. 2000. ISBN 3-87525-145-8.

Band 104: Harald Rottbauer
Modulares Planungswerkzeug zum Produktionsmanagement in der Elektronikproduktion
FAPS, 166 Seiten, 106 Bilder. 2001.
ISBN 3-87525-139-3.

Band 105: Thomas Hennige
Flexible Formgebung von Blechen durch Laserstrahlumformen
LFT, 119 Seiten, 50 Bilder. 2001.
ISBN 3-87525-140-7.

Band 106: Thomas Menzel
Wissensbasierte Methoden für die rechnergestützte Charakterisierung und Bewertung innovativer Fertigungsprozesse
LFT, 152 Seiten, 71 Bilder. 2001.
ISBN 3-87525-142-3.

Band 107: Thomas Stöckel
Kommunikationstechnische Integration der Prozeßebene in Produktionssysteme durch Middleware-Frameworks
FAPS, 147 Seiten, 65 Bilder, 5 Tab.
2001. ISBN 3-87525-143-1.

Band 108: Frank Pitter
Verfügbarkeitssteigerung von Werkzeugmaschinen durch Einsatz mechatronischer Sensorlösungen
FAPS, 158 Seiten, 131 Bilder, 8 Tab.
2001. ISBN 3-87525-144-X.

Band 109: Markus Korneli
Integration lokaler CAP-Systeme in einen globalen Fertigungsdatenverbund
FAPS, 121 Seiten, 53 Bilder, 11 Tab.
2001. ISBN 3-87525-146-6.

Band 110: Burkhard Müller
Laserstrahljustieren mit Excimer-Lasern - Prozeßparameter und Modelle zur Aktorkonstruktion
LFT, 128 Seiten, 36 Bilder, 9 Tab.
2001. ISBN 3-87525-159-8.

Band 111: Jürgen Göhringer
Integrierte Telediagnose via Internet zum effizienten Service von Produktionssystemen
FAPS, 178 Seiten, 98 Bilder, 5 Tab.
2001. ISBN 3-87525-147-4.

Band 112: Robert Feuerstein
Qualitäts- und kosteneffiziente Integration neuer Bauelementetechnologien in die Flachbaugruppenfertigung
FAPS, 161 Seiten, 99 Bilder, 10 Tab.
2001. ISBN 3-87525-151-2.

Band 113: Marcus Reichenberger
Eigenschaften und Einsatzmöglichkeiten alternativer Elektroniklote in der Oberflächenmontage (SMT)
FAPS, 165 Seiten, 97 Bilder, 18 Tab.
2001. ISBN 3-87525-152-0.

Band 114: Alexander Huber
Justieren vormontierter Systeme mit dem Nd:YAG-Laser unter Einsatz von Aktoren
LFT, 122 Seiten, 58 Bilder, 5 Tab.
2001. ISBN 3-87525-153-9.

Band 115: Sami Krimi
Analyse und Optimierung von Montagesystemen in der Elektronikproduktion
FAPS, 155 Seiten, 88 Bilder, 3 Tab.
2001. ISBN 3-87525-157-1.

Band 116: Marion Merklein
Laserstrahlumformen von Aluminiumwerkstoffen - Beeinflussung der Mikrostruktur und der mechanischen Eigenschaften
LFT, 122 Seiten, 65 Bilder, 15 Tab.
2001. ISBN 3-87525-156-3.

Band 117: Thomas Collisi
Ein informationslogistisches Architekturkonzept zur Akquisition simulationsrelevanter Daten
FAPS, 181 Seiten, 105 Bilder, 7 Tab.
2002. ISBN 3-87525-164-4.

Band 118: Markus Koch
Rationalisierung und ergonomische Optimierung im Innenausbau durch den Einsatz moderner Automatisierungstechnik
FAPS, 176 Seiten, 98 Bilder, 9 Tab.
2002. ISBN 3-87525-165-2.

Band 119: Michael Schmidt
Prozeßregelung für das Laserstrahl-Punktschweißen in der Elektronikproduktion
LFT, 152 Seiten, 71 Bilder, 3 Tab.
2002. ISBN 3-87525-166-0.

Band 120: Nicolas Tiesler
Grundlegende Untersuchungen zum Fließpressen metallischer Kleinstteile
LFT, 126 Seiten, 78 Bilder, 12 Tab.
2002. ISBN 3-87525-175-X.

Band 121: Lars Pursche
Methoden zur technologieorientierten Programmierung für die 3D-Lasermikrobearbeitung
LFT, 111 Seiten, 39 Bilder, 0 Tab.
2002. ISBN 3-87525-183-0.

Band 122: Jan-Oliver Brassel
Prozeßkontrolle beim Laserstrahl-Mikroschweißen
LFT, 148 Seiten, 72 Bilder, 12 Tab.
2002. ISBN 3-87525-181-4.

Band 123: Mark Geisel
Prozeßkontrolle und -steuerung beim Laserstrahlschweißen mit den Methoden der nichtlinearen Dynamik
LFT, 135 Seiten, 46 Bilder, 2 Tab.
2002. ISBN 3-87525-180-6.

Band 124: Gerd Eßer
Laserstrahlunterstützte Erzeugung metallischer Leiterstrukturen auf Thermoplastsubstraten für die MID-Technik
LFT, 148 Seiten, 60 Bilder, 6 Tab.
2002. ISBN 3-87525-171-7.

Band 125: Marc Fleckenstein
Qualität laserstrahl-gefügter Mikroverbindungen elektronischer Kontakte
LFT, 159 Seiten, 77 Bilder, 7 Tab.
2002. ISBN 3-87525-170-9.

Band 126: Stefan Kaufmann
Grundlegende Untersuchungen zum Nd:YAG- Laserstrahlfügen von Silizium für Komponenten der Optoelektronik
LFT, 159 Seiten, 100 Bilder, 6 Tab.
2002. ISBN 3-87525-172-5.

Band 127: Thomas Fröhlich
Simultanes Löten von Anschlußkontakten elektronischer Bauelemente mit Diodenlaserstrahlung
LFT, 143 Seiten, 75 Bilder, 6 Tab.
2002. ISBN 3-87525-186-5.

Band 128: Achim Hofmann
Erweiterung der Formgebungsgrenzen beim Umformen von Aluminiumwerkstoffen durch den Einsatz prozessangepasster Platinen
LFT, 113 Seiten, 58 Bilder, 4 Tab. 2002. ISBN 3-87525-182-2.

Band 129: Ingo Kriebitzsch
3 - D MID Technologie in der Automobilelektronik
FAPS, 129 Seiten, 102 Bilder, 10 Tab. 2002. ISBN 3-87525-169-5.

Band 130: Thomas Pohl
Fertigungsqualität und Umformbarkeit laserstrahlgeschweißter Formplatinen aus Aluminiumlegierungen
LFT, 133 Seiten, 93 Bilder, 12 Tab. 2002. ISBN 3-87525-173-3.

Band 131: Matthias Wenk
Entwicklung eines konfigurierbaren Steuerungssystems für die flexible Sensorführung von Industrierobotern
FAPS, 167 Seiten, 85 Bilder, 1 Tab. 2002. ISBN 3-87525-174-1.

Band 132: Matthias Negendanck
Neue Sensorik und Aktorik für Bearbeitungsköpfe zum Laserstrahlschweißen
LFT, 116 Seiten, 60 Bilder, 14 Tab. 2002. ISBN 3-87525-184-9.

Band 133: Oliver Kreis
Integrierte Fertigung - Verfahrensintegration durch Innenhochdruck-Umformen, Trennen und Laserstrahlschweißen in einem Werkzeug sowie ihre tele- und multimediale Präsentation
LFT, 167 Seiten, 90 Bilder, 43 Tab. 2002. ISBN 3-87525-176-8.

Band 134: Stefan Trautner
Technische Umsetzung produktbezogener Instrumente der Umweltpolitik bei Elektro- und Elektronikgeräten
FAPS, 179 Seiten, 92 Bilder, 11 Tab. 2002. ISBN 3-87525-177-6.

Band 135: Roland Meier
Strategien für einen produktorientierten Einsatz räumlicher spritzgegossener Schaltungsträger (3-D MID)
FAPS, 155 Seiten, 88 Bilder, 14 Tab. 2002. ISBN 3-87525-178-4.

Band 136: Jürgen Wunderlich
Kostensimulation - Simulationsbasierte Wirtschaftlichkeitsregelung komplexer Produktionssysteme
FAPS, 202 Seiten, 119 Bilder, 17 Tab. 2002. ISBN 3-87525-179-2.

Band 137: Stefan Novotny
Innenhochdruck-Umformen von Blechen aus Aluminium- und Magnesiumlegierungen bei erhöhter Temperatur
LFT, 132 Seiten, 82 Bilder, 6 Tab. 2002. ISBN 3-87525-185-7.

Band 138: Andreas Licha
Flexible Montageautomatisierung zur Komplettmontage flächenhafter Produktstrukturen durch kooperierende Industrieroboter
FAPS, 158 Seiten, 87 Bilder, 8 Tab. 2003. ISBN 3-87525-189-X.

Band 139: Michael Eisenbarth
Beitrag zur Optimierung der Aufbau- und Verbindungstechnik für mechatronische Baugruppen
FAPS, 207 Seiten, 141 Bilder, 9 Tab. 2003. ISBN 3-87525-190-3.

Band 140: Frank Christoph
Durchgängige simulationsgestützte Planung von Fertigungseinrichtungen der Elektronikproduktion
FAPS, 187 Seiten, 107 Bilder, 9 Tab. 2003. ISBN 3-87525-191-1.

Band 141: Hinnerk Hagenah
Simulationsbasierte Bestimmung der zu erwartenden Maßhaltigkeit für das Blechbiegen
LFT, 131 Seiten, 36 Bilder, 26 Tab. 2003. ISBN 3-87525-192-X.

Band 142: Ralf Eckstein
Scherschneiden und Biegen metallischer Kleinstteile - Materialeinfluss und Materialverhalten
LFT, 148 Seiten, 71 Bilder, 19 Tab. 2003. ISBN 3-87525-193-8.

Band 143: Frank H. Meyer-Pittroff
Excimerlaserstrahlbiegen dünner metallischer Folien mit homogener Lichtlinie
LFT, 138 Seiten, 60 Bilder, 16 Tab. 2003. ISBN 3-87525-196-2.

Band 144: Andreas Kach
Rechnergestützte Anpassung von Laserstrahlschneidbahnen an Bauteilabweichungen
LFT, 139 Seiten, 69 Bilder, 11 Tab. 2004. ISBN 3-87525-197-0.

Band 145: Stefan Hierl
System- und Prozeßtechnik für das simultane Löten mit Diodenlaserstrahlung von elektronischen Bauelementen
LFT, 124 Seiten, 66 Bilder, 4 Tab. 2004. ISBN 3-87525-198-9.

Band 146: Thomas Neudecker
Tribologische Eigenschaften keramischer Blechumformwerkzeuge-Einfluss einer Oberflächenendbearbeitung mittels Excimerlaserstrahlung
LFT, 166 Seiten, 75 Bilder, 26 Tab. 2004. ISBN 3-87525-200-4.

Band 147: Ulrich Wenger
Prozessoptimierung in der Wickeltechnik durch innovative maschinenbauliche und regelungstechnische Ansätze
FAPS, 132 Seiten, 88 Bilder, 0 Tab. 2004. ISBN 3-87525-203-9.

Band 148: Stefan Slama
Effizienzsteigerung in der Montage durch marktorientierte Montagestrukturen und erweiterte Mitarbeiterkompetenz
FAPS, 188 Seiten, 125 Bilder, 0 Tab. 2004. ISBN 3-87525-204-7.

Band 149: Thomas Wurm
Laserstrahljustieren mittels Aktoren-Entwicklung von Konzepten und Methoden für die rechnerunterstützte Modellierung und Optimierung von komplexen Aktorsystemen in der Mikrotechnik
LFT, 122 Seiten, 51 Bilder, 9 Tab. 2004. ISBN 3-87525-206-3.

Band 150: Martino Celeghini
Wirkmedienbasierte Blechumformung: Grundlagenuntersuchungen zum Einfluss von Werkstoff und Bauteilgeometrie
LFT, 146 Seiten, 77 Bilder, 6 Tab.
2004. ISBN 3-87525-207-1.

Band 151: Ralph Hohenstein
Entwurf hochdynamischer Sensor- und Regelsysteme für die adaptiveLaserbearbeitung
LFT, 282 Seiten, 63 Bilder, 16 Tab.
2004. ISBN 3-87525-210-1.

Band 152: Angelika Hutterer
Entwicklung prozessüberwachender Regelkreise für flexible Formgebungsprozesse
LFT, 149 Seiten, 57 Bilder, 2 Tab.
2005. ISBN 3-87525-212-8.

Band 153: Emil Egerer
Massivumformen metallischer Kleinstteile bei erhöhter Prozesstemperatur
LFT, 158 Seiten, 87 Bilder, 10 Tab.
2005. ISBN 3-87525-213-6.

Band 154: Rüdiger Holzmann
Strategien zur nachhaltigen Optimierung von Qualität und Zuverlässigkeit in der Fertigung hochintegrierter Flachbaugruppen
FAPS, 186 Seiten, 99 Bilder, 19 Tab.
2005. ISBN 3-87525-217-9.

Band 155: Marco Nock
Biegeumformen mit Elastomerwerkzeugen Modellierung, Prozessauslegung und Abgrenzung des Verfahrens am Beispiel des Rohrbiegens
LFT, 164 Seiten, 85 Bilder, 13 Tab.
2005. ISBN 3-87525-218-7.

Band 156: Frank Niebling
Qualifizierung einer Prozesskette zum Laserstrahlsintern metallischer Bauteile
LFT, 148 Seiten, 89 Bilder, 3 Tab.
2005. ISBN 3-87525-219-5.

Band 157: Markus Meiler
Großserientauglichkeit trockenschmierstoffbeschichteter Aluminiumbleche im Presswerk Grundlegende Untersuchungen zur Tribologie, zum Umformverhalten und Bauteilversuche
LFT, 104 Seiten, 57 Bilder, 21 Tab.
2005. ISBN 3-87525-221-7.

Band 158: Agus Sutanto
Solution Approaches for Planning of Assembly Systems in Three-Dimensional Virtual Environments
FAPS, 169 Seiten, 98 Bilder, 3 Tab.
2005. ISBN 3-87525-220-9.

Band 159: Matthias Boiger
Hochleistungssysteme für die Fertigung elektronischer Baugruppen auf der Basis flexibler Schaltungsträger
FAPS, 175 Seiten, 111 Bilder, 8 Tab.
2005. ISBN 3-87525-222-5.

Band 160: Matthias Pitz
Laserunterstütztes Biegen höchstfester Mehrphasenstähle
LFT, 120 Seiten, 73 Bilder, 11 Tab.
2005. ISBN 3-87525-223-3.

Band 161: Meik Vahl
Beitrag zur gezielten Beeinflussung des Werkstoffflusses beim Innenhochdruck-Umformen von Blechen
LFT, 165 Seiten, 94 Bilder, 15 Tab.
2005. ISBN 3-87525-224-1.

Band 162: Peter K. Kraus
Plattformstrategien - Realisierung einer varianz- und kostenoptimierten Wertschöpfung
FAPS, 181 Seiten, 95 Bilder, 0 Tab.
2005. ISBN 3-87525-226-8.

Band 163: Adrienn Cser
Laserstrahlschmelzabtrag - Prozessanalyse und -modellierung
LFT, 146 Seiten, 79 Bilder, 3 Tab.
2005. ISBN 3-87525-227-6.

Band 164: Markus C. Hahn
Grundlegende Untersuchungen zur Herstellung von Leichtbauverbundstrukturen mit Aluminiumschaumkern
LFT, 143 Seiten, 60 Bilder, 16 Tab.
2005. ISBN 3-87525-228-4.

Band 165: Gordana Michos
Mechatronische Ansätze zur Optimierung von Vorschubachsen
FAPS, 146 Seiten, 87 Bilder, 17 Tab.
2005. ISBN 3-87525-230-6.

Band 166: Markus Stark
Auslegung und Fertigung hochpräziser Faser-Kollimator-Arrays
LFT, 158 Seiten, 115 Bilder, 11 Tab.
2005. ISBN 3-87525-231-4.

Band 167: Yurong Zhou
Kollaboratives Engineering Management in der integrierten virtuellen Entwicklung der Anlagen für die Elektronikproduktion
FAPS, 156 Seiten, 84 Bilder, 6 Tab.
2005. ISBN 3-87525-232-2.

Band 168: Werner Enser
Neue Formen permanenter und lösbarer elektrischer Kontaktierungen für mechatronische Baugruppen
FAPS, 190 Seiten, 112 Bilder, 5 Tab.
2005. ISBN 3-87525-233-0.

Band 169: Katrin Melzer
Integrierte Produktpolitik bei elektrischen und elektronischen Geräten zur Optimierung des Product-Life-Cycle
FAPS, 155 Seiten, 91 Bilder, 17 Tab.
2005. ISBN 3-87525-234-9.

Band 170: Alexander Putz
Grundlegende Untersuchungen zur Erfassung der realen Vorspannung von armierten Kaltfließpresswerkzeugen mittels Ultraschall
LFT, 137 Seiten, 71 Bilder, 15 Tab.
2006. ISBN 3-87525-237-3.

Band 171: Martin Prechtl
Automatisiertes Schichtverfahren für metallische Folien - System- und Prozesstechnik
LFT, 154 Seiten, 45 Bilder, 7 Tab.
2006. ISBN 3-87525-238-1.

Band 172: Markus Meidert
Beitrag zur deterministischen Lebensdauerabschätzung von Werkzeugen der Kaltmassivumformung
LFT, 131 Seiten, 78 Bilder, 9 Tab.
2006. ISBN 3-87525-239-X.

Band 173: Bernd Müller
Robuste, automatisierte Montagesysteme durch adaptive Prozessführung und montageübergreifende Fehlerprävention am Beispiel flächiger Leichtbauteile
FAPS, 147 Seiten, 77 Bilder, 0 Tab.
2006. ISBN 3-87525-240-3.

Band 174: Alexander Hofmann
Hybrides Laserdurchstrahlschweißen von Kunststoffen
LFT, 136 Seiten, 72 Bilder, 4 Tab.
2006. ISBN 978-3-87525-243-9.

Band 175: Peter Wölflick
Innovative Substrate und Prozesse mit feinsten Strukturen für bleifreie Mechatronik-Anwendungen
FAPS, 177 Seiten, 148 Bilder, 24 Tab. 2006.
ISBN 978-3-87525-246-0.

Band 176: Attila Komlodi
Detection and Prevention of Hot Cracks during Laser Welding of Aluminium Alloys Using Advanced Simulation Methods
LFT, 155 Seiten, 89 Bilder, 14 Tab. 2006. ISBN 978-3-87525-248-4.

Band 177: Uwe Popp
Grundlegende Untersuchungen zum Laserstrahlstrukturieren von Kaltmassivumformwerkzeugen
LFT, 140 Seiten, 67 Bilder, 16 Tab. 2006. ISBN 978-3-87525-249-1.

Band 178: Veit Rückel
Rechnergestützte Ablaufplanung und Bahngenerierung Für kooperierende Industrieroboter
FAPS, 148 Seiten, 75 Bilder, 7 Tab. 2006. ISBN 978-3-87525-250-7.

Band 179: Manfred Dirscherl
Nicht-thermische Mikrojustiertechnik mittels ultrakurzer Laserpulse
LFT, 154 Seiten, 69 Bilder, 10 Tab. 2007. ISBN 978-3-87525-251-4.

Band 180: Yong Zhuo
Entwurf eines rechnergestützten integrierten Systems für Konstruktion und Fertigungsplanung räumlicher spritzgegossener Schaltungsträger (3D-MID)
FAPS, 181 Seiten, 95 Bilder, 5 Tab. 2007. ISBN 978-3-87525-253-8.

Band 181: Stefan Lang
Durchgängige Mitarbeiterinformation zur Steigerung von Effizienz und Prozesssicherheit in der Produktion
FAPS, 172 Seiten, 93 Bilder. 2007. ISBN 978-3-87525-257-6.

Band 182: Hans-Joachim Krauß
Laserstrahlinduzierte Pyrolyse präkeramischer Polymere
LFT, 171 Seiten, 100 Bilder. 2007. ISBN 978-3-87525-258-3.

Band 183: Stefan Junker
Technologien und Systemlösungen für die flexibel automatisierte Bestückung permanent erregter Läufer mit oberflächenmontierten Dauermagneten
FAPS, 173 Seiten, 75 Bilder. 2007. ISBN 978-3-87525-259-0.

Band 184: Rainer Kohlbauer
Wissensbasierte Methoden für die simulationsgestützte Auslegung wirkmedienbasierter Blechumformprozesse
LFT, 135 Seiten, 50 Bilder. 2007. ISBN 978-3-87525-260-6.

Band 185: Klaus Lamprecht
Wirkmedienbasierte Umformung tiefgezogener Vorformen unter besonderer Berücksichtigung maßgeschneiderter Halbzeuge
LFT, 137 Seiten, 81 Bilder. 2007. ISBN 978-3-87525-265-1.

Band 186: Bernd Zolleiß
Optimierte Prozesse und Systeme für die Bestückung mechatronischerBaugruppen
FAPS, 180 Seiten, 117 Bilder. 2007. ISBN 978-3-87525-266-8.

Band 187: Michael Kerausch
Simulationsgestützte Prozessauslegung für das Umformen lokal wärmebehandelter Aluminiumplatinen
LFT, 146 Seiten, 76 Bilder, 7 Tab. 2007. ISBN 978-3-87525-267-5.

Band 188: Matthias Weber
Unterstützung der Wandlungsfähigkeit von Produktionsanlagen durch innovative Softwaresysteme
FAPS, 183 Seiten, 122 Bilder, 3 Tab. 2007. ISBN 978-3-87525-269-9.

Band 189: Thomas Frick
Untersuchung der prozessbestimmenden Strahl-Stoff-Wechselwirkungen beim Laserstrahlschweißen von Kunststoffen
LFT, 104 Seiten, 62 Bilder, 8 Tab. 2007. ISBN 978-3-87525-268-2.

Band 190: Joachim Hecht
Werkstoffcharakterisierung und Prozessauslegung für die wirkmedienbasierte Doppelblech-Umformung von Magnesiumlegierungen
LFT, 107 Seiten, 91 Bilder, 2 Tab. 2007. ISBN 978-3-87525-270-5.

Band 191: Ralf Völkl
Stochastische Simulation zur Werkzeuglebensdaueroptimierung und Präzisionsfertigung in der Kaltmassivumformung
LFT, 178 Seiten, 75 Bilder, 12 Tab. 2008. ISBN 978-3-87525-272-9.

Band 192: Massimo Tolazzi
Innenhochdruck-Umformen verstärkter Blech-Rahmenstrukturen
LFT, 164 Seiten, 85 Bilder, 7 Tab. 2008. ISBN 978-3-87525-273-6.

Band 193: Cornelia Hoff
Untersuchung der Prozesseinflussgrößen beim Presshärten des höchstfesten Vergütungsstahls 22MnB5
LFT, 133 Seiten, 92 Bilder, 5 Tab. 2008. ISBN 978-3-87525-275-0.

Band 194: Christian Alvarez
Simulationsgestützte Methoden zur effizienten Gestaltung von Lötprozessen in der Elektronikproduktion
FAPS, 149 Seiten, 86 Bilder, 8 Tab. 2008. ISBN 978-3-87525-277-4.

Band 195: Andreas Kunze
Automatisierte Montage von makromechatronischen Modulen zur flexiblen Integration in hybride Pkw-Bordnetzsysteme
FAPS, 160 Seiten, 90 Bilder, 14 Tab. 2008.
ISBN 978-3-87525-278-1.

Band 196: Wolfgang Hußnätter
Grundlegende Untersuchungen zur experimentellen Ermittlung und zur Modellierung von Fließortkurven bei erhöhten Temperaturen
LFT, 152 Seiten, 73 Bilder, 21 Tab. 2008. ISBN 978-3-87525-279-8.

Band 197: Thomas Bigl
Entwicklung, angepasste Herstellungsverfahren und erweiterte Qualitätssicherung von einsatzgerechten elektronischen Baugruppen
FAPS, 175 Seiten, 107 Bilder, 14 Tab. 2008.
ISBN 978-3-87525-280-4.

Band 198: Stephan Roth
Grundlegende Untersuchungen zum Excimerlaserstrahl-Abtragen unter Flüssigkeitsfilmen
LFT, 113 Seiten, 47 Bilder, 14 Tab. 2008. ISBN 978-3-87525-281-1.

Band 199: Artur Giera
Prozesstechnische Untersuchungen zum Rührreibschweißen metallischer Werkstoffe
LFT, 179 Seiten, 104 Bilder, 36 Tab. 2008. ISBN 978-3-87525-282-8.

Band 200: Jürgen Lechler
Beschreibung und Modellierung des Werkstoffverhaltens von presshärtbaren Bor-Manganstählen
LFT, 154 Seiten, 75 Bilder, 12 Tab. 2009. ISBN 978-3-87525-286-6.

Band 201: Andreas Blankl
Untersuchungen zur Erhöhung der Prozessrobustheit bei der Innenhochdruck-Umformung von flächigen Halbzeugen mit vor- bzw. nachgeschalteten Laserstrahlfügeoperationen
LFT, 120 Seiten, 68 Bilder, 9 Tab. 2009. ISBN 978-3-87525-287-3.

Band 202: Andreas Schaller
Modellierung eines nachfrageorientierten Produktionskonzeptes für mobile Telekommunikationsgeräte
FAPS, 120 Seiten, 79 Bilder, 0 Tab. 2009. ISBN 978-3-87525-289-7.

Band 203: Claudius Schimpf
Optimierung von Zuverlässigkeitsuntersuchungen, Prüfabläufen und Nacharbeitsprozessen in der Elektronikproduktion
FAPS, 162 Seiten, 90 Bilder, 14 Tab. 2009.
ISBN 978-3-87525-290-3.

Band 204: Simon Dietrich
Sensoriken zur Schwerpunktslagebestimmung der optischen Prozessemissionen beim Laserstrahltiefschweißen
LFT, 138 Seiten, 70 Bilder, 5 Tab. 2009. ISBN 978-3-87525-292-7.

Band 205: Wolfgang Wolf
Entwicklung eines agentenbasierten Steuerungssystems zur Materialflussorganisation im wandelbaren Produktionsumfeld
FAPS, 167 Seiten, 98 Bilder. 2009. ISBN 978-3-87525-293-4.

Band 206: Steffen Polster
Laserdurchstrahlschweißen transparenter Polymerbauteile
LFT, 160 Seiten, 92 Bilder, 13 Tab. 2009. ISBN 978-3-87525-294-1.

Band 207: Stephan Manuel Dörfler
Rührreibschweißen von walzplattiertem Halbzeug und Aluminiumblech zur Herstellung flächiger Aluminiumschaum-Sandwich-Verbundstrukturen
LFT, 190 Seiten, 98 Bilder, 5 Tab. 2009. ISBN 978-3-87525-295-8.

Band 208: Uwe Vogt
Seriennahe Auslegung von Aluminium Tailored Heat Treated Blanks
LFT, 151 Seiten, 68 Bilder, 26 Tab. 2009. ISBN 978-3-87525-296-5.

Band 209: Till Laumann
Qualitative und quantitative Bewertung der Crashtauglichkeit von höchstfesten Stählen
LFT, 117 Seiten, 69 Bilder, 7 Tab. 2009. ISBN 978-3-87525-299-6.

Band 210: Alexander Diehl
Größeneffekte bei Biegeprozessen-Entwicklung einer Methodik zur Identifikation und Quantifizierung
LFT, 180 Seiten, 92 Bilder, 12 Tab. 2010. ISBN 978-3-87525-302-3.

Band 211: Detlev Staud
Effiziente Prozesskettenauslegung für das Umformen lokal wärmebehandelter und geschweißter Aluminiumbleche
LFT, 164 Seiten, 72 Bilder, 12 Tab. 2010. ISBN 978-3-87525-303-0.

Band 212: Jens Ackermann
Prozesssicherung beim Laserdurchstrahlschweißen thermoplastischer Kunststoffe
LPT, 129 Seiten, 74 Bilder, 13 Tab. 2010. ISBN 978-3-87525-305-4.

Band 213: Stephan Weidel
Grundlegende Untersuchungen zum Kontaktzustand zwischen Werkstück und Werkzeug bei umformtechnischen Prozessen unter tribologischen Gesichtspunkten
LFT, 144 Seiten, 67 Bilder, 11 Tab. 2010. ISBN 978-3-87525-307-8.

Band 214: Stefan Geißdörfer
Entwicklung eines mesoskopischen Modells zur Abbildung von Größeneffekten in der Kaltmassivumformung mit Methoden der FE-Simulation
LFT, 133 Seiten, 83 Bilder, 11 Tab. 2010. ISBN 978-3-87525-308-5.

Band 215: Christian Matzner
Konzeption produktspezifischer Lösungen zur Robustheitssteigerung elektronischer Systeme gegen die Einwirkung von Betauung im Automobil
FAPS, 165 Seiten, 93 Bilder, 14 Tab. 2010. ISBN 978-3-87525-309-2.

Band 216: Florian Schüßler
Verbindungs- und Systemtechnik für thermisch hochbeanspruchte und miniaturisierte elektronische Baugruppen
FAPS, 184 Seiten, 93 Bilder, 18 Tab. 2010.
ISBN 978-3-87525-310-8.

Band 217: Massimo Cojutti
Strategien zur Erweiterung der Prozessgrenzen bei der Innhochdruck-Umformung von Rohren und Blechpaaren
LFT, 125 Seiten, 56 Bilder, 9 Tab. 2010. ISBN 978-3-87525-312-2.

Band 218: Raoul Plettke
Mehrkriterielle Optimierung komplexer Aktorsysteme für das Laserstrahljustieren
LFT, 152 Seiten, 25 Bilder, 3 Tab. 2010. ISBN 978-3-87525-315-3.

Band 219: Andreas Dobroschke
Flexible Automatisierungslösungen für die Fertigung wickeltechnischer Produkte
FAPS, 184 Seiten, 109 Bilder, 18 Tab. 2011.
ISBN 978-3-87525-317-7.

Band 220: Azhar Zam
Optical Tissue Differentiation for Sensor-Controlled Tissue-Specific Laser Surgery
LPT, 99 Seiten, 45 Bilder, 8 Tab. 2011. ISBN 978-3-87525-318-4.

Band 221: Michael Rösch
Potenziale und Strategien zur Optimierung des Schablonendruckprozesses in der Elektronikproduktion
FAPS, 192 Seiten, 127 Bilder, 19 Tab. 2011.
ISBN 978-3-87525-319-1.

Band 222: Thomas Rechtenwald
Quasi-isothermes Laserstrahlsintern von Hochtemperatur-Thermoplasten - Eine Betrachtung werkstoff-prozessspezifischer Aspekte am Beispiel PEEK
LPT, 150 Seiten, 62 Bilder, 8 Tab. 2011. ISBN 978-3-87525-320-7.

Band 223: Daniel Craiovan
Prozesse und Systemlösungen für die SMT-Montage optischer Bauelemente auf Substrate mit integrierten Lichtwellenleitern
FAPS, 165 Seiten, 85 Bilder, 8 Tab. 2011. ISBN 978-3-87525-324-5.

Band 224: Kay Wagner
Beanspruchungsangepasste Kaltmassivumformwerkzeuge durch lokal optimierte Werkzeugoberflächen
LFT, 147 Seiten, 103 Bilder, 17 Tab. 2011. ISBN 978-3-87525-325-2.

Band 225: Martin Brandhuber
Verbesserung der Prognosegüte des Versagens von Punktschweißverbindungen bei höchstfesten Stahlgüten
LFT, 155 Seiten, 91 Bilder, 19 Tab. 2011. ISBN 978-3-87525-327-6.

Band 226: Peter Sebastian Feuser
Ein Ansatz zur Herstellung von pressgehärteten Karosseriekomponenten mit maßgeschneiderten mechanischen Eigenschaften: Temperierte Umformwerkzeuge. Prozessfenster, Prozesssimuation und funktionale Untersuchung
LFT, 195 Seiten, 97 Bilder, 60 Tab. 2012. ISBN 978-3-87525-328-3.

Band 227: Murat Arbak
Material Adapted Design of Cold Forging Tools Exemplified by Powder Metallurgical Tool Steels and Ceramics
LFT, 109 Seiten, 56 Bilder, 8 Tab. 2012. ISBN 978-3-87525-330-6.

Band 228: Indra Pitz
Beschleunigte Simulation des Laserstrahlumformens von Aluminiumblechen
LPT, 137 Seiten, 45 Bilder, 27 Tab. 2012. ISBN 978-3-87525-333-7.

Band 229: Alexander Grimm
Prozessanalyse und -überwachung des Laserstrahlhartlötens mittels optischer Sensorik
LPT, 125 Seiten, 61 Bilder, 5 Tab. 2012. ISBN 978-3-87525-334-4.

Band 230: Markus Kaupper
Biegen von höhenfesten Stahlblechwerkstoffen - Umformverhalten und Grenzen der Biegbarkeit
LFT, 160 Seiten, 57 Bilder, 10 Tab. 2012. ISBN 978-3-87525-339-9.

Band 231: Thomas Kroiß
Modellbasierte Prozessauslegung für die Kaltmassivumformung unter Brücksichtigung der Werkzeug- und Pressenauffederung
LFT, 169 Seiten, 50 Bilder, 19 Tab. 2012. ISBN 978-3-87525-341-2.

Band 232: Christian Goth
Analyse und Optimierung der Entwicklung und Zuverlässigkeit räumlicher Schaltungsträger (3D-MID)
FAPS, 176 Seiten, 102 Bilder, 22 Tab. 2012.
ISBN 978-3-87525-340-5.

Band 233: Christian Ziegler
Ganzheitliche Automatisierung mechatronischer Systeme in der Medizin am Beispiel Strahlentherapie
FAPS, 170 Seiten, 71 Bilder, 19 Tab. 2012. ISBN 978-3-87525-342-9.

Band 234: Florian Albert
Automatisiertes Laserstrahllöten und -reparaturlöten elektronischer Baugruppen
LPT, 127 Seiten, 78 Bilder, 11 Tab. 2012. ISBN 978-3-87525-344-3.

Band 235: Thomas Stöhr
Analyse und Beschreibung des mechanischen Werkstoffverhaltens von presshärtbaren Bor-Manganstählen
LFT, 118 Seiten, 74 Bilder, 18 Tab. 2013. ISBN 978-3-87525-346-7.

Band 236: Christian Kägeler
Prozessdynamik beim Laserstrahlschweißen verzinkter Stahlbleche im Überlappstoß
LPT, 145 Seiten, 80 Bilder, 3 Tab. 2013. ISBN 978-3-87525-347-4.

Band 237: Andreas Sulzberger
Seriennahe Auslegung der Prozesskette zur wärmeunterstützten Umformung von Aluminiumblechwerkstoffen
LFT, 153 Seiten, 87 Bilder, 17 Tab. 2013. ISBN 978-3-87525-349-8.

Band 238: Simon Opel
Herstellung prozessangepasster Halbzeuge mit variabler Blechdicke durch die Anwendung von Verfahren der Blechmassivumformung
LFT, 165 Seiten, 108 Bilder, 27 Tab. 2013. ISBN 978-3-87525-350-4.

Band 239: Rajesh Kanawade
In-vivo Monitoring of Epithelium Vessel and Capillary Density for the Application of Detection of Clinical Shock and Early Signs of Cancer Development
LPT, 124 Seiten, 58 Bilder, 15 Tab. 2013. ISBN 978-3-87525-351-1.

Band 240: Stephan Busse
Entwicklung und Qualifizierung eines Schneidclinchverfahrens
LFT, 119 Seiten, 86 Bilder, 20 Tab. 2013. ISBN 978-3-87525-352-8.

Band 241: Karl-Heinz Leitz
Mikro- und Nanostrukturierung mit kurz und ultrakurz gepulster Laserstrahlung
LPT, 154 Seiten, 71 Bilder, 9 Tab. 2013. ISBN 978-3-87525-355-9.

Band 242: Markus Michl
Webbasierte Ansätze zur ganzheitlichen technischen Diagnose
FAPS, 182 Seiten, 62 Bilder, 20 Tab. 2013.
ISBN 978-3-87525-356-6.

Band 243: Vera Sturm
Einfluss von Chargenschwankungen auf die Verarbeitungsgrenzen von Stahlwerkstoffen
LFT, 113 Seiten, 58 Bilder, 9 Tab. 2013. ISBN 978-3-87525-357-3.

Band 244: Christian Neudel
Mikrostrukturelle und mechanisch-technologische Eigenschaften widerstandspunktgeschweißter Aluminium-Stahl-Verbindungen für den Fahrzeugbau
LFT, 178 Seiten, 171 Bilder, 31 Tab. 2014. ISBN 978-3-87525-358-0.

Band 245: Anja Neumann
Konzept zur Beherrschung der Prozessschwankungen im Presswerk
LFT, 162 Seiten, 68 Bilder, 15 Tab. 2014. ISBN 978-3-87525-360-3.

Band 246: Ulf-Hermann Quentin
Laserbasierte Nanostrukturierung mit optisch positionierten Mikrolinsen
LPT, 137 Seiten, 89 Bilder, 6 Tab. 2014. ISBN 978-3-87525-361-0.

Band 247: Erik Lamprecht
Der Einfluss der Fertigungsverfahren auf die Wirbelstromverluste von Stator-Einzelzahnblechpaketen für den Einsatz in Hybrid- und Elektrofahrzeugen
FAPS, 148 Seiten, 138 Bilder, 4 Tab. 2014. ISBN 978-3-87525-362-7.

Band 248: Sebastian Rösel
Wirkmedienbasierte Umformung von Blechhalbzeugen unter Anwendung magnetorheologischer Flüssigkeiten als kombiniertes Wirk- und Dichtmedium
LFT, 148 Seiten, 61 Bilder, 12 Tab. 2014. ISBN 978-3-87525-363-4.

Band 249: Paul Hippchen
Simulative Prognose der Geometrie indirekt pressgehärteter Karosseriebauteile für die industrielle Anwendung
LFT, 163 Seiten, 89 Bilder, 12 Tab. 2014. ISBN 978-3-87525-364-1.

Band 250: Martin Zubeil
Versagensprognose bei der Prozesssimulation von Biegeumform- und Falzverfahren
LFT, 171 Seiten, 90 Bilder, 5 Tab. 2014. ISBN 978-3-87525-365-8.

Band 251: Alexander Kühl
Flexible Automatisierung der Statorenmontage mit Hilfe einer universellen ambidexteren Kinematik
FAPS, 142 Seiten, 60 Bilder, 26 Tab. 2014.
ISBN 978-3-87525-367-2.

Band 252: Thomas Albrecht
Optimierte Fertigungstechnologien für Rotoren getriebeintegrierter PM-Synchronmotoren von Hybridfahrzeugen
FAPS, 198 Seiten, 130 Bilder, 38 Tab. 2014.
ISBN 978-3-87525-368-9.

Band 253: Florian Risch
Planning and Production Concepts for Contactless Power Transfer Systems for Electric Vehicles
FAPS, 185 Seiten, 125 Bilder, 13 Tab. 2014.
ISBN 978-3-87525-369-6.

Band 254: Markus Weigl
Laserstrahlschweißen von Mischverbindungen aus austenitischen und ferritischen korrosionsbeständigen Stahlwerkstoffen
LPT, 184 Seiten, 110 Bilder, 6 Tab. 2014. ISBN 978-3-87525-370-2.

Band 255: Johannes Noneder
Beanspruchungserfassung für die Validierung von FE-Modellen zur Auslegung von Massivumformwerkzeugen
LFT, 161 Seiten, 65 Bilder, 14 Tab. 2014. ISBN 978-3-87525-371-9.

Band 256: Andreas Reinhardt
Ressourceneffiziente Prozess- und Produktionstechnologie für flexible Schaltungsträger
FAPS, 123 Seiten, 69 Bilder, 19 Tab. 2014. ISBN 978-3-87525-373-3.

Band 257: Tobias Schmuck
Ein Beitrag zur effizienten Gestaltung globaler Produktions- und Logistiknetzwerke mittels Simulation
FAPS, 151 Seiten, 74 Bilder. 2014.
ISBN 978-3-87525-374-0.

Band 258: Bernd Eichenhüller
Untersuchungen der Effekte und Wechselwirkungen charakteristischer Einflussgrößen auf das Umformverhalten bei Mikroumformprozessen
LFT, 127 Seiten, 29 Bilder, 9 Tab. 2014. ISBN 978-3-87525-375-7.

Band 259: Felix Lütteke
Vielseitiges autonomes Transportsystem basierend auf Weltmodellerstellung mittels Datenfusion von Deckenkameras und Fahrzeugsensoren
FAPS, 152 Seiten, 54 Bilder, 20 Tab. 2014.
ISBN 978-3-87525-376-4.

Band 260: Martin Grüner
Hochdruck-Blechumformung mit formlos festen Stoffen als Wirkmedium
LFT, 144 Seiten, 66 Bilder, 29 Tab. 2014. ISBN 978-3-87525-379-5.

Band 261: Christian Brock
Analyse und Regelung des Laserstrahltiefschweißprozesses durch Detektion der Metalldampffackelposition
LPT, 126 Seiten, 65 Bilder, 3 Tab. 2015. ISBN 978-3-87525-380-1.

Band 262: Peter Vatter
Sensitivitätsanalyse des 3-Rollen-Schubbiegens auf Basis der Finite Elemente Methode
LFT, 145 Seiten, 57 Bilder, 26 Tab. 2015. ISBN 978-3-87525-381-8.

Band 263: Florian Klämpfl
Planung von Laserbestrahlungen durch simulationsbasierte Optimierung
LPT, 169 Seiten, 78 Bilder, 32 Tab. 2015. ISBN 978-3-87525-384-9.

Band 264: Matthias Domke
Transiente physikalische Mechanismen bei der Laserablation von dünnen Metallschichten
LPT, 133 Seiten, 43 Bilder, 3 Tab.
2015. ISBN 978-3-87525-385-6.

Band 265: Johannes Götz
Community-basierte Optimierung des Anlagenengineerings
FAPS, 177 Seiten, 80 Bilder, 30 Tab.
2015.
ISBN 978-3-87525-386-3.

Band 266: Hung Nguyen
Qualifizierung des Potentials von Verfestigungseffekten zur Erweiterung des Umformvermögens aushärtbarer Aluminiumlegierungen
LFT, 137 Seiten, 57 Bilder, 16 Tab.
2015. ISBN 978-3-87525-387-0.

Band 267: Andreas Kuppert
Erweiterung und Verbesserung von Versuchs- und Auswertetechniken für die Bestimmung von Grenzformänderungskurven
LFT, 138 Seiten, 82 Bilder, 2 Tab.
2015. ISBN 978-3-87525-388-7.

Band 268: Kathleen Klaus
Erstellung eines Werkstofforientierten Fertigungsprozessfensters zur Steigerung des Formgebungsvermögens von Alumi-niumlegierungen unter Anwendung einer zwischengeschalteten Wärmebehandlung
LFT, 154 Seiten, 70 Bilder, 8 Tab.
2015. ISBN 978-3-87525-391-7.

Band 269: Thomas Svec
Untersuchungen zur Herstellung von funktionsoptimierten Bauteilen im partiellen Presshärtprozess mittels lokal unterschiedlich temperierter Werkzeuge
LFT, 166 Seiten, 87 Bilder, 15 Tab.
2015. ISBN 978-3-87525-392-4.

Band 270: Tobias Schrader
Grundlegende Untersuchungen zur Verschleißcharakterisierung beschichteter Kaltmassivumformwerkzeuge
LFT, 164 Seiten, 55 Bilder, 11 Tab.
2015. ISBN 978-3-87525-393-1.

Band 271: Matthäus Brela
Untersuchung von Magnetfeld-Messmethoden zur ganzheitlichen Wertschöpfungsoptimierung und Fehlerdetektion an magnetischen Aktoren
FAPS, 170 Seiten, 97 Bilder, 4 Tab.
2015. ISBN 978-3-87525-394-8.

Band 272: Michael Wieland
Entwicklung einer Methode zur Prognose adhäsiven Verschleißes an Werkzeugen für das direkte Presshärten
LFT, 156 Seiten, 84 Bilder, 9 Tab.
2015. ISBN 978-3-87525-395-5.

Band 273: René Schramm
Strukturierte additive Metallisierung durch kaltaktives Atmosphärendruckplasma
FAPS, 136 Seiten, 62 Bilder, 15 Tab.
2015. ISBN 978-3-87525-396-2.

Band 274: Michael Lechner
Herstellung beanspruchungsangepasster Aluminiumblechhalbzeuge durch eine maßgeschneiderte Variation der Abkühlgeschwindigkeit nach Lösungsglühen
LFT, 136 Seiten, 62 Bilder, 15 Tab.
2015. ISBN 978-3-87525-397-9.

Band 275: Kolja Andreas
Einfluss der Oberflächenbeschaffenheit auf das Werkzeugeinsatzverhalten beim Kaltfließpressen
LFT, 169 Seiten, 76 Bilder, 4 Tab.
2015. ISBN 978-3-87525-398-6.

Band 276: Marcus Baum
Laser Consolidation of ITO Nanoparticles for the Generation of Thin Conductive Layers on Transparent Substrates
LPT, 158 Seiten, 75 Bilder, 3 Tab.
2015. ISBN 978-3-87525-399-3.

Band 277: Thomas Schneider
Umformtechnische Herstellung dünnwandiger Funktionsbauteile aus Feinblech durch Verfahren der Blechmassivumformung
LFT, 188 Seiten, 95 Bilder, 7 Tab.
2015. ISBN 978-3-87525-401-3.

Band 278: Jochen Merhof
Sematische Modellierung automatisierter Produktionssysteme zur Verbesserung der IT-Integration zwischen Anlagen-Engineering und Steuerungsebene
FAPS, 157 Seiten, 88 Bilder, 8 Tab.
2015. ISBN 978-3-87525-402-0.

Band 279: Fabian Zöller
Erarbeitung von Grundlagen zur Abbildung des tribologischen Systems in der Umformsimulation
LFT, 126 Seiten, 51 Bilder, 3 Tab.
2016. ISBN 978-3-87525-403-7.

Band 280: Christian Hezler
Einsatz technologischer Versuche zur Erweiterung der Versagensvorhersage bei Karosseriebauteilen aus höchstfesten Stählen
LFT, 147 Seiten, 63 Bilder, 44 Tab.
2016. ISBN 978-3-87525-404-4.

Band 281: Jochen Bönig
Integration des Systemverhaltens von Automobil-Hochvoltleitungen in die virtuelle Absicherung durch strukturmechanische Simulation
FAPS, 177 Seiten, 107 Bilder, 17 Tab.
2016.
ISBN 978-3-87525-405-1.

Band 282: Johannes Kohl
Automatisierte Datenerfassung für diskret ereignisorientierte Simulationen in der energieflexibelen Fabrik
FAPS, 160 Seiten, 80 Bilder, 27 Tab.
2016.
ISBN 978-3-87525-406-8.

Band 283: Peter Bechtold
Mikroschockwellenumformung mittels ultrakurzer Laserpulse
LPT, 155 Seiten, 59 Bilder, 10 Tab.
2016. ISBN 978-3-87525-407-5.

Band 284: Stefan Berger
Laserstrahlschweißen thermoplastischer Kohlenstofffaserverbundwerkstoffe mit spezifischem Zusatzdraht
LPT, 118 Seiten, 68 Bilder, 9 Tab.
2016. ISBN 978-3-87525-408-2.

Band 285: Martin Bornschlegl
Methods-Energy Measurement - Eine Methode zur Energieplanung für Fügeverfahren im Karosseriebau
FAPS, 136 Seiten, 72 Bilder, 46 Tab. 2016.
ISBN 978-3-87525-409-9.

Band 286: Tobias Rackow
Erweiterung des Unternehmenscontrollings um die Dimension Energie
FAPS, 164 Seiten, 82 Bilder, 29 Tab. 2016.
ISBN 978-3-87525-410-5.

Band 287: Johannes Koch
Grundlegende Untersuchungen zur Herstellung zyklisch-symmetrischer Bauteile mit Nebenformelementen durch Blechmassivumformung
LFT, 125 Seiten, 49 Bilder, 17 Tab. 2016. ISBN 978-3-87525-411-2.

Band 288: Hans Ulrich Vierzigmann
Beitrag zur Untersuchung der tribologischen Bedingungen in der Blechmassivumformung - Bereitstellung von tribologischen Modellversuchen und Realisierung von Tailored Surfaces
LFT, 174 Seiten, 102 Bilder, 34 Tab. 2016. ISBN 978-3-87525-412-9.

Band 289: Thomas Senner
Methodik zur virtuellen Absicherung der formgebenden Operation des Nasspressprozesses von Gelege-Mehrschichtverbunden
LFT, 156 Seiten, 96 Bilder, 21 Tab. 2016. ISBN 978-3-87525-414-3.

Band 290: Sven Kreitlein
Der grundoperationsspezifische Mindestenergiebedarf als Referenzwert zur Bewertung der Energieeffizienz in der Produktion
FAPS, 185 Seiten, 64 Bilder, 30 Tab. 2016.
ISBN 978-3-87525-415-0.

Band 291: Christian Roos
Remote-Laserstrahlschweißen verzinkter Stahlbleche in Kehlnahtgeometrie
LPT, 123 Seiten, 52 Bilder, 0 Tab. 2016. ISBN 978-3-87525-416-7.

Band 292: Alexander Kahrimanidis
Thermisch unterstützte Umformung von Aluminiumblechen
LFT, 165 Seiten, 103 Bilder, 18 Tab. 2016. ISBN 978-3-87525-417-4.

Band 293: Jan Tremel
Flexible Systems for Permanent Magnet Assembly and Magnetic Rotor Measurement / Flexible Systeme zur Montage von Permanentmagneten und zur Messung magnetischer Rotoren
FAPS, 152 Seiten, 91 Bilder, 12 Tab. 2016. ISBN 978-3-87525-419-8.

Band 294: Ioannis Tsoupis
Schädigungs- und Versagensverhalten hochfester Leichtbauwerkstoffe unter Biegebeanspruchung
LFT, 176 Seiten, 51 Bilder, 6 Tab. 2017. ISBN 978-3-87525-420-4.

Band 295: Sven Hildering
Grundlegende Untersuchungen zum Prozessverhalten von Silizium als Werkzeugwerkstoff für das Mikroscherschneiden metallischer Folien
LFT, 177 Seiten, 74 Bilder, 17 Tab. 2017. ISBN 978-3-87525-422-8.

Band 296: Sasia Mareike Hertweck
Zeitliche Pulsformung in der Lasermikromaterialbearbeitung – Grundlegende Untersuchungen und Anwendungen
LPT, 146 Seiten, 67 Bilder, 5 Tab. 2017. ISBN 978-3-87525-423-5.

Band 297: Paryanto
Mechatronic Simulation Approach for the Process Planning of Energy-Efficient Handling Systems
FAPS, 162 Seiten, 86 Bilder, 13 Tab. 2017. ISBN 978-3-87525-424-2.

Band 298: Peer Stenzel
Großserientaugliche Nadelwickeltechnik für verteilte Wicklungen im Anwendungsfall der E-Traktionsantriebe
FAPS, 239 Seiten, 147 Bilder, 20 Tab. 2017.
ISBN 978-3-87525-425-9.

Band 299: Mario Lušić
Ein Vorgehensmodell zur Erstellung montageführender Werkerinformationssysteme simultan zum Produktentstehungsprozess
FAPS, 174 Seiten, 79 Bilder, 22 Tab. 2017.
ISBN 978-3-87525-426-6.

Band 300: Arnd Buschhaus
Hochpräzise adaptive Steuerung und Regelung robotergeführter Prozesse
FAPS, 202 Seiten, 96 Bilder, 4 Tab. 2017. ISBN 978-3-87525-427-3.

Band 301: Tobias Laumer
Erzeugung von thermoplastischen Werkstoffverbunden mittels simultanem, intensitätsselektivem Laserstrahlschmelzen
LPT, 140 Seiten, 82 Bilder, 0 Tab. 2017. ISBN 978-3-87525-428-0.

Band 302: Nora Unger
Untersuchung einer thermisch unterstützten Fertigungskette zur Herstellung umgeformter Bauteile aus der höherfesten Aluminiumlegierung EN AW-7020
LFT, 142 Seiten, 53 Bilder, 8 Tab. 2017. ISBN 978-3-87525-429-7.

Band 303: Tommaso Stellin
Design of Manufacturing Processes for the Cold Bulk Forming of Small Metal Components from Metal Strip
LFT, 146 Seiten, 67 Bilder, 7 Tab. 2017. ISBN 978-3-87525-430-3.

Band 304: Bassim Bachy
Experimental Investigation, Modeling, Simulation and Optimization of Molded Interconnect Devices (MID) Based on Laser Direct Structuring (LDS) / Experimentelle Untersuchung, Modellierung, Simulation und Optimierung von Molded Interconnect Devices (MID) basierend auf Laser Direktstrukturierung (LDS)
FAPS, 168 Seiten, 120 Bilder, 26 Tab. 2017.
ISBN 978-3-87525-431-0.

Band 305: Michael Spahr
Automatisierte Kontaktierungsverfahren für flachleiterbasierte Pkw-Bordnetzsysteme
FAPS, 197 Seiten, 98 Bilder, 17 Tab. 2017. ISBN 978-3-87525-432-7.

Band 306: Sebastian Suttner
Charakterisierung und Modellierung des spannungszustandsabhängigen Werkstoffverhaltens der Magnesiumlegierung AZ31B für die numerische Prozessauslegung
LFT, 150 Seiten, 84 Bilder, 19 Tab. 2017. ISBN 978-3-87525-433-4.

Band 307: Bhargav Potdar
A reliable methodology to deduce thermo-mechanical flow behaviour of hot stamping steels
LFT, 203 Seiten, 98 Bilder, 27 Tab. 2017. ISBN 978-3-87525-436-5.

Band 308: Maria Löffler
Steuerung von Blechmassivumformprozessen durch maßgeschneiderte tribologische Systeme
LFT, viii u. 166 Seiten, 90 Bilder, 5 Tab. 2018. ISBN 978-3-96147-133-1.

Band 309: Martin Müller
Untersuchung des kombinierten Trenn- und Umformprozesses beim Fügen artungleicher Werkstoffe mittels Schneidclinchverfahren
LFT, xi u. 149 Seiten, 89 Bilder, 6 Tab. 2018.
ISBN: 978-3-96147-135-5.

Band 310: Christopher Kästle
Qualifizierung der Kupfer-Drahtbondtechnologie für integrierte Leistungsmodule in harschen Umgebungsbedingungen
FAPS, xii u. 167 Seiten, 70 Bilder, 18 Tab. 2018.
ISBN 978-3-96147-145-4.

Band 311: Daniel Vipavc
Eine Simulationsmethode für das 3-Rollen-Schubbiegen
LFT, xiii u. 121 Seiten, 56 Bilder, 17 Tab. 2018. ISBN 978-3-96147-147-8.

Band 312: Christina Ramer
Arbeitsraumüberwachung und autonome Bahnplanung für ein sicheres und flexibles Roboter-Assistenzsystem in der Fertigung
FAPS, xiv u. 188 Seiten, 57 Bilder, 9 Tab. 2018.
ISBN 978-3-96147-153-9.

Band 313: Miriam Rauer
Der Einfluss von Poren auf die Zuverlässigkeit der Lötverbindungen von Hochleistungs-Leuchtdioden
FAPS, xii u. 209 Seiten, 108 Bilder, 21 Tab. 2018.
ISBN 978-3-96147-157-7.

Band 314: Felix Tenner
Kamerabasierte Untersuchungen der Schmelze und Gasströmungen beim Laserstrahlschweißen verzinkter Stahlbleche
LPT, xxiii u. 184 Seiten, 94 Bilder, 7 Tab. 2018.
ISBN 978-3-96147-160-7.

Band 315: Aarief Syed-Khaja
Diffusion Soldering for High-temperature Packaging of Power Electronics
FAPS, x u. 202 Seiten, 144 Bilder, 32 Tab. 2018.
ISBN 978-3-87525-162-1.

Band 316: Adam Schaub
Grundlagenwissenschaftliche Untersuchung der kombinierten Prozesskette aus Umformen und Additive Fertigung
LFT, xi u. 192 Seiten, 72 Bilder, 27 Tab. 2019.
ISBN 978-3-96147-166-9.

Band 317: Daniel Gröbel
Herstellung von Nebenformelementen unterschiedlicher Geometrie an Blechen mittels Fließpressverfahren der Blechmassivumformung
LFT, x u. 165 Seiten, 96 Bilder, 13 Tab. 2019. ISBN 978-3-96147-168-3.

Band 318: Philipp Hildenbrand
Entwicklung einer Methodik zur Herstellung von Tailored Blanks mit definierten Halbzeugeigenschaften durch einen Taumelprozess
LFT, ix u. 153 Seiten, 77 Bilder, 4 Tab. 2019. ISBN 978-3-96147-174-4.

Band 319: Tobias Konrad
Simulative Auslegung der Spann- und Fixierkonzepte im Karosserierohbau: Bewertung der Baugruppenmaßhaltigkeit unter Berücksichtigung schwankender Einflussgrößen
LFT, x u. 203 Seiten, 134 Bilder, 32 Tab. 2019.
ISBN 978-3-96147-176-8.

Band 320: David Meinel
Architektur applikationsspezifischer Multi-Physics-Simulationskonfiguratoren am Beispiel modularer Triebzüge
FAPS, xii u. 166 Seiten, 82 Bilder, 25 Tab. 2019.
ISBN 978-3-96147-184-3.

Band 321: Andrea Zimmermann
Grundlegende Untersuchungen zum Einfluss fertigungsbedingter Eigenschaften auf die Ermüdungsfestigkeit kaltmassivumgeformter Bauteile
LFT, ix u. 160 Seiten, 66 Bilder, 5 Tab. 2019.
ISBN 978-3-96147-190-4.

Band 322: Christoph Amann
Simulative Prognose der Geometrie nassgepresster Karosseriebauteile aus Gelege-Mehrschichtverbunden
LFT, xvi u. 169 Seiten, 80 Bilder, 13 Tab. 2019.
ISBN 978-3-96147-194-2.

Band 323: Jennifer Tenner
Realisierung schmierstofffreier Tiefziehprozesse durch maßgeschneiderte Werkzeugoberflächen
LFT, x u. 187 Seiten, 68 Bilder, 13 Tab. 2019.
ISBN 978-3-96147-196-6.

Band 324: Susan Zöller
Mapping Individual Subjective Values to Product Design
KTmfk, xi u. 223 Seiten, 81 Bilder, 25 Tab. 2019.
ISBN 978-3-96147-202-4.

Band 325: Stefan Lutz
Erarbeitung einer Methodik zur semiempirischen Ermittlung der Umwandlungskinetik durchhärtender Wälzlagerstähle für die Wärmebehandlungssimulation
LFT, xiv u. 189 Seiten, 75 Bilder, 32 Tab. 2019.
ISBN 978-3-96147-209-3.

Band 326: Tobias Gnibl
Modellbasierte Prozesskettenabbildung rührreibgeschweißter Aluminiumhalbzeuge zur umformtechnischen Herstellung höchstfester Leichtbau-strukturteile
LFT, xii u. 167 Seiten, 68 Bilder, 17 Tab. 2019.
ISBN 978-3-96147-217-8.

Band 327: Johannes Bürner
Technisch-wirtschaftliche Optionen zur Lastflexibilisierung durch intelligente elektrische Wärmespeicher
FAPS, xiv u. 233 Seiten, 89 Bilder, 27 Tab. 2019.
ISBN 978-3-96147-219-2.

Band 328: Wolfgang Böhm
Verbesserung des Umformverhaltens von mehrlagigen Aluminiumblechwerkstoffen mit ultrafeinkörnigem Gefüge
LFT, ix u. 160 Seiten, 88 Bilder, 14 Tab. 2019.
ISBN 978-3-96147-227-7.

Band 329: Stefan Landkammer
Grundsatzuntersuchungen, mathematische Modellierung und Ableitung einer Auslegungsmethodik für Gelenkantriebe nach dem Spinnenbeinprinzip
LFT, xii u. 200 Seiten, 83 Bilder, 13 Tab. 2019.
ISBN 978-3-96147-229-1.

Band 330: Stephan Rapp
Pump-Probe-Ellipsometrie zur Messung transienter optischer Materialeigen-schaften bei der Ultrakurzpuls-Lasermaterialbearbeitung
LPT, xi u. 143 Seiten, 49 Bilder, 2 Tab. 2019.
ISBN 978-3-96147-235-2.

Band 331: Michael Scholz
Intralogistics Execution System mit integrierten autonomen, servicebasierten Transportentitäten
FAPS, xi u. 195 Seiten, 55 Bilder, 11 Tab. 2019.
ISBN 978-3-96147-237-6.

Band 332: Eva Bogner
Strategien der Produktindividualisierung in der produzierenden Industrie im Kontext der Digitalisierung
FAPS, ix u. 201 Seiten, 55 Bilder, 28 Tab. 2019.
ISBN 978-3-96147-246-8.

Band 333: Daniel Benjamin Krüger
Ein Ansatz zur CAD-integrierten muskuloskelettalen Analyse der Mensch-Maschine-Interaktion
KTmfk, x u. 217 Seiten, 102 Bilder, 7 Tab. 2019.
ISBN 978-3-96147-250-5.

Band 334: Thomas Kuhn
Qualität und Zuverlässigkeit laserdirektstrukturierter mechatronisch integrierter Baugruppen (LDS-MID)
FAPS, ix u. 152 Seiten, 69 Bilder, 12 Tab. 2019.
ISBN: 978-3-96147-252-9.

Band 335: Hans Fleischmann
Modellbasierte Zustands- und Prozessüberwachung auf Basis sozio-cyber-physischer Systeme
FAPS, xi u. 214 Seiten, 111 Bilder, 18 Tab. 2019.
ISBN: 978-3-96147-256-7.

Band 336: Markus Michalski
Grundlegende Untersuchungen zum Prozess- und Werkstoffverhalten bei schwingungsüberlagerter Umformung
LFT, xii u. 197 Seiten, 93 Bilder, 11 Tab. 2019.
ISBN: 978-3-96147-270-3.

Band 337: Markus Brandmeier
Ganzheitliches ontologiebasiertes Wissensmanagement im Umfeld der industriellen Produktion
FAPS, xi u. 255 Seiten, 77 Bilder, 33 Tab. 2020.
ISBN: 978-3-96147-275-8.

Band 338: Stephan Purr
Datenerfassung für die Anwendung lernender Algorithmen bei der Herstellung von Blechformteilen
LFT, ix u. 165 Seiten, 48 Bilder, 4 Tab. 2020.
ISBN: 978-3-96147-281-9.

Band 339: Christoph Kiener
Kaltfließpressen von gerad- und schrägverzahnten Zahnrädern
LFT, viii u. 151 Seiten, 81 Bilder, 3 Tab. 2020.
ISBN 978-3-96147-287-1.

Band 340: Simon Spreng
Numerische, analytische und empirische Modellierung des Heißcrimpprozesses
FAPS, xix u. 204 Seiten, 91 Bilder, 27 Tab. 2020.
ISBN 978-3-96147-293-2.

Band 341: Patrik Schwingenschlögl
Erarbeitung eines Prozessverständnisses zur Verbesserung der tribologischen Bedingungen beim Presshärten
LFT, x u. 177 Seiten, 81 Bilder, 8 Tab. 2020.
ISBN 978-3-96147-297-0.

Band 342: Emanuela Affronti
Evaluation of failure behaviour of sheet metals
LFT, ix u. 136 Seiten, 57 Bilder, 20 Tab. 2020.
ISBN 978-3-96147-303-8.

Band 343: Julia Degner
Grundlegende Untersuchungen zur Herstellung hochfester Aluminiumblechbauteile in einem kombinierten Umform- und Abschreckprozess
LFT, x u. 172 Seiten, 61 Bilder, 9 Tab. 2020.
ISBN 978-3-96147-307-6.

Band 344: Maximilian Wagner
Automatische Bahnplanung für die Aufteilung von Prozessbewegungen in synchrone Werkstück- und Werkzeugbewegungen mittels Multi-Roboter-Systemen
FAPS, xxi u. 181 Seiten, 111 Bilder, 15 Tab. 2020.
ISBN 978-3-96147-309-0.

Band 345: Stefan Härter
Qualifizierung des Montageprozesses hochminiaturisierter elektronischer Bauelemente
FAPS, ix u. 194 Seiten, 97 Bilder, 28 Tab. 2020.
ISBN 978-3-96147-314-4.

Band 346: Toni Donhauser
Ressourcenorientierte Auftragsregelung in einer hybriden Produktion mittels betriebsbegleitender Simulation
FAPS, xix u. 242 Seiten, 97 Bilder, 17 Tab. 2020.
ISBN 978-3-96147-316-8.

Band 347: Philipp Amend
Laserbasiertes Schmelzkleben von Thermoplasten mit Metallen
LPT, xv u. 154 Seiten, 67 Bilder. 2020. ISBN 978-3-96147-326-7.

Band 348: Matthias Ehlert
Simulationsunterstützte funktionale Grenzlagenabsicherung
KTmfk, xvi u. 300 Seiten, 101 Bilder, 73 Tab. 2020.
ISBN 978-3-96147-328-1.

Band 349: Thomas Sander
Ein Beitrag zur Charakterisierung und Auslegung des Verbundes von Kunststoffsubstraten mit harten Dünnschichten
KTmfk, xiv u. 178 Seiten, 88 Bilder, 21 Tab. 2020.
ISBN 978-3-96147-330-4.

Band 350: Florian Pilz
Fließpressen von Verzahnungselementen an Blechen
LFT, x u. 170 Seiten, 103Bilder, 4 Tab. 2020.
ISBN 978-3-96147-332-8.

Band 351: Sebastian Josef Katona
Evaluation und Aufbereitung von Produktsimulationen mittels abweichungsbehafteter Geometriemodelle
KTmfk, ix u. 147 Seiten, 73 Bilder, 11 Tab. 2020.
ISBN 978-3-96147-336-6.

Band 352: Jürgen Herrmann
Kumulatives Walzplattieren. Bewertung der Umformeigenschaften mehrlagiger Blechwerkstoffe der ausscheidungshärtbaren Legierung AA6014
LFT, x u. 157 Seiten, 64 Bilder, 5 Tab. 2020.
ISBN 978-3-96147-344-1.

Band 353: Christof Küstner
Assistenzsystem zur Unterstützung der datengetriebenen Produktentwicklung
KTmfk, xii u. 219 Seiten, 63 Bilder, 14 Tab. 2020.
ISBN 978-3-96147-348-9.

Band 354: Tobias Gläßel
Prozessketten zum Laserstrahlschweißen von flachleiterbasierten Formspulenwicklungen für automobile Traktionsantriebe
FAPS, xiv u. 206 Seiten, 89 Bilder, 11 Tab. 2020.
ISBN 978-3-96147-356-4.

Band 355: Andreas Meinel
Experimentelle Untersuchung der Auswirkungen von Axialschwingungen auf Reibung und Verschleiß in Zylinderrol-lenlagern
KTmfk, xii u. 162 Seiten, 56 Bilder, 7 Tab. 2020.
ISBN 978-3-96147-358-8.

Band 356: Hannah Riedle
Haptische, generische Modelle weicher anatomischer Strukturen für die chirurgische Simulation
FAPS, xxx u. 179 Seiten, 82 Bilder, 35 Tab. 2020.
ISBN 978-3-96147-367-0.

Band 357: Maximilian Landgraf
Leistungselektronik für den Einsatz dielektrischer Elastomere in aktorischen, sensorischen und integrierten sensomotorischen Systemen
FAPS, xxiii u. 166 Seiten, 71 Bilder, 10 Tab. 2020.
ISBN 978-3-96147-380-9.

Band 358: Alireza Esfandyari
Multi-Objective Process Optimization for Overpressure Reflow Soldering in Electronics Production
FAPS, xviii u. 175 Seiten, 57 Bilder, 23 Tab. 2020.
ISBN 978-3-96147-382-3.

Band 359: Christian Sand
Prozessübergreifende Analyse komplexer Montageprozessketten mittels Data Mining
FAPS, XV u. 168 Seiten, 61 Bilder, 12 Tab. 2021.
ISBN 978-3-96147-398-4.

Band 360: Ralf Merkl
Closed-Loop Control of a Storage-Supported Hybrid Compensation System for Improving the Power Quality in Medium Voltage Networks
FAPS, xxvii u. 200 Seiten, 102 Bilder, 2 Tab. 2021.
ISBN 978-3-96147-402-8.

Band 361: Thomas Reitberger
Additive Fertigung polymerer optischer Wellenleiter im Aerosol-Jet-Verfahren
FAPS, xix u. 141 Seiten, 65 Bilder, 11 Tab. 2021.
ISBN 978-3-96147-400-4.

Band 362: Marius Christian Fechter
Modellierung von Vorentwürfen in der virtuellen Realität mit natürlicher Fingerinteraktion
KTmfk, x u. 188 Seiten, 67 Bilder, 19 Tab. 2021.
ISBN 978-3-96147-404-2.

Band 363: Franziska Neubauer
Oberflächenmodifizierung und Entwicklung einer Auswertemethodik zur Verschleißcharakterisierung im Presshärteprozess
LFT, ix u. 177 Seiten, 42 Bilder, 6 Tab. 2021.
ISBN 978-3-96147-406-6.

Band 364: Eike Wolfram Schäffer
Web- und wissensbasierter Engineering-Konfigurator für roboterzentrierte Automatisierungslösungen
FAPS, xxiv u. 195 Seiten, 108 Bilder, 25 Tab. 2021.
ISBN 978-3-96147-410-3.

Band 365: Daniel Gross
Untersuchungen zur kohlenstoffdioxidbasierten kryogenen Minimalmengenschmierung
REP, xii u. 184 Seiten, 56 Bilder, 18 Tab. 2021.
ISBN 978-3-96147-412-7.

Band 366: Daniel Junker
Qualifizierung laser-additiv gefertigter Komponenten für den Einsatz im Werkzeugbau der Massivumformung
LFT, vii u. 142 Seiten, 62 Bilder, 5 Tab. 2021.
ISBN 978-3-96147-416-5.

Band 367: Tallal Javied
Totally Integrated Ecology Management for Resource Efficient and Eco-Friendly Production
FAPS, xv u. 160 Seiten, 60 Bilder, 13 Tab. 2021.
ISBN 978-3-96147-418-9.

Band 368: David Marco Hochrein
Wälzlager im Beschleunigungsfeld – Eine Analysestrategie zur Bestimmung des Reibungs-, Axialschub- und Temperaturverhaltens von Nadelkränzen –
KTmfk, xiii u. 279 Seiten, 108 Bilder, 39 Tab. 2021.
ISBN 978-3-96147-420-2.

Band 369: Daniel Gräf
Funktionalisierung technischer Oberflächen mittels prozessüberwachter aerosolbasierter Drucktechnologie
FAPS, xxii u. 175 Seiten, 97 Bilder, 6 Tab. 2021.
ISBN 978-3-96147-433-2.

Band 370: Andreas Gröschl
Hochfrequent fokusabstandsmodulierte Konfokalsensoren für die Nanokoordinatenmesstechnik
FMT, x u. 144 Seiten, 98 Bilder, 6 Tab. 2021.
ISBN 978-3-96147-435-6.

Band 371: Johann Tüchsen
Konzeption, Entwicklung und Einführung des Assistenzsystems D-DAS für die Produktentwicklung elektrischer Motoren
KTmfk, xii u. 178 Seiten, 92 Bilder, 12 Tab. 2021.
ISBN 978-3-96147-437-0.

Band 372: Max Marian
Numerische Auslegung von Oberflächenmikrotexturen für geschmierte tribologische Kontakte
KTmfk, xviii u. 276 Seiten, 85 Bilder, 45 Tab. 2021.
ISBN 978-3-96147-439-4.

Band 373: Johannes Strauß
Die akustooptische Strahlformung in der Lasermaterialbearbeitung
LPT, xvi u. 113 Seiten, 48 Bilder. 2021. ISBN 978-3-96147-441-7.

Band 374: Martin Hohmann
Machine learning and hyper spectral imaging: Multi Spectral Endoscopy in the Gastro Intestinal Tract towards Hyper Spectral Endoscopy
LPT, x u. 137 Seiten, 62 Bilder, 29 Tab. 2021.
ISBN 978-3-96147-445-5.

Band 375: Timo Kordaß
Lasergestütztes Verfahren zur selektiven Metallisierung von epoxidharzbasierten Duromeren zur Steigerung der Integrationsdichte für dreidimensionale mechatronische Package-Baugruppen
FAPS, xviii u. 198 Seiten, 92 Bilder, 24 Tab. 2021.
ISBN 978-3-96147-443-1.

Band 376: Philipp Kestel
Assistenzsystem für den wissensbasierten Aufbau konstruktionsbegleitender Finite-Elemente-Analysen
KTmfk, xviii u. 209 Seiten, 57 Bilder, 17 Tab. 2021.
ISBN 978-3-96147-457-8.

Band 377: Martin Lerchen
Messverfahren für die pulverbettbasierte additive Fertigung zur Sicherstellung der Konformität mit geometrischen Produktspezifikationen
FMT, x u. 150 Seiten, 60 Bilder, 9 Tab. 2021.
ISBN 978-3- 96147-463-9.

Band 378: Michael Schneider
Inline-Prüfung der Permeabilität in weichmagnetischen Komponenten
FAPS, xxii u. 189 Seiten, 79 Bilder, 14 Tab. 2021.
ISBN 978-3-96147-465-3.

Band 379: Tobias Sprügel
Sphärische Detektorflächen als Unterstützung der Produktentwicklung zur Datenanalyse im Rahmen des Digital Engineering
KTmfk, xiii u. 213 Seiten, 84 Bilder, 33 Tab. 2021.
ISBN 978-3-96147-475-2.

Band 380: Tom Häfner
Multipulseffekte beim Mikro-Materialabtrag von Stahllegierungen mit Pikosekunden-Laserpulsen
LPT, xxviii u. 159 Seiten, 57 Bilder, 13 Tab. 2021.
ISBN 978-3-96147-479-0.

Band 381: Björn Heling
Einsatz und Validierung virtueller Absicherungsmethoden für abweichungs-behaftete Mechanismen im Kontext des Robust Design
KTmfk, xi u. 169 Seiten, 63 Bilder, 27 Tab. 2021.
ISBN 978-3-96147-487-5.

Band 382: Tobias Kolb
Laserstrahl-Schmelzen von Metallen mit einer Serienanlage – Prozesscharakterisierung und Erweiterung eines Überwachungssystems
LPT, xv u. 170 Seiten, 128 Bilder, 16 Tab. 2021.
ISBN 978-3-96147-491-2.

Band 383: Mario Meinhardt
Widerstandselementschweißen mit gestauchten Hilfsfügeelementen - Umformtechnische Wirkzusammenhänge zur Beeinflussung der Verbindungsfestigkeit
LFT, xii u. 189 Seiten, 87 Bilder, 4 Tab. 2022.
ISBN 978-3-96147-473-8.

Band 384: Felix Bauer
Ein Beitrag zur digitalen Auslegung von Fügeprozessen im Karosseriebau mit Fokus auf das Remote-Laserstrahlschweißen unter Einsatz flexibler Spanntechnik
LFT, xi u. 185 Seiten, 74 Bilder, 12 Tab. 2022.
ISBN 978-3-96147-498-1.

Band 385: Jochen Zeitler
Konzeption eines rechnergestützten Konstruktionssystems für optomechatronische Baugruppen
FAPS, xix u. 172 Seiten, 88 Bilder, 11 Tab. 2022.
ISBN 978-3-96147-499-8.

Band 386: Vincent Mann
Einfluss von Strahloszillation auf das Laserstrahlschweißen hochfester Stähle
LPT, xiii u. 172 Seiten, 103 Bilder, 18 Tab. 2022.
ISBN 978-3-96147-503-2.

Band 387: Chen Chen
Skin-equivalent opto-/elastofluidic in-vitro microphysiological vascular models for translational studies of optical biopsies
LPT, xx u. 126 Seiten, 60 Bilder, 10 Tab. 2022.
ISBN 978-3-96147-505-6.

Band 388: Stefan Stein
Laser drop on demand joining as bonding method for electronics assembly and packaging with high thermal requirements
LPT, x u. 112 Seiten, 54 Bilder, 10 Tab. 2022.
ISBN 978-3-96147-507-0

Band 389: Nikolaus Urban
Untersuchung des Laserstrahlschmelzens von Neodym-Eisen-Bor zur additiven Herstellung von Permanentmagneten
FAPS, x u. 174 Seiten, 88 Bilder, 18 Tab. 2022.
ISBN 978-3-96147-501-8.

Band 390: Yiting Wu
Großflächige Topographiemessungen mit einem Weißlichtinterferenzmikroskop und einem metrologischen Rasterkraftmikroskop
FMT, xii u. 142 Seiten, 68 Bilder, 11 Tab. 2022.
ISBN: 978-3-96147-513-1.

Band 391: Thomas Papke
Untersuchungen zur Umformbarkeit hybrider Bauteile aus Blechgrundkörper und additiv gefertigter Struktur
LFT, xii u. 194 Seiten, 71 Bilder, 16 Tab. 2022.
ISBN 978-3-96147-515-5.

Band 392: Bastian Zimmermann
Einfluss des Vormaterials auf die mehrstufige Kaltumformung vom Draht
LFT, xi u. 182 Seiten, 36 Bilder, 6 Tab. 2022.
ISBN 978-3-96147-519-3.

Band 393: Harald Völkl
Ein simulationsbasierter Ansatz zur Auslegung additiv gefertigter FLM-Faserverbundstrukturen
KTmfk, xx u. 204 Seiten, 95 Bilder, 22 Tab. 2022.
ISBN 978-3-96147-523-0.

Band 394: Robert Schulte
Auslegung und Anwendung prozessangepasster Halbzeuge für Verfahren der Blechmassivumformung
LFT, x u. 163 Seiten, 93 Bilder, 5 Tab. 2022.
ISBN 978-3-96147-525-4.

Band 395: Philipp Frey
Umformtechnische Strukturierung metallischer Einleger im Folgeverbund für mediendichte Kunststoff-Metall-Hybridbauteile
LFT, ix u. 180 Seiten, 83 Bilder, 7 Tab. 2022.
ISBN 978-3-96147-534-6.

Band 396: Thomas Johann Luft
Komplexitätsmanagement in der Produktentwicklung - Holistische Modellierung, Analyse, Visualisierung und Bewertung komplexer Systeme
KTmfk, xiii u. 510 Seiten, 166 Bilder, 16 Tab. 2022.
ISBN 978-3-96147-540-7.

Band 397: Li Wang
Evaluierung der Einsetzbarkeit des lasergestützten Verfahrens zur selektiven Metallisierung für die Verbesserung passiver Intermodulation in Hochfrequenzanwendungen
FAPS, xxii u.151 Seiten, 72 Bilder, 22 Tab. 2022.
ISBN 978-3-96147-542-1.

Band 398: Sebastian Reitelshöfer
Der Aerosol-Jet-Druck Dielektrischer Elastomere als additives Fertigungsverfahren für elastische mechatronische Komponenten
FAPS, xxv u. 206 Seiten, 87 Bilder, 13 Tab. 2022.
ISBN 978-3-96147-547-6.

Band 399: Alexander Meyer
Selektive Magnetmontage zur Verringerung des Rastmomentes permanenterregter Synchronmotoren
FAPS, xv u. 164 Seiten, 90 Bilder, 18 Tab. 2022.
ISBN 978-3-96147-555-1.

Band 400: Rong Zhao
Design verschleißreduzierender amorpher Kohlenstoffschichtsysteme für trockene tribologische Gleitkontakte
KTmfk, x u. 148 Seiten, 69 Bilder, 14 Tab. 2022.
ISBN 978-3-96147-557-5.

Band 401: Christian P. J. Schwarzer
Kupfersintern als Fügetechnologie für Leistungselektronik
FAPS, xxvii u. 234 Seiten, 125 Bilder, 24 Tab. 2022.
ISBN 978-3-96147-566-7.

Band 402: Alexander Horn
Grundlegende Untersuchungen zur Gradierung der mechanischen Eigenschaften pressgehärteter Bauteile durch eine örtlich begrenzte Aufkohlung
LFT, xii u. 204 Seiten, 58 Bilder, 6 Tab. 2022.
ISBN 978-3-96147-568-1.

Band 403: Artur Klos
Werkstoff- und umformtechnische Bewertung von hochfesten Aluminiumblechwerkstoffen für den Karosseriebau
LFT, x u. 192 Seiten, 73 Bilder, 12 Tab. 2022.
ISBN 978-3-96147-572-8.

Band 404: Harald Schmid
Ganzheitliche Erarbeitung eines Prozessverständnisses von Tiefziehprozessen mit Ziehsicken auf Basis mechanischer und tribologischer Analysen
LFT, xiii u. 211 Seiten, 78 Bilder, 5 Tab. 2022.
ISBN 978-3-96147-577-3.

Band 405: Johannes Henneberg
Blechmassivumformung von Funktionsbauteilen aus Bandmaterial
LFT, viii u. 176 Seiten, 101 Bilder, 2 Tab. 2022.
ISBN 978-3-96147-579-7.

Band 406: Anton Schmailzl
Festigkeits- und zeitoptimierte Prozessführung beim quasi-simultanen Laser-Durchstrahlschweißen
LPT, xiii u. 157 Seiten, 84 Bilder, 7 Tab. 2022.
ISBN 978-3-96147-583-4.

Band 407: Alexander Wolf
Modellierung und Vorhersage menschlichen Interaktionsverhaltens zur Analyse der Mensch-Produkt Interaktion
KTmfk, x u. 207 Seiten, 69 Bilder, 10 Tab. 2022.
ISBN 978-3-96147-585-8.

Band 408: Tim Weikert
Modifikationen amorpher Kohlenstoffschichten zur Anpassung der Reibungsbedingungen und zur Erhöhung des Verschleißschutzes
KTmfk, xvii u. 258 Seiten, 91 Bilder, 9 Tab. 2022.
ISBN 978-3-96147-589-6.

Band 409: Stefan Götz
Frühzeitiges konstruktionsbegleitendes Toleranzmanagement
KTmfk, ix u. 276 Seiten, 127 Bilder, 13 Tab. 2022.
ISBN 978-3-96147-593-3.

Band 410: Markus Hubert
Einsatzpotenziale der Rotationsschneidtechnologie in der Verarbeitung von metallischen Funktionsfolien für mechatronische Produkte
FAPS, xviii u. 139 Seiten, 86 Bilder, 7 Tab. 2022.
ISBN 978-3-96147-603-9.

Band 411: Manfred Vogel
Grundlagenuntersuchungen und Erarbeitung einer Methodik zur Herstellung maßgeschneiderter Halbzeuge auf Basis eines neuartigen flexiblen Walzprozesses
LFT, ix u. 176 Seiten, 61 Bilder, 11 Tab. 2022.
ISBN 978-3-96147-605-3.

Band 412: Michael Weigelt
Multidimensionale Optionenanalyse alternativer Antriebskonzepte für die individuelle Langstreckenmobilität
FAPS, xv u. 222 Seiten, 89 Bilder, 38 Tab. 2022.
ISBN 978-3-96147-607-7.

Band 413: Frank Bodendorf
Machine Learning im Cost Engineering des Supply Managements
FAPS, xiii u. 165 Seiten, 75 Bilder, 13 Tab. 2023.
ISBN 978-3-96147-609-1.

Band 414: Maximilian Metzler
Planung und Simulation taktiler, intelligenter und kollaborativer Roboterfähigkeiten in der Montage
FAPS, xix u. 174 Seiten, 72 Bilder, 3 Tab. 2023.
ISBN 978-3-96147-611-4.

Band 415: Tina Buker
Ein Ansatz zur Reduktion produktinduzierter Nutzerstigmatisierung durch Förderung einer gleichermaßen gebrauchstauglichen wie emotionalen Produktgestalt
KTmfk, x u. 236 Seiten, 54 Bilder, 44 Tab. 2022.
ISBN 978-3-96147-613-8.

Band 416: Marlene Kuhn
Model-based Traceability System Development for Complex Manufacturing Applying Blockchain and Graphs
FAPS, xv u. 167 Seiten, 63 Bilder, 10 Tab. 2022.
ISBN 978-3-96147-615-2.

Band 417: Benjamin Lengenfelder
Remote photoacoustic sensing using speckle-analysis for biomedical imaging
LPT, xv u. 124 Seiten, 86 Bilder, 10 Tab. 2023.
ISBN 978-3-96147-617-6.

Band 418: Benjamin Pohrer
Analyse des Zusammenhangs zwischen dem tribochemischen Aufbau von Grenzschichten und der Ausbildung von White Etching Crack-Schäden
KTmfk, xv u. 258 Seiten, 103 Bilder, 10 Tab. 2023.
ISBN 978-3-96147- 621-3.

Band 419: Matthias Friedlein
Zuverlässigkeitsmethoden zur Beschleunigung von Qualifizierungsuntersuchungen für Steckkontakte
FAPS, xxv u. 162 Seiten, 98 Bilder, 7 Tab. 2023.
ISBN 978-3-96147-625-1.

Band 420: Thomas Stoll
Laser Powder Bed Fusion von Kupfer auf Aluminiumoxid-Keramiken
FAPS, xxvii u. 236 Seiten, 103 Bilder, 11 Tab. 2023.
ISBN 978-3-96147-631-2.

Band 421: Eric Eschner
Relation of Particle Motion and Process Zone Formation as a Basis for Sensing Approaches within PBF-LB/M
LPT, xiv u. 143 Seiten, 87 Bilder, 0 Tab. 2023.
ISBN 978-3-96147-633-6.

Band 422: Mehari, Fanuel
Laser-induced Breakdown Spectroscopy (LIBS) as a diagnostics tool for biological tissue analysis.
LPT, xv u. 145 Seiten, 68 Bilder, 12 Tab. 2023.
ISBN 978-3-96147-641-1

Kurzzusammenfassung

In dieser Arbeit wird die aufkommende Analysetechnik der Laser-induced Breakdown-Spektroscopy (LIBS) als Diagnoseinstrument für die Analyse biologischer Gewebe untersucht. Die beiden Hauptziele der Arbeit sind die Verwendung von LIBS zur Bereitstellung von Informationen über den Gewebetyp während laserchirurgischer Eingriffe und die Verwendung von LIBS als bildgebendes Verfahren durch Kartierung der Verteilung von Elementen in Geweben. Die Machbarkeit von LIBS für die direkte Messung von Elementen in biologischem Gewebe und die indirekte Messung von Molekülen wurde vorgestellt. Die Anwendbarkeit von LIBS für die Echtzeit-Gewebeklassifizierung zur Verwendung als Feedback-Kontrollmechanismus für klinische Laserchirurgiesysteme wurde nachgewiesen. Es wurde eine hohe Klassifizierungsgenauigkeit für verschiedene Gewebe erreicht. Die Ergebnisse der Messung der Verteilung von Elementen in Geweben zeigen, dass LIBS ein leistungsfähiges bildgebendes Verfahren für medizinische Anwendungen sein kann, die die Zielsetzung haben, die chemische Mikroumgebung von Geweben verstehen zu wollen. Dies wurde durch die Kartierung der unterschiedlichen Verteilung bestimmter Elemente zwischen krebsartigem und gesundem Gewebe nachgewiesen.

In this thesis, the emerging analytical technique laser-induced breakdown spectroscopy(LIBS) is investigated as a diagnostic tool for biological tissues analysis. The two main objectives of the work are using LIBS to provide tissue type feedback information during laser surgery and to use LIBS as an imaging modality by mapping the distribution of elements in tissues. The viability of LIBS for the direct measurement of elements in biological tissue and indirect measurement of molecules has been presented. The applicability of LIBS for real-time tissue classification to use it as a feedback control mechanism of clinical laser surgery systems has been demonstrated. High classification accuracy of different tissues has been achieved. The results of measuring the distribution of elements in tissues shows that LIBS can be a powerful imaging modality for medical applications that seek to understand the chemical microenvironment of tissues. This has been demonstrated by mapping the different distribution of certain elements between cancerous and healthy tissues.

ISBN 978-3-96147-641-1

9 783961 476411

FAU UNIVERSITY PRESS 2023